

ATOMIC DIFFUSION AND PHASE PRECIPITATION STUDIES IN  
AMORPHOUS METALLIC ALLOYS USING RUTHERFORD BACKSCATTERING  
SPECTROMETRY AND MOSSBAUER SPECTROSCOPY

*by*

NOBIN BANERJI

PHY  
1992  
D  
BAN  
ATO



DEPARTMENT OF PHYSICS

INDIAN INSTITUTE OF TECHNOLOGY KANPUR

JULY, 1992

**ATOMIC DIFFUSION AND PHASE PRECIPITATION STUDIES IN  
AMORPHOUS METALLIC ALLOYS USING RUTHERFORD BACKSCATTERING  
SPECTROMETRY AND MOSSBAUER SPECTROSCOPY**

*A Thesis Submitted  
In Partial Fulfilment of the Requirements  
for the Degree of*  
**DOCTOR OF PHILOSOPHY**

*by*  
**NOBIN BANERJI**

*to the*  
**DEPARTMENT OF PHYSICS  
INDIAN INSTITUTE OF TECHNOLOGY KANPUR  
JULY, 1992**

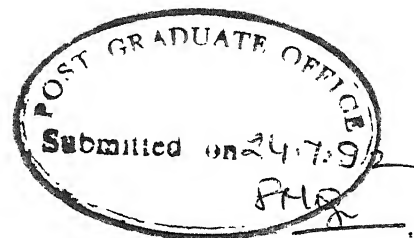
27 JUN 1994, Phy

CENTRAL LIBRARY  
U.S. AIR FORCE

**Doc. No. A. 117962**

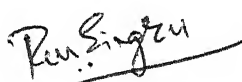
TH  
5395212  
B2230


PHY-1992-D-DAN-ATO



## CERTIFICATE

It is certified that the work contained in the thesis entitled "ATOMIC DIFFUSION AND PHASE PRECIPITATION STUDIES IN AMORPHOUS METALLIC ALLOYS USING RUTHERFORD BACKSCATTERING SPECTROMETRY AND MÖSSBAUER SPECTROSCOPY" by Nobin Banerji has been carried out under our supervision. This work has not been submitted elsewhere for a degree.

  
( R. M. SINGRU )  
Professor  
Department of Physics  
I. I. T. Kanpur, INDIA

  
( V. N. KULKARNI )  
Assistant Professor  
Department of Physics  
I. I. T. Kanpur, INDIA

JULY, 1992



*DEDICATED*

*TO*

*MA - BABAI*

# ACKNOWLEDGEMENTS

I sincerely express my deep sense of gratitude to my thesis advisors, Professor R. M. Singru and Dr. V. N. Kulkarni, for understanding and motivating me, and providing expert guidance throughout my research work. I am indebted to them for their help in identifying the thesis problem at a very crucial stage of my career. This thesis owes a lot to them for patiently going through it several times, giving critical remarks and improving the contents, while keeping in view the overall objectives of the work.

I am whole-heartedly grateful to Professor Y. R. Waghmare (Dean of Students Affairs), Department of Physics, for initiating me into this field. I am indebted to him for his fatherly advice and help throughout the period of my stay in IIT Kanpur.

Dr. Umesh C. Johri helped me a lot in getting acquainted with the Mössbauer set-up. I convey my sincere gratitude to him for the same. I am grateful to all my friends, especially to Ranjit Pradhan, Rita Singhal, Surojit Mukherjee, Shankar Dhar and Tapobrato Som for providing timely aid and making my stay in the Institute a pleasant experience.

The brotherly companionship and sincere advice from Dr. K.V.Jayakumar in all matters needs special mention and I am truly and sincerely indebted to him.

Sincere and special appreciation are due to the technical staff of the Van-de-Graaff lab, namely Jhasahab, Masoodji, Guptaji, Shivprakash and Rajput for their excellent cooperation and encouragement and maintaining a lively atmosphere in the lab. Working with them was quite an enjoyable experience.

I wish to thank the technical staff of the Physics Workshop for their excellent lathe work, especially Mr. J. S. Sharma, Mr. Gosai and Mr. Ram Mangal Singh, for fabricating in time, various items required for the experimental set-up.

And finally, I sincerely acknowledge the last minute help from Mr. S. S. Pathak, while photocopying the thesis in its final form.

The constant encouragement, excellent understanding and abundant affection provided to me by my mother, father, brothers, and bhabiji's, throughout my research career had boosted my morale culminating in this thesis. Their blessings and best wishes have brought out the best in me. Kudos to my wife Anjana for patiently bearing my gloominess, providing mental support during critical periods, managing the house all alone, and never complaining of my regular absence for long hours away from home.

NORIN BANERJI

# SYNOPSIS

Name of Student : NOBIN BANERJI                      Roll No. : 8420961

Degree for which submitted : Ph.D.                      Department : Physics

Thesis Title : ATOMIC DIFFUSION AND PHASE PRECIPITATION  
STUDIES IN AMORPHOUS METALLIC ALLOYS USING  
RUTHERFORD BACKSCATTERING SPECTROMETRY AND  
MOSSBAUER SPECTROSCOPY.

Thesis Supervisors : Dr. R. M. Singru, Professor of Physics,  
I.I.T. Kanpur - 208016, India.

Dr. V. N. Kulkarni, Asst. Professor of  
Physics, I.I.T. Kanpur - 208016, India.

Month and Year of thesis submission : July - 1992

Amorphous metallic alloys, also called as glassy alloys or metallic glasses have drawn the attention of scientists, engineers and technologists alike, because these alloys possess a variety of highly desirable properties (electrical, magnetic, mechanical, thermal, etc.,) useful in industrial and scientific work. For example, transformer cores and laminations made of iron based metallic glasses ( $\text{Fe}_{78}\text{B}_{13}\text{Si}_9$ ,  $\text{Fe}_{81}\text{B}_{13}\text{Si}_4\text{C}_2$ ,  $\text{Fe}_{82}\text{B}_{10}\text{Si}_8$ , etc.,) have higher efficiency, lower cost and considerable energy saving potential. The properties of an amorphous alloy are determined by its atomic structure and both are very sensitive to heat treatment. On annealing it tends to relax and become denser by atomic rearrangement, which in turn is controlled by the diffusion of the atoms through the amorphous structure. Therefore a knowledge of the atomic transport or diffusion in metallic glasses is important in understanding the changes

occurring in these structure-sensitive thermal, electrical, magnetic and mechanical properties.

The first diffusion experiment performed on metallic glasses was reported by Gupta et. al. in 1975. Since then, there has been a steady increase in the volume of diffusion data and these have been reviewed from time to time [Luborsky 1983; Cantor 1985; Mehrer and Dorner 1989]. In most cases the Arrhenius dependence of the diffusion coefficient ( $D$ ) on the annealing temperature ( $T$ ) has been reported, which is given by the equation  $D = D_0 \exp(-Q/kT)$ , where  $D_0$  is called as pre-exponential factor,  $Q$  is activation energy and  $k$  is Boltzmann constant. Correlations between these parameters and the physical properties of the alloys and those of the diffusing species, lead the authors to make speculations on the possible diffusion mechanisms. However for several cases of diffusion studies reported in the literature the relaxation effect in the metallic glasses was not considered. In the diffusion measurements on amorphous alloys, it is essential to study the  $D$  versus time dependence, to delineate the effect of relaxation. The  $D_0$  and  $Q$  values obtained by properly taking into account the relaxation effect should be used to identify the diffusion mechanism on the basis of a theoretical formalism. Keeping in view this important fact, in the present work we have studied the diffusion of various elements (Ge, Pd, Au, Ag) in amorphous metal-metalloid metallic glasses  $\text{Fe}_{79}\text{B}_{16}\text{Si}_5$ ,  $\text{Fe}_{78}\text{B}_{13}\text{Si}_9$ , and  $\text{Fe}_{40}\text{Ni}_{38}\text{B}_{18}\text{Mo}_4$ . The crystallization onset temperature  $T_x$  for these metallic glasses as reported in literature [Goodfellow Metals-Catalogue 1991/92] are  $515^\circ\text{C}$ ,  $550^\circ\text{C}$  and  $410^\circ\text{C}$  respectively. The elements selected for diffusion studies provide mass variation from 73 to 197, variation in atomic radii from 1.37 to 1.44 Å and ionic radii from 0.93 to 1.37 Å. The atomic mass of each element is larger than that of Fe (the constituent having the greatest mass in the Fe-B-Si metallic glass substrates). Therefore the signals from the elements are well separated in the Rutherford backscattering

measurements. This leads to accurate measurements of the depth profiles and the diffusion coefficients. These elements do not form globules on the surface of the metallic glass after heat treatment. The globular formations can obscure the diffusion profile. Good quality films of these elements can be prepared by vacuum evaporation technique.

*Transmission Mössbauer spectroscopy (TMS) and X-ray diffraction (XRD)* measurements were carried out on the Fe-B-Si metallic glasses. The samples were heat-treated at various temperatures ranging from a value well below their  $T_x$  to a value well above  $T_x$ , to identify the temperatures and annealing time-periods which retain the amorphous structure of the metallic glasses. The crystallization kinetics of these alloys (after successive heat-treatment) has also been studied at the same time.

The topographical changes occurring on the surface of the samples during annealing were studied using *Scanning electron microscopy (SEM)*, specifically to detect globule formation on the surface of the samples.

The diffusion measurements were performed by *Rutherford backscattering spectrometry (RBS)*.

The thesis is divided into six chapters. The importance of metallic glasses is brought out in Chapter 1, along with a brief discussion of the various models proposed in understanding their structure, and the various methods employed for their production. The alternative methods of diffusion measurement and the various formalism applicable to diffusion in metallic glasses is also given in this chapter.

A compilation of diffusion measurements in metallic glasses, obtained by using direct methods is presented. A similar compilation of phase precipitation studies in metallic glasses performed using Mössbauer spectroscopy is also presented. The chapter ends with an outline of the aim and necessity of the present study.

The theoretical background and formalism required for the understanding of Mössbauer spectroscopy and Rutherford backscattering spectrometry are highlighted in Chapter 2.

Chapter 3 deals with the methodology of sample preparation along with a description of the experimental details of the present work. The diffusion couples in the form of thin films of the diffusing element on the metallic glasses  $\text{Fe}_{79}\text{B}_{16}\text{Si}_5$  and  $\text{Fe}_{78}\text{B}_{13}\text{Si}_9$  were prepared by the process of vacuum evaporation of high purity (99.99%) elements, namely Au, Ge, Pd and Ag. The diffusion couples for Pd/ $\text{Fe}_{40}\text{Ni}_{38}\text{B}_{18}\text{Mo}_4$  system were also prepared in a similar manner. These diffusion couples were isothermally annealed in a clean and high vacuum for various time intervals (ranging upto 16 hr) and temperatures (ranging from  $300^\circ\text{C}$  to  $475^\circ\text{C}$ ), using separate samples for different temperatures. The RBS studies were carried out using the 2 MeV Van-de-Graaff accelerator system in the Central Nuclear Facility, Department of Physics, Indian Institute of Technology, Kanpur.  $\text{He}^+$  ions of energy 1.0 and 1.4 MeV, were utilized for RBS measurements. A silicon surface barrier detector was used for detecting the ions backscattered from the sample surface at an angle of  $150^\circ$ . The detector was cooled down to  $10^\circ\text{C}$ , to reduce the detector leakage current. The detection and data acquisition system consisted of the detector, preamplifier, amplifier, biased amplifier and a multichannel analyzer (MCA). The method of backscattering analysis has been explained by giving an example of Pd diffusion in a Fe-B-Si metallic glass. The diffusion coefficients were obtained by comparing the experimentally observed depth profiles with those derived theoretically from the solution of the diffusion equation under appropriate boundary condition pertinent to the couple configuration.

Mössbauer studies have been performed using  $^{57}\text{Co}$  embedded in Rh matrix source, and the transmitted  $\gamma$ -rays were detected using a counter. The Mössbauer spectrometer (briefly described in this

chapter), consists of the radioactive source, the detection and amplification system and a MCA for data storage. Optimization methods as considered in this technique are mentioned too. The methodology for the analysis of phase characterization of the crystallized samples is also explained. Finally a brief outline of the specifications of the XRD and SEM measurements are mentioned.

The results on Mössbauer and X-ray studies in the Fe-B-Si metallic glasses are discussed in Chapter 4. These results reveal that the metallic glass samples remain amorphous below 450°C. The amorphous samples showed a definite increase in internal magnetic field (H) and isomer shift (IS) with increasing silicon concentration. Definite indication of the crystallization process in the case of  $\text{Fe}_{79}\text{B}_{16}\text{Si}_5$  glass appears after heat-treatment for 4 hr at 450°C. While for  $\text{Fe}_{78}\text{B}_{13}\text{Si}_9$  the precipitation commences after heat-treatment for 1 hr at 475°C. The various phases precipitated above these temperature and time-period of annealing for the Fe-B-Si glasses were identified as  $\text{t-Fe}_3\text{B}$ ,  $\text{Fe}_2\text{B}$ ,  $\alpha\text{-Fe}$  and  $\alpha\text{-(Fe-Si)}$  (solid solution, formed at 8nn (nearest neighbour), 7nn, 6nn, 5nn, and 4nn Fe sites). However the amount of  $\text{Fe}_3\text{B}$  phase precipitated in  $\text{Fe}_{78}\text{B}_{13}\text{Si}_9$  was observed to be less than that in the  $\text{Fe}_{79}\text{B}_{16}\text{Si}_5$  glass. These results indicate that the replacement of B with Si improves the thermal stability in the Fe-B-Si metallic glasses.

X-ray diffraction studies of the Fe-B-Si metallic glasses after heat-treatment at 600°C (2 hr) and 700°C (15 min.), (which are well above  $T_x$  for these glasses) indicate that a complete conversion of  $\text{Fe}_3\text{B}$  phase into  $\text{Fe}_2\text{B}$  and  $\alpha\text{-Fe}$  has not yet taken place, as small  $\text{Fe}_3\text{B}$  peaks were still observed in the XRD spectra.

Metalloid dependence of the magnetic anisotropy i.e., a decrease in  $\theta$  (the angle between the magnetic moment and the gamma-ray direction) with Si concentration, has been observed in the Fe-B-Si alloys. For the as-received sample of amorphous  $\text{Fe}_{79}\text{B}_{16}\text{Si}_5$  the value of  $\theta$  is 90°, whereas in the case of



$\text{Fe}_{78}\text{B}_{13}\text{Si}_9$  it is  $68^\circ$ . As the time-period of heat treatment, or the temperature is increased the magnetization direction rotates out of the plane for both the glasses. The results indicate that annealing does relieve internal stresses in the sample which are invariably present in the rapidly quenched alloys. Since the direction of magnetization is stress sensitive, this relief in the internal stress gets reflected in the directional change of the magnetization axis. The effects of annealing is usually interpreted in terms of a reduction of the number of vacancies and an increase in the topological order approaching a relaxed, ideal glass.

The penultimate chapter, Chapter 5, deals with the results and discussion of the RBS/diffusion studies on the three type of metallic glasses mentioned above. During the initial stages of relaxation (i.e., for annealing times  $\leq 1$  hr), the  $D$  vs  $1/T$  plots show zero activation energy similar to the one reported for radiation enhanced type diffusion in crystalline solids. This similarity has been noticed and pointed out for the first time. The time dependence of the diffusion coefficient has been observed in all the three metallic glasses. The decrease in the diffusivity towards a plateau value, during the first few hours of isothermal annealing of the diffusion couple samples, has been attributed to the effect of structural relaxation. For these metallic glasses the relaxation process ends after an annealing time-period of 1 hr at  $450^\circ\text{C}$ , after 4 hr at  $400^\circ\text{C}$ , after 8 hr at  $350^\circ\text{C}$  and after 12 hr at  $300^\circ\text{C}$ . Beyond these durations of heat-treatment, the  $D$ -values become independent of the annealing time.

The temperature dependence of diffusivity in the relaxed state has been studied in these metallic glasses in order to obtain some systematic understanding of the impurity diffusion mechanism. Arrhenius type of behavior was observed in all the three amorphous metallic glasses, indicating that diffusion in these metallic glasses in the relaxed condition is limited by a single activation barrier over the temperature range investigated. The values of

activation energy and pre-exponential factor for diffusion of various species in the metallic glasses are given in the table below.

Metallic glass	Diffusing species	Q (eV)	$D_0$ (m <sup>2</sup> /s)
Fe <sub>79</sub> B <sub>16</sub> Si <sub>5</sub>	Au	0.70 ± 0.20	10 <sup>-15.17 ± 1.55</sup>
	Ge	0.56 ± 0.05	10 <sup>-17.04 ± 0.22</sup>
	Pd	0.46 ± 0.08	10 <sup>-18.08 ± 0.55</sup>
Fe <sub>78</sub> B <sub>13</sub> Si <sub>9</sub>	Au	0.77 ± 0.20	10 <sup>-14.55 ± 1.55</sup>
	Ge	0.62 ± 0.18	10 <sup>-16.42 ± 1.46</sup>
	Pd	0.31 ± 0.02	10 <sup>-19.16 ± 0.42</sup>
Fe <sub>40</sub> Ni <sub>38</sub> B <sub>18</sub> Mo <sub>4</sub>	Pd	1.57 ± 0.37	10 <sup>-8.29 ± 3.05</sup>

A correlation between the radii of the diffusing species and the diffusion coefficients has been observed for the amorphous Fe-B-Si metallic glasses. These correlations have been compared with that for diffusion in amorphous Fe-B alloys and crystalline  $\alpha$ -Fe reported in the literature, and an intriguing similarity has been observed.

The fifth chapter ends with a discussion on the possible diffusion mechanisms in metallic glasses. The analysis of the diffusion data yields large absolute values of the entropy of migration  $S_m$  (>20k) in the Fe-B-Si metallic glasses, which indicate that diffusion occurs in these alloys by a direct mechanism involving a cooperative motion of groups of atoms. For the metallic glass Fe<sub>40</sub>Ni<sub>38</sub>B<sub>18</sub>Mo<sub>4</sub>,  $S_m$  is 5.75k, which indicates a direct diffusion mechanism involving quasi-vacancies. A cooperative type of mechanism via small displacements (i.e., 3-4% of atomic distance) of individual atoms forming a group of 10-14 atoms, has also been inferred for the Fe-B-Si metallic glasses, from the relative value of the critical jump distance, resulting in diffusion

transport. and the ratio of the mean vibration frequency in the ground and transient states.

The last chapter, Chapter 6, highlights the important conclusions inferred from Mössbauer, X-ray diffraction and diffusion studies of the metallic glasses mentioned above.

*References:*

- Gupta D., Tu K.N., Asai K.W, *Phys. Rev. Lett.*, 35, 1975, 796  
Luborsky F.E., *J. Appl. Phys.*, 54 1983, 5732  
Cantor B., *Proceedings on Rapidly Quenched Metals -V*, 1985, 595  
Mehrer H., Dorner W., *Defect and Diffusion Forum*, 66-69, 1989, 189

# CONTENTS

LIST OF FIGURES	xviii
LIST OF TABLES	xxxi

## CHAPTER 1. INTRODUCTION

1.1 PREAMBLE.....	1
1.2 OBJECT OF THE PRESENT STUDY.....	2
1.3 METALLIC GLASSES.....	5
1.3.1 Formation and kinetics of formation.....	6
1.3.2 Preparation.....	9
1.3.3 Structural models.....	13
1.3.4 Structural relaxation.....	15
(an effect of annealing)	
1.3.5 Crystallization (an effect of annealing).....	17
1.3.6 Reversible relaxation.....	18
(an effect of annealing)	
1.4 DIFFUSION.....	19
1.4.1 Techniques of diffusion measurement.....	19
1.4.2 Diffusion equation and solution.....	21
1.5 ARRHENIUS LAW AND ACTIVATION ENERGY.....	25
1.6 BRIEF REVIEW OF DIFFUSION IN METALLIC.....	26
GLASSES	
1.7 BRIEF REVIEW OF PHASE PRECIPITATION STUDIES.....	34
IN METALLIC GLASSES BY MÖSSBAUER SPECTROSCOPY	

## CHAPTER 2. THEORETICAL BACKGROUND AND FORMALISM

2.1 RUTHERFORD BACKSCATTERING SPECTROMETRY.....	39
2.1.1 Kinematic factor and mass identification.....	40
2.1.2 Scattering cross-section.....	42
2.1.3 Stopping cross-section factor.....	44
2.1.4 Stopping in a multi-elemental target.....	45
2.1.5 Determination of film thickness.....	46
2.1.6 The depth profile.....	48
2.1.7 Energy straggling.....	48

2.1.8 Energy and Depth resolution.....	49
2.2 MÖSSBAUER SPECTROSCOPY.....	51
2.2.1 Recoil energy loss.....	52
2.2.2 Natural line-width and resonance.....	53
2.2.3 Doppler broadening and resonance.....	55
2.2.4 Einstein energy and resonance.....	55
2.2.5 Observation of Mössbauer effect.....	56
2.2.6 Hyperfine interactions.....	57
2.2.7 Electric monopole interaction: isomer shift.....	58
2.2.8 Electric quadrupole interaction: quadrupole splitting.....	60
2.2.9 Magnetic dipole interaction: magnetic hyperfine splitting.....	62
2.2.10 Phase determination by Mössbauer spectroscopy.....	64

## CHAPTER 3. EXPERIMENTAL METHODS AND ANALYSIS

3.1 INTRODUCTION.....	66
3.2 PREPARATION OF DIFFUSION COUPLES FOR RBS.....	66
3.3 ANNEALING OF THE DIFFUSION COUPLES.....	68
3.4 THE RUTHERFORD BACKSCATTERING (RBS) SETUP.....	69
3.4.1 Van-De-Graaff accelerator.....	69
3.4.2 The analyzing magnet.....	72
3.4.3 The beam line.....	72
3.4.4 Rutherford backscattering (RBS) chamber.....	73
3.4.5 Pulse-shaping electronics and multichannel analyzer.....	75
3.5 BACKSCATTERING SPECTRA ANALYSIS.....	76
3.5.1 Calibration of the MCA.....	78
3.5.2 Analysis by hand calculation using the basic formulae.....	80
3.5.3 Analysis by simulation.....	80
3.5.4 Calculation of diffusion coefficient by simulation.....	81
3.6 ERROR IN D VALUES.....	83
3.7 PREPARATION OF MÖSSBAUER ABSORBERS.....	85
3.8 THE MÖSSBAUER SETUP.....	86
3.8.1 The radioactive source.....	86
3.8.2 Mössbauer drive.....	87

3.8.3 The Detection System.....	88
3.8.4 The multichannel analyzer..... (Data storage in the MCS mode)	88
3.9 EFFECT OF GEOMETRY.....	90
3.9.1 Distance variation effect.....	90
3.9.2 Cosine effect.....	91
3.10 CALIBRATION OF THE MCA.....	91
3.11 ANALYSIS OF MÖSSBAUER SPECTRA BY SIMULATION.....	92
3.12 X-RAY MEASUREMENTS.....	94

## CHAPTER 4. MOSSBAUER SPECTROSCOPY AND X-RAY DIFFRACTION STUDIES

4.1 INTRODUCTION.....	95
4.2 X-RAY ANALYSIS OF $\text{Fe}_{79}\text{B}_{16}\text{Si}_5$ AND $\text{Fe}_{78}\text{B}_{13}\text{Si}_9$ .....	96
4.3 MÖSSBAUER ANALYSIS OF AS-RECEIVED SAMPLES.....	101
4.4 MÖSSBAUER ANALYSIS OF HEAT-TREATED SAMPLES..... OF $\text{Fe}_{79}\text{B}_{16}\text{Si}_5$ .	103
4.5 MÖSSBAUER ANALYSIS OF HEAT-TREATED SAMPLES..... OF $\text{Fe}_{78}\text{B}_{13}\text{Si}_9$ .	118
4.6 MAGNETIC ORDERING.....	132
4.7 INFERENCES FOR DIFFUSION STUDIES.....	134

## CHAPTER 5. DIFFUSION STUDIES

5.1 INTRODUCTION.....	135
5.2 DIFFUSION OF Ge IN METALLIC GLASS $\text{Fe}_{79}\text{B}_{16}\text{Si}_5$ .....	136
5.2.1 Dependence of $D(t)$ on annealing time.....	143
5.2.2 Dependence of $D$ on annealing temperature.....	148
5.3 DIFFUSION OF Ge IN METALLIC GLASS $\text{Fe}_{78}\text{B}_{13}\text{Si}_9$ .....	151
5.3.1 Dependence of $D(t)$ on annealing time.....	151
5.3.2 Dependence of $D$ on annealing temperature.....	161
5.4 DIFFUSION OF PD IN METALLIC GLASS $\text{Fe}_{79}\text{B}_{16}\text{Si}_5$ .....	161
5.4.1 Dependence of $D(t)$ on annealing time.....	167
5.4.2 Dependence of $D$ on annealing temperature.....	170
5.5 DIFFUSION OF PD IN METALLIC GLASS $\text{Fe}_{78}\text{B}_{13}\text{Si}_9$ .....	170
5.5.1 Dependence of $D(t)$ on annealing time.....	176
5.5.2 Dependence of $D$ on annealing temperature.....	176
5.6 DIFFUSION OF AU IN METALLIC GLASS $\text{Fe}_{79}\text{B}_{16}\text{Si}_5$ .....	179
5.6.1 Dependence of $D(t)$ on annealing time.....	179
5.6.2 Dependence of $D$ on annealing temperature.....	183

5.7	DIFFUSION OF AU IN METALLIC GLASS $\text{Fe}_{78}\text{B}_{13}\text{Si}_9$ .....	186
5.7.1	Dependence of $D(t)$ on annealing time.....	190
5.7.2	Dependence of $D$ on annealing temperature.....	193
5.8	DIFFUSION OF AG IN METALLIC GLASS $\text{Fe}_{79}\text{B}_{16}\text{Si}_5$ .....	193
5.8.1	Dependence of $D(t)$ on annealing time.....	196
5.9	DIFFUSION OF AG IN METALLIC GLASS $\text{Fe}_{78}\text{B}_{13}\text{Si}_9$ .....	197
5.9.1	Dependence of $D(t)$ on annealing time.....	200
5.10	DIFFUSION OF PD IN METALLIC GLASS.....	201
	$\text{Fe}_{40}\text{Ni}_{38}\text{B}_{18}\text{Mo}_4$ .	
5.10.1	Dependence of $D(t)$ on annealing time.....	201
5.10.2	Dependence of $D$ on annealing temperature.....	207
5.11	TIME DEPENDENCE OF DIFFUSIVITY DURING.....	210
	RELAXATION.	
5.12	TEMPERATURE DEPENDENCE OF $D$ AFTER RELAXATION.....	215
	(Arrhenius behaviour)	
5.13	DIFFUSION DURING EARLY STAGES OF RELAXATION.....	220
	(Comparison with radiation enhanced diffusion)	
5.14	CORRELATIONS.....	225
5.14.1	Correlation between $D$ and atomic radii.....	226
5.14.2	Correlation of $Q$ with atomic species.....	231
	and radii.	
5.14.3	Correlation of $Q$ with $D_0$ .....	231
5.15	DIFFUSION AND DEFECT MECHANISM.....	236
5.15.1	DEFECTS.....	237
5.15.2	MECHANISM.....	239

CHAPTER 6. CONCLUSION .....	246
-----------------------------	-----

REFERENCES .....	250
------------------	-----

APPENDIX 1 .....	261
------------------	-----

# LIST OF FIGURES

FIGURE NO.	TITLE	PAGE NO.
Figure 1.1	Temperature dependence of the shear viscosity in.....6 amorphous metallic alloys.	6
Figure 1.2	Temperature dependence of volume V ,enthalphy H, .....7 coefficient of thermal expansion $\alpha$ and the specific heat $C_p$ in amorphous metallic alloys. $T_g$ and $T_m$ are glass transition and melting temperature respectively. L, ML, G and C are the phases, liquid, metastable liquid, glass and crystal, respectively.	7
Figure 1.3	A few illustrations of Spray Method of.....10 production of metallic glasses.	10
Figure 1.4	A few illustrations of Chill Method of.....12 production of metallic glasses.	12
Figure 1.5	Structural models for amorphous alloys.....14 (a) DRPHS model, (b) Gaskel's trigonal units.	14
Figure 1.6	Temperature dependence of volume V and Gibbs free.....16 energy in amorphous metallic alloys.	16
Figure 1.7	Solution to various diffusion geometries.....23 (a)thin layer, (b)thick layer and (c)semi-infinite.	23
Figure 2.1	Schematic diagram of the backscattering process.....39	39
Figure 2.2	RBS spectrum of thick film of Au on Al substrate.....47	47
Figure 2.3	Effect of energy resolution and straggling.....50	50
Figure 2.4	(a)Schematic and (b)Energy level diagram .....52 of the Mössbauer process.	52
Figure 2.5	Lorentzian shape of the energy E, with linewidth $\Gamma$ .....53	53
Figure 2.6	(a)Similar line-shape of the emitting and absorbing photon.....54 (b)on overlapping there is resonance and absorption.	54
Figure 2.7	Essential aspects of the decay scheme of $Fe^{57}$ and $Fe^{58}$ .....56	56
Figure 2.8	Comparison of R, and $E_E$ in $Fe^{57}$ and $Fe^{58}$ .....56	56
Figure 2.9	Effect of monopole interaction (a)on the energy levels of.....59 the source and absorber, and (b)the resulting Mössbauer spectrum showing isomer shift.	59
Figure 2.10	Effect of quadrupole interaction (a)on the nuclear energy.....61	61



levels of the source and absorber, and (b) the resulting Mössbauer spectrum showing quadrupole splitting.

Figure 2.11 Effect of magnetic hyperfine interaction (a) on the.....	62
energy levels of $^{57}\text{Fe}$ , and (b) the resulting peak	
positions of the six-finger Mössbauer spectrum.	
Figure 3.1 Schematic diagram of the vacuum evaporator system.....	67
Figure 3.2 Photograph of the evaporator.....	67a
Figure 3.3 Photograph of the annealing set-up.....	67a
Figure 3.4 Schematic diagram of the annealing set-up.....	68
Figure 3.5 Block diagram of the Van-de-Graaff.....	70
accelerator system.	
Figure 3.6 The Van-de-Graaff accelerator (machine room).....	71
Figure 3.7 The analyzing magnet and beam line (beam room).....	71
Figure 3.8 Block diagram of the RBS chamber.....	74
Figure 3.9 The RBS chamber and other accessories.....	74
Figure 3.10 RBS spectrum of Pd on $\text{Fe}_{78}\text{B}_{13}\text{Si}_9$ .....	77
Figure 3.11 RBS spectra of calibration samples.....	79
(a) Thin film of Au on Al (b) Pure Fe (c) Pure Zn.	
Figure 3.12 RBS spectrum of Pd on $\text{Fe}_{78}\text{B}_{13}\text{Si}_9$ , after.....	82
annealing at $400^\circ\text{C}$ for 8 hr.	
Figure 3.13 Schematic block diagram of the Mössbauer spectrometer.....	86
Figure 3.14 Schematic diagram of the velocity transducer.....	87
Figure 3.15 PHA spectrum of the radioactive source.....	89
Figure 3.16 Mössbauer spectra of $\alpha\text{-Fe}$ used for calibrating the MCA.....	92
Figure 4.1 X-ray diffraction pattern (at RT) of $\text{Fe}_{79}\text{B}_{16}\text{Si}_5$ .....	97
heat-treated at various temperatures for 16 hr.	
Figure 4.2 X-ray diffraction pattern (at RT) of $\text{Fe}_{78}\text{B}_{13}\text{Si}_9$ .....	98
heat-treated at various temperatures for 16 hr.	
Figure 4.3 X-ray diffraction pattern (at RT) of:.....	100
(a) $\text{Fe}_{78}\text{B}_{13}\text{Si}_9$ , $600^\circ\text{C}$ (2 hr); (b) $\text{Fe}_{78}\text{B}_{13}\text{Si}_9$ , $700^\circ\text{C}$ (15 min);	
(c) $\text{Fe}_{79}\text{B}_{16}\text{Si}_5$ , $600^\circ\text{C}$ (2 hr); (d) $\text{Fe}_{79}\text{B}_{16}\text{Si}_5$ , $700^\circ\text{C}$ (15 min).	
Figure 4.4 Mössbauer (RT) spectra of as-received samples of.....	102
metallic glasses $\text{Fe}_{79}\text{B}_{16}\text{Si}_5$ and $\text{Fe}_{78}\text{B}_{13}\text{Si}_9$ .	
Figure 4.5 Mössbauer spectra of $\text{Fe}_{79}\text{B}_{16}\text{Si}_5$ samples (at RT).	
(a) heat-treated at $300^\circ\text{C}$ for various time periods.....	107
(b) heat-treated at $350^\circ\text{C}$ for various time periods.....	107
(c) heat-treated at $400^\circ\text{C}$ for various time periods.....	108
(d) heat-treated at $450^\circ\text{C}$ for various time periods.....	108

	(e)heat-treated at 475°C for various time periods.....	109
	(f)comparison of as-received with 475°C (8 hr).....	109
Figure 4.6	Analyzed (RT) Mössbauer spectrum of heat-treated sample of..... Fe <sub>79</sub> B <sub>16</sub> Si <sub>5</sub> , indicating the various phases precipitated. The symbols refer to the phases as indicated below.	111
Figure 4.7	Analyzed (RT) Mössbauer spectrum of heat-treated sample of..... Fe <sub>79</sub> B <sub>16</sub> Si <sub>5</sub> , indicating the various phases precipitated. The symbols refer to the phases as mentioned in figure 4.6.	112
Figure 4.8	Analyzed (RT) Mössbauer spectrum of heat-treated sample of..... Fe <sub>79</sub> B <sub>16</sub> Si <sub>5</sub> , indicating the various phases precipitated. The symbols refer to the phases as mentioned in figure 4.6.	113
Figure 4.9	Analyzed (RT) Mössbauer spectrum of heat-treated sample of..... Fe <sub>79</sub> B <sub>16</sub> Si <sub>5</sub> , indicating the various phases precipitated. The symbols refer to the phases as mentioned in figure 4.6.	114
Figure 4.10	Analyzed (RT) Mössbauer spectrum of heat-treated sample of..... Fe <sub>79</sub> B <sub>16</sub> Si <sub>5</sub> , indicating the various phases precipitated. The symbols refer to the phases as mentioned in figure 4.6.	115
Figure 4.11	Variation in the ratio of the areas under the..... Fe <sub>3</sub> B and Fe <sub>2</sub> B sextets obtained from the computer analysis of (a) Fe <sub>78</sub> B <sub>13</sub> Si <sub>9</sub> (475°C), (b) Fe <sub>79</sub> B <sub>16</sub> Si <sub>5</sub> (450°C), and(c) Fe <sub>79</sub> B <sub>16</sub> Si <sub>5</sub> (475°C).	116
Figure 4.12	Mössbauer spectra of Fe <sub>78</sub> B <sub>13</sub> Si <sub>9</sub> samples (at RT). (a)heat-treated at 300°C for various time periods..... (b)heat-treated at 350°C for various time periods..... (c)heat-treated at 400°C for various time periods..... (d)heat-treated at 450°C for various time periods..... (e)heat-treated at 475°C for various time periods..... (f)comparison of as-received with 475°C (8 hr).....	121 121 122 122 123 123
Figure 4.13	Analyzed (RT) Mössbauer spectrum of heat-treated sample of..... Fe <sub>79</sub> B <sub>16</sub> Si <sub>5</sub> indicating the various phases precipitated. The symbols refer to the phases as indicated below.	125
Figure 4.14	Analyzed (RT) Mössbauer spectrum of heat-treated sample of..... Fe <sub>79</sub> B <sub>16</sub> Si <sub>5</sub> indicating the various phases precipitated. The symbols refer to phases as mentioned in figure 4.13.	126
Figure 4.15	Analyzed (RT) Mössbauer spectrum of heat-treated sample of..... Fe <sub>79</sub> B <sub>16</sub> Si <sub>5</sub> indicating the various phases precipitated. The symbols refer to phases as mentioned in figure 4.13.	127

- Figure 4.16 Analyzed (RT) Mössbauer spectrum of heat-treated sample of.....128  
 $\text{Fe}_{79}\text{B}_{16}\text{Si}_5$  indicating the various phases precipitated.  
 The symbols refer to phases as mentioned in figure 4.13.
- Figure 4.17 Analyzed (RT) Mössbauer spectrum of heat-treated sample of.....129  
 $\text{Fe}_{79}\text{B}_{16}\text{Si}_5$  indicating the various phases precipitated.  
 The symbols refer to phases as mentioned in figure 4.13.
- Figure 4.18 Variation in the line-width (FWHM) of  $\text{Fe}_2\text{B}$  and  $\text{Fe}_3\text{B}$ .....131  
 lines with the time period of heat-treatment in:  
 (a) $\text{Fe}_{79}\text{B}_{16}\text{Si}_5$ , heat-treated at  $450^\circ\text{C}$ . (b) $\text{Fe}_{79}\text{B}_{16}\text{Si}_5$ ,  
 heat-treated at  $475^\circ\text{C}$ . (c) $\text{Fe}_{78}\text{B}_{13}\text{Si}_9$ , heat-treated at  $475^\circ\text{C}$ .
- Figure 4.19 Comparison of spectra heat-treated at  $475^\circ\text{C}$  for 8 hr.....132  
 (a) $\text{Fe}_{79}\text{B}_{16}\text{Si}_5$  and (b) $\text{Fe}_{78}\text{B}_{13}\text{Si}_9$ .
- Figure 5.1 Normalized RBS spectra of a- $\text{Fe}_{79}\text{B}_{16}\text{Si}_5$ - Ge diffusion.....137  
 couple before and after annealing at  $400^\circ\text{C}$  for 2 hr  
 and 8 hr respectively. The thickness of the  
 as-evaporated film is  $300 \text{ \AA}$ . The arrow indicates the  
 surface position.
- Figure 5.2 Normalized RBS spectra of a- $\text{Fe}_{79}\text{B}_{16}\text{Si}_5$ - Ge diffusion.....138  
 couple before and after annealing at  $350^\circ\text{C}$  for 2 hr and  
 12 hr respectively. The thickness of the as-evaporated  
 film is  $320 \text{ \AA}$ . The arrow indicates the surface position.
- Figure 5.3 Comparison of experimental (1.4 MeV  $\text{He}^+$ , scattering angle.....139  
 $150^\circ$ ) and simulated RBS spectra to determine the D-value of Ge  
 in  $\text{Fe}_{79}\text{B}_{16}\text{Si}_5$  at  $300^\circ\text{C}$  (12 hr). The simulation was performed  
 using the error function solution of the diffusion equation.
- Figure 5.4 Comparison of experimental (1.4 MeV  $\text{He}^+$ , scattering angle.....140  
 $150^\circ$ ) and simulated RBS spectra to determine the D-value of Ge  
 in  $\text{Fe}_{79}\text{B}_{16}\text{Si}_5$  at  $350^\circ\text{C}$  (4 hr). The simulation was performed  
 using the error function solution of the diffusion equation.
- Figure 5.5 Comparison of experimental (1.4 MeV  $\text{He}^+$ , scattering angle.....141  
 $150^\circ$ ) and simulated RBS spectra to determine the D-value of Ge  
 in  $\text{Fe}_{79}\text{B}_{16}\text{Si}_5$  at  $400^\circ\text{C}$  (2 hr). The simulation was performed  
 using the error function solution of the diffusion equation.
- Figure 5.6 Comparison of experimental (1.4 MeV  $\text{He}^+$ , scattering angle.....142  
 $150^\circ$ ) and simulated RBS spectra to determine the D-value of Ge  
 in  $\text{Fe}_{79}\text{B}_{16}\text{Si}_5$  at  $450^\circ\text{C}$  (1 hr). The simulation was performed  
 using the error function solution of the diffusion equation.

- Figure 5.7(a-d) Diagrams showing variation of the diffusion coefficient.....145  
 $D(t)$  as a function of annealing time  $t$ , for diffusion of Ge in  $\text{Fe}_{79}\text{B}_{16}\text{Si}_5$ . The vertical bars on the data points indicate error in the diffusion coefficients. The solid circles indicate that the crystallization of the metallic glass is observed by us using X-ray and Mössbauer techniques for these data points. The solid line, drawn as a best visual fit to the data points, asymptotically approaches a plateau value ( $D_p$ ) shown by the dashed line (except for  $450^\circ\text{C}$ , see text).
- Figure 5.7(e) Diagram showing variation of the diffusion coefficient  $D(t)$ ....146  
 as a function of annealing time  $t$ , for diffusion of Ge in  $\text{Fe}_{79}\text{B}_{16}\text{Si}_5$  at  $475^\circ\text{C}$ . In this case crystallization has been observed by us using X-ray and Mössbauer techniques for all the data points. The solid line indicates a best visual fit to the data points.
- Figure 5.8 Temperature dependence of diffusivity of Ge in metallic.....150  
 glass  $\text{Fe}_{79}\text{B}_{16}\text{Si}_5$  (Arrhenius plot). The open circles indicate the plateau values ( $D_p$ ) obtained from the  $D(t)$  vs. annealing time diagrams (Figs. 5.7 (a),(b),(c)), and the solid line is a least square fitting to these data points. The values of  $Q$  and  $D_0$  obtained from the fit is also mentioned. The open squares depict the  $D(t)$  values at  $450^\circ\text{C}$  for  $t \leq 4$  hr. The  $D(t)$  values for  $475^\circ\text{C}$  are not shown because onset of crystallization is observed at this temperature even for the lowest annealing duration.
- Figure 5.9 Normalized RBS spectra of a- $\text{Fe}_{78}\text{B}_{13}\text{Si}_9$ - Ge diffusion.....152  
 couple before and after annealing at  $400^\circ\text{C}$  for 1 hr and 8 hr respectively. The thickness of the as-evaporated film is  $280 \text{ \AA}$ . The arrow indicates the surface position.
- Figure 5.10 Normalized RBS spectra of a- $\text{Fe}_{78}\text{B}_{13}\text{Si}_9$ - Ge diffusion.....153  
 couple before and after annealing at  $350^\circ\text{C}$  for 1, 4 and 12 hr respectively. The thickness of the as-evaporated film is  $230 \text{ \AA}$ . The arrow indicates the surface position.
- Figure 5.11 Comparison of experimental ( $1.4 \text{ MeV He}^+$ , scattering angle.....154  
 $150^\circ$ ) and simulated RBS spectra to determine the  $D$ -value of Ge in  $\text{Fe}_{78}\text{B}_{13}\text{Si}_9$  at  $400^\circ\text{C}$  (1 hr). The simulation was performed using the error function solution of the diffusion equation.

- Figure 5.12 Comparison of experimental (1.4 MeV  $\text{He}^+$ , scattering angle.....155  $150^\circ$ ) and simulated RBS spectra to determine the D-value of Ge in  $\text{Fe}_{78}\text{B}_{13}\text{Si}_9$  at  $350^\circ\text{C}$  (8 hr). The simulation was performed using the error function solution of the diffusion equation.
- Figure 5.13 Comparison of experimental (1.4 MeV  $\text{He}^+$ , scattering angle.....156  $150^\circ$ ) and simulated RBS spectra to determine the D-value of Ge in  $\text{Fe}_{78}\text{B}_{13}\text{Si}_9$  at  $300^\circ\text{C}$  (4 hr). The simulation was performed using the error function solution of the diffusion equation.
- Figure 5.14(a-d) Diagrams showing variation of the diffusion coefficient.....158  $D(t)$  as a function of annealing time  $t$ , for diffusion of Ge in  $\text{Fe}_{78}\text{B}_{13}\text{Si}_9$ . The vertical bars on the data points indicate error in the diffusion coefficients. The solid line, drawn as a best visual fit to the data points, asymptotically approaches a plateau value ( $D_p$ ) shown by the dashed line (except for  $450^\circ\text{C}$ , see text).
- Figure 5.14(e) Diagram showing variation of the diffusion coefficient .....159  $D(t)$  as a function of annealing time  $t$ , for diffusion of Ge in  $\text{Fe}_{78}\text{B}_{13}\text{Si}_9$  at  $475^\circ\text{C}$ . In this case crystallization has been observed by us using X-ray and Mössbauer techniques for all the data points. The solid line indicates a best visual fit to the data points.
- Figure 5.15 Temperature dependence of diffusivity of Ge in metallic.....160 glass  $\text{Fe}_{78}\text{B}_{13}\text{Si}_9$  (Arrhenius plot). The open circles indicate the plateau values ( $D_p$ ) obtained from the  $D(t)$  vs. annealing time diagrams (Figs. 5.14 (a),(b),(c)), and the solid line is a least square fitting to these data points. The values of  $Q$  and  $D_0$  obtained from the fit is also mentioned. The open squares depict the  $D(t)$  values at  $450^\circ\text{C}$  for  $t \leq 4$  hr. The  $D(t)$  values for  $475^\circ\text{C}$  are not shown because onset of crystallization is observed at this temperature even for the lowest annealing duration.
- Figure 5.16 Normalized RBS spectra of a- $\text{Fe}_{79}\text{B}_{16}\text{Si}_5$ - Pd diffusion.....162 couple before and after annealing at  $450^\circ\text{C}$  for 2 hr and 8 hr respectively. The thickness of the as-evaporated film is  $230 \text{ \AA}$ . The arrow indicates the surface position.
- Figure 5.17 Normalized RBS spectra of a- $\text{Fe}_{79}\text{B}_{16}\text{Si}_5$ - Pd diffusion.....163 couple before and after annealing at  $400^\circ\text{C}$  for 4 hr and

12 hr respectively. The thickness of the as-evaporated film is  $250 \text{ \AA}$ . The arrow indicates the surface position.

Figure 5.18 Comparison of experimental ( $1.4 \text{ MeV He}^+$ , scattering angle..... $164^\circ$ ) and simulated RBS spectra to determine the D-value of Pd in  $\text{Fe}_{79}\text{B}_{16}\text{Si}_5$  at  $450^\circ\text{C}$  (1 hr). The simulation was performed using the error function solution of the diffusion equation.

Figure 5.19 Comparison of experimental ( $1.4 \text{ MeV He}^+$ , scattering angle..... $165^\circ$ ) and simulated RBS spectra to determine the D-value of Pd in  $\text{Fe}_{79}\text{B}_{16}\text{Si}_5$  at  $350^\circ\text{C}$  (2 hr). The simulation was performed using the error function solution of the diffusion equation.

Figure 5.20(a-d) Diagrams showing variation of the diffusion coefficient..... $168$   $D(t)$  as a function of annealing time  $t$ , for diffusion of Pd in  $\text{Fe}_{79}\text{B}_{16}\text{Si}_5$ . The vertical bars on the data points indicate error in the diffusion coefficients. The solid circles indicate that the crystallization of the metallic glass is observed by us using X-ray and Mössbauer techniques for these data points. The solid line, drawn as a best visual fit to the data points, asymptotically approaches a plateau value ( $D_p$ ) shown by the dashed line.

Figure 5.21 Temperature dependence of diffusivity of Pd in metallic..... $169$  glass  $\text{Fe}_{79}\text{B}_{16}\text{Si}_5$  (Arrhenius plot). The open circles indicate the plateau values ( $D_p$ ) obtained from the  $D(t)$  vs. annealing time diagrams (Figs. 5.20 (a),(b),(c)), and the solid line is a least square fitting to these data points. The values of  $Q$  and  $D_0$  obtained from the fit is also mentioned. The open squares depict the  $D(t)$  values at  $450^\circ\text{C}$ , and is shown for the sake of comparison.

Figure 5.22 Normalized RBS spectra of a- $\text{Fe}_{78}\text{B}_{13}\text{Si}_9$ - Pd diffusion..... $171$  couple before and after annealing at  $450^\circ\text{C}$  for 2 hr and 8 hr respectively. The thickness of the as-evaporated film is  $165 \text{ \AA}$ . The arrow indicates the surface position.

Figure 5.23 Normalized RBS spectra of a- $\text{Fe}_{78}\text{B}_{13}\text{Si}_9$ - Pd diffusion..... $172$  couple before and after annealing at  $400^\circ\text{C}$  for 12 hr. The thickness of the as-evaporated film is  $190 \text{ \AA}$ . The arrow indicates the surface position.

Figure 5.24 Comparison of experimental ( $1.4 \text{ MeV He}^+$ , scattering angle..... $173$   $150^\circ$ ) and simulated RBS spectra to determine the D-value of Pd

in  $\text{Fe}_{78}\text{B}_{13}\text{Si}_9$  at  $450^\circ\text{C}$  (1 hr). The simulation was performed using the error function solution of the diffusion equation.

Figure 5.25 Comparison of experimental ( $1.4\text{ MeV He}^+$ , scattering angle.....174  $150^\circ$ ) and simulated RBS spectra to determine the D-value of Pd

in  $\text{Fe}_{78}\text{B}_{13}\text{Si}_9$  at  $300^\circ\text{C}$  (2 hr). The simulation was performed using the error function solution of the diffusion equation.

Figure 5.26(a-d) Diagrams showing variation of the diffusion coefficient.....177

$D(t)$  as a function of annealing time  $t$ , for diffusion of Pd in  $\text{Fe}_{78}\text{B}_{13}\text{Si}_9$ . The vertical bars on the data points indicate error in the diffusion coefficients. The solid line, drawn as a best visual fit to the data points, asymptotically approaches a plateau value ( $D_p$ ) shown by the dashed line.

Figure 5.27 Temperature dependence of diffusivity of Pd in metallic.....178

glass  $\text{Fe}_{78}\text{B}_{13}\text{Si}_9$  (Arrhenius plot). The open circles indicate the plateau values ( $D_p$ ) obtained from the  $D(t)$  vs. annealing time diagrams (Figs. 5.26 (a) to (d)), and the solid line is a least square fitting to these data points. The values of  $Q$  and  $D_0$  obtained from the fit is also mentioned.

Figure 5.28 Normalized RBS spectra of a- $\text{Fe}_{79}\text{B}_{16}\text{Si}_5$ - Au diffusion.....180

couple before and after annealing at  $350^\circ\text{C}$  for 8 hr.

The thickness of the as-evaporated film is  $130\text{ \AA}$ .

The arrow indicates the surface position.

Figure 5.29 Comparison of experimental ( $1.0\text{ MeV He}^+$ , scattering angle.....181

$150^\circ$ ) and simulated RBS spectra to determine the D-value of Au

in  $\text{Fe}_{79}\text{B}_{16}\text{Si}_5$  at  $350^\circ\text{C}$  (8 hr). The simulation was performed using the error function solution of the diffusion equation.

Figure 5.30(a-c) Diagrams showing variation of the diffusion coefficient.....184

$D(t)$  as a function of annealing time  $t$ , for diffusion of Au in  $\text{Fe}_{79}\text{B}_{16}\text{Si}_5$ . The vertical bars on the data points indicate error in the diffusion coefficients. The solid circles indicate that the crystallization of the metallic glass is observed by us using X-ray and Mössbauer techniques for these data points. The solid line, drawn as a best visual fit to the data points, asymptotically approaches a plateau value ( $D_p$ ) shown by the dashed line (for  $400^\circ\text{C}$ ).

Figure 5.31 Temperature dependence of diffusivity of Au in metallic.....185

glass  $\text{Fe}_{79}\text{B}_{16}\text{Si}_5$  (Arrhenius plot). The solid line is a

least square fitting to the data points at 300°C (16 hr), 350°C (8 hr), 400°C (1 hr) and 450°C (1 hr), (see text Sec.5.6.2). The values of  $Q$  and  $D_0$  obtained from the fit is also mentioned.

- Figure 5.32 Normalized RBS spectra of a- $\text{Fe}_{78}\text{B}_{13}\text{Si}_9$ - Au diffusion.....187 couple before and after annealing at 350°C 8 hr. The thickness of the as-evaporated film is 230 Å. The arrow indicates the surface position.
- Figure 5.33 Comparison of experimental (1.0 MeV  $\text{He}^+$ , scattering angle.....188 150°) and simulated RBS spectra to determine the D-value of Au in  $\text{Fe}_{78}\text{B}_{13}\text{Si}_9$  at 350°C (8 hr). The simulation was performed using the error function solution of the diffusion equation.
- Figure 5.34(a-c) Diagrams showing variation of the diffusion coefficient.....191  $D(t)$  as a function of annealing time  $t$ , for diffusion of Au in  $\text{Fe}_{78}\text{B}_{13}\text{Si}_9$ . The vertical bars on the data points indicate error in the diffusion coefficients. The solid circles indicate that the crystallization of the metallic glass is observed by us using X-ray and Mössbauer techniques for these data points. The solid line, drawn as a best visual fit to the data points, asymptotically approaches a plateau value ( $D_p$ ) shown by the dashed line (for 400°C, see text).
- Figure 5.35 Temperature dependence of diffusivity of Au in metallic.....192 glass  $\text{Fe}_{78}\text{B}_{13}\text{Si}_9$  (Arrhenius plot). The solid line is asquare fitting to the data points at 300°C (16 hr), 350°C (8 hr), 400°C (1 hr) and 450°C (1 hr), (see text Sec.5.7.2). The values of  $Q$  and  $D_0$  obtained from the fit are also mentioned.
- Figure 5.36 Normalized RBS spectra of a- $\text{Fe}_{79}\text{B}_{16}\text{Si}_5$ - Ag diffusion.....194 couple before and after annealing at 350°C 8 hr. The thickness of the as-evaporated film is 230 Å. The arrow indicates the surface position.
- Figure 5.37 Comparison of experimental (1.0 MeV  $\text{He}^+$ , scattering angle.....195 150°) and simulated RBS spectra to determine the D-value of Ag in  $\text{Fe}_{79}\text{B}_{16}\text{Si}_5$  at 350°C (8 hr). The simulation was performed using the error function solution of the diffusion equation.
- Figure 5.38 Diagram showing variation of the diffusion coefficient  $D(t)$ .....196 as a function of annealing time  $t$ , at 350°C, for diffusion



of Ag in  $\text{Fe}_{79}\text{B}_{16}\text{Si}_5$ . The vertical bars on the data points indicate error in the diffusion coefficients. The solid line, drawn as a best visual fit to the data points, asymptotically approaches a plateau value ( $D_p$ ) shown by the dashed line.

- Figure 5.39 Normalized RBS spectra of a- $\text{Fe}_{78}\text{B}_{13}\text{Si}_9$ -Ag diffusion.....198  
couple before and after annealing at  $350^\circ\text{C}$  for 8 hr.  
The thickness of the as-evaporated film is  $220 \text{ \AA}$ . The arrow indicates the surface position.
- Figure 5.40 Comparison of experimental ( $1.0 \text{ MeV He}^+$ , scattering angle.....199  
 $150^\circ$ ) and simulated RBS spectra to determine the D-value of Ag  
in  $\text{Fe}_{78}\text{B}_{13}\text{Si}_9$  at  $350^\circ\text{C}$  (8 hr). The simulation was performed  
using the error function solution of the diffusion equation.
- Figure 5.41 Diagram showing variation of the diffusion coefficient  $D(t)$ .....200  
as a function of annealing time  $t$ , at  $350^\circ\text{C}$ , for diffusion  
of Ag in  $\text{Fe}_{78}\text{B}_{13}\text{Si}_9$ . The vertical bars on the data points  
indicate error in the diffusion coefficients. The solid line,  
drawn as a best visual fit to the data points, asymptotically  
approaches a plateau value ( $D_p$ ) shown by the dashed line.
- Figure 5.42 Normalized RBS spectra of a- $\text{Fe}_{40}\text{Ni}_{38}\text{B}_{18}\text{Mo}_4$ -Pd diffusion.....202  
couple before and after annealing at  $450^\circ\text{C}$  for 2 hr and  
8 hr respectively. The thickness of the as-evaporated  
film is  $230 \text{ \AA}$ . The arrow indicates the surface position.
- Figure 5.43 Normalized RBS spectra of a- $\text{Fe}_{40}\text{Ni}_{38}\text{B}_{18}\text{Mo}_4$ -Pd diffusion.....203  
couple before and after annealing at  $400^\circ\text{C}$  for 2 hr and  
8 hr respectively. The thickness of the as-evaporated  
film is  $250 \text{ \AA}$ . The arrow indicates the surface position.
- Figure 5.44 Comparison of experimental ( $1.4 \text{ MeV He}^+$ , scattering angle.....204  
 $150^\circ$ ) and simulated RBS spectra to determine the D-value of Pd  
in  $\text{Fe}_{40}\text{Ni}_{38}\text{B}_{18}\text{Mo}_4$  at  $450^\circ\text{C}$  (2 hr). The simulation was performed  
using the error function solution of the diffusion equation.
- Figure 5.45 Comparison of experimental ( $1.4 \text{ MeV He}^+$ , scattering angle.....205  
 $150^\circ$ ) and simulated RBS spectra to determine the D-value of Pd  
in  $\text{Fe}_{40}\text{Ni}_{38}\text{B}_{18}\text{Mo}_4$  at  $400^\circ\text{C}$  (1 hr). The simulation was performed  
using the error function solution of the diffusion equation.
- Figure 5.46(a-d) Diagrams showing variation of the diffusion coefficient.....208  
 $D(t)$  as a function of annealing time  $t$ , for diffusion of Pd  
in  $\text{Fe}_{40}\text{Ni}_{38}\text{B}_{18}\text{Mo}_4$ . The vertical bars on the data points

indicate error in the diffusion coefficients. The solid circles indicate crystallization of the metallic glass for these data points. The solid line, drawn as a best visual fit to the data points, asymptotically approaches (for 300°C and 350°C) a plateau value ( $D_p$ ) shown by the dashed line.

Figure 5.47 Temperature dependence of diffusivity of Pd in metallic.....209

glass  $\text{Fe}_{40}\text{Ni}_{38}\text{B}_{18}\text{Mo}_4$  (Arrhenius plot). The open circles indicate the plateau values ( $D_p$ ) obtained from the  $D(t)$  vs. annealing time diagrams (Figs. 5.46 (a),(b)), and the solid line is a least square fitting to these data points along with the  $D(t)$  value at 400°C (1 hr). The values of  $Q$  and  $D_0$  obtained from the fit are also mentioned. The solid square indicates the  $D(t)$  values at 450°C (1hr) which represents diffusion in crystallized  $\text{Fe}_{40}\text{Ni}_{38}\text{B}_{18}\text{Mo}_4$ .

Figure 5.48(i), (a-d) Diagrams showing variation of the diffusion .....213

coefficient  $D(t)$  as a function of annealing time  $t$ , for diffusion of Ge in  $\text{Fe}_{79}\text{B}_{16}\text{Si}_5$ . The vertical bars on the data points indicate error in the diffusion coefficients. The solid circles indicate that the crystallization of the metallic glass is observed by us using X-ray and Mössbauer techniques for these data points. The solid line, drawn as a best visual fit to the data points, asymptotically approaches a plateau value ( $D_p$ ) shown by the dashed line (except for 450°C). The arrows indicate the annealing time ( $\tau$ ) at which the  $D(t)$  value approaches to within 20% of the plateau value.

Figure 5.48(ii) Diagram showing the variation of the relaxation time.....214

$\tau$  with respect to the inverse of the annealing temperature for the diffusion of Ge in the metallic glasses  $\text{Fe}_{79}\text{B}_{16}\text{Si}_5$ . The value of  $\tau$  for 300°C, 350°C and 400°C is obtained from the  $D(t)$  vs. annealing time diagrams shown in Figs. 5.48(i). The value of  $\tau$  is that annealing duration for which the  $D(t)$  value approaches to within 20% of the plateau value  $D_p$  in each case. The lower end of the vertical bars on the data points indicate the annealing duration at which the  $D(t)$  value approaches to within 30% of the  $D_p$  value and the upper end indicates the annealing

duration at which the  $D(t)$  value approaches to within 10% of  $D_p$ . For 450°C the value of  $\tau$  is taken as 1 hr (lowest annealing duration). The least squares fitting to the data points give an activation energy ( $Q$ ) equal to 0.55 eV and a pre-exponential factor ( $\tau_0$ ) of value 0.64 s.

- Figure 5.49 Comparison of variation in viscosity ( $\eta$ ) and diffusivity.....216  
(D) with respect to the annealing duration.  
(a) Viscosity plot of  $\text{Fe}_{78}\text{B}_{13}\text{Si}_9$  [Bhatti and Cantor 1988],  
(b) Diffusivity plot of Ge in  $\text{Fe}_{78}\text{B}_{13}\text{Si}_9$  [present study].
- Figure 5.50 Normalized ( $1/T$ ) dependence of diffusivity of Au in.....218  
Fe-B (from literature) and Fe-B-Si amorphous alloys.  $T_x$  is the crystallization temperature of the metallic glasses. The slope changes with the addition of Si to the Fe-B alloys.
- Figure 5.51(a) Comparison of the temperature dependence of diffusivity.....221  
of Ge in  $\text{Fe}_{79}\text{B}_{16}\text{Si}_5$ , during early stages of relaxation (dashed line) and after relaxation (solid line). Note the similarity with the radiation enhanced diffusion shown Figure 5.51(b) for Si in  $\alpha$ -Fe.
- Figure 5.51(b) Comparison of enhanced diffusivity for Si in Fe substrate.....221  
(under bombardment with 300 keV  $\text{Ar}^+$  ions) and thermal diffusivity at various temperatures (after Dearnaley 1982).
- Figure 5.51(c) Comparison of the temperature dependence of diffusivity.....222  
of Ge in  $\text{Fe}_{78}\text{B}_{13}\text{Si}_9$ , during early stages of relaxation (dashed line) and after relaxation (solid line).
- Figure 5.51(d) Comparison of the temperature dependence of diffusivity.....222  
of Pd in  $\text{Fe}_{79}\text{B}_{16}\text{Si}_5$ , during early stages of relaxation (dashed line) and after relaxation (solid line).
- Figure 5.51(e) Comparison of the temperature dependence of diffusivity.....223  
of Pd in  $\text{Fe}_{78}\text{B}_{13}\text{Si}_9$ , during early stages of relaxation (dashed line) and after relaxation (solid line).
- Figure 5.51(f) Comparison of the temperature dependence of diffusivity.....223  
of Au in  $\text{Fe}_{79}\text{B}_{16}\text{Si}_5$ , during early stages of relaxation (dashed line) and after relaxation (solid line).
- Figure 5.51(g) Comparison of the temperature dependence of diffusivity.....224  
of Au in  $\text{Fe}_{78}\text{B}_{13}\text{Si}_9$ , during early stages of relaxation (dashed line) and after relaxation (solid line).
- Figure 5.51(h) Comparison of the temperature dependence of diffusivity.....224

of Pd in  $\text{Fe}_{40}\text{Ni}_{38}\text{B}_{18}\text{Mo}_4$ , during early stages of relaxation (dashed line) and after relaxation (solid line).

- Figure 5.52 Correlation between diffusivity (at 600 K, calculated.....227 from the Arrhenius plot), and atomic radii of the diffusing species in Fe-B and Fe-B-Si metallic glasses. The lines have been drawn to guide the eye. Note that the radius dependence is similar to the one observed in crystalline Fe and Cu (as shown in figures 5.53(a) and (b).
- Figure 5.53(a) Variation of diffusivity with the atomic radii of the.....228 diffusing species in crystalline Cu, (after Hood 1978).
- Figure 5.53(b) Variation of diffusivity with the atomic radii of the.....228 diffusing species in crystalline Fe, (after Askil 1979).
- Figure 5.53(c) Variation of diffusivity with the atomic radii of the.....229 diffusing species in crystalline Zr, (after Hood 1978).
- Figure 5.53(d) Variation of diffusivity with the atomic radii of the.....229 diffusing species in a-Ni-Zr alloy.
- Figure 5.54 Correlation between activation energy (Q) and the.....232 atomic radii of the diffusing species in Fe-B (from literature) and Fe-B-Si (present work) amorphous alloys. The plot does not show any definite trend in the variation of Q with r.
- Figure 5.55 Correlation between activation energy (Q) and .....233 pre-exponential factor ( $D_0$ ) for diffusion of various elements in Fe-B and Fe-B-Si metallic glasses. The lines are least squares fitting to the data points. The solid line depicts the trend in Fe-B-Si alloys, the larger dashed line represents the Fe-B alloys, the smaller dashed line represents the Ni-Zr alloy and dashed line at the extreme left depicts hydrogen diffusion in metallic glasses.

# LIST OF TABLES

TABLE NO.	TITLE	PAGE NO.
able 1.1	Characteristic properties of the diffusing species.....	3
able 1.2	Comparison of the characteristics of traditional..... metal and traditional glass with that of metallic glass.	5
able 1.3	Literature survey of diffusion in metallic glasses.....	27
able 1.4	Brief review of phase formation studies in metallic..... glasses using Mössbauer spectroscopy.	35
able 4.1	X-ray analysis of $\text{Fe}_{79}\text{B}_{16}\text{Si}_5$ and $\text{Fe}_{78}\text{B}_{13}\text{Si}_9$ samples..... heat-treated at $475^\circ\text{C}$ for 16 hr.	99
able 4.2	Mössbauer parameters for the as-received samples.....	102
able 4.3	Mössbauer parameters, obtained from computer analysis for..... metallic glass $\text{Fe}_{79}\text{B}_{16}\text{Si}_5$ after various heat treatments.	104
able 4.4	Reported values of internal magnetic field (H) of..... phases observed in the metallic glasses.	117
able 4.5	Mössbauer parameters obtained from computer analysis for..... metallic glass $\text{Fe}_{78}\text{B}_{13}\text{Si}_9$ after various heat treatments.	119
able 5.1	Sample identification for $\text{Fe}_{79}\text{B}_{16}\text{Si}_5$ - Ge..... diffusion couple.	136
able 5.2	The D-values for the diffusion of Ge in metallic..... glass $\text{Fe}_{79}\text{B}_{16}\text{Si}_5$ .	144
able 5.3	Sample identification for $\text{Fe}_{78}\text{B}_{13}\text{Si}_9$ - Ge..... diffusion couple.	151
able 5.4	The D-values for the diffusion of Ge in metallic..... glass $\text{Fe}_{78}\text{B}_{13}\text{Si}_9$ .	157
able 5.5	Sample identification for $\text{Fe}_{79}\text{B}_{16}\text{Si}_5$ - Pd..... diffusion couple.	161
able 5.6	The D-values for the diffusion of Pd in metallic..... glass $\text{Fe}_{79}\text{B}_{16}\text{Si}_5$ .	166
able 5.7	Sample identification for $\text{Fe}_{78}\text{B}_{13}\text{Si}_9$ - Pd..... diffusion couple.	170
able 5.8	The D-values for the diffusion of Pd in metallic..... glass $\text{Fe}_{78}\text{B}_{13}\text{Si}_9$ .	175

Table 5.9	Sample identification for $\text{Fe}_{79}\text{B}_{16}\text{Si}_5$ - Au.....	179
	diffusion couple.	
Table 5.10	The D-values for the diffusion of Au in metallic.....	182
	glass $\text{Fe}_{79}\text{B}_{16}\text{Si}_5$ .	
Table 5.11	Sample identification for $\text{Fe}_{78}\text{B}_{13}\text{Si}_9$ - Au.....	186
	diffusion couple.	
Table 5.12	The D-values for the diffusion of Au in metallic.....	189
	glass $\text{Fe}_{78}\text{B}_{13}\text{Si}_9$ .	
Table 5.13	Sample identification for $\text{Fe}_{79}\text{B}_{16}\text{Si}_5$ - Ag.....	193
	diffusion couple.	
Table 5.14	The D-values for the diffusion of Ag in metallic.....	196
	glass $\text{Fe}_{79}\text{B}_{16}\text{Si}_5$ .	
Table 5.15	Sample identification for $\text{Fe}_{78}\text{B}_{13}\text{Si}_9$ - Ag.....	197
	diffusion couple.	
Table 5.16	The D-values for the diffusion of Ag in metallic.....	197
	glass $\text{Fe}_{78}\text{B}_{13}\text{Si}_9$ .	
Table 5.17	Sample identification for $\text{Fe}_{40}\text{Ni}_{38}\text{B}_{18}\text{Mo}_4$ -Pd.....	201
	diffusion couple.	
Table 5.18	The D-values for the diffusion of Pd in metallic.....	206
	glass $\text{Fe}_{40}\text{Ni}_{38}\text{B}_{18}\text{Mo}_4$ .	
Table 5.19	Values of activation energy and pre-exponential factor.....	217
	for diffusion of various species in the metallic glasses.	
Table 5.20	Values of migration entropies of the diffusing species.....	243
	and the quasi-vacancies, and the relative value of critical displacement and the mean vibration frequency, in the metallic glasses studied.	

# CHAPTER 1

## INTRODUCTION

### 1.1 PREAMBLE

In 1960, an alloy of Au-25atom%Si (near its eutectic), was solidified from its melt at a very high cooling rate and an unexpected metallic alloy, amorphous in nature, was formed. This exciting and unexpected development was performed by Pol Duwez and his co-workers [Klement *et al.* 1960] at Caltech, Pasadena, USA. This entirely new species of non-crystalline alloys obtained by rapid quenching with cooling rates in the range of  $10^4$ - $10^8$  K/s were called amorphous metallic alloys, glassy alloys or Metallic Glasses. In 1967, the same group discovered strong ferromagnetic properties in an iron based amorphous alloy,  $\text{Fe}_{75}\text{P}_{15}\text{C}_{10}$  [Duwez *et al.* 1967]. Finally metallic glasses were produced in the form of a continuous ribbon [Pond *et al.* 1969] suitable for commercial applications. With these three historic events, glassy amorphous alloys / metallic glasses invoked the attention of scientists, engineers and technologists alike, because of their interesting variety of desirable properties (electrical, magnetic, mechanical, thermal, etc.), highly useful in technological applications. For example, transformer cores and laminations made of iron based metallic glasses ( $\text{Fe}_{78}\text{B}_{13}\text{Si}_9$ ,  $\text{Fe}_{81}\text{B}_{13}\text{Si}_4\text{C}_2$ ,  $\text{Fe}_{82}\text{B}_{10}\text{Si}_8$ , etc.,) have a higher efficiency, lower cost and a considerable energy saving potential. The properties of an amorphous alloy are determined by its atomic structure and both are very sensitive to heat treatment. On annealing it tends to relax and become denser by atomic rearrangement, which in turn is controlled by the diffusion of the atoms through the amorphous structure. Therefore a knowledge of the atomic transport or diffusion in metallic glasses is important in understanding the changes

changes occurring in these structure-sensitive thermal, electrical, magnetic and mechanical properties.

The first diffusion experiment performed on metallic glasses was reported in 1975 by Gupta et al.. Since then, there has been a steady increase in the volume of diffusion data and these have been reviewed from time to time [Luborsky 1983; Cantor 1985; Mehrer and Dorner 1989]. In most cases the Arrhenius dependence of the diffusion coefficient ( $D$ ), on the annealing temperature ( $T$ ) has been reported which is given by the expression  $D = D_0 \exp(-Q/kT)$ , where  $D_0$  is called as pre-exponential or frequency factor,  $Q$  is activation energy and  $k$  is Boltzmann constant. Correlations between these parameters and the physical properties of the alloys and those of the diffusing species, lead the authors to make speculations on the possible diffusion mechanisms. However for several cases of diffusion studies reported in the literature the relaxation effect in the metallic glasses was not considered. In the diffusion measurements on amorphous alloys, it is essential to study the  $D$  versus time dependence, to delineate the effect of relaxation. The  $D_0$  and  $Q$  values obtained by properly taking into account the relaxation effect should be used to identify the diffusion mechanism on the basis of a theoretical formalism.

## 1.2 OBJECT OF PRESENT STUDY

Keeping in view the above mentioned important facts, in the present work we have studied the diffusion of various elements (Ge, Pd, Ag, Au) in amorphous metal-metalloid metallic glasses  $\text{Fe}_{79}\text{B}_{16}\text{Si}_5$  and  $\text{Fe}_{78}\text{B}_{13}\text{Si}_9$ . Diffusion of Fe in metallic glass  $\text{Fe}_{40}\text{Ni}_{38}\text{B}_{18}\text{Mo}_4$ , was also studied to compare the results with the Fe-B-Si glasses with it. The crystallization onset temperature  $T_x$  for these metallic glasses as reported in literature [Goodfellow Metals-Catalogue 1991/92] are 515°C, 550°C and 410°C respectively.



The properties of the diffusing elements are given in Table 1.1. The study of correlations between some of these properties and the diffusing parameters (viz., radius dependence of diffusivity) is an important way to understand the diffusion mechanism in amorphous alloys. The selected species provide mass variation from 73 to 197, variation in atomic radii from 1.37 to 1.44 Å and ionic radii from 0.93 to 1.37 Å.

**TABLE 1.1**  
**CHARACTERISTIC PROPERTIES OF THE DIFFUSING SPECIES STUDIED**

DIFFUSING SPECIES	At.No.	At.Wt.	AT.DEN. (at/cc)	M.P. (°C)	G.R. (Å)	I.R. (Å)	C.R. (Å)
Ge	32	73	4.42e+22	937	1.39	0.93(+3) 0.53(+4)	1.22
Pd	46	106	6.80e+22	1554	1.37	0.86(+2)	1.28
Ag	47	108	5.85e+22	962	1.44	1.26(+1)	1.34
Au	79	197	5.90e+22	1064	1.44	1.37(+1)	1.34

G.R. = Goldschmidt radius.

I.R. = Ionic radius (with specific valency).

C.R. = Covalent radius.

Other important reasons of selecting these species for diffusion measurements in the Fe-B-Si alloys are: (a) The atomic mass of each element is larger than that of Fe (the constituent having the greatest mass in the Fe-B-Si metallic glass substrates). Therefore the signals from the elements are well separated in the Rutherford backscattering measurements. This leads to accurate measurements of the depth profiles and the diffusion coefficients. (b) These elements do not form globules on the surface of the metallic glass after heat treatment. The globular formations can obscure the diffusion profile. (c) Good quality films of these elements can be prepared by vacuum evaporation technique. The main objectives of the present thesis are summarized below:

- (i) To anneal the Fe-B-Si metallic glasses at various temperatures ranging from a value well below their crystallization temperature ( $T_x$ ), to a value

well above  $T_x$ , in order to identify from X-ray and Mössbauer studies the temperatures and annealing time-periods which retain the amorphous structure of these metallic glasses.

- (ii) To identify the various phases precipitating in these alloys after successive heat-treatment, and to study the dependence of the stability on the composition of the metallic glasses.
- (iii) To get an insight on the dependence of the magnetization direction on
  - (a) the metalloid content in the Fe-B-Si alloys, and
  - (b) annealing of the metallic glasses.
- (iv) To determine the time dependence of diffusivity of the selected diffusing elements (Ge, Pd, Ag and Au) in the metallic glass systems mentioned above.
- (v) To determine the temperature dependence of diffusivity in these metallic glasses in the relaxed state, and to obtain the diffusion parameters, viz.  $Q$  and  $D_0$  values from it.
- (vi) To determine the correlation between the diffusion parameters and the various physical properties of the diffusing species.
- (vii) To get an insight on the diffusion mechanism in these metallic glasses on the basis of the diffusion data and the correlations thus obtained.

For the sake of completeness, we present in the following sections a discussion on metallic glasses (its importance, kinetics of formation, structural models and methods of preparation); diffusion (alternative methods of diffusion measurement, various formalism applicable to diffusion in metallic glasses, and a compilation of diffusion measurements in metallic glasses); and a compilation of phase precipitation studies in metallic glasses performed using Mössbauer spectroscopy.

## 1.3 METALLIC GLASSES

The properties of metallic glasses are different as compared to those of the traditional oxide glasses and ordinary metal alloys in several important respects as shown in Table 1.1. The inter-atomic bond in metallic glasses is essentially metallic, like metallic alloys, (the traditional glasses have covalent bonds), whereas its structure is amorphous or non-periodic like that of traditional glasses. Some of the special features recently discovered are zero resistance to corrosion, propagation of acoustic waves for a larger distance, super-conductivity at low temperatures and propagation of spin waves.

TABLE 1.2

COMPARISON OF THE CHARACTERISTICS OF TRADITIONAL METAL AND  
TRADITIONAL GLASSES WITH THAT OF METALLIC GLASSES

PROPERTY	TRADITIONAL METAL	TRADITIONAL GLASS	METALLIC GLASS
structure	crystalline	amorphous	amorphous
bonding	metallic	covalent	metallic
yield stress	non-ideal	almost ideal	almost ideal
workability	good, ductile	poor, brittle	good, ductile
hardness	low to high	very high	very high
UTS	low to high	low	high to very high
optical- transmission	opaque	transparent	opaque
thermal- conductivity	very good	poor	very good
resistance	very low	high	very low
corrosion- resistance	poor to good	very good	very good
magnetic properties	various	non-existent	various

### 1.3.1 Formation and kinetics of formation

Almost all types of glasses — silicates, polymers and metallic, can be prepared by continuous cooling of the liquid melt provided that crystallization can be bypassed. In the so called ordinary glasses or silicate glasses, the transition from liquid melt to solid glass takes place at low rates of cooling often less than  $10^{-2}$  K/s. In case of metallic melts, the non-directional bondings present, produce rapid atomic rearrangements, even at high degrees of undercooling i.e., much below their equilibrium freezing temperature  $T_m$ . Also the latent heat of solidification i.e., the thermal energy released during the transformation, is very high for metals, running upto thousands of calories per gram-atom.

If the metallic-alloy melt is cooled rapidly at cooling rates  $\dot{T}$  approaching  $10^6$  K/s, the equilibrium, due to atomic rearrangement (i.e., crystallization) is suppressed because of insufficient time for nucleation. And hence, the metastable liquid solidifies into a supercooled metallic liquid i.e., an amorphous metallic alloy. This transition occurs within a narrow temperature interval called as the glass transition temperature  $T_g$ , and at this temperature range (Figure 1.1) the shear viscosity ( $\eta$ ) of the under-cooled liquid increases very rapidly to a value of about  $10^{13}$  Poise.

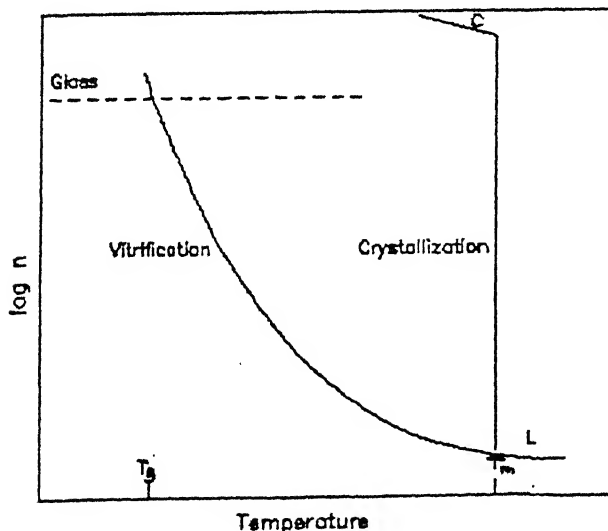


FIGURE 1.1 Temperature dependance of shear viscosity ( $\eta$ ) in amorphous metallic alloys.



has been observed [Davies 1975] that on increasing certain solutes in a metal i.e., on alloying,  $T_g$  generally increases but relatively slowly and  $T_1$ , the absolute melting point of the alloy most often decreases, and hence GFA increases. It was also found [Donald and Davies 1978] that in many cases, substitution of a second solute (metal or metalloid) converted a difficult binary glass former or an already RGF (readily glass forming alloy) to a more easily glass forming alloy, due to the ternary eutectic formation.

In the past thirty years, several different kinds of metallic alloys have been obtained in the amorphous state by liquid quenching. Most of these belong to one of the four distinct categories [Davies 1983].

The first group to be discovered consist of the transition metal-metalloid (TM-M) glasses, which has further two divisions: the late transition (TL-M) and the early transition (TE-M) metal-metalloid glasses. Besides some exceptions, the glass forming range (GFR) in the case of (TL-M) is rather narrow and is about 13-25 atom% of metalloid, e.g.,  $\text{Fe}_{80}\text{B}_{20}$ . The exceptions in this case being  $\text{Ni-B}_{31-41}$ ,  $\text{Ni-B}_{17-18.5}$ ,  $\text{Co-B}_{17-41}$  etc.,. The technologically useful Fe-Si-B alloys have 13 to 35 atom% (Si+B). In case of (TE-M) alloys, the general tendency for RGF is in the range 15-30 atom% metalloid, e.g.  $\text{Ti-Si}_{15-20}$  and  $\text{Nb}_{80}\text{Si}_{20}$ . The second group combines an early transition metal with a late transition metal (TE-TL), e.g.,  $\text{Nb}_{40}\text{Ni}_{60}$ . The alloys in the third group are made up exclusively of simple metals, e.g.,  $\text{Ca}_{65}\text{Al}_{35}$ . And those in the fourth group are the rare-earth metal (RE-TM) transition metal type e.g., Gd-Co alloys.

A general characteristic of glass formation for the four groups of metallic alloys is that they are obtained in a relatively narrow concentration range around those compositions which corresponds to deep eutectics in their phase diagram. However it appears that a single parameter or criteria cannot satisfactorily explain the observed composition ranges for glass formation, even in related systems [Ramachandrarao 1984].

### 1.3.2 Preparation

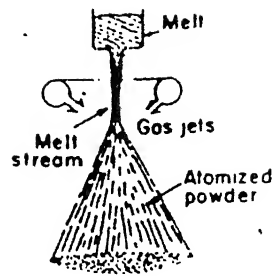
A great variety of techniques have been introduced by now to produce amorphous alloys. No doubt, the production of metallic glasses in bulk is done by various (Rapid Solidification Process) RSP techniques. The RSP techniques can be divided into two categories [Anantharaman 1988] namely: spray methods involving fragmentation of melt into droplets prior to quenching ; and chill methods preserving continuity of the melt upto and during quenching. There are several non RSP or surface methods too, which induce surface modifications of the substrate to a limited depth. However the rate of production obtained using these techniques is much lower than that of the RSP techniques.

#### [a] Spray methods:

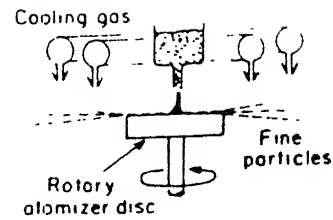
In these methods [Anantharaman 1988] continuous stream of liquid metal is atomized, i.e., the molten melt is sprayed out into fine droplets and quenched by means of gas, liquid or solid (Figure 1.3). The mechanism of achieving atomization and successive quenching is different for the various techniques (quenching rates varying from  $10^5$  to  $10^8$  K/s).

Droplets or granules are formed by Gas and Ultrasonic gas atomization method; Water atomization method; Centrifugal atomization method; Rapid Solidification Rate Centrifugal Atomization Process (RSR-CAP); Laser Spin Atomization (LSA) and the Rotating Electrode Process (REP).

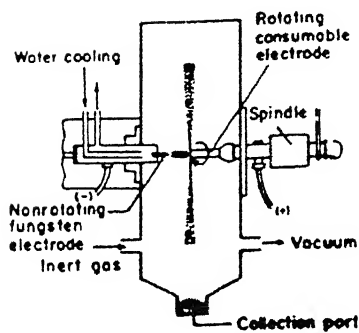
Powders on a continuous basis is now possible by the Rapid Spinning Cup (RSC) process; the Twin Roll atomization method and the Spark Erosion technique. Granules typically 1000-5000  $\mu\text{m}$  long and 1000  $\mu\text{m}$  in diameter as produced by the Rotating Perforated Cup (RPC) method, are consolidated as sheets. Droplets are consolidated into strips of thickness upto 18 mm and 0.5 mm widthin the Spray Rolling method. The Gun technique used for the first time by Pol Duwez and his co-workers in 1959, remained the most popular of all RSP techniques till the advent of the continuous production methods in the seventies. Thin foils upto



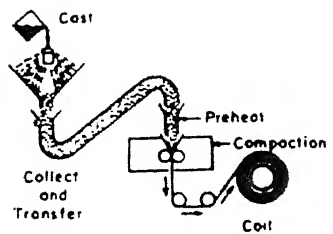
(a)



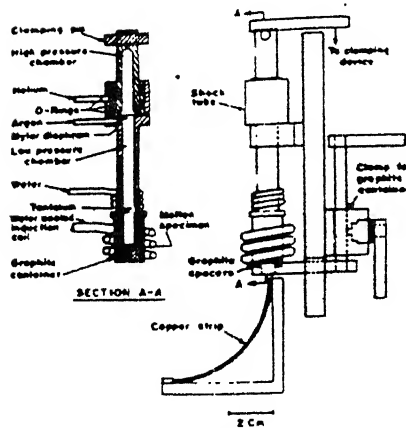
(b)



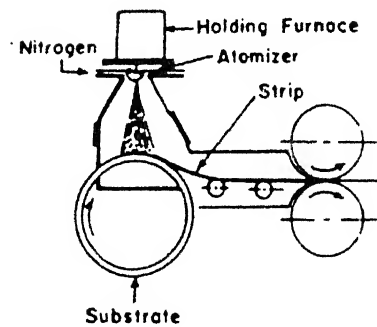
(c)



(d)



(e)



(f)

**FIGURE 1.3 Various SPRAY Methods for production of Metallic Glass.**

- (a) Inert Gas atomization method, (b) RSR-Centrifugal atomization process, (c) Rotating electrode process, (d) Rotating perforated cup method, (e) Gun technique, (f) Spray rolling method - using a cooled drum.



15 $\mu$ m thick are produced by the this method. Flakes are produced by the Alcoa process. Thin films of thickness of 100  $\mu$ m and more, can be obtained by the Plasma Spray Deposition technique.

[b] Chill Methods:

In these methods (Figure 1.4) the melt is quenched by fast moving or stationary highly cooled surfaces so as to obtain continuous alloys in the form of wires, ribbons, tapes and sheets. The various methods mainly in use for producing wires are: the Die method; the Taylor process; Crucible Melt Extraction (CME), Pendant Drop Melt Extraction (PDME) method; Melt Drag process; and the Melt Overflow method. Melt spinning and Planar flow process are used for producing strips.

In the Piston and Anvil technique foils of about 4-5 cm. in diameter and about 100  $\mu$ m. in thickness can be obtained.

Free Flight Melt Spinning (FFMS) technique [Pond 1961]; and the Chill Block Melt Spinning (CBMS) method [Pond et al. 1969] are the most commonly used methods now-a-days to produce long and continuous ribbons and tapes. The cooling rates achieved in CBMS are about  $10^6$  K/s and the ribbons produced are few mm wide. Modifications have been made in CBMS to produce helical glassy alloy ribbons, composite alloys, and multilayer deposits.

The need for continuous and wide amorphous ribbons or tapes, spurred the development of the Planar Flow Casting (PFC) process or strip casting process in 1979 by Narasimhan . By this process ribbons/tapes upto 300 mm in width and 20 to 100  $\mu$ m in thickness can be produced. The CBMS and PFC processes and its modifications are extensively used now-a-days for fabrication of rapidly quenched materials in industries because of its inherent simplicity and facility for making wide variety of continuous ribbons and tapes.

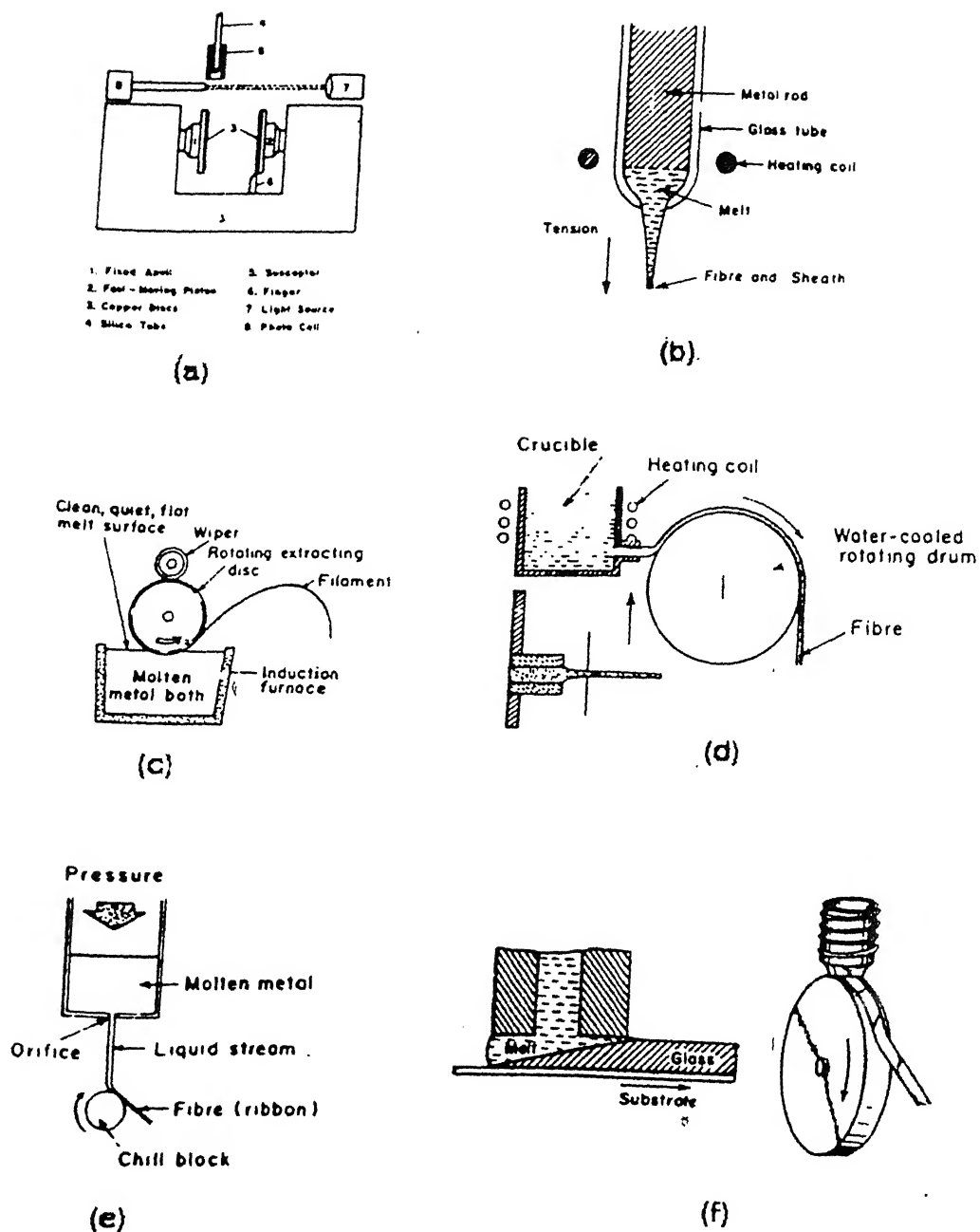


FIGURE 1.4 Various CHILL methods for production of metallic glass.

- (a) Piston and anvil method, (b) Taylor process,  
 (c) Crucible melt extraction process, (d) Melt drag  
 process, (e) Chill-block melt spinning technique,  
 (f) Planar flow process.

### [c] Surface methods:

The various surface modification techniques include: sputtering; thermal, chemical and electro-deposition techniques; ion or electron irradiation; ion implantation; ion mixing; laser surface treatment and solid state diffusion reactions. These involve rapid melting and solidification of a limited depth at the surface of a more substantial thickness of material acting as the heat sink. The starting material in the non RSP surface techniques can be in the form of either a solid, liquid or vapour. Only the quantity of material produced per run is low when the starting material is in the vapour phase.

The inherent high quench rates in the sputtering and the evaporation methods i.e.,  $10^8$  K/s, allows the formation of some metallic glasses (alloys of lanthanides) which cannot be produced by other methods. Ion-implantation methods [Grant et al. 1970] can achieve an effective quench rate of  $10^{14}$  K/s. The use of directed energy and ion beam processing methods for surface modification of metallic materials has been reviewed in literature [Kear et al. 1981]. Electron and laser beams are particularly suitable for melting small surface areas ranging from 10 to  $1,000 \mu\text{m}^2$  of a substrate. Typical quench rates derived from such process range from  $10^4$  to  $10^8$  K/s. Surface melting by lasers has practical applications like forming new surface compositions by melting thin films, wire or powder on to the substrate surface. Particle injection laser layer technique produces thick films by joining amorphous layers.

### 1.3.3 Structural models

Just like crystalline materials, a knowledge of the structure of the metallic glasses gives a basis for understanding its physical properties. Structural information obtained by experimental techniques can only be fully exploited, when this information is compared with the theoretical predictions of structural models. The structural models for amorphous metallic alloys have

evolved in three differently distinct steps.

In the first attempt, models based on the pioneering work of *Bernal* [1960 and 1964] and *Finney* [1970] were constructed. Their dense random packing of hard spheres (DRPHS) model (Figure 1.5(a)) is based on space filling requirements only and no attention is paid to bond directionality.

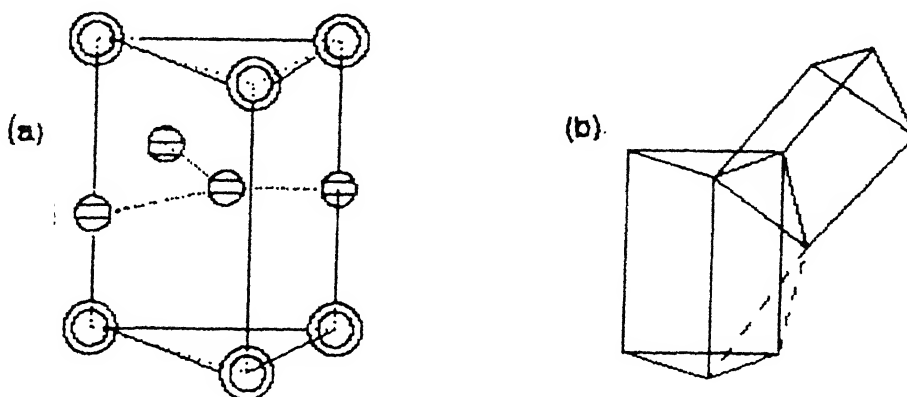


FIGURE 1.5 Structural models for amorphous alloys (a) DRPHS model and (b) Gaskell's trigonal units

The second type of modeling attempted, can be briefly characterized as the reappearance of order amidst the disorder and was introduced by Gaskell in 1979. These models take into account the directional effects of chemical bonding between atoms, and are based on a quasi-random packing of crystalline structural units (basically trigonal prisms) rather than on a packing of single atoms as depicted in Figure 1.5(b).

The third type of modeling uses the molecular dynamics technique to build the amorphous structure by simulation.

There are three major problems [Finney 1983] which crop up while modeling binary or more complex amorphous alloys via the above two methods. The first problem is the requirement of an adequate knowledge of the interatomic forces or potentials and pseudopotentials. The second problem is of knowing the chemical ordering in the amorphous alloys properly. The third problem is concerned with the 'packing constraints' applied to construct an amorphous alloy model. These

packing constraints are strong structure determinants, yet are poorly understood.

Several techniques are available for the study of atomic scale structure of amorphous solids [Schaafsma 1981], and is conveniently divided as: the direct methods and the indirect methods. The first group, consists of determination of the total structure factor  $S(Q)$  of the metallic glasses by diffraction studies using x-rays, electron beam and neutron scattering experiments. These methods give direct information about the interatomic distances and their distribution. The general conclusion on the basis of numerous modeling studies is that no model seems to be satisfactory as yet in explaining quantitatively all features of the diffraction profile even in a single metallic glass [Wagner 1985].

The indirect method consists of nuclear techniques like Mössbauer spectroscopy (MS) and nuclear magnetic resonance (NMR). These techniques give information about the local environment of the probe atom or nucleus and the distribution of nearest neighbours around it, which is complementary to that obtained with the direct methods. In favourable cases of metallic glasses, the symmetry of the local environment is also reflected. The Mössbauer effect of  $^{57}\text{Fe}$  in Fe-Si-B metallic glasses is one such case as discussed in Chapter 4.

#### 1.3.4 Structural relaxation (an effect of annealing)

Amorphous alloys or metallic glasses exist in a frozen metastable state. On thermal annealing, these alloys have a likelihood to undergo three different processes, namely structural relaxation, crystallization and reversible relaxation. This can be clearly understood from the plots of volume ( $V$ ) [Schaafsma 1981], and Gibb's free energy ( $G$ ) [Mehrer and Dorner 1989] change with respect to temperature as shown in the Figure 1.6. The two solid lines in each plot represent the particular property for the liquid and the crystalline solid. The liquid state (i.e., above the melting temperature  $T_m$ ) has a greater volume and

lower Gibbs free energy. During glass formation as the temperature is reduced the process of the liquid state is followed uptill the glass transition temperature  $T_g$ . Below that the metastable state (having higher free energy and volume) of the liquid gets frozen and the amorphous metallic glass is formed.

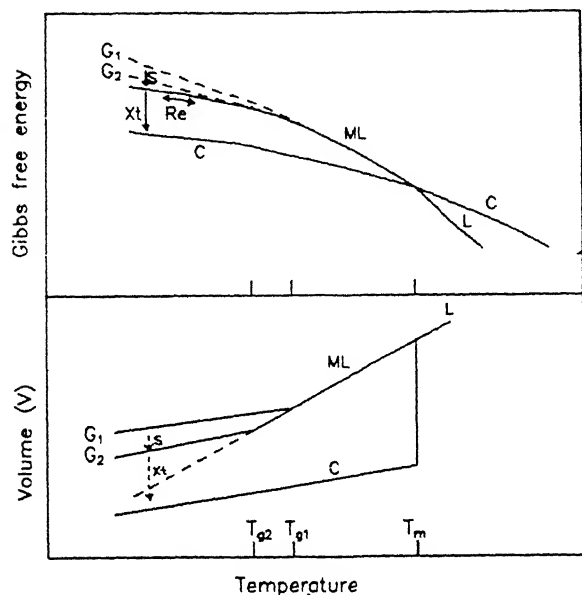


FIGURE 1.6 Temperature dependence of volume  $V$  and Gibbs free energy in amorphous alloys.

On annealing the as-prepared samples of these glassy metallic alloys for the first time for long durations (indicated by  $S$  in Figure 1.6), at a temperature below  $T_g$ , there is a tendency to relax their structure towards a state having a lower free volume and free energy which causes changes in their atomic structure. These irreversible changes, collectively known as structural relaxation, affects to some extent all physical properties [Inove et al. 1985] of the metallic glasses. Among these, properties well described by a free-volume theory such as density, viscosity, and diffusivity also show changes. The decrease in atomic diffusivity can be quite drastic as observed by us (Chapter 5) and by Horvath and collaborators. This strongly suggests that structural relaxation involves principally a decrease in free energy and free volume through an increase in packing fraction (e.g., by elimination of voids), a process leading to an increase in topological short range order (TSRO). In general, this has been supported by x-ray diffraction studies.

### 1.3.5 Crystallization (an effect of annealing)

On annealing for still longer time periods (as shown in Figure 1.6 by the arrow Xt) the process tends towards the curve of the crystalline state and hence crystallization of the metallic glass takes place. This is also an irreversible process leading to an increase in topological short range order (TSRO). The temperature at which spontaneous crystallization begins when metallic glass is heated is defined as the crystallization temperature  $T_x$ . For majority of the metallic glasses  $T_x$  is between 40% to 65% of the absolute melting temperature ( $T_m$ ) of the alloy. It varies from 400 K for magnesium based glasses to more than 1200 K for glasses based on refractory metals. Most of the commercially important ferro-magnetic iron-based glasses have  $T_x$  around 700 K [Scott 1986]. Depending on the composition of the glasses, the following reactions have been observed during crystallization [Scott 1983, Ranganathan and Banerjee 1983, Köster and Herold 1981].

[a] Polymorphous crystallization- transformation of the glass to a crystalline phase with no change in composition. Though it is the simplest of reactions, it is the least common.

[b] Eutectic crystallization- transformation of the glassy phase into two phases that grow in a coupled fashion. It requires diffusion to enable the partition of solute between the two growing phases.

[c] Primary crystallization- in which the crystals have a composition completely different from that of the glassy matrix. It is considered as the initial stage of crystallization in many metallic glasses with the primary phase being either a terminal solid solution e.g.,  $\alpha$ -Fe, or an intermediate phase e.g.,  $\text{Cu}_{10}\text{Zr}_7$  in  $\text{Cu}_{56}\text{Zr}_{44}$ .

[d] Phase separation- a process where the glass separates into two compositionally distinct glassy phases, which then crystallizes independently. Though it is the basis of many glass ceramics, it is relatively scarce in

metallic glasses.

Though metallic glasses crystallize according to one of the above mechanisms; most often the dominant crystallization mechanism is unclear. In many cases of crystallization, one or more metastable phases are formed before the equilibrium phases occur. The measured crystal growth rates in metallic glasses do not in general agree with the independent measurements of diffusion rates or diffusion coefficients [Cantor 1982].

The devitrification or crystallization of metallic glasses has enormous practical implications. The soft ferromagnetic properties of glassy Fe-B-Si alloys are drastically reduced at the onset of crystallization [Luborsky 1979]. However, partial or full crystallization in some metallic glasses is used to produce novel and useful microstructures within the glassy appliances, unobtainable by other means.

Therefore for industrial applications, it is essential that the glassy alloys are guaranteed to resist crystallization over a span of 20 years at typical working temperatures of 100-200 °C. Hence without a detailed knowledge of their long term thermal stability, one cannot use them confidently. The atomic diffusion is one such process which can be studied to understand and confirm the thermal stability of the metallic glasses.

#### 1.3.6 Reversible relaxation (an effect of annealing)

Reversible relaxation process refers to the cycling of the system between different structures by annealing at different temperatures (indicated by Re in Figure 1.6). However, since the energy of a metal is a strong function of volume, it seems unlikely a priori, that reversible relaxation involves significant changes in volume. For this reason there has been a tendency to attribute reversible effects to a volume conserving anelastic deformation (e.g., by local shear through bond reorientation affecting the arrangement of the various



chemical species), with the driving force being a change in compositional or chemical short range order(CSRO). Unfortunately only few measurements have been made to test these results directly and quantitatively. Probably the most complete and direct evidence of structural changes has been obtained [Inove *et al.* 1985, BrÜning *et al.* 1978, Chen 1981] by measuring the enthalphy of relaxation.

## 1.4 DIFFUSION

The migration of an atom through any material by random motion is called diffusion. The making and breaking of chemical bonds in matter always require some diffusive motion by the ions or atoms. As a result, the energetics and mechanism of diffusion control the kinetics of nearly all solid state chemical reactions. Some of the important solid-state reactions where diffusion plays an important role are: (i)corrosion; (ii)hardening of structure alloys by precipitation; (iii)doping of semiconductors; (iv)sintering; (v)radiation damage; and in the present context (vi)crystallization and phase precipitation in amorphous structures. Hence diffusion is of considerable practical importance. In certain types of solid state reactions the diffusion lengths vary from a few nm to few hundred nm, over a temperature range of practical interest. This makes the diffusion experiments difficult and challenging.

### 1.4.1 Techniques of diffusion measurement

Experimental measurements of diffusion in the solid state were first made by Roberts-Austen [1896]. The radioactive tracer technique was established for accurate measurements of diffusion in solid state materials by the use of radioisotopes for the first time by Tomizuka [1959]. The first diffusion measurements on amorphous alloys was performed [Gupta *et al.* 1975], by studying the diffusivity of Ag in  $\text{Pd}_{81}\text{Si}_{19}$ . Several direct and indirect methods [Cantor and Cahn 1983, Mehrer and Dorner 1989] are presently employed for diffusion studies in

metallic glasses. A few of these methods are mentioned below.

[a] Direct methods:

In all direct methods of investigation of diffusivity the diffusion couples are made by either thermal evaporation of natural elements or ion-implantation / sputter deposition of the diffusing species (in the form of natural elements or radioactive tracers) on to the alloy surface. The main disadvantage of ion-implantation is of a possibility of damaging the alloy structure and locally enhancing the diffusivity. The advantage of using radioactive tracers is of conveniently studying the self-diffusivity of the amorphous alloys.

Migration of the diffusing atoms of the diffusion couples are obtained by thermal annealing or by heavy ion irradiation. The depth versus concentration profiles of the diffusing elements is then obtained by (a) sputter erosion of the surface layers and determining the radioactivity of the radioactive tracers; (b) sputter erosion of the surface and composition analysis by secondary ion mass spectroscopy (SIMS), Auger electron spectroscopy (AES) and secondary neutral particle mass spectroscopy (SNMS); (c) Rutherford back-scattering spectrometry (RBS) or Nuclear reaction analysis (NRA) using MeV ion beams.

Sputter erosion techniques are destructive in nature; profiling of the eroded surface can cause errors in the depth measurements. Self diffusion can be studied conveniently by SIMS or SNMS as it discriminates between different isotopes while AES and RBS discriminates between different elements only. Hence the diffusing species has to be different from the constituents of the alloy in case of AES, RBS and NRA. By RBS, diffusion of heavy atoms can be studied in an alloy having comparatively lower atomic weights constituents; by NRA light elements can be studied; while this factor is not observed in AES. In contrast to sputter profiling methods, RBS and NRA are non-destructive.

#### [b] Indirect methods:

Several indirect methods are being used for studying diffusion in metallic glasses. There are several phenomenon related to atomic migration and hence by studying their variation with annealing time and temperature one can obtain the diffusivity in the metallic glasses. The important methods applied in the case of metallic glasses are: (a) estimation of the self-diffusivity from measurements of crystal growth rates during thermal annealing [Koster et al. 1981]; (b) estimation of self-diffusivity from measurements of segregation of the diffusing species to a free surface [Baer et al. 1981]; (c) estimation of the inter-diffusivity on annealing of thermally deposited films of amorphous alloys [Greer et al. 1982].

Indirect determination of diffusivity should be treated with caution [Cantor and Cahn 1983, Mehrer and Dorner 1989], because additional assumptions are made while employing these processes.

#### 1.4.2 Diffusion equation and its solution

The rate of flow (flux) of an atomic species in a medium is directly proportional to its concentration gradient. The proportionality constant is called as the diffusion coefficient or diffusivity (of dimension  $\text{m}^2/\text{s}$ ). The phenomenological relationship between the two is known as the Fick's Law and is given by the three dimensional equation [Fick 1855, Manning 1968],

$$J = - \left( D_{xx} \frac{\partial C}{\partial x} + D_{yy} \frac{\partial C}{\partial y} + D_{zz} \frac{\partial C}{\partial z} \right) = -D_{ii} \vec{\nabla} C_i \quad (1.1)$$

where  $J$  (the flux), is the number of particles passing through a plane of unit area per unit time;  $C$  is the concentration; and  $D_{ii}$  are the diffusion coefficients along the three principal crystallographic axes. The diffusion coefficient  $D$  is characteristic of each system and all the physics of the mass transport is contained in it. In the temperature range 20-1500 °C, the values of  $D$  for solids are within the limits from  $10^{-20}$  to  $10^{-4} \text{ cm}^2/\text{s}$ . For an isotropic

medium or a solid with cubic symmetry  $D_{xx} = D_{yy} = D_{zz}$ . Equation 1.1 reduces to

$$J = -D \frac{\partial C}{\partial x} \quad (1.2)$$

When Equation 1.1 is combined with the equation of continuity :

$$\frac{\partial C}{\partial t} = - \vec{\nabla} \cdot \vec{J} \quad (1.3)$$

it yield's Fick's second law :

$$\frac{\partial C}{\partial t} = \vec{\nabla} \cdot (D \vec{\nabla} C) \quad (1.4)$$

For a homogeneous medium,  $D$  is independent of concentration, hence in three dimension the diffusion equation is written as :

$$\frac{\partial C}{\partial t} = D_{xx} \frac{\partial^2 C}{\partial x^2} + D_{yy} \frac{\partial^2 C}{\partial y^2} + D_{zz} \frac{\partial^2 C}{\partial z^2} = D_{ii} \nabla^2 C_i \quad (1.5)$$

Considering an isotropic medium and one dimensional diffusion direction, we can write :

$$\frac{\partial C}{\partial t} = D \frac{\partial^2 C}{\partial x^2} \quad (1.6)$$

In general  $D$  is obtained by Fick's second law, i.e., Equations 1.3 to 1.6, rather than the first, because concentrations are easier to measure than fluxes (exceptions being diffusion of a gas into or out of a solid). Also the magnitudes of  $D$  in the solid state are so small that the required steady state is seldom reached.

The analytical solution  $\{C(x,t)\}$  of the diffusion equation, has been reported in the literature for various initial (IC) and boundary conditions (BC), which are related to the different experimental configurations viz., thin film geometry, thick film geometry, etc.. The initial conditions corresponds to the distribution of the diffusing species in the sample before diffusion, and the boundary conditions describes what happens to the diffusing species at the boundaries of the sample while diffusion takes place. One most often determines,  $C(x)$  at constant  $t$ , i.e., concentration distribution along the diffusion direction after a time period  $t$ . The solutions to the diffusion equation for some common geometries are described below [Crank 1975, Borg et al. 1988] :

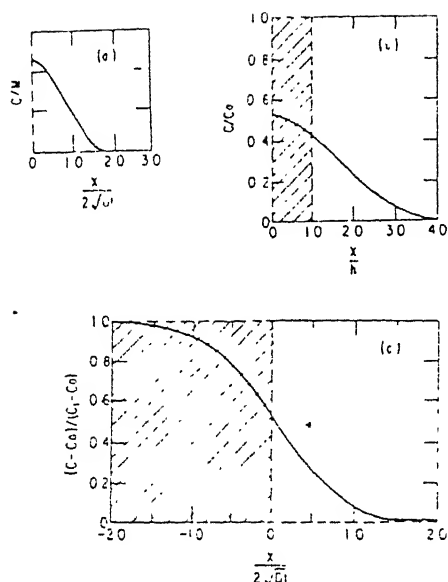


FIGURE 1.7 Solutions to various diffusion geometries: (a) thin layer (b) thick layer and (c) semi-infinite.

[a] Thin layer or Instantaneous source geometry

In this geometry an infinitesimally thin layer ( $\ll \sqrt{Dt}$ ), of diffusing substance is deposited on one surface of a semi-infinite substrate as shown in Figure 1.7(a). Considering  $C_0$  as the initial concentration of the diffusing substance,  $t$  as the time taken for diffusion and  $\delta$  as the dirac-delta function we get,

$$\text{IC : } C(x, 0) = C_0 \delta(x)$$

$$\text{BC : } \frac{\partial C}{\partial x}(0, t) = 0$$

$$\text{Solution : } C(x, t) = \frac{C_0}{\sqrt{\pi Dt}} \exp\left(-\frac{x^2}{4Dt}\right) \quad (1.7)$$

[b] Thick layer geometry

In this case the film thickness  $h$ , is of the order of the diffusion distance ( $\sqrt{Dt}$ ). Considering  $C_0$  as the initial concentration of the diffusing substance (Figure 1.7(b)), we have,

$$\text{IC : } C(x, 0) = C_0 \quad h \geq x \geq 0$$

$$C(x, 0) = 0 \quad x > h$$

$$\text{BC : } \frac{\partial C}{\partial t}(0, t) = 0$$

$$\text{Solution : } C(x, t) = \frac{C_0}{2} \left[ \operatorname{erf}\left(\frac{x+h}{\sqrt{4Dt}}\right) + \operatorname{erf}\left(\frac{x-h}{\sqrt{4Dt}}\right) \right] \quad (1.8)$$

[c] Semi-infinite couple geometry

The edges of the couple are well beyond the diffusion distance ( $\gg \sqrt{Dt}$ ), such that the concentrations at the edges remain unchanged (Figure 1.7(c)). In this case:

$$\begin{aligned} \text{IC :} \quad C(x,0) &= C_0 & x < 0 \\ C(x,0) &= 0 & x > 0 \end{aligned}$$

$$\text{Solution :} \quad C(x,t) = C_0 \left[ 1 - \operatorname{erf} \left( \frac{x}{\sqrt{4Dt}} \right) \right] \quad (1.9)$$

The error function  $\operatorname{erf}(z)$  in the above equation is given by

$$\operatorname{erf}(z) = \left( \frac{4}{\pi} \right)^{1/2} \int_0^z e^{-\eta^2} d\eta \quad (1.10)$$

Numerical values of the error function are available in tabular form, which are computed by using the following series expansion [Borg et al. 1988]

$$\int_0^x e^{-\eta^2} d\eta = \frac{2}{(\pi)^{1/2}} \left( x - \frac{x^3}{1!3} + \frac{x^5}{2!5} - \frac{x^7}{3!7} + \dots \right) \quad (1.11)$$

[d] Numerical method

Apart from the analytical solution given above, the diffusion equation can be solved numerically to obtain the concentration profile. This method has been utilized by Sharma [1986] to obtain diffusion coefficients of various elements in metallic glasses. In this method the sample surface region is divided into  $N$  number of layers each of width  $\Delta x$ .  $N$  is chosen such that

$$N \times (\Delta x) \gg \sqrt{4Dt} \quad (1.12)$$

The time period for diffusion is divided into time steps  $\Delta t$ , with the condition that

$$2 \times D \times (\Delta t) \leq (\Delta x)^2 \quad \text{or} \quad [D \times (\Delta t)] / (\Delta x)^2 \leq \frac{1}{2} \quad (1.13)$$

The concentration profile is then obtained from the finite difference analogue

$$C_i(t + \Delta t) = C_i(t) + \frac{D \times (\Delta t)}{(\Delta x)^2} \left[ C_{i+1}(t) - 2C_i(t) + C_{i-1}(t) \right] \quad (1.14)$$

for  $i = 1, 2, 3, \dots, N$ .

In each of the above four cases, the concentration profile is obtained by giving an approximate value to the diffusion coefficient  $D$ . The theoretical profile thus obtained is then folded with a Gaussian type depth resolution function and compared visually with the experimentally determined profile. The diffusion coefficient of the diffusing species (film) is the one, which has been used to obtain the best fit profile.

In the present work both analytical solutions and the numerical method have been utilized to obtain the diffusion coefficients and both procedure gave similar results.

## 1.5 ARRHENIUS LAW AND ACTIVATION ENERGY

The diffusion coefficient  $D$  has been observed to vary with the annealing temperature, according to the following equation

$$D = D_0 \exp\left(-\frac{Q}{kT}\right) \quad (1.15)$$

where  $Q$  is the activation energy,  $D_0$  is the pre-exponential factor,  $k$  is the Boltzmann's constant and  $T$  is the temperature at which diffusion takes place. This is known as the Arrhenius law, and is observed in all crystalline materials. The  $D$ -values are plotted (along the y-axis) against the inverse annealing temperature ( $1/T$ ) in a semi-log graph. The slope obtained from the plot gives  $Q/k$  and the intercept on the y-axis, gives the  $D_0$  value. For most crystalline materials, characteristic values of  $Q$  range from 8 to 30 eV/atom (i.e., 20 to 70 kcal/mole) and that of  $D_0$  are generally in the vicinity of unity [Borg et al. 1988].

Though the diffusion data available for amorphous materials is much less (as compared to it's crystalline counterpart), Arrhenius type of behaviour has been observed (within experimental error) in these too. In general activation energy of metallic glasses is determined from the Equation 1.15, which is considered as a direct method. It is possible to determine the activation energy by

indirect methods too. Some of these are (i) by X-ray diffraction methods [Meng and Wang 1986, Egami 1978]; from viscosity measurements [Taub and Spaepen 1980]; from internal friction method [Berry 1978, Yoon and Eisenberg 1978, Tyagi and Lord-Jr. 1979]; stress relaxation method [Luborsky and Walter 1978, Ast and Krenitsky 1979, Berry 1978]; steady state creep [Patterson and Jones 1980]; magnetic annealing [Luborsky 1976]; etc.,.

Activation energies in relaxed amorphous alloys are in the range 0.6 to 3.5 eV, similar to crystalline self-diffusion and substitutional impurity diffusion. Frequency factors are very varied, ranging from  $10^{-16}$  to  $10^{12}$   $\text{m}^2/\text{s}$ . An approximately constant activation energy and frequency factor in each diffusion couple indicates, that within experimental error a single diffusion mechanism is operating over the range of temperatures studied. For amorphous metallic glasses the diffusion data available at present, has not yet given any definite indication about the diffusion mechanism in them.

## 1.6 BRIEF REVIEW OF DIFFUSION IN METALLIC GLASSES

Diffusion data on amorphous metallic alloys or metallic glasses have recently started to accumulate, inspite of the difficulties associated with measuring the small diffusion rates. These diffusion measurements have made it possible to make reasonable generalizations about diffusion rates and mechanisms in amorphous alloys [Cantor and Cahn 1983, Cantor 1985, Horvath and Mehrer 1986, Mehrer and Dorner 1989] although several questions still remain unsolved. A compilation of diffusion studies (by direct measurements) on metallic glasses is given in Table 1.2. Diffusion coefficients determined by indirect methods [Baer et al. 1981, Greer et al. 1983, Greer 1987], have yet to be understood thoroughly.

Kijek et al. [1984] have proposed two types of diffusion mechanism on the basis of comparison of D-values of different diffusing species in metal-



**TABLE 1.3**  
**LITERATURE SURVEY OF DIFFUSION IN METALLIC GLASSES**

ELE (Å)	RADII	METALLIC GLASS	METHOD USED X	TEMP. RANGE(K)	CONDITION B	Q (ev)	D <sub>0</sub> (m <sup>2</sup> /s)	MECHANISM PROPOSED	REFERENCE
B	0.97	Co <sub>75</sub> B <sub>25</sub>	E,AES	573-633	U	0.59	$1.20 \times 10^{-14}$	N	Misse et al.(1985)
Si	1.17	Co <sub>75</sub> B <sub>25</sub>	E,AES	573-633	U	0.97	$3.50 \times 10^{-12}$	N	Misse et al.(1985)
Ag	1.44	Cu <sub>50</sub> Zr <sub>50</sub>	E,AES	590-658	U	0.82	$1.18 \times 10^{-14}$	C	Stelster et al.(1987)
Au	1.44	Cu <sub>50</sub> Zr <sub>50</sub>	E,RBS	590-658	U	1.55	$1.70 \times 10^{-7}$	C	Stelster et al.(1987)
B	0.97	Fe <sub>1-x</sub> B <sub>x</sub>	S,AES	523-623	U	2.00	$3.00 \times 10^{-3}$	N	Reill et al.(1985)
Fe	1.28	Fe <sub>24</sub> Zr <sub>76</sub>	T,AES	493-613	R	2.30	$6.00 \times 10^{-1}$	D	Horvath et al.(1988)
Zr	1.60	Fe <sub>24</sub> Zr <sub>76</sub>	T,AES	533-613	R	3.20	$7.00 \times 10^6$	D	Horvath et al.(1988)
Fe	1.28	Fe <sub>28</sub> Zr <sub>72</sub>	T,AES	533-593	R	2.60	$2.60 \times 10^1$	D	Horvath et al.(1988)
Si	1.17	Fe <sub>75</sub> B <sub>25</sub>	E,AES	573-633	U	0.29	$2.50 \times 10^{-17}$	N	Misse et al.(1985)
B	0.97	Fe <sub>75</sub> B <sub>25</sub>	E,AES	573-633	U	non-Arrhenius		N	Misse et al.(1985)
Fe	1.28	Fe <sub>80</sub> B <sub>20</sub>	T,AES	543-655	R	2.40	$7.90 \times 10^{-2}$	D,I	Horvath et al.(1988)
Au	1.44	Fe <sub>80</sub> B <sub>20</sub>	E,RBS	643-546	U	1.55	$1.28 \times 10^{-7}$	C	Sharma et al.(1987a)
Au	1.44	Fe <sub>80</sub> B <sub>20</sub>	E,RBS	643-546	R	1.58	$2.20 \times 10^{-7}$	C	Sharma et al.(1987a)

A,B,C: The symbols are defined below:

R=relaxed; U=unrelaxed; X=crystallized; I=interstitial; V=vacancy; C=cooperative motion;  
D=direct diffusion; F=indirect diffusion; T=tracer element; E=vacuum evaporation; XRD=X-ray  
diffraction; AES=auger electron spectroscopy; RBS=backscattering spectrometry; SIMS=secondary  
ion mass spectroscopy; NR=nuclear reaction; N=not known; GZ=Gruzin method; IP=ion-implantation;  
S=segregation; P= Sputter deposition; IBS=ion beam sputtering; ABS=absorption method.

## LITERATURE SURVEY OF DIFFUSION IN METALLIC GLASSES (continued)

ELE RADII (Å)	METALLIC GLASS	METHOD USED	TEMP. RANGE(K)	CONDITION B	Q (ev)	D <sub>0</sub> (m <sup>2</sup> /s)	MECHANISM PROPOSED	REFERENCE
Au 1.44	Fe <sub>80</sub> B <sub>20</sub>	E, AES	546-645	U	1.56	10 <sup>-7</sup>	N	Sharma et al. (1987b)
Pb 1.75	Fe <sub>80</sub> B <sub>20</sub>	E, RBS	546-643	U	2.34	4.30	C	Sharma et al. (1987a)
Au 1.44	Fe <sub>82</sub> B <sub>18</sub>	E, RBS	575-645	U	1.20	10 <sup>-9</sup>	C	Sharma et al. (1988a)
Au 1.44	Fe <sub>82</sub> B <sub>18</sub>	E, AES	546-645	U	1.34	10 <sup>-9</sup>	N	Sharma et al. (1987b)
Pb 1.75	Fe <sub>82</sub> B <sub>18</sub>	E, RBS	601-636	R	0.77	10 <sup>-13</sup>	C	Sharma et al. (1988a)
Sb 1.61	Fe <sub>82</sub> B <sub>18</sub>	E, RBS	575-640	R	1.65	2.50×10 <sup>-6</sup>	C	Sharma et al. (1988b)
Cu 1.28	Fe <sub>82</sub> B <sub>18</sub>	E, AES	546-645	U	1.51	2.03×10 <sup>-7</sup>	C	Sharma et al. (1988c)
Al 1.43	Fe <sub>82</sub> B <sub>18</sub>	E, RBS	575-640	U	1.71	6.94×10 <sup>-6</sup>	C	Sharma (1986)
Si 1.17	Fe <sub>82</sub> B <sub>18</sub>	P, AES	571-646	U, R	2.00	5.70×10 <sup>-4</sup>	I	Luborsky (1983)
P 1.28	Fe <sub>85</sub> B <sub>15</sub>	T, SIMS	488-543	U	1.85	4.50×10 <sup>-5</sup>	N	Edelin et al. (1981)
Fe 1.28	Fe <sub>91</sub> Zr <sub>9</sub>	T, IBS	473-773	R	1.50	3.10×10 <sup>-7</sup>	D	Horvath et al. (1988)
Zr 1.60	Fe <sub>91</sub> Zr <sub>9</sub>	T, IBS	633-773	R	2.50	2.10×10 <sup>-3</sup>	D	Horvath et al. (1988)
Au 1.44	Ni <sub>33.3</sub> Zr <sub>66.7</sub>	P, RBS	550-610	U	1.87	3.30×10 <sup>-5</sup>	C	Akthar et al. (1982)
Au 1.44	Ni <sub>33.3</sub> Zr <sub>66.7</sub>	P, RBS	550-610	R	2.38	4.40×10 <sup>-1</sup>	C	Akthar et al. (1982)
Pt 1.38	Ni <sub>33.3</sub> Zr <sub>66.7</sub>	P, RBS	550-610	U	2.48	3.40×10 <sup>1</sup>	N	Akthar et al. (1982)

A, B, C: see footnote at beginning of the table

## LITERATURE SURVEY OF DIFFUSION IN METALLIC GLASSES (continued)

ELE RADII (Å)	METALLIC GLASS	METHOD USED	TEMP. RANGE(K)	CONDITION B	Q (ev)	D <sub>0</sub> (m <sup>2</sup> /s)	MECHANISM PROPOSED	REFERENCE
Pt 1.38	Ni <sub>33.3</sub> Zr <sub>66.7</sub>	P,RBS	550-610	R	2.38	2.20×10 <sup>0</sup>	N	Akthar et al.(1982)
Pb 1.75	Ni <sub>33.3</sub> Zr <sub>66.7</sub>	P,RBS	550-610	U	2.80	5.80×10 <sup>5</sup>	N	Akthar et al.(1982)
Pb 1.75	Ni <sub>33.3</sub> Zr <sub>66.7</sub>	P,RBS	550-610	R	2.64	1.20×10 <sup>4</sup>	N	Akthar et al.(1982)
Au 1.44	Ni <sub>39</sub> Zr <sub>61</sub>	E,AES	546-645	U	1.60	10 <sup>-6</sup>	N	Sharma et al.(1987b)
Al 1.43	Ni <sub>39</sub> Zr <sub>61</sub>	E,AES	100-100	R	1.68		C	Sharma et al.(1990)
Cu 1.28	Ni <sub>39</sub> Zr <sub>61</sub>	E,AES	100-100	R	1.33		C	Sharma et al.(1990)
Si 1.17	Ni <sub>40</sub> Ti <sub>60</sub>	E,AES	100-100	R	2.35	5.82×10 <sup>-14</sup>	C	Sharma et al.(1991)
Co 1.25	Ni <sub>50</sub> Zr <sub>50</sub>	T,IBS	486-641	U	1.40	3.60×10 <sup>-7</sup>	I	Hahn et al.(1988)
Ni 1.25	Ni <sub>50</sub> Zr <sub>50</sub>	T,IBS	527-638	U	1.45	1.70×10 <sup>-7</sup>	I	Hahn et al.(1988)
Cu 1.28	Ni <sub>50</sub> Zr <sub>50</sub>	T,SIMS	527-638	U	1.57	1.80×10 <sup>-7</sup>	I	Hahn et al.(1988)
Fe 1.28	Ni <sub>50</sub> Zr <sub>50</sub>	T,SIMS	527-638	U	1.64	7.50×10 <sup>-7</sup>	I	Hahn et al.(1988)
Au 1.44	Ni <sub>50</sub> Zr <sub>50</sub>	T,RBS	527-638	U	1.77	0.15×10 <sup>-7</sup>	C	Hahn et al.(1988)
Au 1.44	Ni <sub>50</sub> Nb <sub>50</sub>	T,NR	100-100	U	1.60	2.00×10 <sup>-10</sup>	N	Kijek et al.(1984)
B 0.97	Ni <sub>59.5</sub> Nb <sub>40.5</sub>	T,NR	573-873	U	non-Arrhenius		N	Kijek et al.(1986)
B 0.97	Ni <sub>59.5</sub> Nb <sub>40.5</sub>	T,NR	573-873	R	2.50	3.90×10 <sup>-3</sup>	N	Kijek et al.(1986)

A,B,C: see footnote at beginning of the table

## LITERATURE SURVEY OF DIFFUSION IN METALLIC GLASSES (continued)

ELE RADI (Å)	METALLIC GLASS	METHOD USED	TEMP. RANGE (K)	CONDITION B	Q (eV)	D <sub>0</sub> (m <sup>2</sup> /s)	MECHANISM PROPOSED	REFERENCE
Au 1.44	Ni <sub>64</sub> Zr <sub>36</sub>	P, RBS	610-770	U	1.98	4.20×10 <sup>-6</sup>	C	Akthar et al. (1982)
Au 1.44	Ni <sub>64</sub> Zr <sub>36</sub>	P, RBS	610-770	R	1.84	4.90×10 <sup>-7</sup>	C	Akthar et al. (1982)
Au 1.44	Ni <sub>65</sub> Zr <sub>35</sub>	T, RBS	630-770	U	1.69		N	Bottiger et al. (1986)
Pb 1.75	Ni <sub>65</sub> Zr <sub>35</sub>	T, RBS	630-770	U	1.55		N	Bottiger et al. (1986)
Bi 1.82	Ni <sub>65</sub> Zr <sub>35</sub>	T, RBS	630-770	U	1.49		N	Bottiger et al. (1986)
Hg 1.55	Ni <sub>65</sub> Zr <sub>35</sub>	T, RBS	630-770	U	2.30		N	Bottiger et al. (1986)
B 0.97	Ni <sub>80</sub> P <sub>20</sub>	E, SIMS	500-530	R	non-Arrhenius		N	Doi et al. (1984)
Au 1.44	Pd <sub>80</sub> Si <sub>20</sub>	T, XRD	498-543	R	1.90	2.44×10 <sup>-22</sup>	N	Gupta et al. (1982)
Li 1.57	Pd <sub>80</sub> Si <sub>20</sub>	IP, NR	513-563	U	non-Arrhenius		I	Birac et al. (1976)
Ag 1.44	Pd <sub>81</sub> Si <sub>19</sub>	T, XRD	459-552	U	1.30	2.00×10 <sup>-10</sup>	C	Gupta et al. (1975)
Au 1.44	Fe-Co-B	A, BCD	100-100	N	1.6	1.41×10 <sup>-8</sup>	N	Bohac (1990)
B 0.97	Fe <sub>40</sub> Ni <sub>40</sub> B <sub>20</sub>	T, SIMS	613-643	U	3.40	1.80×10 <sup>-11</sup>	M	Cahn et al. (1980)
Au 1.44	Fe <sub>40</sub> Ni <sub>40</sub> B <sub>20</sub>	P, RBS	575-650	U	2.04	9.40×10 <sup>-5</sup>	C	Akthar et al. (1982)
Au 1.44	Fe <sub>40</sub> Ni <sub>40</sub> B <sub>20</sub>	P, RBS	575-650	R	2.09	1.90×10 <sup>-4</sup>	C	Akthar et al. (1982)
Fe 1.28	Fe <sub>40</sub> Ni <sub>40</sub> B <sub>20</sub>	T, IBS	533-643	R	2.40	2.70×10 <sup>-2</sup>	C	Horvath et al. (1986a)

A, B, C: see footnote at beginning of the table

LITERATURE SURVEY OF DIFFUSION IN METALLIC GLASSES (continued)

ELE RADII (Å)	METALLIC GLASS	METHOD USED	TEMP. RANGE(K)	CONDITION B	Q (ev)	D <sub>0</sub> (m <sup>2</sup> /s)	MECHANISM PROPOSED	REFERENCE
P 1.28	Fe <sub>40</sub> Ni <sub>40</sub> B <sub>20</sub>	T, IBS	573-744	R	3.10	1.00×10 <sup>-4</sup>	C	Horvath et al. (1986b)
Fe 1.28	Fe <sub>40</sub> Ni <sub>40</sub> B <sub>20</sub>	T, IBS	533-643	R	2.30	1.10×10 <sup>-2</sup>	C	Ulfert (1985)
Fe 1.28	Fe <sub>41</sub> Ni <sub>41</sub> B <sub>18</sub>	T, IBS	512-643	R	2.29	1.05×10 <sup>-2</sup>	C	Pfahler et al. (1985)
Fe 1.28	Fe <sub>78</sub> B <sub>13</sub> Si <sub>9</sub>	T, IBS	551-783	R	2.09	4.60×10 <sup>-5</sup>	C	Horvath et al. (1988)
B 0.97	Fe <sub>78</sub> P <sub>15</sub> C <sub>7</sub>	E, SIMS	575-640	U	1.13	10 <sup>-8</sup>	N	Doi et al. (1984)
B 0.97	Fe <sub>78</sub> P <sub>15</sub> C <sub>7</sub>	E, SIMS	575-640	R	2.68	10 <sup>-4</sup>	N	Doi et al. (1984)
Ni 1.25	Fe <sub>79</sub> B <sub>11</sub> Si <sub>10</sub>	T, ABS	523-683	U	0.83	2.50×10 <sup>-14</sup>	C	Bokshtyn et al. (1981)
Si 1.17	Fe <sub>82</sub> B <sub>12</sub> Si <sub>6</sub>	A, BCD	573-693	U	2.20	2.90×10 <sup>-2</sup>	I	Luborsky et al. (1982)
Au 1.44	Ni <sub>77</sub> B <sub>20</sub> Si <sub>3</sub>	E, RBS+ AES	442-506	R	1.37	1.50×10 <sup>-8</sup>	V	Bohac et al. (1989b)
Ti 1.47	Ni <sub>77</sub> B <sub>20</sub> Si <sub>3</sub>	E, RBS	473-527	R	1.70	8.60×10 <sup>-3</sup>	V	Bohac et al. (1989a)
B 0.97	Ni <sub>78</sub> P <sub>15</sub> C <sub>7</sub>	E, SIMS	415-475	R	0.64	2.00×10 <sup>-12</sup>	N	Doi et al. (1984)
B 0.97	Ni <sub>80</sub> P <sub>15</sub> C <sub>5</sub>	E, SIMS	500-550	R	1.13	10 <sup>-9</sup>	N	Doi et al. (1984)
Au 1.44	Pd <sub>77.5</sub> Si <sub>16.5</sub> Cu <sub>6</sub>	IP, RBS	533-653	U	0.75	3.30×10 <sup>-10</sup>	C	Chen et al. (1978)
Au 1.44	Pd <sub>77.5</sub> Si <sub>16.5</sub> Cu <sub>6</sub>	IP, RBS	533-653	R	1.67	1.50×10 <sup>-4</sup>	C	Chen et al. (1978)
Au 1.44	Pd <sub>77.5</sub> Si <sub>16.5</sub> Cu <sub>6</sub>	P, RBS	530-650	U	1.82	3.00×10 <sup>-5</sup>	C	Akthar et al. (1982)

A, B, C: see footnote at beginning of the table

## LITERATURE SURVEY OF DIFFUSION IN METALLIC GLASSES (continued)

ELE RADII (Å)	METALLIC GLASS	METHOD USED	TEMP. RANGE(K)	CONDITION B	Q (ev)	D <sub>0</sub> (m <sup>2</sup> /s)	MECHANISM PROPOSED	REFERENCE
Ar 1.44	Pd <sub>77.5</sub> Si <sub>16.5</sub> Cu <sub>6</sub>	P, RBS	530-650	R	1.78	1.20×10 <sup>-5</sup>	C	Akthar et al. (1982)
B 0.97	Co <sub>70</sub> Fe <sub>5</sub> Si <sub>5</sub> B <sub>10</sub>	A, BCD	100-100	N	1.32	4.40×10 <sup>-11</sup>	N	Bokstein et al. (1990)
Fe 1.28	Fe <sub>40</sub> Ni <sub>40</sub> P <sub>14</sub> B <sub>6</sub>	IP, IBS	541-617	U	2.00	1.00×10 <sup>-3</sup>	C	Valenta et al. (1981a)
P 1.28	Fe <sub>40</sub> Ni <sub>40</sub> P <sub>14</sub> B <sub>6</sub>	IP, IBS	553-573	U	3.10	10 <sup>6</sup>	C	Valenta et al. (1981b)
Fe 1.28	Fe <sub>40</sub> Ni <sub>40</sub> P <sub>14</sub> B <sub>6</sub>	T, GZ	423-573	U	0.59	2.60×10 <sup>-16</sup>	V	Schuehmacher et al.
P 1.28	Fe <sub>40</sub> Ni <sub>40</sub> P <sub>14</sub> B <sub>6</sub>	T, GZ	423-573	U	1.03	2.40×10 <sup>-13</sup>	V	Schuehmacher et al.
P 1.28	Fe <sub>40</sub> Ni <sub>40</sub> P <sub>14</sub> B <sub>6</sub>	S, AES	350-800	R	1.95	7.00×10 <sup>-6</sup>	N	Baer et al. (1981)
Si 1.17	Fe <sub>81</sub> B <sub>13.5</sub> Si <sub>3.5</sub> C <sub>2</sub>	A, BCD	100-100	U	0.75	1.70×10 <sup>-15</sup>	N	Van (1986)
Si 1.17	Fe <sub>81</sub> B <sub>13.5</sub> Si <sub>3.5</sub> C <sub>2</sub>	A, BCD	100-100	X	1.59	3.60×10 <sup>-10</sup>	N	Van (1986)
P 1.28	Fe <sub>32</sub> Ni <sub>36</sub> Cr <sub>14</sub> P <sub>12</sub> B <sub>6</sub>	S, AES	350-800	R	1.75	2.90×10 <sup>-7</sup>	N	Baer et al. (1981)

A, B, C: see footnote at beginning of the table

metalloid metallic glasses on a  $D$ -vs- $1/T$  plot, showing higher diffusing rates for B and Si as compared to others. Though on a normalized arrhenius plot, this difference was not observed [Cantor and Cahn 1983], and a progressive change in diffusion mechanism from large atoms such as Au to lighter atoms such as Li has been suggested. A general trend of increase in diffusion coefficient with decreasing atomic size of the diffusing species has been suggested too.

In almost all investigations, the diffusion coefficients of metallic glasses have been found to decrease with decreasing temperature as is observed in crystalline counterparts. Recent observations [Horvath and Mehrer 1986, Horvath et al. 1988, Mehrer and Dorner 1989] have shown the time dependence of the diffusion rate. The diffusion coefficients decrease in the course of isothermal annealing to a constant value as a result of structural relaxation in the alloy. They have also observed that in the as-quenched samples,  $D$ -values are higher and activation enthalphy  $Q$  is smaller than that of the relaxed samples. Since relaxation increases the volume density in melt-spun metallic glasses [Gerling 1985], the elimination of excess free volume, must be involved in this process.

Bokstein et al. [1989], have suggested that the typical value of diffusion path is less than 10-20 nm. irrespective of annealing time. Hahn et al. [1988] and Hoshino et al. [1988] have observed a trend of decrease in diffusion coefficients with increasing atomic radii of diffusing species to some extent. In some cases, (i.e., for larger diffusing atoms) the reverse has been observed. The diffusion of atoms with smaller radii, has been suggested to take place by an interstitial-like process and that of the larger atoms like Au, Ti, Zr, etc. via a vacancy-like mechanism.

Diffusion of hydrogen in metallic glasses has a special interest and characteristics of its own. Technological importance like hydrogen storage and hydrogen embrittlement being a few of the possible reasons. There has been a

large number of measurements and publications of diffusivity of hydrogen in metallic glasses in recent years [Berrv et al. 1981, Takagi et al. 1981, Kircheim et al. 1982, Sakamoto et al. 1984, Yamakawa et al. 1989].

## 1.7 BRIEF REVIEW OF PHASE PRECIPITATION STUDIES IN METALLIC GLASSES BY MOSSBAUER SPECTROSCOPY

Phase precipitation and amorphous to crystalline transformation in metallic glasses has drawn considerable attention in recent years. Mössbauer spectroscopic technique which has become an important tool for the study of phase identification in several metallurgical systems, has shown interesting results in the case of metallic glasses too. A brief compilation of phase formation studies in metallic glasses by Mössbauer spectroscopy is given in Table 1.3. It should be pointed out that the Table may not be complete and some published work may not be listed.

The most intensively studied glasses are the binary ones,  $\text{Fe}_{1-x}\text{B}_x$ , [Sanchez et al. 1989, Kemeny et al. 1979, Chien 1978, Takacs et al. 1985] because they have the simplest possible forms. Two types of crystallization process have been observed in these alloys. Fe-B alloys having boron concentration less than 16at.%B, precipitate  $\alpha$ -Fe and metastable  $\text{Fe}_3\text{B}$ , which decomposes at still higher temperatures into  $\alpha$ -Fe and  $\text{Fe}_2\text{B}$  [Kemeny et al. 1979, Schaafsma 1981, Singru et al. 1985, Sanchez et al. 1989]. Alloys with more than 16at.%B concentration, crystallizes into  $\alpha$ -Fe and  $\text{Fe}_3\text{B}$  only [Kemeny et al. 1979, Sanchez et al. 1989]. Bauer-Grosse et al. [1985], have obtained several Fe-C phases in their studies on Fe-C metallic glasses.

Ternary metallic glasses have been studied too, with extensive work being done in the alloys having the composition Fe-Si-B. Masumoto et al. [1976], had reported that  $\alpha$ -Fe precipitated during the crystallization process of the alloy  $\text{Fe}_{78}\text{B}_{12}\text{Si}_{10}$ , whereas Ok and Morrish [1980] found Fe-Si phase instead of  $\alpha$ -Fe in



TABLE 1.4

BRIEF REVIEW OF PHASE FORMATION STUDIES IN METALLIC GLASSES  
BY MÖSSBAUER SPECTROSCOPY

Metallic glass	Final Phases Obtained at $T > T_x$	Reference
$\text{Fe}_{1-x}\text{B}_x$ ( $25 \leq x \leq 12$ )	$\alpha\text{-Fe, Fe}_3\text{B} \rightarrow$ $2\alpha\text{-Fe, Fe}_2\text{B}$	Kemeny et al. 1979
$\text{Fe}_{1-x}\text{B}_x$ ( $26 \leq x \leq 13$ )	$\alpha\text{-Fe, Fe}_3\text{B} \rightarrow$ $2\alpha\text{-Fe, Fe}_2\text{B}$	Singru et al. 1985
$\text{Fe}_{86}\text{B}_{14}$	$\alpha\text{-Fe, o-Fe}_3\text{B, t-Fe}_3\text{B}$	Sanchez et al. 1989
$\text{Fe-17at.\%B}$	$\alpha\text{-Fe, Fe}_3\text{B} \rightarrow$ $2\alpha\text{-Fe, Fe}_2\text{B}$	Oshima et al. 1981
$\text{Fe}_{1-x}\text{B}_x$ ( $22.3 \leq x \leq 15$ )	$\alpha\text{-Fe, Fe}_3\text{B} \rightarrow$ $2\alpha\text{-Fe, Fe}_2\text{B}$	Schaafsma 1981
$\text{Fe}_{80}\text{B}_{20}$	$\alpha\text{-Fe, Fe}_3\text{B} \rightarrow$ $2\alpha\text{-Fe, Fe}_2\text{B}$	Chien and Hasegawa 1977
$\text{Fe}_{80}\text{B}_{20}$	$\text{o-Fe}_3\text{B, t-Fe}_3\text{B, } \alpha\text{-Fe}$	Sanchez et al. 1989
$\text{Fe}_{80}\text{B}_{20}$	$\alpha\text{-Fe, t-Fe}_3\text{B}$	Singhal et al. 1992
$\text{Fe}_{75}\text{B}_{25}$	$\alpha\text{-Fe, o-Fe}_3\text{B, Fe}_2\text{B}$	Sanchez et al. 1989
$\text{Fe}_{1-x}\text{C}_x$ ( $19 \leq x \leq 50$ )	$\text{Fe}_3\text{C, Fe}_5\text{C}_2, \text{Fe}_7\text{C}_3$	Bauer-Grosse et al. 1985
$\text{Fe}_{50}\text{Si}_{50}$	$\alpha\text{-Fe, Fe}_3\text{Si}$	Yamakawa et al. 1979
$\text{Fe}_{30}\text{Si}_{70}$	$\beta\text{-FeSi}_2$	Yamakawa et al. 1979
$\text{Fe}_{91}\text{Zr}_9$	$\alpha\text{-Fe, Fe}_3\text{Zr}$	Ghafari et al. 1982
$\text{Fe}_{90}\text{Zr}_{10}$	$\alpha\text{-Fe, Fe}_3\text{Zr, Fe}_2\text{Zr}$	Fujinama & Ujihara 1985
$\text{Zr}_{1-x}\text{Fe}_x$ ( $25 < x < 29$ )	$\text{Zr}_3\text{Fe, Zr}_2\text{Fe}$	Ghafari et al. 1982
$\text{Fe}_{60}\text{B}_{20}\text{Co}_{20}$	$\text{Fe-Co, (Fe, Co)}_2\text{B}$	Klein et al. 1982

Fe-Co : b.c.c. solid solution.

$\text{Fe}_2\text{B, Fe}_3\text{B, Fe}_3\text{Si, Fe}_3\text{Zr, (Fe-Co)}_2\text{B, etc.,}$  : tetragonal phases

BRIEF REVIEW OF PHASE FORMATION STUDIES IN METALLIC GLASSES  
BY MÖSSBAUER SPECTROSCOPY (continued)

Metallic glass	Final Phases Obtained at $T > T_x$	References
$\text{Fe}_{74}\text{B}_{16}\text{Co}_{10}$	$\alpha\text{-(Fe-Co)}, \text{Fe}_2\text{B}, (\text{Fe-Co})_2\text{B}, \text{Fe}_3\text{B}$	Bhatnagar et al. 1985
$(\text{Fe}_x\text{Ni}_{1-x})_{80}\text{B}_{20}$ ( $0.875 \leq x \leq 0.5$ )	$\alpha\text{-(Fe-Ni)}, (\text{Fe-Ni})_2\text{B}$	Sitek & Gabris 1982
$(\text{Fe}_{1-x}\text{Ni}_x)_3\text{B}$	$\text{Fe}_3\text{B}, \text{Ni}_3\text{B}$	Schaafsma 1981
$\text{Fe}_{40}\text{Ni}_{40}\text{B}_{20}$	$\alpha\text{-(Fe-Ni-B)}, o\text{-(Fe-Ni)}_3\text{B}$	Bauer et al. 1985
$\text{Fe}_{80}\text{B}_{12}\text{Sb}_8$	$\alpha\text{-Fe}, \text{Fe}_3\text{B}, \text{Fe}_{1+x}\text{Sb}$	Verma & Wappling 1985
$\text{Fe}_{84}\text{B}_{10}\text{Si}_6$	$\text{Fe}_2\text{B}, \text{Fe-Si}$	Zaluska et al. 1982
$\text{Fe}_{83}\text{B}_{12}\text{Si}_5$	$\alpha\text{-Fe}, \text{Fe}_2\text{B}, \text{Fe-Si}$	Nowik et al. 1988
$\text{Fe}_{82}\text{B}_{12}\text{Si}_6$	$\text{Fe-Si(8nn)}, \text{Fe-Si(7nn)}, \text{Fe-Si(6nn)}, \text{Fe}_2\text{B}$	Ok & Morrish 1980
$\text{Fe}_{80}\text{B}_{18}\text{Si}_2$	$\alpha\text{-Fe}, \text{Fe}_3\text{B}$	Singhal et al. 1992
$\text{Fe}_{80}\text{B}_{12}\text{Si}_8$	$\alpha\text{-Fe}, \text{Fe}_2\text{B}, \text{Fe-Si}$	Singhal et al. 1992
$\text{Fe}_{79}\text{B}_{16}\text{Si}_5$	$\alpha\text{-Fe}, \text{Fe}_2\text{B}, \text{Fe-10at.\%Si}$	Bahgat et al. 1983
$\text{Fe}_{78}\text{B}_{12}\text{Si}_{10}$	$\alpha\text{-Fe}, \text{Fe}_2\text{B}$	Masumoto et al. 1976
$\text{Fe}_{78}\text{B}_{13}\text{Si}_9$	$\text{Fe-Si(8nn)}, \text{Fe-Si(7nn)}, \text{Fe-Si(6nn)}, \text{Fe-Si(5nn)}, \text{Fe-Si(4nn)}, \text{Fe}_2\text{B}$	Nagarajan et al. 1988
$\text{Fe}_{75.4}\text{B}_{14.2}\text{Si}_{10.4}$	$\text{Fe}_2\text{B}, \text{Fe-Si(5 sextets)}$	Ok et al. 1981
$\text{Fe}_{75}\text{B}_{25-x}\text{Si}_x$ ( $18 \leq x \leq 6$ )	$\text{Fe}_2\text{B}, \text{Fe-Si(3 sextets)}$	Zaluska et al. 1982
<hr/>		
$\text{Fe-Si}, \text{Fe-Ni}, \text{Fe-Co}$ , etc. : b.c.c. solid solution.		
$\text{Fe}_2\text{B}, \text{Fe}_3\text{B}, \text{Ni}_3\text{B}$ , etc. : tetragonal phases.		

BRIEF REVIEW OF PHASE FORMATION STUDIES IN METALLIC GLASSES  
BY MÖSSBAUER SPECTROSCOPY (continued)

Metallic glass	Final Phases Obtained at $T > T_x$	References
$\text{Fe}_{75}\text{P}_{18}\text{C}_7$	$\alpha\text{-Fe, Fe}_3\text{P, Fe}_2\text{P} \rightarrow$ $\alpha\text{-Fe, Fe}_2\text{P}$	Shaafsma et al. 1977
$\text{Fe}_{80}\text{P}_{13}\text{C}_7$	$\alpha\text{-Fe, Fe}_3\text{P, Fe}_3\text{C}$	Shaafsma et al. 1977
$\text{Fe}_{83}\text{P}_{11}\text{C}_6$	$\alpha\text{-Fe, Fe}_3\text{P, Fe}_3\text{C}$	Shaafsma et al. 1977
$\text{Fe}_{81}\text{B}_{13.5}\text{Si}_{3.5}\text{C}_2$	$\text{Fe-Si, Fe}_2\text{B, Fe}_3\text{C}$	Saegusa & Morrish 1982
$\text{Fe}_{81}\text{B}_{13.5}\text{Si}_{3.5}\text{C}_2$	$\alpha\text{-Fe, Fe}_2\text{B, Fe}_3\text{C}$	Bhanu Prasad et al. 1983
$\text{Fe}_{81}\text{B}_{13.5}\text{Si}_{3.5}\text{C}_2$	$\text{Fe-Si(8nn), Fe-Si(8nn), Fe-Si(7nn), Fe-Si(7nn),}$ $\text{Fe}_2(\text{BC})_{0.91}$	Nagarajan et al. 1988
$\text{Fe}_{78}\text{B}_{11}\text{Si}_9\text{C}_2$	2-step crystallization	Gupta et al. 1985
$\text{Fe}_{67}\text{B}_{14}\text{Si}_1\text{Co}_{18}$	$\text{Fe-Co(5nn), Fe-Co(6nn), Fe-Co(7nn), (Fe-Co)}_2\text{B}$	Nagarajan et al. 1988
$\text{Fe}_{67}\text{B}_{14}\text{Si}_1\text{Co}_{18}$	$\alpha\text{-(Fe-Co), (Fe-Co)}_2\text{B, (Fe-Co)}_3\text{B}$	Bhatnagar et al. 1985
$\text{Co}_{70.3}\text{Fe}_{4.7}\text{Si}_{15}\text{B}_{10}$	$\alpha\text{-Co, } \beta\text{-Co, Co}_2\text{Si, Co}_2\text{B}$	Wolny et al. 1982
$\text{Fe}_{40}\text{Ni}_{38}\text{B}_{18}\text{Mo}_4$	$\text{Fe-Ni, (Fe-Ni)}_3\text{B}$	Mizgalski et al. 1981
$\text{Fe}_{40}\text{Ni}_{38}\text{B}_{18}\text{Mo}_4$	$(\text{fcc})\text{Fe-Ni, o-(Fe-Ni)}_3\text{B, Fe}_{23}\text{B}_6(\text{c})$	Battezzatti et al. 1982
$\text{Fe}_{40}\text{Ni}_{38}\text{B}_{18}\text{Mo}_4$	$\alpha\text{-(Fe-Ni), o-(Fe-Ni)}_3\text{B, Fe}_2\text{B, MoFeB}_2$	Battezzatti et al. 1982
$\text{Fe}_{40}\text{Ni}_{38}\text{B}_{18}\text{Mo}_4$	$\text{Fe-Ni(5nn), Fe-Ni(6nn), Fe-Ni(7+8nn), (Fe, Ni)}_3\text{B, (Fe-25at.\%Ni-16at.\%Mo)}_2\text{B}$	Nagarajan et al. 1988
<hr/> Fe-Si, Fe-Ni, Fe-Co : b.c.c. solid solution.		
<hr/> Fe <sub>2</sub> B, Fe <sub>3</sub> B, Fe <sub>3</sub> B, (Fe-Co) <sub>3</sub> B, Co <sub>2</sub> B, (Fe <sub>3</sub> Ni) B : tetragonal phases.		

the system  $\text{Fe}_{82}\text{B}_{12}\text{Si}_6$ . *Ok et al.* [1981] obtained as final products  $\text{Fe}_2\text{B}$  and Fe-18.1at.%Si phase in the alloy  $\text{Fe}_{75.4}\text{B}_{14.2}\text{Si}_{10.4}$ . In the crystallization study of the series  $\text{Fe}_{75}\text{B}_{25-x}\text{Si}_x$  alloys, *Zaluska et al.* [1982] observed  $\text{Fe}_2\text{B}$  and Fe-Si phases, besides observing an ordered  $\text{Fe}_3\text{Si}$  phase for higher Si concentration alloys. *Bahgat and Shaisha* [1983] reported a fully crystallized material of metallic glass  $\text{Fe}_{79}\text{B}_{16}\text{Si}_5$  at 708 K which contained three phases,  $\alpha\text{-Fe}$ ,  $\text{Fe}_2\text{B}$  and Fe-10at.%Si. The crystallized products of  $\text{Fe}_{78}\text{B}_{13}\text{Si}_9$ , after annealing the sample at 800 K (5h), as reported by *Nagarajan et al.* [1988] were  $\text{Fe}_2\text{B}$  and Fe-14.8at.%Si. *Klein et al.* [1982] showed the final crystalline products of  $\text{Fe}_{60}\text{Co}_{20}\text{B}_{20}$  after annealing at 1000 K to be Fe-Co and  $(\text{Fe-Co})_2\text{B}$ . *Nowik et al.* [1988] reported that the final products of metallic glass  $\text{Fe}_{83}\text{B}_{12}\text{Si}_5$  after annealing at 700 K are  $\alpha\text{-Fe}$ ,  $\text{Fe}_2\text{B}$  and Fe-Si.

*Nagarajan et al.* [1988] studied the crystallization mechanism of quaternary iron based metallic glasses  $\text{Fe}_{81}\text{B}_{13.5}\text{Si}_{3.5}\text{C}_2$ ,  $\text{Fe}_{40}\text{Ni}_{38}\text{B}_{18}\text{Mo}_4$  and  $\text{Fe}_{67}\text{Co}_{18}\text{B}_{14}\text{Si}_1$  too. The final phases of  $\text{Fe}_{81}\text{B}_{13.5}\text{Si}_{3.5}\text{C}_2$  after annealing at 1000 K (5h) were  $\text{Fe}_2(\text{BC})_{0.91}$  and Fe-6.9at.%Si. Crystallized  $\text{Fe}_{40}\text{Ni}_{38}\text{B}_{18}\text{Mo}_4$  precipitated Fe-Ni,  $(\text{Fe-Ni})_3\text{B}$  and  $\text{Fe}_{15}\text{Ni}_6\text{Mo}_4\text{B}_{12}$  phases. The final crystalline products of the alloy  $\text{Fe}_{67}\text{Co}_{18}\text{B}_{14}\text{Si}_1$  on annealing at 1000 K were  $\text{Fe}_{42}\text{Co}_{15}\text{Si}_1$  and  $\text{Fe}_{25}\text{Co}_3\text{B}_{14}$ . For  $\text{Fe}_{81}\text{B}_{13.5}\text{Si}_{3.5}\text{C}_2$ , *Saegusa and Morrish* [1982] reported the crystalline products to be Fe-7at.%Si,  $\text{Fe}_2\text{B}$  and  $\text{Fe}_3\text{C}$ . *Bhanu Prasad et al.* [1983], obtained  $\alpha\text{-Fe}$  instead of Fe-Si for the same alloy. *Mizgalski et al.* [1981], concluded that the final products in  $\text{Fe}_{40}\text{Ni}_{38}\text{B}_{18}\text{Mo}_4$  are Fe-Ni and  $(\text{Fe-Ni})_3\text{B}$ . According to *Battezzatti et al.* [1982], this metallic glass after annealing at 1000 K yields Fe-Ni,  $(\text{Fe-Ni})_3\text{B}$  and  $\text{Fe}_{23}\text{B}_6$  and after annealing at 1200 K yields  $\text{Fe}_2\text{B}$  and  $\text{Mo}_2\text{FeB}_2$  besides Fe-Ni and  $(\text{Fe-Ni})_3\text{B}$ . Both *Omori et al.* [1977] and *Wolny et al.* [1982] observed the final products in  $\text{Co}_{70.3}\text{Fe}_{4.7}\text{Si}_{15}\text{B}_{10}$ , as Co,  $\text{Co}_2\text{Si}$  and  $\text{Co}_2\text{B}$ .

## CHAPTER 2

### THEORETICAL BACKGROUND AND FORMALISM

#### 2.1 RUTHERFORD BACKSCATTERING SPECTROMETRY

Rutherford backscattering spectrometry (RBS) is a well established method for determining the depth versus concentration profile of an impurity in a host material and identifying the mass of the impurity and the host atoms. It is based on the framework of the discoveries of *Rutherford* [1911] and of *Geiger and Marsden* [1913]. The method has been described in detail by *Chu et al.* [1978]. We wish to highlight the basic principles involved in this method for the sake of completeness.

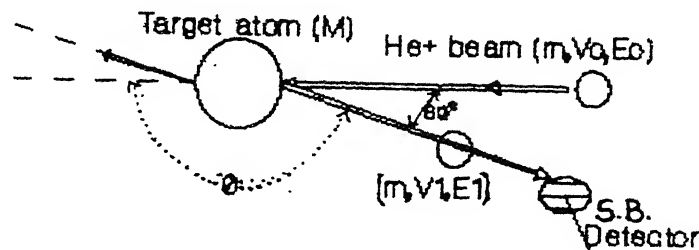


FIGURE 2.1 Schematic diagram of the backscattering process

The technique (as described schematically in Figure 2.1) basically involves the scattering of monoenergetic, collimated beam of particles ( $\text{H}^+$ ,  $\text{He}^+$ , etc.), from a target (sample). The particles scattered backwards by angles of more than  $90^\circ$  from the incident direction are detected and energy analyzed by a detector. The basic physical phenomenon occurring at the target are:

(i) The process of energy transfer from the incident particle to the target nucleus in an elastic two-body collision. This leads to the concept of kinematic

factor (K) and the capability to determine the mass of the target nucleus.

(ii) The process of the probability of occurrence of a two-body collision, which leads to the concept of scattering crosssection ( $\sigma$ ) and the capability to quantitatively analyze the atomic composition of the target.

(iii) The process of average energy loss of the projectile atom through the target. This leads to the concept of stopping cross-section ( $\epsilon$ ) and to the capability of depth perception.

(iv) The process of statistical fluctuations in the energy loss of the projectile in the dense target. This phenomenon leads to the concept of energy straggling ( $\Omega$ ) and to a limitation in the ultimate mass and depth resolution of backscattering spectrometry.

### 2.1.1 Kinematic factor and mass identification

When a particle of mass  $m$  (atm.no.  $z$ ), moving with constant velocity  $v_0$ , collides elastically with a stationary particle of mass  $M$  (atm.no.  $Z$ ), energy will be transferred from the moving particle to the stationary one (Figure 2.1). For the collision between the atoms to be elastic, the following conditions must be satisfied:

(i) the projectile energy of the incident atom (i.e., the incident energy  $E_0$ ) must be larger than the binding energy of the atoms in the target i.e., above 10eV and

(ii) the projectile energy should not be so high so as to cause nuclear reactions and resonances in the target. For a  $\text{He}^+$  projectile beam these start to occur at 2 MeV.

The ratio of the projectile energy after the collision ( $E_1$ ) to that before the collision ( $E_0$ ) is defined as the kinematic factor  $K$  and provides the basis for mass identification in backscattering spectrometry i.e.,

$$K = (E_1)/(E_0) \quad (2.1)$$

and from conservation of energy and momentum one obtains

$$K_M = \frac{\left[ \left( 1 - \left( \frac{m}{M} \right)^2 \sin^2 \theta \right)^{1/2} + \left( \frac{m}{M} \right) \cos \theta \right]^2}{\left[ 1 + \left( \frac{m}{M} \right) \right]^2} \quad (2.2)$$

if  $m/M = X$ , we get

$$K_M = \frac{\left[ \left( 1 - X^2 \sin^2 \theta \right)^{1/2} + X \cos \theta \right]^2}{\left[ 1 + X \right]^2} \quad (2.3)$$

When the projectile and target masses are equal i.e.,  $X=1$ ,  $K_M$  is zero for scattering angle  $\theta$ , larger than  $90^\circ$ , which means the incident atom can only be scattered forward and not backwards; for  $\theta = 180^\circ$

$$K = \left( \frac{1 - X}{1 + X} \right)^2 \quad (2.4)$$

and for  $\theta = 90^\circ$

$$K = \frac{(1 - X)}{(1 + X)} \quad (2.5)$$

i.e., the value of the kinematic factor at  $\theta=180^\circ$  is the square of its value at  $\theta=90^\circ$ . Hence values of  $\theta$  near  $180^\circ$  are of special interest in backscattering spectroscopy. Considering  $\theta=\pi-\delta$  or  $\delta=\pi-\theta$ , where  $\delta$  is the minute deviation of  $\theta$  from  $\pi$  (in units of arc) one gets on expanding the kinematic factor as

$$K = \left( \frac{1 - X}{1 + X} \right)^2 (1 + X \delta^2) \quad (2.6)$$

Equations 2.1 and 2.2 give an idea of how backscattering spectroscopy acquires its ability to determine the mass of the target. If  $E_0$ ,  $m$  and  $\theta$  are known, then on measuring the energy  $E_1$  after collision, the mass  $M$  of the target can be determined, thus providing the mass analysis. Now if the target contains two types of atoms whose masses are close to each other i.e., their mass difference  $\Delta M$  is small, then the variation of energy after collision of the two target masses, i.e.,  $\Delta E_1$  should be quite large so that it can be measured. In quantitative terms,  $\Delta E_1$  and  $\Delta M$  are related as:

$$\Delta E_1 = E_0 \left( \frac{dK}{dM} \right) \Delta M \quad (2.7)$$

Values of  $K$  near  $\theta=180^\circ$  is approximated by Equation 2.6. Inserting the

derivative of  $K$  (with respect to  $m$ ) in Equation 2.7, we get

$$\Delta E_1 = E_0 (4 - \delta^2) (m/M) \Delta M \quad (2.8)$$

Hence to obtain a good mass resolution i.e., to increase  $\Delta E_1$ , the coefficient of  $\Delta M$  should be large i.e., either  $E_0$  should be high, or  $\delta$  should be small i.e.,  $\theta$  should be as near to  $180^\circ$  as possible, or  $m$  should be large. Therefore for good mass resolution, Rutherford backscattering is done for values of  $\theta$  ranging from  $150^\circ$  to  $180^\circ$ .

### 2.1.2 Scattering cross-section

The differential scattering cross-section  $\frac{d\sigma}{d\Omega}$ , (which has dimensions of area), is the concept introduced to determine the occurrence of the two-body collision which ultimately results in a scattering event at a certain angle  $\theta$  and the reception of a signal at the detector.

If  $Q$  is the total number of particles impinging on the target and  $dQ$  the number recorded by the detector, then the differential scattering cross-section is given by:

$$\frac{d\sigma}{d\Omega} = (1/Nt) \left[ (dQ/d\Omega) / Q \right] \quad (2.9)$$

where  $d\Omega$  is the differential solid angle scanned by the detector and it is so small that the scattering angle  $\theta$  is well defined;  $N$  is the volume density of the atoms in the target and  $t$  is the thickness of the target. Therefore  $Nt$  is the area density of the target in atoms per unit area. The thickness  $t$  is such that the energy loss of the incident beam is minimal within the target. Also  $\frac{dQ}{Q}$  has to be a well determined value, hence  $Q \gg dQ$ .

The differential scattering cross-section  $\frac{d\sigma}{d\Omega}$  is imagined to be the area presented by each nucleus of the target atom to the beam of incident particles, such that the areas of the nuclei do not overlap. It is calculated on the basis of conservation of energy and momentum by implementing the force acting during the collision. In most cases it is represented by the coulomb like forces, as



long as the distance of closest approach is large compared to nuclear dimensions and small compared to the Bohr radius  $a$  (equal to  $\frac{\hbar}{m_e} = 0.53 \text{ \AA}$ ). With these assumptions in the laboratory frame of reference, Equation 2.9, turns out to be:

$$\frac{d\sigma}{d\Omega} = \left[ \frac{Z z e^2}{4E} \right]^2 \frac{4}{\sin^4 \theta} \frac{\left[ \left( 1 - \left( \frac{m}{M} \right)^2 \sin^2 \theta \right)^{1/2} + \cos \theta \right]^2}{\left[ \left( 1 - \left( \frac{m}{M} \right)^2 \sin^2 \theta \right)^2 \right]} \quad (2.10)$$

In the vicinity of  $180^\circ$ , the scattering angle  $\theta$  is equal to  $\pi - \delta$ . The scattering cross-section expanded in terms of  $\delta$  is then given as

$$\frac{d\sigma}{d\Omega} = \left[ \frac{Z z e^2}{4E} \right]^2 \left[ 1 - \left( \frac{m}{M} \right)^2 \right]^2 + \frac{1}{2} b \delta^2 \quad (2.11)$$

here  $b = 1 - 3 \left( \frac{m}{M} \right)^4 + 2 \left( \frac{m}{M} \right)^6$ .

This predicts that for values of  $\theta$  near  $180^\circ$ , the scattering cross-section  $\Omega$  does not change much with scattering angle  $\theta$ . For  $m \ll M$ , Equation 2.10 can be expanded in the power series (Marion and Young, 1968)

$$\frac{d\sigma}{d\Omega} = \left[ \frac{Z z e^2}{4E} \right]^2 \left[ \left( \sin \frac{\theta}{2} \right)^{-4} - 2 \left( \frac{m}{M} \right)^2 + \dots \right] \quad (2.12)$$

where the first omitted term is of the order of  $\left( \frac{m}{M} \right)^6$ . This expression reveals the significant functional dependence of the Rutherford differential scattering cross-section, i.e.,

(i)  $\frac{d\sigma}{d\Omega}$  is proportional to  $[Z]^2$ ; hence the backscattering yield obtained from  $\text{He}^+$  beam is four times as large with a proton beam ( $\text{H}^+$ ) but a ninth of that produced by a carbon beam.

(ii)  $\frac{d\sigma}{d\Omega}$  is proportional to  $[z]^2$ ; hence for a given projectile, heavier the target atom, more efficient is the scattering as seen in the case of heavy elements like Au as compared to Al.

(iii)  $\frac{d\sigma}{d\Omega}$  is inversely proportional to the projectile energy, hence scattering yield rises rapidly with decreasing projectile energy.

(iv)  $\frac{d\sigma}{d\Omega}$  is proportional to the scattering angle  $\theta$ .

(v)  $\frac{d\sigma}{d\Omega}$  is inversely proportional to the fourth power of  $\sin \frac{\theta}{2}$  for  $m \ll M$ ,

i.e., the scattering yield is more when the scattering angle is reduced.

Scattering cross-section is usually expressed in barns per unit steradian, (where 1 barn is equal  $10^{-24} \text{ cm}^2$ ).

### 2.1.3 Stopping cross-section factor

As we know from section 2.1.1, if the incident projectile has energy  $E_0$ , then on scattering from the surface of the target it has energy  $K E_0$ . Actually as the energetic incident projectile penetrates into the target, it slows down and its kinetic energy decreases. It loses energy by encountering an electron of an atom causing electronic energy loss  $[s_e]$ , or interacting with atomic core causing nuclear energy loss  $[s_n]$ . The important point is that electronic energy loss is dominant in the energy range at which backscattering is performed. The amount of energy lost ( $\Delta E$ ) per distance traversed ( $\Delta x$ ) depends on the identity of the projectile. The energy  $E$  at any depth  $t$  below the surface is then given by the expression

$$E(x) = E_0 - \int_0^t \left( \frac{dE}{dx} \right) dx \quad (2.13)$$

where  $(dE/dx)$  is the energy loss or stopping power of the target. This is the energy of the projectile just before scattering from a depth. The energy  $E_1$  of the projectile after scattering and emergence from the target (which is detected by the detector) is given by the expression

$$E_1 = K E - \int_0^T \left( \frac{dE}{dx} \right) dx \quad (2.14)$$

where  $T = \frac{t}{\cos(\pi-\theta)}$ . The difference in energies of the particles scattered from the surface and at depth  $t$  is then given by

$$\Delta E = K E_0 - E_1 \quad (2.15)$$

Substituting Equations (2.13) and (2.14) in Equation (2.15) we get

$$\Delta E = K \int_0^t \left( \frac{dE}{dx} \right) dx + \int_0^T \left( \frac{dE}{dx} \right) dx \quad (2.16)$$

If the energy loss  $(dE/dx)$  is assumed to be constant over each segment of the path we can write Equation (2.16) as

$$\Delta E = [S]t \quad (2.17)$$

where  $[S]$  the energy loss factor or S-factor, and is given by

$$[S]_{\blacksquare}^h = \left[ K_{\blacksquare} \left( \frac{dE}{dx} \right) \right]_{E=E_0}^h + \frac{1}{\cos(\pi-\theta)} \left( \frac{dE}{dx} \right)_{E=K_{\blacksquare}E_0}^h \quad (2.18)$$

here  $h$  stands for host target and  $\blacksquare$  the incident projectile mass. It is to be noted from the above equation that  $[S]$  depends on the stopping power of the target and the kinematic factor of the incident projectile with respect to the target. One can also write Equation (2.17) in terms of atoms/cm<sup>2</sup> i.e.,

$$\Delta E = \left( \frac{1}{N} \right) [S] (Nt) \quad (2.19)$$

$$\Delta E = [\epsilon] (Nt) \quad (2.20)$$

where  $(Nt)$  is the depth in atoms/cm<sup>2</sup> and  $N$  is the volume density of target in atoms/cc, i.e.,  $[\epsilon]$  is the stopping cross-section factor in eV-cm<sup>2</sup>/atom, i.e.

$$[\epsilon] = \left( \frac{1}{N} \right) [S] \quad (2.21)$$

or

$$[\epsilon]_{\blacksquare}^h = \frac{1}{N} \left[ K_{\blacksquare} \left( \frac{dE}{dx} \right) \right]_{E=E_0}^h + \frac{1}{\cos(\pi-\theta)} \left( \frac{dE}{dx} \right)_{E=K_{\blacksquare}E_0}^h \quad (2.22a)$$

or

$$[\epsilon]_{\blacksquare}^h = K_{\blacksquare} \left[ \epsilon \right]_{E_0}^h + \frac{1}{\cos(\pi-\theta)} \left[ \epsilon \right]_{E=K_{\blacksquare}E_0}^h \quad (2.22b)$$

where  $\epsilon$  is the stopping cross-section in eV-cm<sup>2</sup>/atom., and is given by

$$\epsilon = \left( \frac{1}{N} \right) \frac{dE}{dx} \quad (2.23)$$

Semi-empirical tables are available [Zeigler 1977] to calculate the values of  $\epsilon$  from a polynomial with given coefficients.

#### 2.1.4 Stopping in a multi-elemental target

In a multi-species target, the projectile will encounter various atomic species and lose energy. So the total energy loss in the target medium composed of various atomic species is the sum of losses in the constituent

elements, weighted proportionately to their abundance in the compound. This is known as the principle of additivity of stopping cross-section or Bragg's rule, as it was first postulated by *Bragg and Kleeman [1905]*. The stopping cross-section  $\epsilon$  of a molecule  $A_x B_y$  is given according to the above rule as

$$\epsilon^{AB} = \frac{[x\epsilon^A + y\epsilon^B]}{(x + y)} \quad (2.24)$$

where  $\epsilon^A$  and  $\epsilon^B$  are stopping cross-sections of the atomic constituents A and B. Similarly the specific energy loss of the target is given as

$$\left[ \frac{dE}{dx} \right]^{A_x B_y} = [N]^{A_x B_y} [\epsilon]^{A_x B_y} \quad (2.25)$$

Hence from Equations (2.16), (2.17) and (2.19) the depth  $t$  can be determined if  $\Delta E$  is measured. In the present study the targets which are amorphous metallic alloys are multi-elemental species, and the energy loss in these were calculated using the above procedure.

### 2.1.5 Determination of film thickness

The backscattering geometry and the spectrum for a film of thickness  $t$  of a heavy element of mass  $M_1$  on a light substrate of mass  $M_2$  is depicted in Figure 2.2. The edge of the substrate is shifted towards the lower energy side than the true position. This is due to the loss of energy of the incident particle in the film. There are three methods to determine the film thickness:

(i) The FWHM ( $\Delta E_1$ ) of the film peak after subtracting the detector resolution quadratically, gives the film thickness i.e.,

$$t = \Delta E_1 / [S]_1^1 \quad (2.26)$$

where  $[S]_1^1$  is the energy loss factor for the film.

(ii) The energy shift ( $\Delta E_2$ ) in the position of the light substrate can also give the thickness of the film i.e.,

$$t = \Delta E_2 / [S]_1^2 \quad (2.27)$$

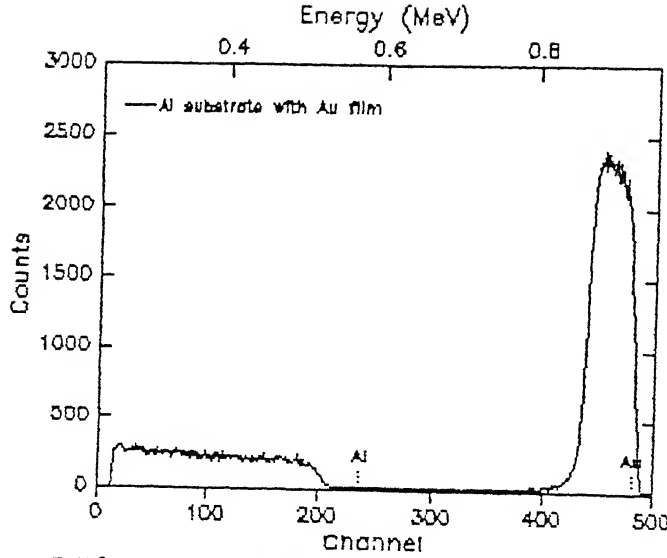


FIGURE 2.2 RBS spectrum of thick film (of Au) on lighter substrate (Al).

here  $[S]_1^2$  is determined by considering the film (1) as the stopping medium and the substrate (2) as the scattering centre.

(iii) The thickness  $Nt_1$  (in atoms/cm<sup>2</sup>) of the film can be calculated from the area (or counts) under the impurity or film peak. If  $Q$  is the number of incident particles,  $\sigma_1$  and  $\sigma_2$  are scattering cross-section for the impurity atom and the substrate atom respectively,  $\Omega$  is the average solid angle subtended by the detector, the area under the film peak is then given by

$$A_1 = Q \sigma_1 \Omega (Nt)_1 \quad (2.28)$$

and the substrate height is obtained from the following

$$H_2 = (Q \sigma_2 \Omega \delta E) / [\epsilon]_2 \quad (2.29)$$

where  $\delta E$  is the calibration and  $[\epsilon]_2$  is the stopping cross-section factor. Using Equations 2.28 and 2.29, the film thickness  $Nt_1$  is given as

$$Nt_1 = (A_1 \sigma_2 \delta E) / (H_2 \sigma_1 [\epsilon]_2) \quad (2.30)$$

Considering the ratio of the scattering cross-sections as

$$\sigma_2 / \sigma_1 = (Z_2 / Z_1)^2 \quad (2.31)$$

the above Equation 2.30 reduces to

$$Nt_1 = (A_1 Z_2^2 \delta E) / (H_2 Z_1^2 [\epsilon]_2) \quad (2.32a)$$

from which the thickness of the film in units of atoms/cm<sup>2</sup>, can be calculated.

Using the energy loss factor  $[S]_1^2$  instead of the stopping power in the above

equation i.e.,

$$Nt_1 = (A_1 z_2^2 \delta E) / (H_2 z_1^2 [S]_1^2) \quad (2.32b)$$

we get the value of the film thickness in Å units.

### 2.1.6 The depth profile

As shown in Figure 2.2, the RBS spectra is obtained in the form of channel number versus yield (or counts) in the MCA. The depth versus concentration profile for the film in the substrate has to be obtained first, from the RBS spectrum in order to determine the diffusivity of the film species in the substrate material. For the film, the depth  $d_i$  and the concentration  $C_i$  at the channel  $i$ , are respectively given by:

$$d_i = (j-i) \times \delta E / [S]_1^2 \quad (2.33)$$

and

$$C_i = \frac{H_{1,i} \sigma_2 [S]_1^2}{H_2 \sigma_1 [S]_2^2} \times 100 \text{ (in atm.\%)} \quad (2.34)$$

where  $j$  is the channel number of the surface position or the film edge,  $H_{1,i}$  is the number of counts of the film in channel  $i$ , and  $H_2$  is the height of the substrate plateau. The  $[S]$  factors are determined from Equation 2.18.

### 2.1.7 Energy straggling

Due to statistical fluctuations in any process, the energy loss of two identical particles in the target is not same, i.e.,  $(dE/dx)$  is subject to fluctuations. This phenomenon is called energy straggling. Because of these fluctuations, the identical projectiles do not have the same energy  $E$  on reaching the detector. Hence an uncertainty is produced in depth resolution and mass identification. For these reasons it is important to know about the energy straggling of the system. The initial determination of energy straggling was done by Bohr [1915] and it is referred to as the Bohr value of energy straggling ( $\Omega_B$ ) i.e.

$$\Omega_s^2 = 4\pi \left( z e^2 \right)^2 N Z t \quad (2.35)$$

where  $z$  and  $Z$  are the atomic number of projectile and target respectively,  $NZ$  is the number of particles per unit area, and  $t$  is the thickness of target layer.

For quick estimates of energy straggling it is found that  $(\Omega_s^2)/Nt$  is equal to 4% of  $Z_2$  in units of  $10^{-12}(\text{eV-cm})^2$ . Bohr's theory of energy straggling also predicts that the distribution of a beam traversed in a medium is Gaussian and is given by

$$g(x) = (2\pi \Omega_s^2)^{-1/2} \exp \left[ -\left( \frac{x^2}{2\Omega_s^2} \right) \right] \quad (2.36)$$

Scattering spectra most often display the integral of the Gaussian distribution, i.e., the error function defined as

$$\text{erf}(x) = (2\pi \Omega_s^2)^{-1/2} \int_{-a}^x \exp \left[ -\left( \frac{x^2}{2\Omega_s^2} \right) \right] \quad (2.37)$$

The full width at half maximum (FWHM) of a gaussian corresponds to the 12% to 88% range of the error function and the  $\pm \Omega$  points in the gaussian corresponds to 16% to 84% of the error function. This shows that FWHM is wider than  $\Omega$  by a factor of  $2(2\ln 2)^{1/2}$  equal to 2.355.

### 2.1.8 Energy and Depth resolution

Any experimental system is subject to statistical fluctuation of some kind or other. The source of this cause can be characterized by a gaussian and a standard deviation value  $\Omega_r$  and is commonly referred to as the system resolution of the setup. The two important contributions to  $\Omega_r$  are the beam resolution  $\Omega_b$  and the detector resolution  $\Omega_d$  and they add up in quadrature in the Gaussian system i.e.,

$$(\Omega_r)^2 = K^2 \Omega_b^2 + \Omega_d^2 \quad (2.38)$$

The system resolution is based not only on the characteristic of the detector, but also that of the preamplifier, the amplifier and the multichannel analyzer.

The ability to detect the lowest value of energy of the scattered beam is termed as the energy resolution ( $\Omega_e$ ) of the system. The energy resolution is normally determined by two major contributions, one stemming from the system resolution ( $\Omega_r$ ) and the other from the energy straggling ( $\Omega_s$ ). In the gaussian approximation they add up in quadrature i.e.

$$(\Omega_e)^2 = (\Omega_s)^2 + (\Omega_r)^2 \quad (2.39)$$

The influence of the system resolution and energy straggling can be seen in Figure 2.3, for the high and low energy edges of the backscattering spectrum of a 1000 Å film.

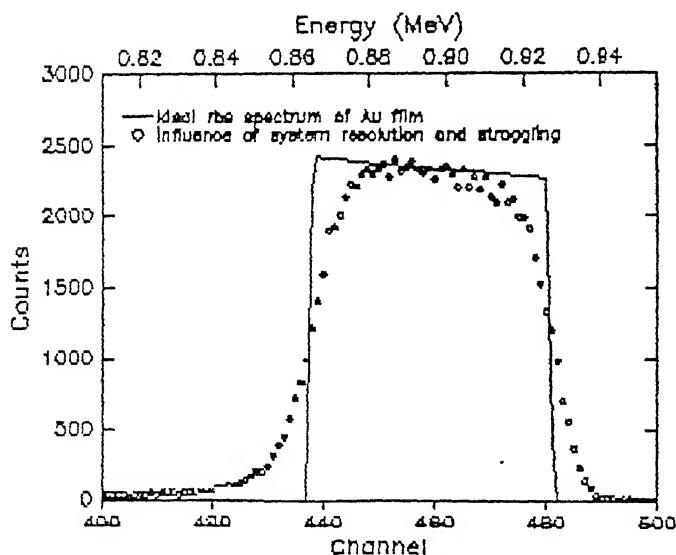


FIGURE 2.3 Effect of energy resolution and straggling.

The high energy edge of the spectrum is broadened or smoothed out because of the system resolution as there is no energy straggling on the surface. The system resolution along with energy straggling broadens the low energy edge. For thick films, the width of the low energy edge of the signal is dominated by the energy straggling.

The energy resolution of the backscattering system is independent of the detected energy and it can be measured from the slope of the high energy edge (Figure 2.3). The FWHM of the negative gaussian produced by differentiating the slope gives the energy resolution of the system. As mentioned in sec.2.1.7, it can also be obtained by measuring the energy spread of the slope from 12% to 88%



of the height of the substrate. With conventional surface barrier detectors an energy resolution of about 15 keV is obtained for 1 to 2 MeV  $\text{He}^+$  beams.

The ability to sense composition changes with depth or variations in impurity distributions with depth is referred to as the depth resolution ( $\delta x$ ) and is an important factor in the application of backscattering spectrometry to the analysis of materials. Just as the energy scale of the detected particles of the backscattering spectrum is translated into the depth scale through  $[\epsilon]$  or  $[S]$  factors, so is the lowest resolvable energy  $\Omega_e$  translated into the smallest resolvable depth interval  $\delta x$ . The depth resolution is hence defined as

$$\delta x = \Omega_e / [S] \quad (2.40)$$

The energy resolution of the high energy edge (Figure 2.3) gives the depth resolution at the surface and the energy resolution of the low energy edge gives the depth resolution at the thickness  $t$  of the film i.e., at the interface.

LIBRARY  
KANPUR  
No. A. 117962

## 2.2 MÖSSBAUER SPECTROSCOPY

The phenomenon of recoilless emission and resonant absorption of nuclear gamma rays is called Mössbauer effect. It was first observed by Rudolf Mössbauer during his PhD work and later reported [Mössbauer 1958], that certain nuclei bound in solids can emit or absorb gamma-ray photons to a large extent without any loss of recoil energy or without doppler broadening.

The importance of the Mössbauer technique was considerably acknowledged soon after its discovery and its use steadily shifted from the arena of nuclear physics to various other fields like material science, solid state physics, solid state chemistry, metallurgy, etc. Many of the leaders of Mössbauer spectroscopy who used to be concerned with nuclear problems like nuclear spin, parities, beta-decay, etc., are now concerned with solid state problems like measurement of electron density distribution, relaxation and diffusion times, magnetism, etc.

Since several excellent and authentic articles exist on Mössbauer effect and its application, we shall only briefly discuss the same, giving an outline on the basic principle, methodology and its application in following sections.

### 2.2.1 Recoil energy loss

Consider a nucleus (n) at rest having mass  $M$  and energy  $E_0$ , i.e., it is at an energy level  $E_0$  with respect to a ground level. Generally on de-excitation it emits a photon ( $\gamma$ ) of energy  $E_\gamma$  and the nucleus gets recoiled (by energy  $R$ ) because of this decay (see Figures 2.4 (a) and (b)).

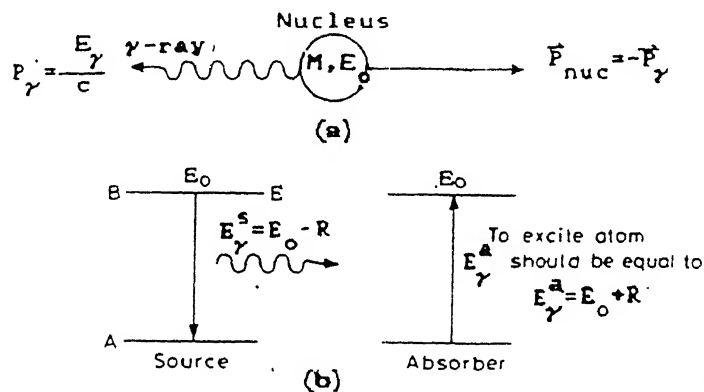


FIGURE 2.4 (a) Schematic and (b) energy level diagram of the Mössbauer process.

From conservation of momentum of the decaying system we get:

$$\vec{p}_n = -\vec{p}_\gamma \quad (2.41)$$

where the magnitude of photon momentum is connected with photon energy ( $E_\gamma$ ) as:

$$p_\gamma = \frac{E_\gamma}{c} \quad (2.42)$$

And from conservation of energy we get:

$$E_0 = E_\gamma + R \quad \text{or} \quad E_\gamma = E_0 - R \quad (2.43)$$

Since the decaying nuclei are very heavy, using the non-relativistic approximation, the recoil energy  $R$  is given as:

$$R = \frac{p_n^2}{2M} \quad (2.44)$$

As  $R$  will always be smaller than  $E_0$ , we can set  $E_\gamma$  equal to  $E_0$ . Hence from Equations 2.41 to 2.44, we get:

$$R = \frac{E_\gamma^2}{2 M c^2} = \frac{E_0^2}{2 M c^2} \quad (2.45)$$

For a quick evaluation we can write in numerical form:

$$R \text{ (in eV)} = 5.37 \times 10^{-4} \frac{E_0^2 \text{ (in keV)}}{Z} \quad (2.46)$$

where  $Z$  is the atomic number of the decaying nucleus. Similarly in a transition from a lower level A to a higher level B (Figure 2.4) by absorption of photon, the conservation of energy gives

$$E_\gamma = E_0 + R \quad (2.47)$$

i.e., the photon incident on the nucleus has to provide an extra amount of energy  $R$ , over the transition energy  $E_0$ , as recoil of the system takes place.

### 2.2.2 Natural line-width and resonance

It is however well known that the energy  $E$  of an excited state is not sharp (Figure 2.5), but has a Lorentzian shape spread over a certain energy range and described by

$$I(E) = C_1 \times \frac{\frac{\Gamma}{2\pi}}{\left\{ \left( \frac{\Gamma}{2} \right)^2 + (E - E_0)^2 \right\}} \quad (2.48)$$

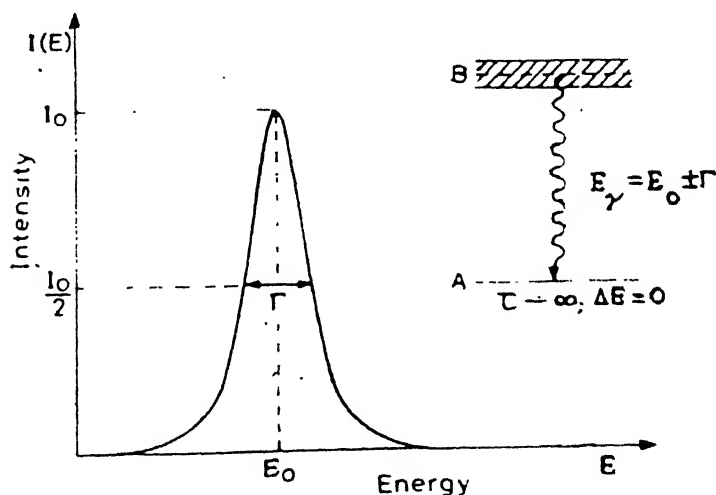


FIGURE 2.5 Lorentzian shape of the energy  $E$ , with linewidth  $\Gamma$ .

where  $C_1$  is a constant and  $\Gamma$  is the natural line-width of the state i.e., the full width of the energy distribution at half height and is related to the mean life time  $\tau$  of the state under consideration by the Heisenberg's uncertainty principle viz.,

$$\Gamma = \frac{\hbar}{\tau} \quad (2.49)$$

where  $\hbar = h/2\pi$ , and  $h$  = Plank's constant. Because of this spread or lineshape of the excited state, the emitted photon of energy  $E_\gamma^s$  and absorbing photon of energy  $E_\gamma^a$  will show a similar line shape (Figure 2.6(a)) centered around  $E_\gamma^s$  and  $E_\gamma^a$  respectively, such that

$$I_s(E) = C_1 \times \frac{\frac{\Gamma}{2\pi}}{\left(\frac{\Gamma}{2}\right)^2 + (E - E_\gamma^s)^2} \quad (2.50a)$$

$$I_a(E) = C_2 \times \frac{\frac{\Gamma}{2\pi}}{\left(\frac{\Gamma}{2}\right)^2 + (E - E_\gamma^a)^2} \quad (2.50b)$$

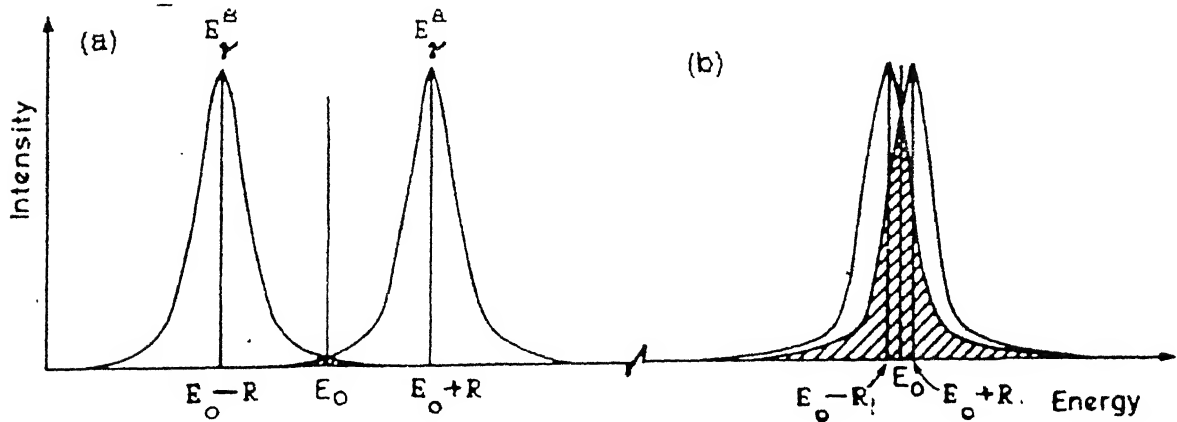


FIGURE 2.6 (a) Similar lineshape of the emitting and absorbing photon, (b) On overlapping there is resonance and absorption

where  $C_1$  and  $C_2$  are constants. Only when the lineshapes of the source nuclei  $I_s$  overlaps with that of the absorbing nuclei  $I_a$ , we (Figure 2.6(b)) get resonance and excitation in the absorbing nuclei. Since in all cases of interest, the recoil energy  $R$  is much larger than the natural linewidth  $\Gamma$ , no overlap and hence no excitation can take place.

### 2.2.3 Doppler broadening and resonance

Another natural property of the nuclei is that they are not at rest, but move with large velocities of the order of few hundred m/s. Such a velocity ( $v_0$ ) leads to a Doppler broadening of the lineshape. Considering the velocity ( $v$ ) along the direction of emission, the energy of the gamma ray emitted shifts by an amount  $\Delta E$  given by

$$\Delta E = \frac{v}{c} E \quad (2.51)$$

This velocity ( $v$ ) will vary from  $+v_0$  to  $-v_0$  and hence the lineshape of the decaying nuclei will be broadened by an amount  $\bar{D}$  where

$$\bar{D} = 2(v_0/c)E \quad (2.52)$$

and a small overlap occurs causing resonance fluorescence. But this causes the line height to be drastically reduced which effects considerably the number of observed fluorescence photons.

Both the above conditions i.e., decrease in recoil energy loss and Doppler broadening can be achieved by classically freezing the emitting and absorbing nuclei in the solid. Indeed, the Mössbauer effect is just such a freezing process, discovered by Rudolf Mössbauer during his doctoral thesis research. The problem given to him originally was the study of nuclear resonance fluorescence at low temperatures.

### 2.2.4 Einstein energy and resonance

A simple calculation shows that the probability for emission of  $\gamma$ -ray photons without recoil energy loss is given by

$$f = \exp \left( -3R/E_E \right) \quad (2.53a)$$

where  $R$  is the recoil energy and  $E_E$  is the Einstein energy. It was later shown by Debye that it is slightly more complicated than above i.e.

$$f = \exp \left( -3R/2k\theta_D \right) \quad (2.53b)$$

where  $\theta_D$  is the Debye temperature and  $k$  is Boltzmann's constant.

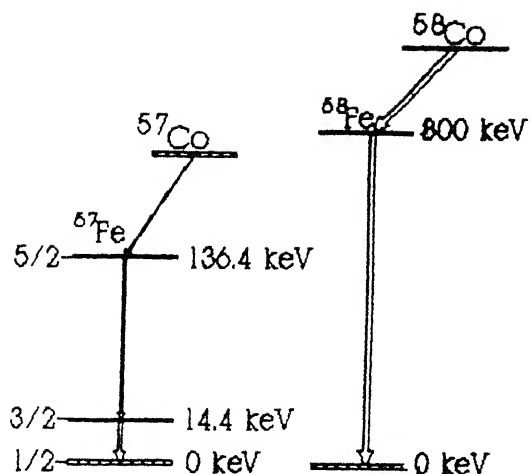


FIGURE 2.7 Essential aspects of the decay scheme of  $^{57}\text{Fe}$  and  $^{58}\text{Fe}$ .

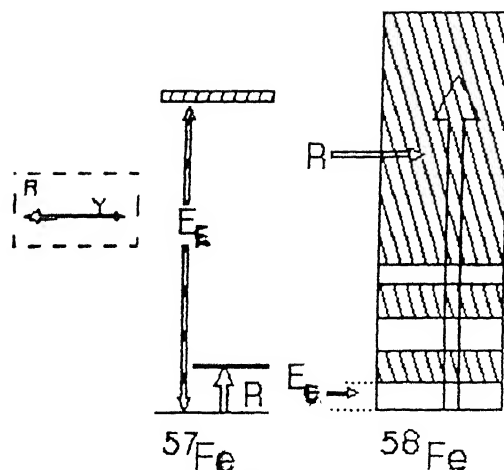


FIGURE 2.8 Comparison of  $R$  and  $E_E$ , in  $^{57}\text{Fe}$  and  $^{58}\text{Fe}$ .

For the observation of Mössbauer effect,  $f$  must be significantly large and this means that  $R \ll E_E$ . Now let us consider the two different isotopes of iron. Assuming the decay scheme as shown in Figure 2.7 of  $^{57}\text{Co}$  and  $^{58}\text{Co}$  nuclei to  $^{57}\text{Fe}$  and  $^{58}\text{Fe}$  nuclei respectively, we obtain for  $^{57}\text{Fe}$ , the decay energy ( $E_0$ ) as 14.4 keV, recoil energy ( $R$ ) as 0.002 eV and Einstein energy ( $E_E$ ) as 0.04 eV. While for  $^{58}\text{Fe}$  these values are 800 KeV, 6.0 eV and 0.04 eV respectively. For  $^{57}\text{Fe}$  transition, the recoil energy (Figure 2.8) is much smaller than the Einstein energy, whereas the opposite is true for  $^{58}\text{Fe}$  nuclei. The internal energy of the solid is also unchanged, hence Doppler broadening does not occur. Therefore the 14.4 keV  $\gamma$ -ray photon is emitted from  $^{57}\text{Co}$  with the full energy  $E_0$ .

### 2.2.5 Observation of Mössbauer effect

Consider a stationary source  $S$  of  $^{57}\text{Fe}$  emitting  $\gamma$ -rays of varied energies (along with 14.4 keV  $\gamma$ -rays). While passing through the absorber a fraction of it is absorbed while the rest is transmitted through and counted in the detector system. Most of the absorption takes place due to photoelectric and Compton — effect. A fraction  $f$  of the total, is incident on the absorber without recoil

energy loss and Doppler broadening. A fraction  $f'$  of these recoilless photons excite the  $^{57}\text{Fe}$  nuclei of the absorber producing resonant absorption and hence are removed from the beam before reaching the detector. This excess absorption was first noticed by Mössbauer and is more than that anticipated, by well established laws of photoelectric and Compton — effect. The nuclei of the absorber thus excited, decays by re-emitting conversion electrons or 14.4 keV  $\gamma$ -rays, the fraction of which reaching the detector is negligible.

The second effect first noticed by Mössbauer was that, if the stationary source described above is vibrated about its mean position, the 'natural line-shape' of the absorbed  $\gamma$ -rays in the absorber can be observed. In other words if the energy of the  $\gamma$ -rays incident on the absorber is shifted about its mean value (i.e., 14.4 keV), there will be an energy shift in the absorption spectrum as observed in the transmitted lines. If the source is moved with a constant velocity ( $v$ ), the emitted photons will have an energy  $E$  as given below,

$$E = E_0 \left( 1 + v/c \right) \quad (2.54)$$

Because of the 'freezing effect', the emission and absorption lines completely overlap each other and absorption is maximum. If the source is moved, the energy of the incident  $\gamma$ -rays is changed, the emission line is shifted, the overlap decreases and absorption is smaller. Hence the counting rate in the detector is increased.

#### 2.2.6 Hyperfine interactions

Much of the Mössbauer effect studies are performed using the  $^{57}\text{Fe}$  source and absorbers having iron as one of its components. Because of various nuclear interactions in and around the Mössbauer nuclei of the absorber, the absorption spectrum shows several absorption lines, i.e., a combination of singlets, doublets or sextets. These nuclear interactions are caused by the presence of nuclear moments of the Mössbauer nuclei ( $^{57}\text{Fe}$  in this case) and the extranuclear

electromagnetic fields produced by electrons and ligands. Since the interaction energy is in the range of  $10^{-6}$  to  $10^{-9}$  eV, it is termed as 'hyperfine'.

These hyperfine interactions (HI) can be described in terms of the Hamiltonian  $H$  of the nucleus:

$$H = H_0 + E_0 + M_1 + E_2 + \text{higher order terms} \quad (2.55)$$

here  $H_0$  is the nuclear Hamiltonian and it excludes HI. The term  $E_0$  describes the electric monopole interaction between the nucleus and the surrounding electrons, causing isomer shift (IS) in the Mössbauer spectrum. The term  $M_1$  describes the magnetic dipole interaction between the nuclear magnetic dipole moment and the surrounding extranuclear magnetic fields giving rise to nuclear Zeeman splitting. The term  $E_2$  describes the electric quadrupole interaction between the nuclear electric quadrupole moment and the electric field gradient of the surrounding electrons. So far, only the above three interactions are studied by Mössbauer spectroscopy (MS). The interactions of higher order ( $M_2$ ,  $E_3$ , etc.,) are negligible because of their interaction energies being too small to be resolved by Mössbauer spectroscopy. The electric dipole ( $E_1$ ) interaction is ruled out by symmetry considerations.

#### 2.2.7 Electric monopole interaction: isomer shift

Electric monopole interactions occur between the nuclear charge and the atomic electrons around the nucleus, which gives rise to a measurable shift in the Mössbauer energy levels. This affects the position (or centroid) of the resonance lines on the energy or velocity scale (Figure 2.9). The difference observed in the energy levels of the source and the absorber is called isomer shift (IS) and is of the order of  $10^{-9}$  eV.

Hence to observe resonance in the absorber, the source is provided with a Doppler velocity ( $v$ ) such that

$$E_{\gamma}^a = E_{\gamma}^s \left( 1 + \frac{v}{c} \right) \quad (2.56)$$



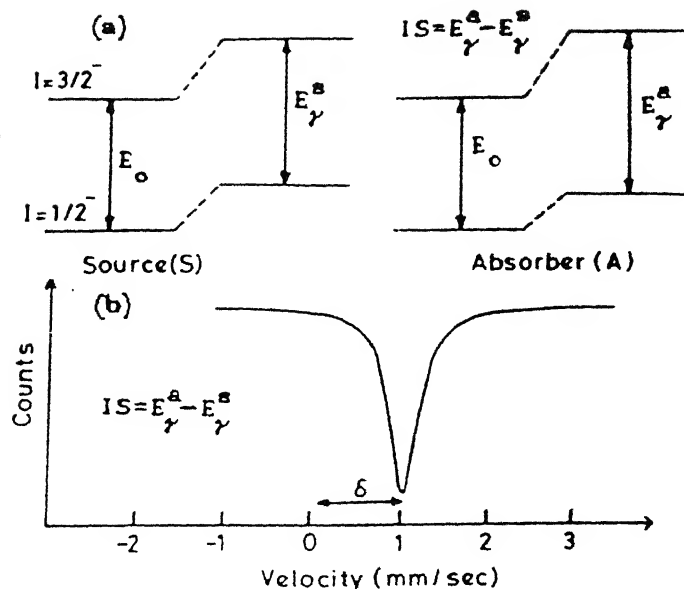


FIGURE 2.9 Effect of monopole interaction (a) on the energy levels of the source and absorber, and (b) the resulting Mössbauer spectrum showing isomer shift.

The difference of the electric monopole interaction (EMI) energy of the source and the absorber is a measure of the isomer shift (Figure 2.9) and is given in units of mm/s by the following:

$$IS = \delta = \frac{2\pi cZe^2}{5E_\gamma} \left[ R_e^2 - R_g^2 \right] \left[ |\psi(0)|_a^2 - |\psi(0)|_s^2 \right] \quad (2.57)$$

where  $Z$  is the atomic number of Mössbauer nucleus,  $e$  is the electronic charge,  $R_e$  and  $R_g$  are the respective radii of the excited and the ground state of Mössbauer nuclei.  $|\psi|_a^2$  and  $|\psi|_s^2$  are the respective density of  $s$ -electrons at the nucleus in the absorber and source. It is assumed here that  $|\psi|^2$  is spherically symmetric. As a usual practice, one uses a standard source material, e.g.,  $^{57}\text{Co}$  in Rh matrix for Fe Mössbauer spectra (as in our case).

Considering  $\delta R = (R_e - R_g)$ , and  $(R_e + R_g) = 2R$ , we get

$$\delta = C_1 R^2 \left( \frac{\delta R}{R} \right) \left[ |\psi(0)|_a^2 - C_2 \right] \quad (2.58)$$

where  $C_1$ ,  $C_2$  are constants. From above it is clear that IS depends on two factors, the nuclear factor  $\delta R$  and the extranuclear factor  $|\psi(0)|_a^2$ . For a given standard nucleus like  $^{57}\text{Fe}$ ,  $\delta R$  is a constant and IS depends solely on the

-electron density at the nucleus. Hence IS is dependant on the valence state and coordination number of the Mössbauer nucleus of the absorber as both of these lead to different values of  $|\psi(0)|_a^2$ .

## 2.8 Electric quadrupole interaction: quadrupole splitting

In reality, the nuclear charge distribution is not uniform or spherically symmetric as assumed earlier. It also possesses electric multipole moments if the spin of the nucleus  $I$ , is a multiple of  $1/2$ . These multipole moments are  $2^l$  in number (where  $l$  is an even number), and because of these moments, there will be an interaction with the extranuclear electric field. These extranuclear fields or charges produce an electric field gradient (EFG), the  $z$ -component of which (in the principal coordinate system) is expressed as:

$$V_{zz} = (1 - \gamma_\alpha) (v_{zz})_{lat} + (1 - R) (v_{zz})_{val} \quad (2.59)$$

where  $(1 - \gamma_\alpha)$  and  $(1 - R)$  are known as Sternheimer shielding factors,  $(v_{zz})_{lat}$  and  $(v_{zz})_{val}$  are contributions to EFG in the  $z$ -direction from external charges of Mössbauer atom, and valence and partially filled inner electron shells of the Mössbauer nucleus respectively.

The electric quadrupole moment (EQM) plays a major role in Mössbauer spectroscopy and its interaction with EFG leads to quadrupole splitting ( $\Delta E_1$ ) in the nuclear energy levels and observed in the Mössbauer spectrum as transmission dips. The electric quadrupole moment is defined by the expression

$$Q_{ij} = \int \rho_n(r) [x_i x_j - \delta_{ij} r^2] d\tau \quad (2.60a)$$

and in the principal coordinate system it reduces to

$$Q_{ij} = \frac{1}{e} \int \rho_n(r) r^2 (3 \cos^2 \theta - 1) d\tau \quad (2.60b)$$

where  $\rho_n(r)$  is the nuclear charge density at point  $r$ ,  $x_i x_j$  are the cartesian coordinates of the position vector and  $\delta_{ij}$  is the Kronecker symbol.

In a symmetric case the electric quadrupole interaction energy turns out to

$$E_2 = E_Q = \frac{e Q v_{zz}}{4 I(2I - 1)} \left[ 3m_I^2 - I(I + 1) \right] \quad (2.61)$$

where  $I$  is the nuclear spin operator,  $eQ$  is the quadrupole moment of the nucleus,  $m_I$  is the magnetic spin quantum number and has values from  $+I, 0, \dots, -I$ .

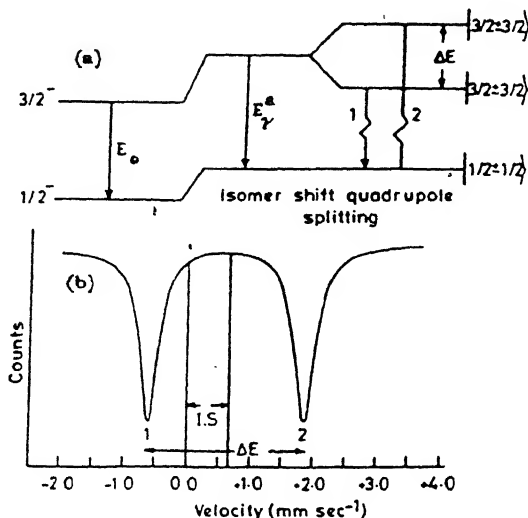


FIGURE 2.10 Effect of quadrupole interaction (a) on the nuclear energy levels of the source and absorber, and (b) the resulting Mossbauer spectrum showing quadrupole splitting.

In case of  $^{57}\text{Fe}$  the spins of the excited ( $I_e$ ) and the ground states ( $I_g$ ) are of value  $\frac{3}{2}$  and  $\frac{1}{2}$  respectively (see Figure 2.10). For  $I_g$  equal to  $\frac{1}{2}$ ,  $E_Q$  is equal to 0 and hence there is no change or splitting in the ground state and it remains degenerate. For  $I_e$  equal to  $\frac{3}{2}$ ,  $m_I$  has values  $\pm \frac{3}{2}, \pm \frac{1}{2}$ ; hence the excited levels splits into two levels (or a doublet) with energy shifts given by

$$E_Q = \frac{1}{4} e Q v_{zz} \quad , \text{ for } I = \frac{3}{2}, m_I = \pm \frac{3}{2} \quad (2.62a)$$

and

$$E_Q = -\frac{1}{4} e Q v_{zz} \quad , \text{ for } I = \frac{1}{2}, m_I = \pm \frac{1}{2} \quad (2.62b)$$

With  $^{57}\text{Fe}$  source, the Mössbauer spectrum shows two absorption lines at velocities  $v_1$  and  $v_2$  where

$$v_1 = \frac{e Q v_{zz}}{4} \frac{c}{E_0} \quad (2.63a)$$

$$v_2 = \frac{-e Q v_{zz}}{4} \frac{c}{E_0} \quad (2.63b)$$

The electric quadrupole splitting energy  $\Delta E$  for the absorber is then given as

$$\Delta E = \frac{1}{4} eQv_{zz} - \left( -\frac{1}{4} eQv_{zz} \right) = \frac{1}{2} eQv_{zz} \quad (2.64)$$

and its determination from the Mössbauer spectrum gives an insight to the valence state, coordination number, etc., of the absorbing nuclei.

### 2.2.9 Magnetic dipole interaction: magnetic hyperfine splitting

When the nuclear spin quantum number  $I > 0$ , it possesses magnetic multipole moments  $2^l$  in number, where  $l$  is an odd number. For  $l$  equal to 3, we get the magnetic dipole moment  $\mu_N$  given as

$$\mu_N = g_N \beta_N I_N \quad (2.65)$$

where  $g_N$  is the nuclear Landé splitting and  $\beta_N$  is equal to  $eh/2m$ . As a result of the interaction between this magnetic dipole moment and the extranuclear effective magnetic field  $H_{\text{eff}}$  at the Mössbauer nucleus, the nuclear levels further split up (called as magnetic hyperfine splitting) and the degeneracy of the levels is completely removed (see Figure 2.11).

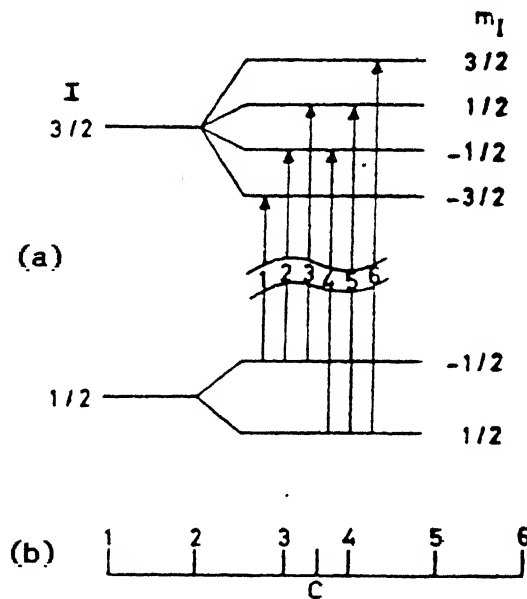


FIGURE 2.11 Effect of magnetic hyperfine interaction (a) on the energy levels of  $^{57}\text{Fe}$ , and (b) the resulting peak position of the six-finger Mössbauer spectrum.

The effective magnetic field at the Mössbauer nucleus is then given by

$$H_{\text{eff}} = H_{\text{ext}} + H_{\text{c}} + H_{\text{L}} + H_{\text{d}} \quad (2.66)$$

where  $H_{\text{ext}}$  is the externally applied magnetic field;  $H_{\text{c}}$  is the Fermi contact field arising from s-electron spin density at the nucleus;  $H_{\text{L}}$  is the contribution from orbital motion of valence and partially filled inner shell electrons; and  $H_{\text{d}}$  is the spin dipolar term arising from the spin of the electrons outside the Mössbauer atom.

The Hamiltonian for the magnetic dipole interaction caused by the magnetic dipole moment and the effective magnetic field is given by

$$M_1 = -\mu H_{\text{eff}} = -g_N \beta_N I H_{\text{eff}} \quad (2.67)$$

and hence the energy eigen values of  $M_1$  are given by

$$E_M = -g_N \beta_N M_I H_{\text{eff}} \quad (2.68)$$

Taking into account the different  $g_N$  values of the ground and the excited states, and considering the selection rule  $\Delta m_I = 0, \pm 1$  it can be shown that the nuclear states split up into  $2I+1$  substates. The state  $I$  of value  $\frac{3}{2}$  splits up into four substates and the state  $I$  of value  $\frac{1}{2}$  splits up into two substates, producing a six line Mössbauer spectrum as shown in Figure 2.11.

Although the linewidths of the six peaks are in general equal, their intensities are different and are given by:

$$\begin{aligned} I_1 &= I_6 = 3(1 + \cos^2 \theta) \\ I_2 &= I_5 = 4 \sin^2 \theta \\ I_3 &= I_4 = 1 + \cos^2 \theta \end{aligned} \quad (2.69)$$

where  $\theta$  is the relative angle between the quantisation axis and the gamma propagation direction. In the case of  $^{57}\text{Fe}$ , the relative intensities of the six lines are in the ratio

$$I_1 : I_2 : I_3 :: I_4 : I_5 : I_6 = 3 : 2 : 1 :: 1 : 2 : 3 \quad (2.70)$$

where

$$Z = 4(\sin^2 \theta) / (1 + \cos^2 \theta). \quad (2.71)$$

In order to observe Zeeman or magnetic hyperfine splitting in the absorber,

the  $^{57}\text{Co}$  source has to emit a  $\gamma$ -ray photon of energy  $[E_0 \pm \Gamma + \delta]$  and the source is provided with a Doppler velocity given by

$$v = \delta + \mu_g H \left( \frac{c}{E_0} \right) \left[ \frac{I_g}{I_g} - \frac{I_e}{I_e} \left( \frac{\mu_e}{\mu_g} \right) \right] \quad (2.72)$$

The value of the  $H_{\text{eff}}$  at the  $^{57}\text{Fe}$  nucleus of the absorber is given as:

$$H(1/2) = \frac{E_0}{\mu_g c} \left[ v \left( \frac{3}{2} \frac{1}{2} \rightarrow \frac{1}{2} \frac{1}{2} \right) - v \left( \frac{3}{2} \frac{1}{2} \rightarrow \frac{1}{2} \frac{-1}{2} \right) \right] \quad (2.73a)$$

$$H(3/2) = \frac{E_0}{\mu_e c} \left[ v \left( \frac{3}{2} \frac{3}{2} \rightarrow \frac{1}{2} \frac{1}{2} \right) - v \left( \frac{3}{2} \frac{1}{2} \rightarrow \frac{1}{2} \frac{1}{2} \right) \right] \quad (2.73b)$$

The value of  $\mu_g$  as determined by other techniques is given as  $0.0903 \pm 0.0007$ .

Using the values of  $\mu_g$ ,  $E_0$ ,  $c$ , etc., we get the value of  $H$  as

$$H = 0.843 \times 10^5 \left[ v \left( \frac{3}{2} \frac{1}{2} \rightarrow \frac{1}{2} \frac{1}{2} \right) - v \left( \frac{3}{2} \frac{1}{2} \rightarrow \frac{1}{2} \frac{-1}{2} \right) \right]$$

or

$$H = 0.843 \times 10^5 [L_5 - L_3] \times \delta E \quad \text{oersted} \quad (2.74)$$

where  $\delta E$  is the calibration constant in mm/s. per channel and  $L_3$  and  $L_5$  are the positions of the third and fifth lines of the spectrum. By using this value of  $H$  one can find the value of  $\mu_e$  - the magnetic moment of the excited state.

#### 2.2.10 Phase determination by Mössbauer spectroscopy

Though Mössbauer spectroscopy cannot compete with ordinary methods of chemical analysis, with its high resolution of the electric and magnetic hyperfine interactions (isomer shift, magnetic hyperfine splitting, and electric quadrupole splitting), it provides valuable information regarding determination of various phases, precipitating in any system during various stages of annealing processes.

The various phases formed in any system, gives its characteristic singlet, doublet or sextet spectra in the transmission Mössbauer spectrum obtained for that system or sample. The actual spectrum of the sample is a resultant of several such sextets or doublets. Using a computer program, the characteristic

sextets or doublets of these phases can be simulated, its resultant can be compared with that of the experimentally obtained spectrum in an iterative manner till a minimum  $\chi^2$  value is achieved, and its various Mössbauer parameters obtained numerically. By comparing these parameters with the standard data available in the literature, the exact phases precipitated can be determined.

## CHAPTER 3

### EXPERIMENT AND ANALYSIS

#### 3.1 INTRODUCTION

For the investigation of diffusion or atomic migration in a material (in the present case metallic glasses) the measurements of depth versus concentration profile of the diffusing species is required. For this purpose we have utilized the technique of Rutherford backscattering spectroscopy (RBS), using 1-2 MeV  $\text{He}^+$  beams obtained from the 2-MeV Van-de-Graaff accelerator at IIT Kanpur. It was mentioned in Chapter 1, that the structural changes (phase precipitation / crystallization) occurring during annealing of the metallic glasses are linked with the diffusion of the individual atomic species. For studying these structural changes we have employed the techniques of Transmission Mössbauer spectroscopy (TMS) and X-ray diffraction (XRD). The topographical changes occurring on the surface of the samples during annealing were studied by utilizing Scanning electron microscopy (SEM). This chapter gives the details of the sample preparation along with the description of the various experimental methods mentioned above.

#### 3.2 PREPARATION OF DIFFUSION COUPLES FOR RBS

The metallic glasses used in the present studies, namely  $\text{Fe}_{79}\text{B}_{16}\text{Si}_5$ ,  $\text{Fe}_{78}\text{B}_{13}\text{Si}_9$ , and  $\text{Fe}_{40}\text{Ni}_{38}\text{B}_{18}\text{Mo}_4$ , were obtained in the form of thin ribbons (of thickness 0.025 mm), from Goodfellow Metals, UK. Samples of dimensions 10x10 mm were cut from these ribbons or foils. One side of the ribbons were shiny while the other side was relatively dull. The shiny surface of the samples were polished by a fine emery paper of 0.25 grits and then thoroughly cleaned with



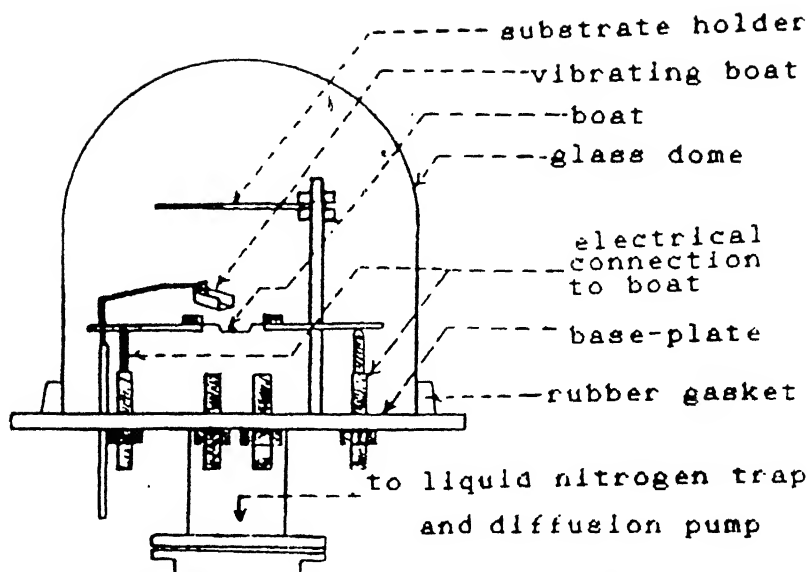


FIGURE 3.1 Schematic diagram of the vacuum evaporator system.

high purity ethyl alcohol and acetone.

Diffusion couples (in the form of a thin layer of diffusing element deposited on the shining surface of the polished sample) were prepared by the process of thermal evaporation of high purity (99.99% pure) elements, namely Au, Ge, Pd and Ag, under clean and high vacuum conditions. A schematic diagram of the vacuum evaporating system (Model CVE-18, CVC) used in the present study is shown in Figure 3.1 and a photograph of the same is presented in Figure 3.2. An electrically heated tungsten boat was utilized for the evaporation of these elements. The polished and clean samples were placed on a stand above the boat at a distance of 10 cm (with the shiny surface of the metallic glass samples facing the boat). The belljar was then evacuated to a clean and high vacuum of  $5 \times 10^{-6}$  Torr, using a diffusion pump equipped with a liquid nitrogen trap.

The quantity  $m$  of element to be evaporated was predetermined, (considering a  $2\pi$  geometry) from the formula:

$$m = 2\pi \rho t r^2 \quad (3.1)$$

where  $2\pi$  is the solid angle subtended by the element in the boat;  $\rho$  is the density of the evaporating element;  $t$  is the thickness of the film to be deposited; and  $r$  is the distance of the boat from the sample holder. Later, the

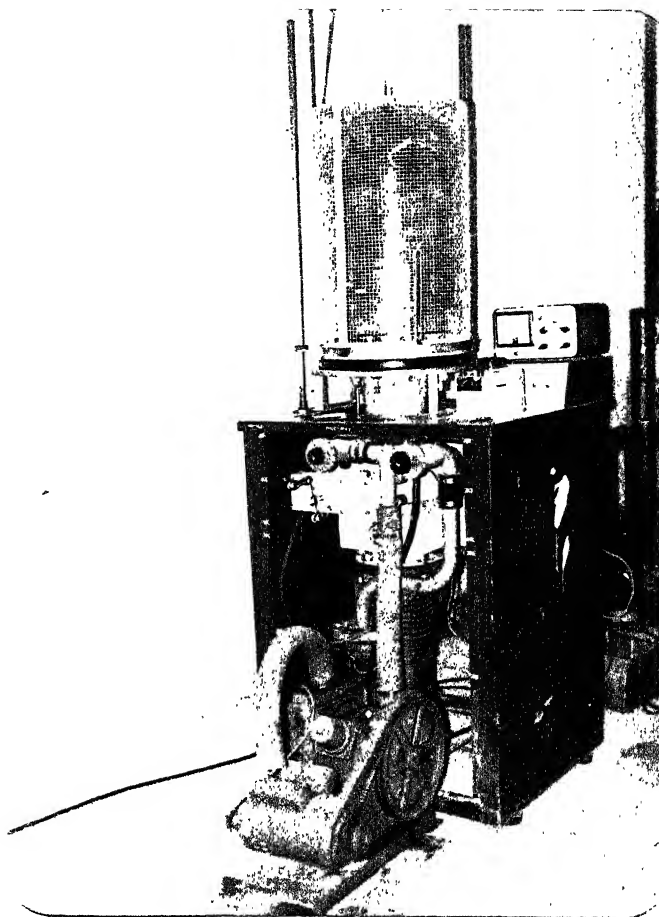


FIGURE 3.2 Photograph of the vacuum evaporator system.

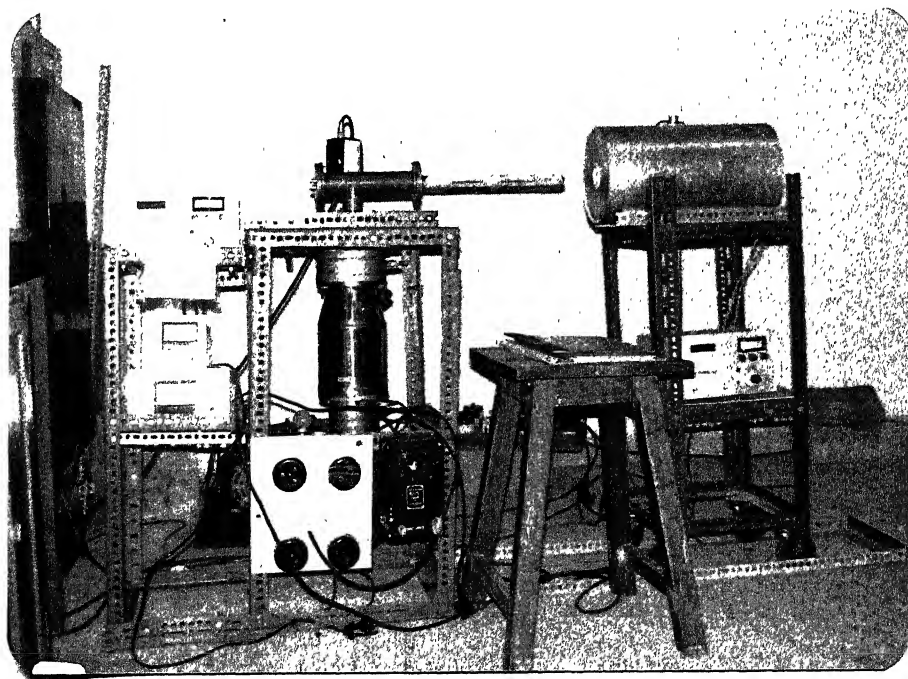


FIGURE 3.3 Photograph of the annealing set-up.

film thicknesses were accurately measured by RBS. The thickness of the films for an element were primarily decided by the diffusion-couple geometry (thin layer, thick layer etc.). In this way diffusion couples of pre-determined thickness in the range of 50-300 Å, were prepared.

### 3.3 ANNEALING OF THE DIFFUSION COUPLES

The samples to be annealed were kept in the quartz tube (i.d.=1") which was continuously evacuated by an oil diffusion pump equipped with a liquid nitrogen trap. A photograph of the annealing set-up is presented in Figure 3.3 and the schematic diagram is depicted in Figure 3.4. The furnace used for annealing had a ceramic tube (i.d.=2"), wound with nichrome wire and insulated with asbestos powder. A uniform temperature (maximum 1100°C) zone of 4" length could be obtained in the central portion of the ceramic tube. The furnace temperature was measured by a chromel-alumel thermocouple. The power to the furnace was given through a PID type temperature controller (Indotherm 400) which controlled the temperature of the furnace to  $\pm 2^\circ\text{C}$ .

The furnace was kept on a horizontal movable platform. After the furnace had reached the desired temperature, it was moved such that the quartz tube containing the samples entered in the central portion of the furnace. The temperature of the samples was measured with a chromel-alumel thermocouple

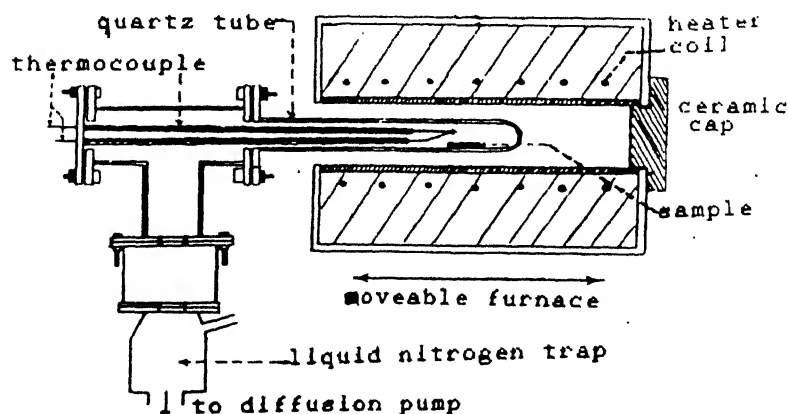


FIGURE 3.4 Schematic diagram of the annealing set-up.

directly in contact with the samples in the quartz tube. After annealing was over for the pre-requisite time, the furnace was withdrawn, and the quartz tube was cooled by using an air blower. The variation of the sample temperature with time, was noted during heating and cooling of the sample. To achieve thermal equilibration, on an average, it took three minutes during heating and six to ten minutes while cooling the sample.

Isothermal annealing of the samples as described above was carried out for several time intervals ranging from one hour to sixteen hours at different annealing temperatures (using separate samples for different temperatures) in the range 300°C to 475°C. The highest temperature employed in annealing (i.e., 475°C) is much below the crystallization temperature of the metallic glasses used (i.e., 525°C for MG2605S-2 and 545°C for MG2605S-3).

### 3.4 THE RUTHERFORD BACKSCATTERING (RBS) SETUP

The complete backscattering spectrometry set-up used in the present study consists of the following main stages :

- (i) production of ions and acceleration, using the 2-MeV Van-de-Graaff accelerator;
- (ii) mass and energy analysis of the accelerated ions using an electromagnet;
- (iii) focusing of the energy analyzed beam and separating the  $O^{++}$  ions from the  $He^{+}$  ions of the same energy; and
- (iv) experimental set-up for backscattering analysis.

#### 3.4.1 Van-De-Graaff accelerator

The Van-de-Graaff accelerator is the most widely used and commonly available electrostatic accelerator. A schematic diagram of the accelerator system is shown in Figure 3.5, and photographs of the same are presented in Figures 3.6 and 3.7. The accelerator (Model AN-2000), is manufactured by High Voltage

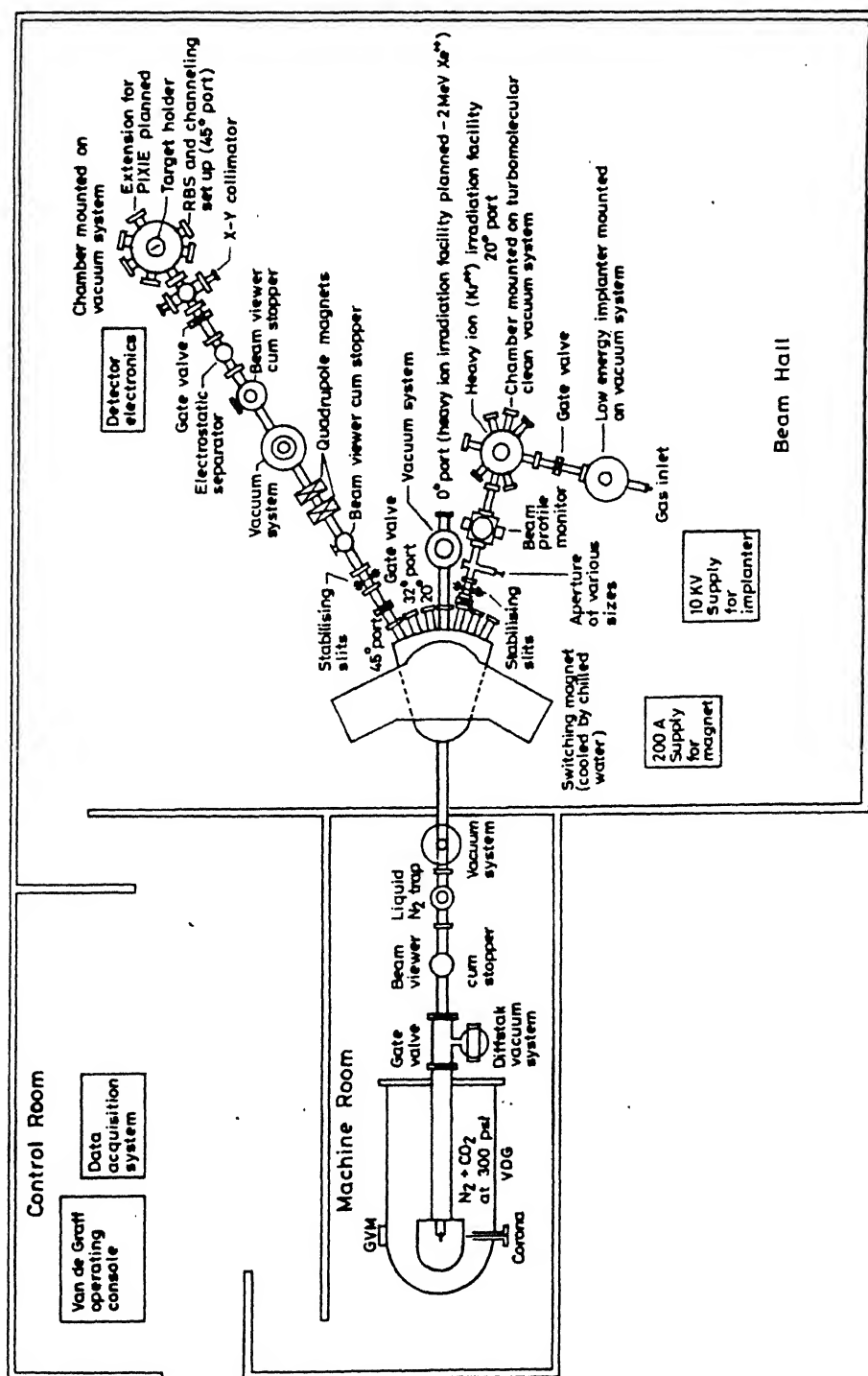


**FIGURE 3.5** Block diagram of the Van-de-Graaff accelerator system situated in Indian Institute of Technology, Kanpur.

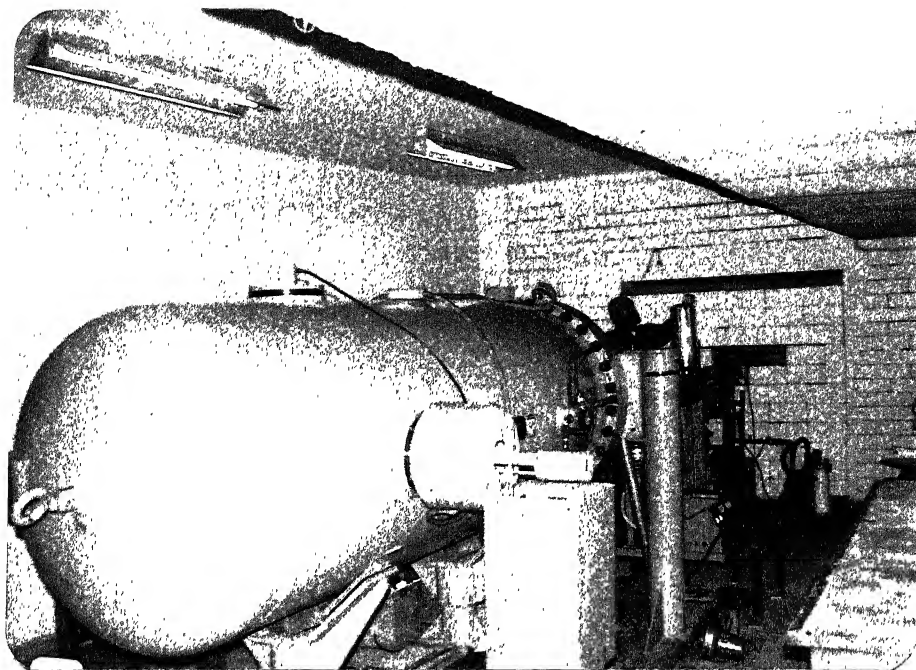


FIGURE 3.6 The Van-de-Graaff accelerator. (machine room)

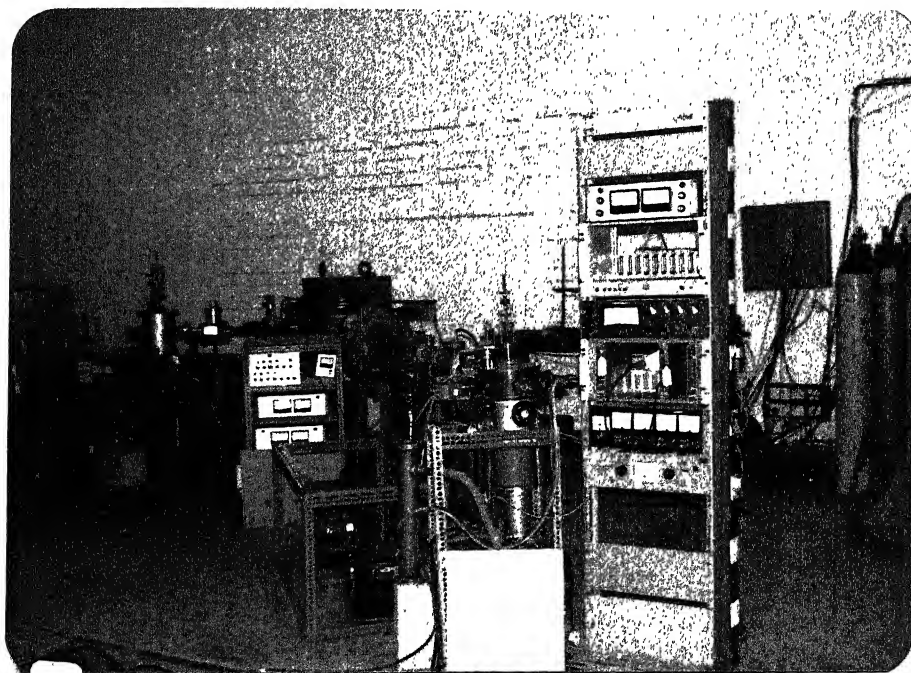


FIGURE 3.7 The analyzing magnet and beam line. (beam room)

Engineering Corporation, USA, and is a precision 2-MeV, high intensity source of positive ions. The accelerator produces a beam of ions which is intense, homogeneous, stable and controllable over a wide range of energies. At present, it is provided with three gas bottles containing hydrogen, helium and krypton gas. An r.f. ion source is used to produce  $H^+$ ,  $He^+$ , and  $Kr^+$  ions.  $He^+$  ions of energies 1 MeV and 1.4 MeV were utilized for the RBS studies.

### 3.4.2 The analyzing magnet

The mass and energy analysis of the accelerated ion-beam is done by an analyzing magnet. The analyzing magnet system consists of a 16 KGauss electro-magnet having aluminium tubular coils, which can carry DC current upto 250 amperes. During operation the magnet is cooled to  $15^{\circ}C$ , by circulating demineralized water through the coils. The magnet power supply has a capability of supplying regulated (0-30V) current of up to 250 amperes. The stainless steel switching chamber has five ports at angles  $0^{\circ}$ ,  $\pm 20^{\circ}$  and  $\pm 45^{\circ}$ . The energy and mass analyzed beam can be directed to the experimental chamber through anyone of the five ports.

### 3.4.3 The beam line

The accelerated ions ejected from the accelerator finally reach the experimental chamber through a clean and highly evacuated beam pipe or beam-line. The beam-line has a specially adapted liquid nitrogen trap fixed in between the accelerator and analyzing magnet to get clean vacuum in that region. The ion-beam after leaving the analyzing magnet, is focused and collimated by a pair of electromagnetic quadrupole lenses. This focused and collimated ion-beam then passes through an uniform electric field generated by parallel plates (electrostatic beam separator) in order to separate out  $O^{++}$  contamination from the  $He^+$  beam [Kulkarni and Singru 1987] of the same energy.

The ion-beam collimating unit placed between the RBS chamber and the ion-beam separator has manually operated horizontal and vertical slits, which define the beam size, so that a beam spot of required dimension can be made incident on the target. Beam viewers and beam stoppers are placed strategically along the beam path to view the ion-beam when diagnosing certain problems and to block the ion-beam from entering the chamber as and when required.

#### 3.4.4 Rutherford backscattering (RBS) chamber

The backscattering chamber used by us has six ports as shown in the Figures 3.8 (schematic diagram) and 3.9 (photograph). The sample holder is fixed from the top in such a way that the ion-beam entering from one of the ports is incident perpendicularly on the sample surface. The sample holder is a plate of dimensions  $130 \times 25 \times 2.5$  mm. Five to six samples can be mounted on it at a time. It can be moved in the vertical direction, such that the desired sample or sample region can be brought in front of the incident beam for analysis, with an accuracy of  $\pm 0.5$  mm. In this way several measurements on different regions of the same sample and measurements on various samples are possible without opening the chamber or breaking vacuum.

An aluminium grid is placed around the holder (inside the chamber) and a negative voltage of -180 V is applied to it, to suppress the secondary electrons emitted from the samples due to the primary ion beam. Beam currents of 5-10 nA were utilized for the present analysis. Currents more than 10-nA increased the detector dead-time and pulse pile-up effect, and hence it was maintained at all times below 10 nA. The target or beam current was measured and integrated to obtain the total fluence or charge (which relates to the number of incident  $\text{He}^+$  ions incident on the target) using a current integrator (Ortec, Model-401). Backscattering spectra, in the present study, were obtained for a total charge collection of 2-10  $\mu\text{C}$  for each target (sample).



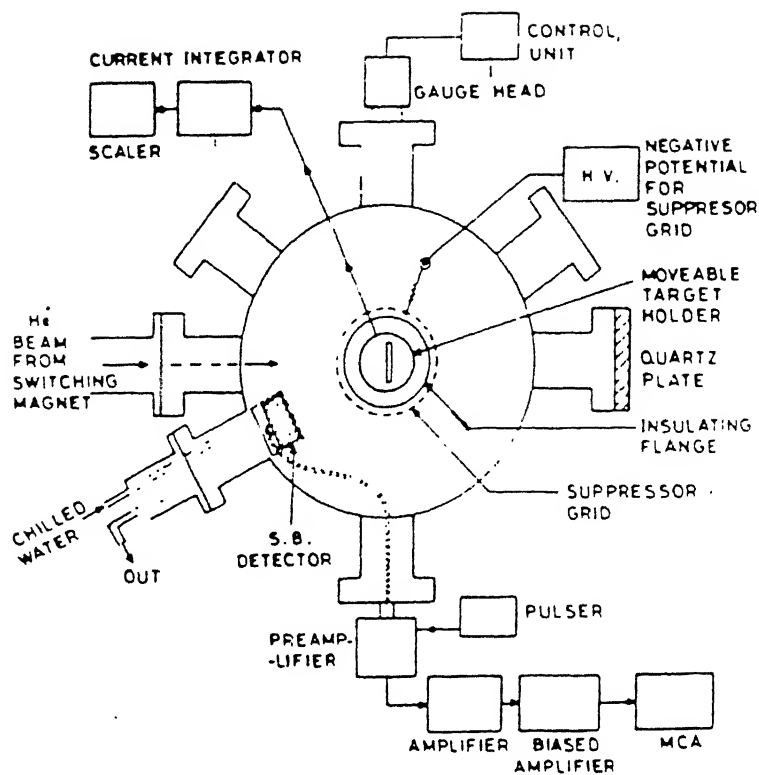


FIGURE 3.8 Block diagram of the RBS chamber.

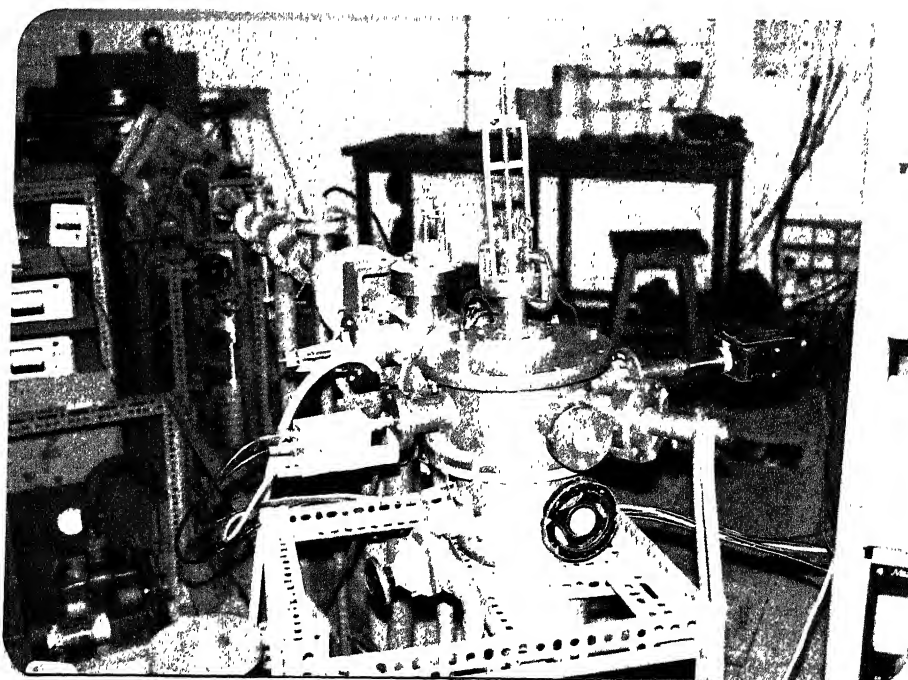


FIGURE 3.9 The RBS chamber and other accessories.

The CR-RC (differentiating-integrating) pulse shaping circuit of the amplifier operates with time constants much shorter than the decay of the preamplifier signal and much longer than its rise time. This effectively removes the slow component of the preamplifier signal preventing pile-up error. It also removes the low and high frequency signals and noise components which significantly enhance the signal-to-noise ratio. Hence the amplifier finally produces individual pulses whose amplitudes convey the quantity of interest, i.e., the energy of the detected particles. The signal output from the main amplifier is then fed to a biased amplifier [Ortec Model-444]. With the help of this, the amplifier signals are compressed or stretched and the edges cut-off as desired, for more efficient analysis in the multichannel analyzer (MCA).

The signals from the biased amplifier are then collected, either in the MCA [Model-ND65, Nuclear Data Inc.], or a PC-based MCA. The MCA has two distinct data analysis modes: the pulse height analysis (PHA) mode and the multichannel scaling (MCS) mode. The PHA mode is exclusively used for RBS measurements.

### 3.5 BACKSCATTERING SPECTRA ANALYSIS

A backscattering spectrum of Pd film evaporated on metallic glass  $\text{Fe}_{78}\text{B}_{13}\text{Si}_9$  is shown in Figure 3.10. This spectrum was obtained using  $\text{He}^+$  ions of 1.4 MeV at a scattering angle ( $\theta$ ) of  $150^\circ$ , the detector solid angle ( $\Omega$ ) equal to 2 milli-steradian and for a beam dose of  $5\mu\text{c}$ . This RBS parameter description is also given below the figure. It is useful to plot the backscattering yield by normalizing it with respect to some of the above mentioned parameters, by using the following equation:

$$\text{Normalized yield} = \frac{\text{raw counts} \times \text{corr}}{Q \times d\Omega \times \delta E} \quad (3.2)$$

where raw counts are the actual counts recorded; corr is the correction factor to compensate for inaccuracies during charge integration;  $Q$  is the beam dose in  $\mu\text{c}$ ;  $d\Omega$  is the solid angle in milli-steradian; and  $\delta E$  is the calibration factor

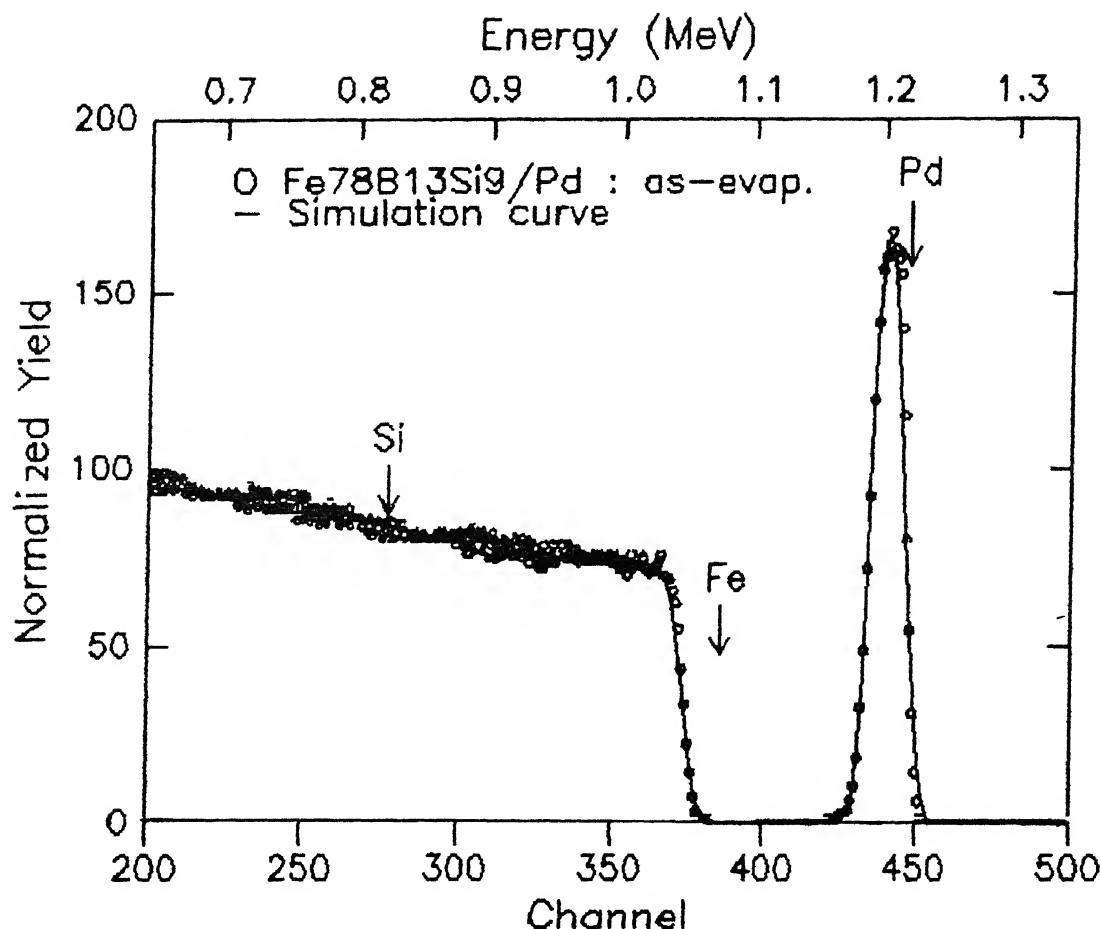


FIGURE 3.10 RBS spectrum of Pd on Fe<sub>78</sub>B<sub>13</sub>Si<sub>9</sub>.

Experimental parameters

Identifier: Fe<sub>78</sub>B<sub>13</sub>Si<sub>9</sub>(MG255)/Pd as-evaporated.  
 Beam: (type)4He<sup>+</sup> (energy)1.400 MeV (dose)5.00  $\mu$ Coul @ (current)8.0 nA  
 Geometry: IBM Theta: 0.0 Phi: 30.0 Psi: 0.0  
 MCA: (calibration factor)2.335 keV/ch. (zero channel energy)175.00  
 First ch.no: 1 NPT(total no. of channels): 512  
 Detector: FWHM(resolution): 14.0 keV Omega(solid angle): 2.000

Elemental surface positions

ele:	B	Si	Fe	Pd
mass	11	28	56	106
energy(MeV):	0.327	0.8195	1.071	1.217
channel:	69	276	384	446

Simulation layer structure

Thickness	Sublayers	Composition . . . .
1 175.00 Å	20.00 Å	Pd 1.000
2 6850.00 Å	auto	Fe 0.780 B 0.130 Si 0.090

of the MCA in keV/channel. The normalized yields are utilized as they are directly comparable between experimental spectra for which beam energy and scattering geometry are same but the dose solid angle and calibration values are different.

The information about the thickness of the film and the depth distribution of the diffusing element (in the case where diffusion has taken place) can be obtained from such a spectrum. The backscattering spectra in the present study have been analyzed as illustrated in the following sections.

### 3.5.1 Calibration of the MCA

The MCA is first calibrated by determining the calibration factor ( $\delta E$ ) of the MCA. For this reason, backscattering spectra of pure elements (or calibration samples) were taken in every run. In each run three to four metallic glass samples were analyzed along with the calibration samples. A set of calibration spectra obtained from the same run as that of the spectrum shown in Figure 3.10, are depicted in Figure 3.11 (a) to (c), for thin film of pure Au on pure Al substrate, pure Fe, and pure Zn, respectively. In these spectra, the position of the Au is peak at ch.no. (channel number) 490, that of the Fe edge is at ch. no. 393, and that of Zn edge at ch.no. 411. The backscattered energy  $E_{1,e}$  for each of these elements (e) is calculated from the following equation:

$$E_{1,e} = K_e \times E_0 \quad \text{keV} \quad (3.3)$$

where  $K_e$  is the kinematic factor of the element e and  $E_0$  is the incident energy of the  $\text{He}^+$  beam (in this case 1.4 MeV). The slope of the straight line drawn between the data points in the graph of ch.no. versus  $E_1^e$  for the three elements mentioned above gives  $\delta E$ , and in this case is equal to 2.335 keV/ch.. The calibration factor can also be calculated from the following equation;

$$\delta E = (K_1 - K_2)E_0 / (ch_1 - ch_2) \quad \text{keV/ch.} \quad (3.4)$$

considering two calibration samples ( $e_1$  and  $e_2$ ) at a time.

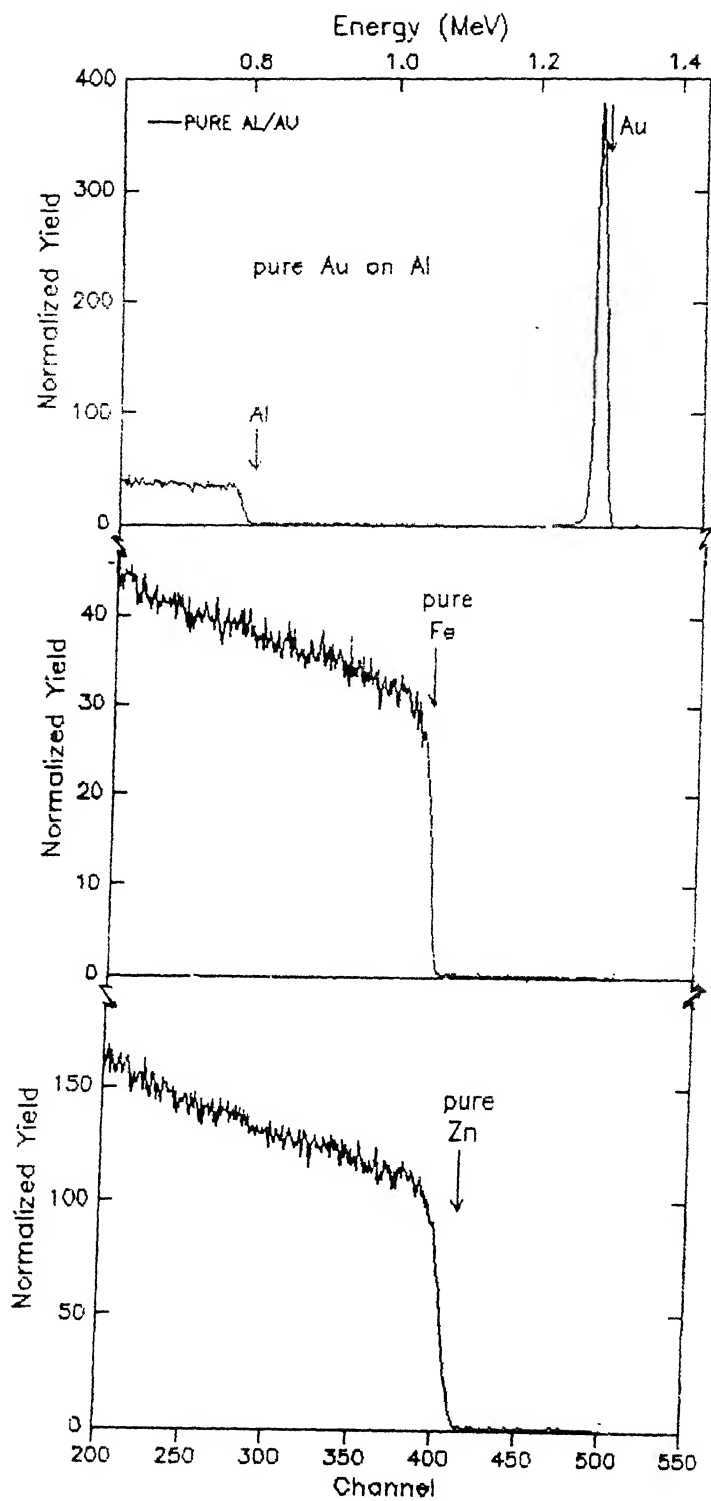


**FIGURE 3.11** RBS spectra of calibration samples: (a) thin film of Au on Al substrate, (b) Pure Fe, and (c) Pure Zn.

### 3.5.2 Analysis by hand calculation using the basic formulae

For the thickness calculation, the formula (Equation 2.32b) obtained earlier in section 2.1.5, can be used i.e.,

$$Nt = \left( A_1 Z_2^2 \delta E \right) / \left( H_2 Z_1^2 [S]_{2,2} \right)$$

where the various parameters have already been discussed in Chapter 2. For the spectrum reported in Figure 3.10, the values of the various parameters mentioned in the equation above, are:

$A_1 = A_{Pd} = 44409$  counts;  $Z_1 = Z_{Pd} = 46$ ;  $Z_2 = Z_{Fe} = 26$ ;  $H_2 = H_{Fe} = 1785$ ;  $\delta E = 2.335$  keV/ch.;  $[S]_{2,2} = [\epsilon]_{2,2} N_1$ ;  $N_1 = N_{Pd} = 6.76 \times 10^{22}$  atoms/cm<sup>3</sup>; and  $[\epsilon]_{2,2} = [\epsilon]_{Fe,Fe} = 161$  eV-cm<sup>2</sup>/10<sup>15</sup> atoms.

Using these values the calculated thickness of Pd film evaporated on the metallic glass Fe<sub>78</sub>B<sub>13</sub>Si<sub>9</sub> is 171 Å. The thickness of the Pd film obtained from simulation is 175 Å (as depicted in Figure 3.10), indicating an error of only 2.5% in the above calculation.

Likewise Equations 2.33 and 2.34 can be used to obtain the depth versus concentration profile of the Pd film, starting from the surface position (depth equal to 0) of the film or impurity.

### 3.5.3 Analysis by simulation

Recently, RBS simulation programs using computers have been developed at several places. One such simulation program developed at the Cornell University by Doolittle [1985 and 1986], has been used in the present studies for the analysis of the backscattering spectra. The simulation program makes use of almost the same equations which have been described in Chapter 2 and illustrated above to describe the hand-calculation method.

In simulation, a theoretical sample structure consisting of several layers of varying thickness is first prepared. The experimental parameters are also fed into the program. A back-scattering spectrum is then constructed using

this sample structure and the experimental parameters. This theoretical profile is then compared with the experimentally obtained RBS spectrum. This procedure is utilized in an iterative manner to arrive at a best set of parameters in the sample structure using which the given sample spectrum compares quite well with the experimental spectrum.

We will now illustrate the analysis of the RBS spectrum of Figure 3.10, by the simulation program. The theoretical layer structure of the sample is given below the figure. The first layer comprising of Pd is of thickness 175 Å and is further divided into sublayers of 20 Å each. The second layer is the substrate (metallic glass  $\text{Fe}_{78}\text{B}_{13}\text{Si}_9$ ) of thickness 6850 Å, which is further divided into sublayers of 500 Å each. The program requires these information along with the experimental parameters (as defined below Figure 3.10). The simulated profile is then compared (as shown in Figure 3.10), with the experimental profile. One of the important features of this simulation is that it is an extremely powerful tool for understanding complex spectra involving overlap of numerous elements. It also takes into account the detector resolution as well as energy straggling of the ions. Thus the thick target yield for metallic glasses has been simulated very correctly giving the analysis of the substrate as well. Such analysis of the multi-elemental target as mentioned above is not possible by hand calculations.

#### 3.5.4 Calculation of diffusion coefficient by simulation

We illustrate in this section the calculation of diffusion coefficients from the RBS spectrum by the simulation procedure. The RBS spectrum taken after annealing the as-evaporated sample  $\text{Fe}_{78}\text{B}_{13}\text{Si}_9/\text{Pd}$  (reported earlier in Figure 3.10), at 400°C for 8 hr is shown in Figure 3.12. The description of the experimental parameters used is given below the figure.

The diffusion of Pd in the metallic glass substrate is indicated by:

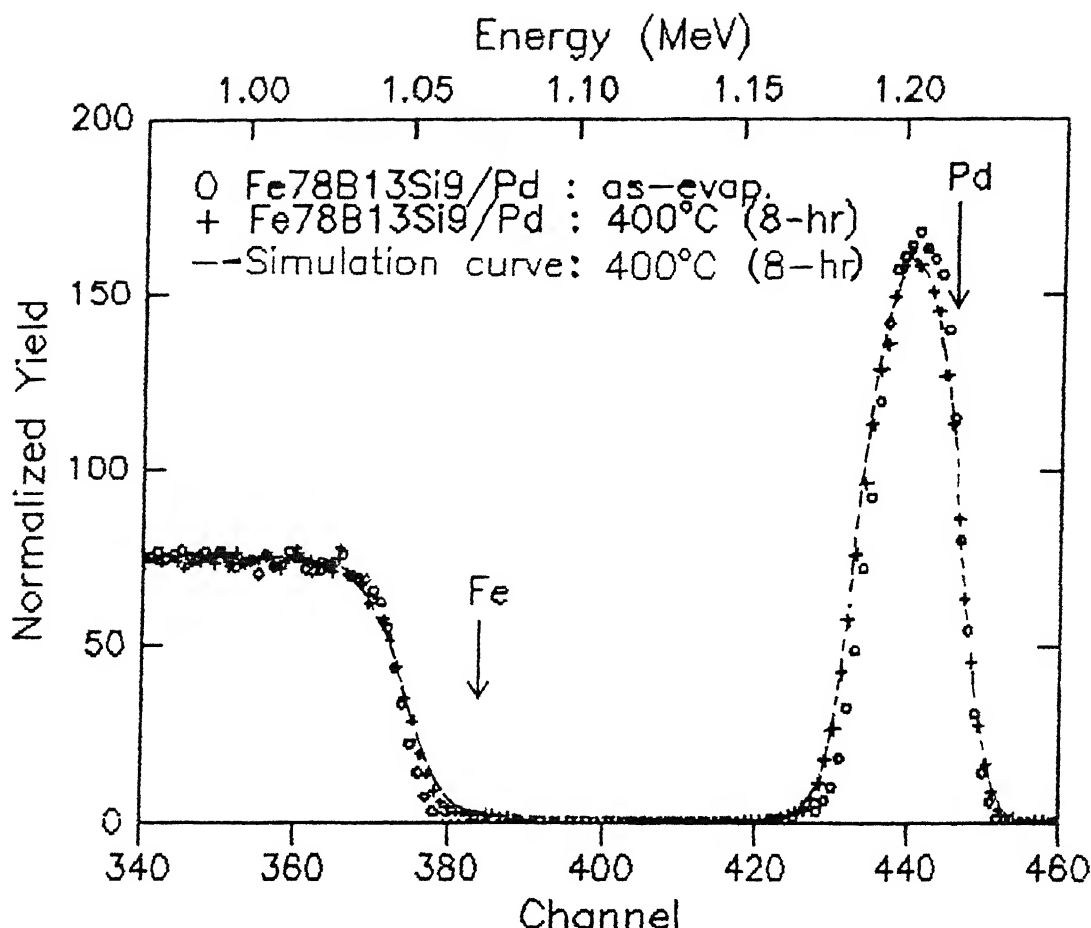


FIGURE 3.12 RBS spectrum of Pd on Fe<sub>78</sub>B<sub>13</sub>Si<sub>9</sub>, after annealing at 400°C for 8 hr.

Experimental parameters

Identifier: Fe<sub>78</sub>B<sub>13</sub>Si<sub>9</sub>(MG255)/Pd (400°C, 8-hr).  
 Beam: (type)4He+ (energy)1.400 MeV (dose)5.00  $\mu$ Coul @ (current)8.0 nA  
 Geometry: IBM Theta: 0.0 Phi: 30.0 Psi: 0.0  
 MCA: (calibration factor)2.363 keV/ch. (zero channel energy)147.00  
 First ch.no: 1 NPT(total no. of channels): 512  
 Detector: FWHM(resolution): 14.0 keV Omega(solid angle): 2.000

Elemental surface positions

ele:	B	Si	Fe	Pd
mass:	11	28	56	106
energy(MeV):	0.327	0.8195	1.071	1.217
channel:	6	285	391	453

Simulation layer structure

Layer No.	Thickness	Sublayers	Composition . . . .
1	150.00 Å	20.00 Å	Pd 100
2	600.00 Å	40.00 Å	Fe 78 B 13 Si 9
	diffusing species: Pd		diffusion equation: error function
	D-value: 0.500E-17		annealing time: 28800 s.
3	10000.00 Å	auto	Fe 78 B 13 Si 9



(i) appearance of Pd signals at lower energy region; (ii) decrease in the height of the Pd peak; and (iii) appearance of Fe counts at higher energies approaching the Fe edge. Now for the simulation of the diffused profile, along with the layer structure, the proper diffusion equation (thick-film, thin-film, etc.,) which define the concentration of the diffusing element is also given. The various diffusion equations have already been discussed in Chapter 1. For the present case, the diffusion equation defining the diffusion of a species into a thick layer from a source, which holds the surface at a fixed concentration, has been used and is defined below:

$$f(x) = p(1) * \text{erfc}(x/\sqrt{4Dt}) \quad (3.5)$$

where  $p(1)$  is the initial concentration of the diffusing species (in this case Pd) at the surface of the layer;  $D$  is the diffusion coefficient and  $t$  is the time for which annealing was done.

This equation is utilized in the simulation to calculate the concentration of diffusing species in each sublayer starting from the surface of the layer for which the equation is defined. The simulation layer structure and the diffusion equation are also illustrated below Figure 3.12. The results of the simulation, i.e., the simulated spectrum is shown in the figure by solid line. The visible comparison clearly indicates that the layer structure and the diffusion equation with the given  $D$  value, are the best set of parameters. In this way the  $D$  values have been obtained for the other spectra. Subsequently, all diffusion analyses in the present study were done by RBS simulation as described above.

### 3.6 ERRORS IN D-VALUES

In general the error in the determination of  $D$ -values arises due to error in the measurements of (i) annealing time ( $t$ ); (ii) annealing temperature ( $T$ ); and (iii) depth resolution ( $\delta x$ ).

During annealing the rise and fall of the sample temperature with annealing

Based on the  $T$ - $t$  plots, we concluded that

not more than 2% error occurred in the time measurements. This 2% error in the annealing time hardly made any observable change in the D-values during RBS simulations.

The measurement of annealing temperature  $T$  is an important factor in the accurate determination of  $D$ . Scatter in  $D$  is most often due to uncertainty in  $T$  [Mallard et al. 1963, Rothman et al. 1980]. Since  $D$  is dependant on temperature by the Arrhenius behaviour (Equation 1.15), an indirect estimate of error in  $D$  due to annealing temperature can be obtained. An error  $\Delta T$  in  $T$  causes a fractional error  $\Delta D$  in  $D$ , such that

$$\frac{\Delta D}{D} = \left( \frac{Q}{kT} \right) \frac{\Delta T}{T} \quad (3.6)$$

For  $Q=1$  eV,  $k=8.614 \times 10^{-5}$  eV/K, and  $T=700$  K, an error of 0.3% in  $T$  causes approximately, 5% error in  $D$ , and in our case the error in the measurement of the sample temperature never exceeded 0.3%.

In the present study the D-values were determined (in most of the cases) by simulation using Equation 3.5. In this equation the parameter  $x$  is the absolute distance from the surface of the diffusion couple considered, for diffusion to have occurred. Significant errors are unavoidably introduced in calibration of the x-axis of the RBS spectrum i.e., the channel number in terms of the absolute distance. These errors are quite high if the depth resolution is bad i.e., these are dependant on the depth resolution  $\delta x$ . The depth resolution is the ratio of the energy resolution and the energy-loss factor  $[S]$ , which itself is dependant on the stopping cross-section  $\epsilon$ .

In the simulation program,  $\epsilon$  is calculated for each element using a least squares fit of the Ziegler's data [Ziegler 1977]. The stopping cross-sections of  $\text{He}^+$  in the metallic glasses, is determined using the linear additivity of stopping cross-sections for a non-elemental material i.e., the Bragg's rule. Experimental values of stopping cross-sections are known to differ from predictions of this rule in various compound targets by upto 20% [Thwaites 1983]. Most

of the inaccuracy observed in the simulation program [Doolittle 1985], is due to the uncertainty of the stopping cross-sections. This is a long standing problem in RBS analysis and has yet to be solved completely. The energy resolution ( $\delta E$ ) is in a broad sense the sum of the energy straggling of the  $\text{He}^+$  ions in the diffusion couple, and the system resolution. These are further dependant on the detector resolution and the calibration factor of the MCA. RBS spectra were obtained for the calibration samples in each run of the data collection (comprising of three to four diffusion couple samples) and the calibration factor was determined. Also the Al edge of the Al/Au diffusion couple, used for calibration (see Figure 3.11(a)), gave an indication of the quality of the detector resolution in each run. In the present study, the energy resolution and straggling were quite small and therefore the depth resolution was also very good as is observed in the backscattering spectra given in Figure 3.11(a). Hence we assume that the error due to depth resolution is not more than 20% in the present study.

Some error also arises in fitting of the experimental spectra to the simulated ones obtained from the solution of the diffusion equation. But since the fittings (see Figure 3.10, 3.12 and Chap. 5) in our case was extremely good, this sort of error cannot be more than 5%.

Taking into account all the above mentioned facts we assume that the maximum error in the determination of the D-values by RBS is not more than 30%.

### 3.7 PREPARATION OF MOSSBAUER ABSORBERS

The metallic glasses studied by Mössbauer spectroscopy are  $\text{Fe}_{79}\text{B}_{16}\text{Si}_5$  and  $\text{Fe}_{78}\text{B}_{13}\text{Si}_9$ . Samples of these metallic glasses, of size of  $8 \times 10$  mm were placed in copper holders for easy handling and were used as Mössbauer absorbers. These absorbers were then annealed at various temperatures and timings as was done

for the RBS samples. Mössbauer spectra of these absorbers were taken before annealing and after each heat treatment. Before every run, the spectrum of  $\alpha$ -Fe foil (used as an absorber) was taken in order to calibrate the multichannel analyzer (MCA) as explained later.

### 3.8 THE MOSSBAUER SETUP

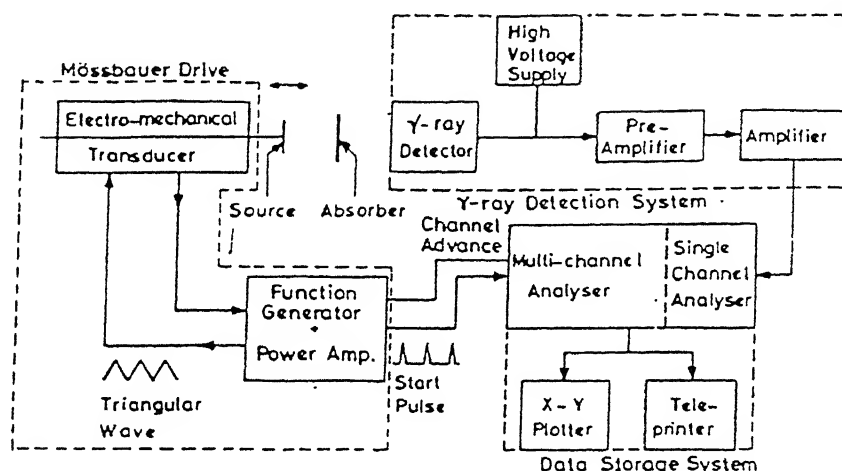


FIGURE 3.13 Schematic block diagram of the Mössbauer spectrometer

The Mössbauer spectrometer used in the present work is shown schematically in Figure 3.13. It can be broadly divided into four stages— (i) the radioactive source; (ii) the Mössbauer drive unit; (iii) the detection system; and (iv) the multichannel analyzer and spectrum storage. These are briefly described below.

#### 3.8.1 The radioactive source

The Mössbauer source used in the present study is radioactive  $^{57}\text{Co}$ , whose atoms are embedded or diffused in a Rh matrix, and it can emit gamma rays or photons of the appropriate energy (i.e., 14.4 keV) to observe Mössbauer effect in various samples containing Fe as one of its constituents. The source in this form had an initial activity of 25.5 mCi and had a recoil free fraction equal to 0.76. It was supplied by New England Nuclear Inc., USA.

### 3.8.2 Mössbauer drive

The Mössbauer drive system is a combination of units which provides measurable relative velocities between the source and the absorber, usually with a constant acceleration.

The Mössbauer drive system used by is based on the assembly supplied by WISSEL (Wissenschaftliche Elektronik GmbH), W.Germany. It consists of a velocity transducer, a function generator and a constant acceleration drive unit or power amplifier.

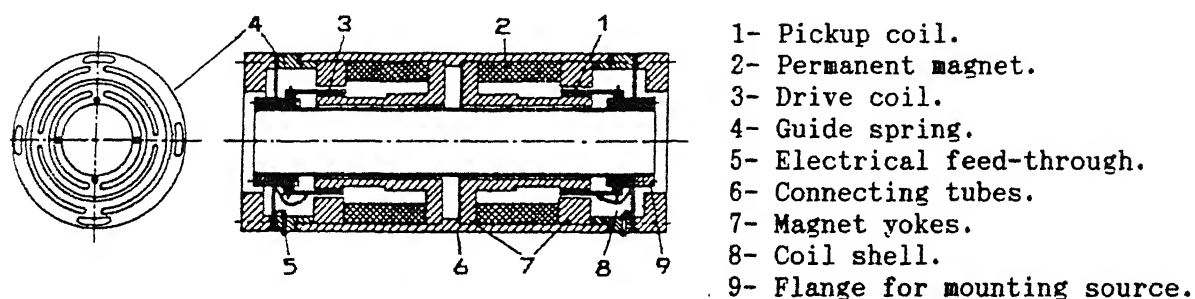


FIGURE 3.14 Schematic diagram of the velocity transducer.

The velocity transducer [model Wissel MA-260] (Figure 3.14), is based on the principle of two mechanically coupled transducers or loud speakers [Shenoy and Wagner 1978]. It consists of a pair of rigidly connected coils called the driving and pickup coils wound on the sample holder. The permanent magnet produces a homogeneous magnetic field in the air gap of the coil system, constant within a few parts in  $10^4$  along the axis of motion. This magnetic induction is approximately 0.25 Tesla.

The function generator [model Wissel DFG-1200] produces a triangular reference signal, which is fed to the power amplifier [model Wissel MR-360]. The output of the power amplifier which is proportional to the ideal velocity of the transducer is fed to the driving coil of the transducer. The actual velocity is sensed by the pickup coil in the form of a pick-up signal. The difference bet-

ween the reference signal and the pick-up signal is known as the difference or error signal. The error signal is proportional to the deviation of the actual velocity from its stipulated value. This error signal is then amplified and fed back to the driving coil through a feedback loop-amplifier to minimise the deviation from the ideal velocity.

The absorption and transmission of gamma rays through the absorber is measured in terms of the relative velocity between the source and absorber. Ranging between  $-v_{\max}$  to  $+v_{\max}$ , the source is swept in both directions by the velocity transducer which in turn receives a symmetric saw-tooth voltage waveform (reference signal) from the function generator.

### 3.8.3 The Detection System

The gamma rays transmitted through the absorber are detected and accumulated using the gamma-ray spectrometer and the MCA. The gas-filled proportional counter [Model I-1331, ECIL] used for detecting the 14.4 keV gamma rays, contains krypton as ionizing gas and has a beryllium window. A high voltage power supply [Model 456, EG&G] capable of supplying upto 3000V at 10 mA current is used to operate the proportional counter. The counter converts a gamma ray of certain energy to a linear charge pulse of a certain amplitude.

The preamplifier [Model 2006, Canberra] receives such a linear charge pulse and produces a gaussian voltage pulse equivalent to its amplitude. These pulses are amplified by a linear spectroscopy amplifier [Model 2021, Canberra] having an output pulse range of 0 to 10 volts. These analog pulses from the amplifier are then fed into the MCA which stores it in the form of a spectrum.

### 3.8.4 The multichannel analyzer: Data storage in the MCS mode

The multichannel analyzer (Model ND-65), initially used by us is manufactured by Nuclear Data Inc., USA. Later we made use of an ORTEC MCA card attached

to our PC. A MCA software program supplied by the same company was used in conjunction with the MCA card to record the Mössbauer spectrum.

Before recording the spectrum in the MCA it is necessary to ensure that the appropriate Mössbauer gamma ray (i.e., of energy 14.4 keV) is selected using the energy window of the MCA in the pulse height analysis (PHA) mode.

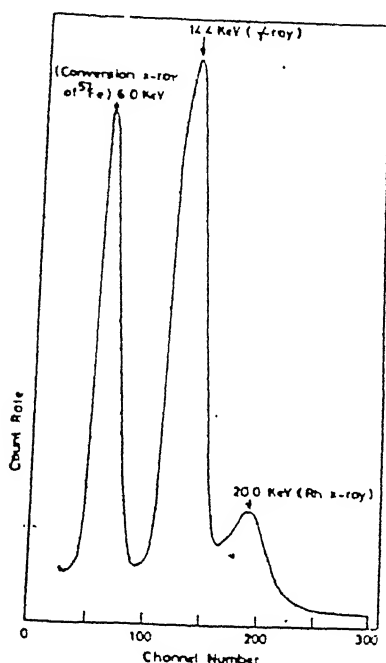


FIGURE 3.15 PHA spectrum of the radioactive source.

The MCA was used in this mode to obtain a pulse height spectrum of the radioactive decay of  $^{57}\text{Co}$  in Rh (Figure 3.15). The intensity of the low energy x-rays were reduced by using an aluminium foil between the source and the absorber. The upper level (ULD) and lower level (LLD) discriminators were adjusted such that gamma rays of energy 14.4 keV could only be stored in the MCA, hence increasing the signal-to-noise ratio.

The transmitted Mössbauer spectrum is finally stored in the 512 channels of the MCA in the MCS (multichannel scaling) mode. Synchronization of the channel number of the MCA with the increment in the relative velocity ( $\Delta v$ ) of the source was achieved by advancing the address of the MCA memory in steps, through an external clock. The reference signal mentioned above is divided into 512 pulses

by the external clock, where the first pulse coincides with the beginning of the reference signal. Each time the MCA receives such a pulse, the address of the memory is advanced to record the signal in the next channel, i.e., starting from channel one. The reference signal (saw-tooth shaped) fed to the transducer is of a symmetric nature, hence two identical Mössbauer spectra are recorded in the (as selected) 512 channels of the MCA.

### 3.9 EFFECT OF GEOMETRY

As mentioned earlier, the shape and the width of the Mössbauer spectrum gets affected by the position and design of the source, absorber and the detector. The two important geometrical effects influencing the Mössbauer spectrum are: (i) the source-to-detector distance variation effect; and (ii) the cosine effect.

#### 3.9.1 Distance variation effect

The counting rate of the detector or the number of gamma rays received per second, by the detector is directly proportional to the solid angle subtended by the source at the detector window; which in turn is proportional to the distance between the source and the detector. In our setup, as is usually done, the source moves about its mean position in accordance with the saw-tooth waveform signal given to the Mössbauer drive unit. Because of this periodic movement, the source to absorber distance, as well as the counting rate changes continuously and periodically. As result of this, the baseline of the Mössbauer spectrum shows a non-flat behaviour.

This type of geometrical effect can be eliminated by folding the two Mössbauer spectra observed in the MCA, as was done in our case. It can also be removed by keeping the source stationary while the absorber is vibrated. This effect is reduced to a large extent by keeping the frequency of the transducer to a minimum value ranging from 20 to 30 Hz.

---



### 3.9.2 Cosine effect

The finite size of the source, absorber, and the detector window gives rise to this effect. Because of the finite size of the detector window, the gamma rays enter it at an angle  $\theta$ , too. These rays will have a Doppler energy shift  $\Delta E$  equal to  $E_0(v/c)\cos\theta$ , and not  $E_0(v/c)$ . This results in the broadening of the Mössbauer spectral lines and a shift in the peak position. This effect was minimized in our experiments by: (i) collimating the gamma rays from the source along the direction of motion; and (ii) by optimizing the distance between the source and detector. If the source-detector distance is small,  $\theta$  increases and hence the lines are broadened. On the other hand, at large distances the cosine effect decreases but the count rate also decreases, hence a longer time is then required for recording the spectrum.

The velocity transducer, the source, the absorber, and the proportional counter coupled with the preamplifier are mounted and aligned on a vibration free optical bench. The selection of these units and their arrangement was such that the geometrical effects mentioned above are minimized. The position of these units, the distance between them, and the effective size of the source, absorber and detector window, influences the shape and intensity of the Mössbauer spectrum quite significantly.

## 3.10 CALIBRATION OF THE MCA

In our experiments we used natural iron ( $\alpha$ -Fe enriched in  $^{57}\text{Fe}$ ) and sodium nitroprusside (SNP) as standard absorbers to calibrate the Mössbauer spectrometer and MCA. These standard absorbers were obtained from Amersham International Ltd., Amersham, U.K. The Mössbauer spectra of the standard absorbers,  $\alpha$ -Fe (Figure 3.16) and SNP were obtained before every run and the positions of the various peaks in terms of the channel number were determined. The peak position of these absorbers in terms of velocity of the source (i.e.,

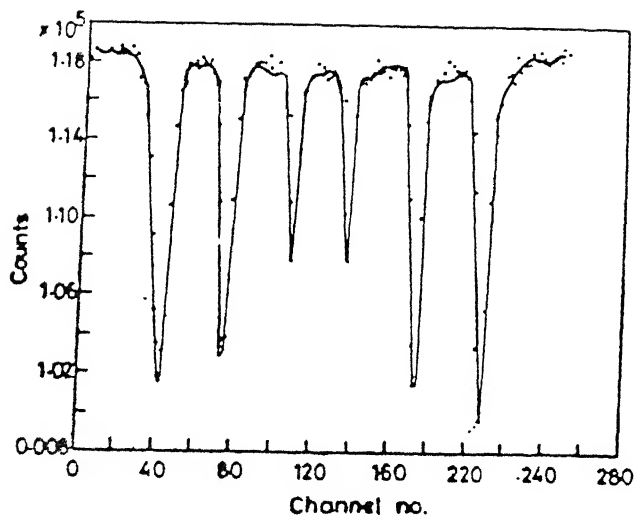
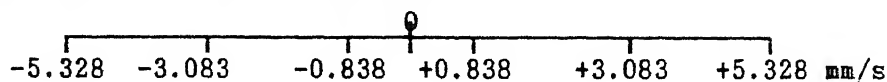


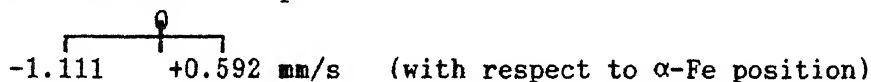
FIGURE 3.16 Mossbauer spectra of  $\alpha$ -Fe used for calibrating the MCA.

in mm/s) are known quantities from literature and given below:

(a)  $\alpha$ -Fe (natural Iron): a sextet—



(b) SNP (sodium-nitro-prusside): a doublet—



The various calibration parameters obtained in the present study from the computer analysis of the Mössbauer spectrum of  $\alpha$ -Fe foil used as a standard absorber are:

- (1) Centroid position:  $127.80 \pm 0.05$  channels.
- (2) FWHM of the inner lines:  $0.28 \pm 0.01$  mm/s.
- (3) Velocity/channel:  $0.097$  mm/s.

These calibration parameters were used by us for analyses of the Mössbauer spectra of the metallic glass samples.

### 3.11 ANALYSIS OF MOSSBAUER SPECTRA BY SIMULATION

Several computer programs are available for the analyses of the Mössbauer spectra in order to obtain precisely the various Mössbauer parameters, peak positions, line-widths, etc.,. The computer program used by us is based on the method developed by *Law and Bailey [1963]*. This program assumes the lines of

the transmission spectrum to be Lorentzian by considering the source and absorber to have a low effective layer thickness [Margulies and Ehrman 1961]. The main purpose of this simulation program is to find those values of the adjustable parameters (guess values), which provide a close agreement between the simulated and the experimental spectrum, using the given experimental parameters.

Using experimental data points  $Y_i$ , an assumed function  $\phi_i$  is obtained from the initially guessed parameters  $B_1 \dots B_k$  i.e.

$$Y_i \cong \phi_i \cong \phi_i (B_1 \dots B_k) \quad (3.7)$$

The sum of the squares of the difference between each of the observed and assumed data points is then determined i.e.,

$$S^2 \cong \sum_{i=1}^n S_i^2 \cong \sum_{i=1}^n (Y_i - \phi_i)^2 \quad (3.8)$$

Here  $n$  is the number of experimental data points. Considering the condition of the minimum value of the above function i.e.,

$$dS^2/dB_k = 0 \quad (3.9)$$

we get  $n$  simultaneous equations, which are solved to get the corrections  $\Delta B_k$  in the approximate value  $B_k$ . Consequently the new parameters  $B_k^{i+1} (=B_k^i + \Delta B_k)$  are then selected for the  $(i+1)^{th}$  iteration. The condition of minimum value (Equation 3.9) is determined after each iteration and this process is continued till a minimum specified value is achieved. The simulated curve thus obtained is then compared with the experimental spectrum and the goodness of the fit is tested by calculating the  $\chi^2$  values. In our analysis, the  $\chi^2$  values ranged from 0.9 to 5, indicating that the theoretical fittings were quite good. Hence the various parameters obtained from the simulation are truly those of the sample under study. The standard error in the fitted parameters  $B_k$ , were obtained from the calculations of the error matrix, using the inversion matrix method. The approximate errors obtained for the internal magnetic field ( $H_{int}$ ) was  $\pm 5$  kOe and that for the isomer shift (IS) and line-width ( $\Gamma$ ) it was  $\pm 0.1$  mm/s.

### 3.12 X-RAY MEASUREMENTS

The transformation from the amorphous to the crystalline state with heat-treatment in the metallic glasses  $\text{Fe}_{79}\text{B}_{16}\text{Si}_5$  and  $\text{Fe}_{78}\text{B}_{13}\text{Si}_9$  were also investigated by the X-ray diffraction (XRD) method to supplement the findings and analysis of Mössbauer spectroscopy.

The XRD measurements were done using a X-ray powder diffractometer [Model ISO-Debyeflex-1001], generating  $\text{Cr-K}\alpha$  radiation along with a graphite monochromator attached to the goniometer. A diffractometer in general consists of the following main units: (i) power supply; (ii) X-ray generator; (iii) goniometer, with monochromator, scintillation counter or proportional counter and preamplifier; (iv) amplifier unit; (v) ratemeter, and (vi) x-y chart recorder.

The spectral lines obtained in the X-ray spectra of the samples in units of  $2\theta$  is converted into d-values using the Bragg's rule i.e.,

$$2d\sin\theta = \lambda \quad \text{or} \quad d = \lambda/(2\sin\theta) \quad (3.10)$$

On comparing these values with standard tables of d-values of various alloys and phases available in literature, the presence of the suggested or probable phases are confirmed in the samples.

## CHAPTER 4

### MOSSBAUER SPECTROSCOPY AND X RAY DIFFRACTION STUDIES

#### 4.1 INTRODUCTION

We shall now describe the results of Mössbauer spectroscopic (TMS) and X-ray diffraction (XRD) studies of the amorphous metallic glasses  $\text{Fe}_{79}\text{B}_{16}\text{Si}_5$  and  $\text{Fe}_{78}\text{B}_{13}\text{Si}_9$ . It is well known that diffusion measurements require very long time-periods of heat-treatment below the crystallization temperature ( $T_x$ ). Upon annealing, the metallic glass undergoes relaxation, condensation, and finally crystallization. In order to study the diffusivity of the metallic glasses in the amorphous state, it is essential to determine the range of annealing period and temperature in which the amorphous structure is maintained. The necessity for TMS and XRD studies, therefore arose, in the present case. For this reason, the samples of these glasses were heat-treated at various temperatures ranging from above their  $T_x$ , to well below it, to identify the range of temperatures and annealing time-periods which retain the amorphous structure of these glasses.

These studies were also carried out to complement the information obtained by the RBS/diffusion studies of these samples. That is, the precipitation and identification of crystalline phases in these metallic glasses (after successive heat-treatment) have been studied. Generally the Mössbauer studies are performed on crystallized metallic glasses for investigating the kinetics of crystallization. However, room temperature (RT=295 K) Mössbauer measurements of metallic glasses annealed for a long time below the crystallization temperature are not reported in the literature for this or any other type of metallic glasses.

## 4.2 X-RAY ANALYSIS OF $\text{Fe}_{79}\text{B}_{16}\text{Si}_5$ AND $\text{Fe}_{78}\text{B}_{13}\text{Si}_9$

The X-ray diffraction patterns of the metallic glasses  $\text{Fe}_{79}\text{B}_{16}\text{Si}_5$  and  $\text{Fe}_{78}\text{B}_{13}\text{Si}_9$  samples (in the as-received form and after giving different heat treatment) are shown in Figures 4.1 and 4.2 respectively. The as-received samples, show a broad but shallow maxima, characteristic of amorphous alloys. Such spectra are seen in both the glasses upto an annealing temperature of  $400^\circ\text{C}$ , for an annealing time-period of 16 hr. At higher temperatures, high intensity peaks of various phases are observed indicating the increasing concentration of these phases in the amorphous matrix.

In the  $\text{Fe}_{79}\text{B}_{16}\text{Si}_5$  alloy, the first indication of precipitation of crystalline  $\alpha$ -Fe phase is seen after annealing for 4 hr at  $450^\circ\text{C}$ . The spectrum after annealing at  $475^\circ\text{C}$  for 8 hr shows well-defined peaks. The results of the analysis for this spectrum is given in Table 4.1. These results confirm the presence of  $\text{Fe}_3\text{B}$ ,  $\alpha$ -Fe, and  $\text{Fe}_2\text{B}$  phases (with the amount of  $\text{Fe}_3\text{B}$  being relatively small).

As seen in Figure 4.2, the  $\text{Fe}_{78}\text{B}_{13}\text{Si}_9$  alloy remains amorphous with heating upto  $450^\circ\text{C}$  for 16 hr. Small peaks of  $\alpha$ -Fe appeared at  $475^\circ\text{C}$  (1 hr). After 16 hr, at the same temperature, the well-established Bragg's peaks of  $\alpha$ -Fe (maybe similar to the solid solution  $\alpha$ -(Fe-Si) peaks as reported in literature),  $\text{Fe}_3\text{B}$  and  $\text{Fe}_2\text{B}$  phase were observed. The results are also shown in Table 4.1.

However the X-ray diffraction spectra do not appear to be sensitive to the presence of the Fe-Si phase, nor do they indicate the presence of  $\alpha$ -Fe,  $\text{Fe}_2\text{B}$ , and  $\text{Fe}_3\text{B}$  for samples heat-treated at  $450^\circ\text{C}$  (for time periods less than 16 hr) as sensitively as Mössbauer spectroscopy. This difference is ascribed to the different sensitivities of the two techniques with Mössbauer spectroscopy being a better microscopic probe.

These observations are quite consistent with those of *Ramanan and Fish* [1982], *Quivy et al.* [1985], and *Bang and Lee* [1991]. *Quivy et al.* have observed

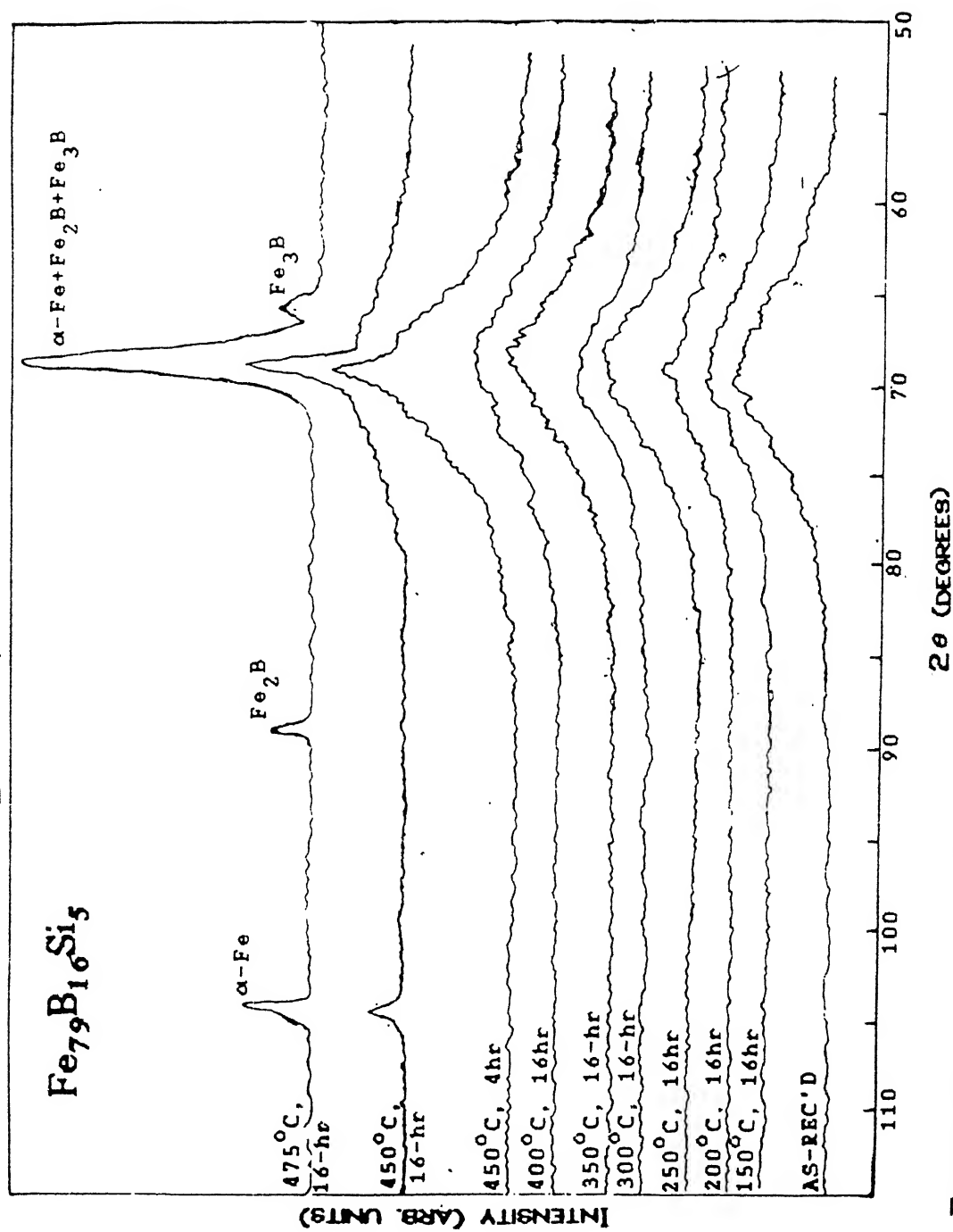


FIGURE 4.1 X-ray diffraction pattern (at RT) of  $\text{Fe}_{79}\text{B}_{16}\text{Si}_5$  heat-treated at various temperatures for 16 hr.

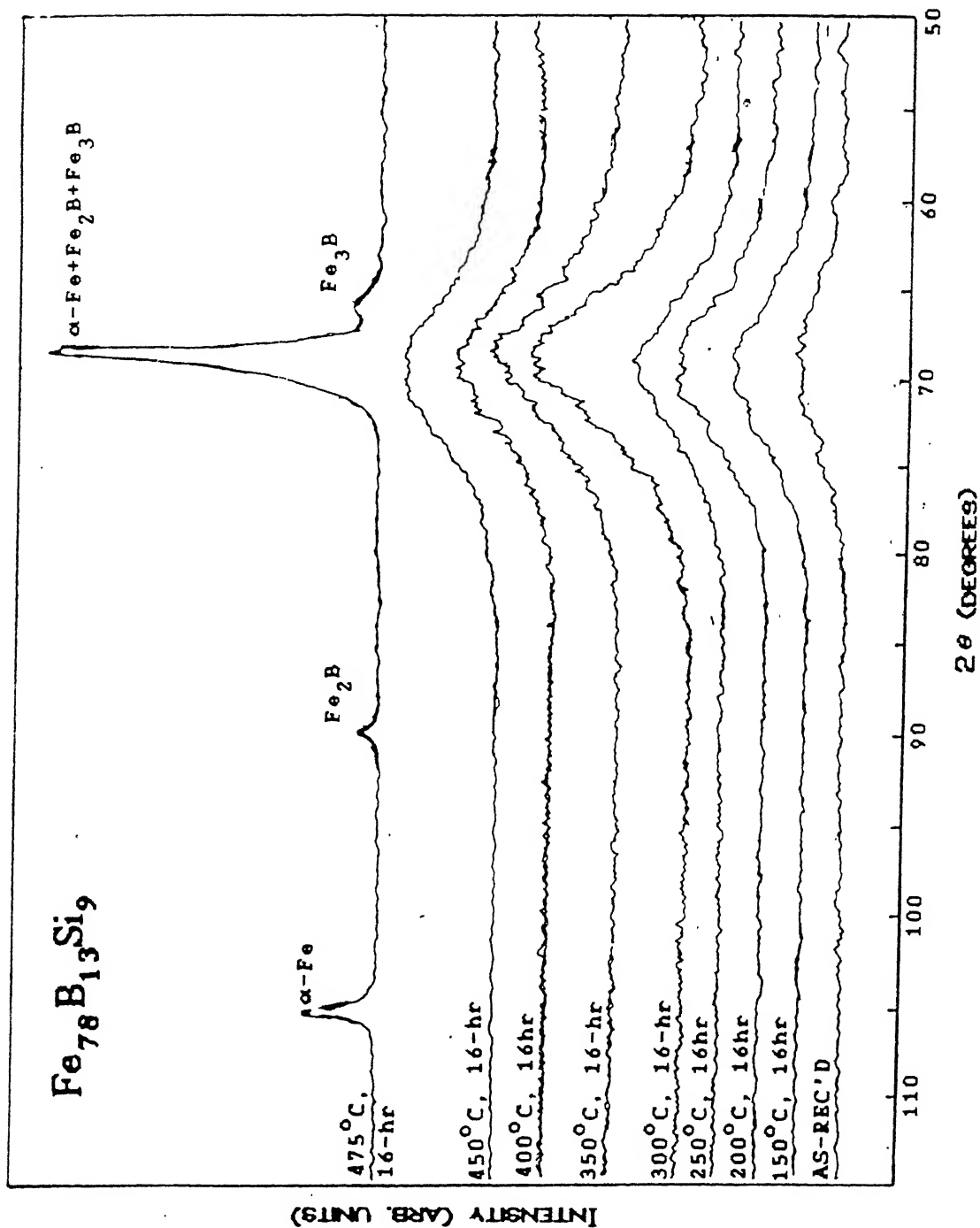


FIGURE 4.2 X-ray diffraction pattern (at RT) of  $\text{Fe}_{78}\text{B}_{13}\text{Si}_9$  heat-treated at various temperatures for 16 hr.



TABLE 4.1

X-RAY ANALYSIS OF SAMPLES HEAT-TREATED AT 475°C FOR 16 HR

$\text{Fe}_{79}\text{B}_{16}\text{Si}_5$				$\text{Fe}_{78}\text{B}_{13}\text{Si}_9$			
$2\theta$	$D_{\text{calc}}$	$D_{\text{std}}$	PHASE	$2\theta$	$D_{\text{calc}}$	$D_{\text{std}}$	PHASE
65.5	2.107	2.124	t- $\text{Fe}_2\text{B}$	65.4	2.110	2.124	t- $\text{Fe}_2\text{B}$
66.5	2.079	2.088	t- $\text{Fe}_3\text{B}$	66.5	2.079	2.088	t- $\text{Fe}_3\text{B}$
69.0	2.013	2.027	$\alpha$ -Fe	69.2	2.008	2.027	$\alpha$ -Fe
		2.028	t- $\text{Fe}_3\text{B}$			2.028	t- $\text{Fe}_3\text{B}$
		2.011	t- $\text{Fe}_2\text{B}$			2.011	t- $\text{Fe}_2\text{B}$
75.2	1.868	1.880	t- $\text{Fe}_3\text{B}$				
89.3	1.622	1.634	t- $\text{Fe}_2\text{B}$	89.5	1.619	1.634	t- $\text{Fe}_2\text{B}$
106.3	1.425	1.433	$\alpha$ -Fe	106.5	1.423	1.433	$\alpha$ -Fe

calc: d value calculated from observed data

std : standard d values of the phases, reported in literature.

$\alpha$ -Fe and  $\text{Fe}_3\text{B}$  in  $\text{Fe}_{79}\text{B}_{16}\text{Si}_5$  and  $\text{Fe}_{78}\text{B}_{13}\text{Si}_9$  metallic glasses after a heat-treatment of 30 min. at 475°C and 495°C respectively. *Bang and Lee*, on the other hand, have observed  $\alpha$ -(Fe,Si) and  $\text{Fe}_3\text{B}$  peaks in  $\text{Fe}_{78}\text{B}_{13}\text{Si}_9$  after annealing at 450°C for 30 minutes. *Meng and Wang [1986]*, have reported commencement of crystallization in  $\text{Fe}_{78}\text{B}_{13}\text{Si}_9$  after annealing at 460°C for 15 minutes. But our samples did not show any crystalline peaks even after annealing at 450°C below 4 hr. The first indication of crystalline peaks in our case was at 450°C (4 hr) for  $\text{Fe}_{79}\text{B}_{16}\text{Si}_5$  and 475°C (1 hr) for  $\text{Fe}_{78}\text{B}_{13}\text{Si}_9$ . However these results differ a lot from that of *Surinach et al. [1980]*, *Zaluska et al. [1983]* and *Nagarajan et al. [1988]*, who have reported the crystallization of  $\alpha$ -(Fe-Si) and  $\text{Fe}_2\text{B}$  only. The reason for this slightly different phase formation at different temperatures and time periods for the same alloy might be associated with the different manufacturing methods which may have slightly different quenching rates and hence different quenched-in nuclei in the amorphous structure.

*Bang and Lee [1991]*, observed a single  $\text{Fe}_3\text{B}$  line at  $2\theta$  equal to 46.2°, two  $\text{Fe}_2\text{B}$  lines at  $2\theta$  equal to 65.4° and 89.3°, and  $\alpha$ -(Fe-Si) lines at  $2\theta$  equal to

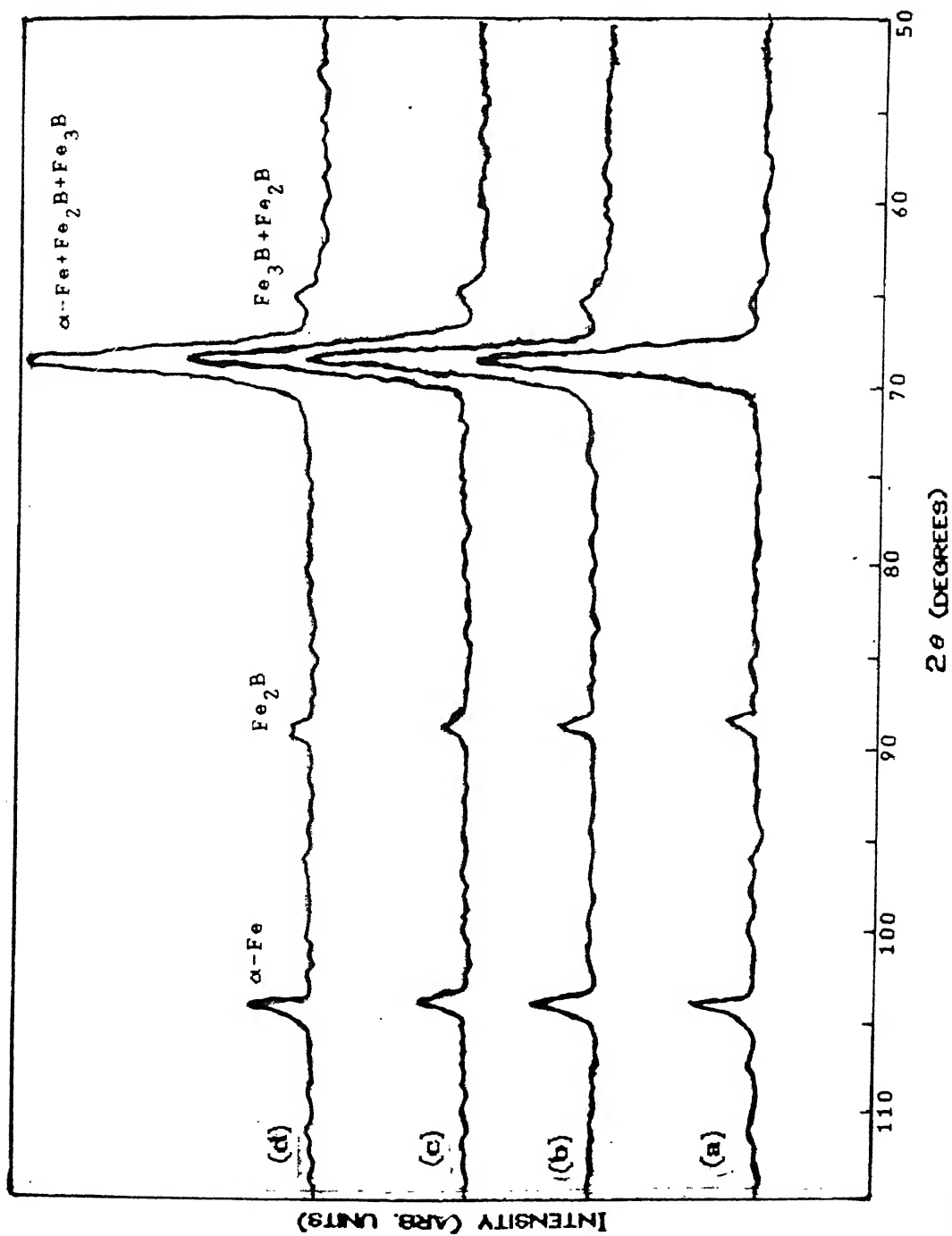


**FIGURE 4.3** X-ray diffraction pattern (at RT) of: (a)  $\text{Fe}_{78}\text{B}_{13}\text{Si}_9$ , 600°C (2 hr); (b)  $\text{Fe}_{78}\text{B}_{13}\text{Si}_9$ , 700°C (15 min); (c)  $\text{Fe}_{79}\text{B}_{16}\text{Si}_5$ , 600°C (2 hr); and (d)  $\text{Fe}_{79}\text{B}_{16}\text{Si}_5$ , 700°C (15 min)

$70^\circ$  and  $106^\circ$ . In our samples (see Table 4.1) the  $\text{Fe}_3\text{B}$  line was observed at  $66.5^\circ$ ,  $68.75^\circ$  and  $75^\circ$ , the  $\text{Fe}_2\text{B}$  lines at  $65.5^\circ$ ,  $69.45^\circ$  and  $89.3^\circ$ , and the  $\alpha\text{-Fe}$  (or  $\alpha\text{-(Fe-Si)}$ ) lines at  $68.7^\circ$  and  $106.3^\circ$ .

To complete the X-ray diffraction studies of crystallization and to monitor the conversion of  $\text{Fe}_3\text{B}$  phase into  $\text{Fe}_2\text{B}$  phase, we have studied these metallic glasses after heat-treatment at  $600^\circ\text{C}$  for 2 hr and at  $700^\circ\text{C}$  for 15 minutes. These temperatures are much above the reported crystallization temperatures, and the results are shown in Figure 4.3. It is evident from the figure that the intensity of the  $\text{Fe}_3\text{B}$  decreases and that of the  $\text{Fe}_2\text{B}$  peak increases as a function of time period of heat-treatment. However a complete conversion of  $\text{Fe}_3\text{B}$  to  $\text{Fe}_2\text{B}$  phase has not taken place for the highest temperature (i.e.,  $700^\circ\text{C}$ ) employed in these final X-ray studies.

### 4.3 MOSSBAUER ANALYSIS OF AS-RECEIVED SAMPLES

Mössbauer absorbers of the metallic glasses  $\text{Fe}_{79}\text{B}_{16}\text{Si}_5$  and  $\text{Fe}_{78}\text{B}_{13}\text{Si}_9$  were prepared using the procedure described in sec. 3.7, and the Mössbauer spectra were recorded (at RT) using a constant acceleration spectrometer as described in section 3.8.

Well-defined but broadened six-line Mössbauer spectra were observed for the Fe-B-Si as-received samples as shown in Figure 4.4. It is well known that there are a large number of structurally inequivalent Fe-sites present in the disordered atomic arrangements of these amorphous alloys [Sharon and Tsuei 1972, Tsuei and Lilienthal 1976, Chien and Hasegawa 1976] which give rise to a distribution of hyperfine interactions. This, in turn, has the effect of broadening the absorption lines in their Mössbauer spectra. On the other hand, in crystalline solids the hyperfine interactions are unique and hence the Mössbauer spectra consists of sharp peaks. Hence the broadened spectra observed in our samples are characteristic of amorphous solids.

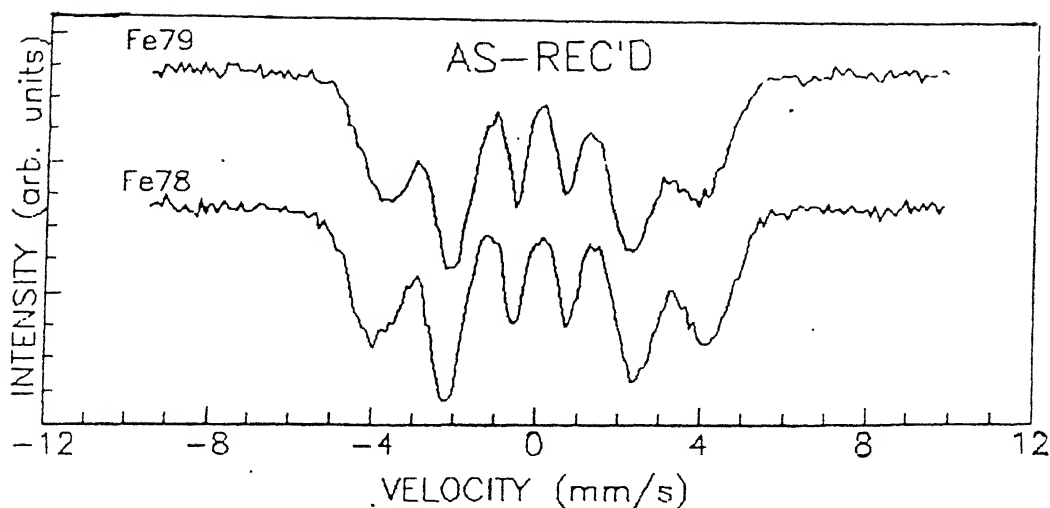


FIGURE 4.4 Mössbauer (RT) spectra of as-recieved metallic glasses  $\text{Fe}_{79}\text{B}_{16}\text{Si}_5$  and  $\text{Fe}_{78}\text{B}_{13}\text{Si}_9$ .

To obtain Mössbauer parameters, the observed Mössbauer spectra were analyzed with a computer program using Lorentzian shapes for the peaks. Mössbauer parameters obtained from such computer analysis for the as-received samples of  $\text{Fe}_{79}\text{B}_{16}\text{Si}_5$  and  $\text{Fe}_{78}\text{B}_{13}\text{Si}_9$  are given in Table 4.2 below. These results indicate that the isomer shift (IS) increases slightly from  $0.06 \pm 0.01$  to  $0.08 \pm 0.01$  mm/s, as the concentration of silicon increases (i.e., decreasing boron concentration) from 5at.% to 9at.%.

TABLE 4.2  
MÖSSBAUER PARAMETERS FOR THE AS-RECEIVED SAMPLES

METALLIC GLASS	Si(wt.%) in alloy	IS (mm/s)	H (kOe)	$\Gamma$ (FWHM) (mm/s)
$\text{Fe}_{79}\text{B}_{16}\text{Si}_5$	5	$0.06 \pm 0.01$	$235 \pm 5$	$1.12 \pm 0.01$
$\text{Fe}_{78}\text{B}_{13}\text{Si}_9$	9	$0.08 \pm 0.01$	$247 \pm 5$	$0.94 \pm 0.01$

A: Isomer shift measured with respect to  $\alpha$ -Fe.  
B: Internal Magnetic field at 57-Fe nucleus site.  
C: Line-width of the spectral lines.

Similar observations have been made by *Taniwaki and Maeda [1988]* in three types of Fe-B-Si metallic glasses and by *Singhal [1991]*, in  $\text{Fe}_{80}\text{B}_{20-x}\text{Si}_x$ . According to *Walker et al. [1961]*, the isomer shift increases with increasing 3d and decreasing 4s electron numbers, for  $^{57}\text{Fe}$  atoms in the absorber. In the present case, the replacement of B by Si, causes more electrons to fill the 3d-holes of Fe through the hybridation of the 3d-orbitals of Fe with s- and p-orbitals of the metalloid Si and these surplus 3d-electrons, in turn, shield more 4s-electrons thereby reducing the electron density at the nucleus.

We have also observed a slight increase in the internal magnetic field (H) from 235 kOe (for 5 atom%Si) to 247 kOe (for 9 atom%Si) with Si concentration. Similar increase in H values with increasing Si concentration have been reported previously [*Gonser et al. 1982, Taniwaki and Maeda 1988, Singhal et al. 1991*], and has been considered to occur due to the strain caused during the replacement of a small metalloid (boron) by a larger metalloid (silicon) atom in the interstitial site.

#### 4.4 MOSSBAUER ANALYSIS OF HEAT-TREATED SAMPLES OF $\text{Fe}_{79}\text{B}_{16}\text{Si}_5$

With an aim of studying the kinetics of crystallization in the metallic glass  $\text{Fe}_{79}\text{B}_{16}\text{Si}_5$ , the as-received samples were heated (annealed) at different temperatures in the range  $300^\circ\text{C}$  to  $475^\circ\text{C}$ , for different time periods ranging from 1 hr to 37 hr. The details of the heat-treatment schedule is described in Table 4.3. As mentioned earlier, these heat-treatment schedules correspond to those used in the RBS/diffusion studies (to be described in chapter V).

Mössbauer spectra of such heat-treated samples were recorded at RT and they are shown in Figure 4.5. Values of Mössbauer parameters obtained from the computer analysis of these spectra are listed in Table 4.3 along with the assignment of the precipitated phases deduced from the TMS and XRD studies.

**TABLE 4.3**  
**MÖSSBAUER PARAMETERS, OBTAINED FROM COMPUTER ANALYSIS FOR METALLIC**  
**GLASS  $\text{Fe}_{79}\text{B}_{16}\text{Si}_5$  AFTER VARIOUS HEAT TREATMENTS**

ANNEALING		IS	H	$\Gamma$	ASSIGNMENT	
TEMP(°C)	TIME(hr)	(mm/s)	(kOe)	(mm/s)	Mössbauer	X.R.D.
300	1	0.10	242	1.09	amorphous	amorphous
	4	0.03	243	1.21	amorphous	amorphous
	8	0.10	239	1.01	amorphous	amorphous
	16	0.10	240	1.04	amorphous	amorphous
350	1	0.01	237	1.00	amorphous	amorphous
	2	0.05	239	1.08	amorphous	amorphous
	4	0.05	238	1.00	amorphous	amorphous
	8	0.03	240	1.07	amorphous	amorphous
	16	0.01	239	1.04	amorphous	amorphous
400	1	0.02	240	1.05	amorphous	amorphous
	2	0.01	239	1.08	amorphous	amorphous
	4	0.02	239	1.05	amorphous	amorphous
	8	0.02	240	1.05	amorphous	amorphous
	16	0.01	239	1.07	amorphous	amorphous
450	1	0.01	242	1.17	amorphous	amorphous
	4	(1) 0.00	334	0.29	$\alpha$ -Fe	$\alpha$ -Fe
		(2) 0.03	331	0.49	Fe-Si (8nn)	N.O.
		(3) 0.08	311	0.39	Fe-Si (7nn)	N.O.
		(4) 0.02	288	0.39	Fe-Si (6nn)	N.O.
					t-Fe <sub>3</sub> B	
	(5)	0.07	268	0.49	t-Fe <sub>3</sub> B	N.O.
		0.09	247	0.43	Fe-Si (5nn)	N.O.
	(6)				Fe <sub>2</sub> B (avg)	N.O.
		0.11	229	0.40	t-Fe <sub>3</sub> B	N.O.
	(8)	0.08	200	0.49	Fe-Si (4nn)	N.O.
450	8	(1) 0.00	334	0.29	$\alpha$ -Fe	$\alpha$ -Fe
		(2) 0.03	331	0.51	Fe-Si (8nn)	N.O.
		(3) 0.08	311	0.39	Fe-Si (7nn)	N.O.
		(4) 0.02	288	0.39	Fe-Si (6nn)	N.O.
					t-Fe <sub>3</sub> B	N.O.
	(5)	0.07	268	0.49	t-Fe <sub>3</sub> B	N.O.
		0.09	247	0.39	Fe-Si (5nn)	N.O.
	(6)				Fe <sub>2</sub> B (avg.)	N.O.
		0.11	229	0.39	t-Fe <sub>3</sub> B	N.O.
	(8)	0.08	200	0.49	Fe-Si (4nn)	N.O.

A, B, C, D : are defined below:

- A = Isomer Shift measured with respect to  $\alpha$ -Fe: typical error  $\pm 0.01$   
 B = Internal Magnetic Field at 57-Fe nuclues : typical error  $\pm 5.00$   
 C = Width of the spectral line : typical error  $\pm 0.01$   
 D : N.O. = Not Observed

## MÖSSBAUER PARAMETERS, OBTAINED FROM COMPUTER ANALYSIS FOR METALLIC

GLASS  $\text{Fe}_{79}\text{B}_{16}\text{Si}_5$  AFTER VARIOUS HEAT TREATMENTS (contd.)

ANNEALING		IS (mm/s)	H (kOe)	$\Gamma$ (mm/s)	ASSIGNMENT	
TEMP(°C)	TIME(hr)				Mössbauer	X.R.D.
450	16	(1) 0.00	334	0.29	$\alpha$ -Fe	$\alpha$ -Fe
		(2) 0.03	331	0.43	Fe-Si (8nn)	N.O.
		(3) 0.06	313	0.43	Fe-Si (7nn)	N.O.
		(4) 0.18	283	0.45	{ Fe-Si (6nn)	N.O.
				t-Fe <sub>3</sub> B	N.O.	
		(5) 0.07	268	0.39	t-Fe <sub>3</sub> B	N.O.
		(6) 0.24	238	0.39	{ Fe-Si (5nn)	N.O.
				Fe <sub>2</sub> B (avg.)	N.O.	
	(7) 0.11	229	0.39	Fe <sub>3</sub> B	N.O.	
	(8) 0.18	200	0.39	Fe-Si (4nn)	N.O.	
450	29	(1) 0.00	334	0.29	$\alpha$ -Fe	$\alpha$ -Fe
		(2) 0.03	331	0.43	Fe-Si (8nn)	N.O.
		(3) 0.06	313	0.43	Fe-Si (7nn)	N.O.
		(4) 0.18	283	0.45	{ Fe-Si (6nn)	N.O.
				t-Fe <sub>3</sub> B	Fe <sub>3</sub> B	
		(5) 0.07	268	0.39	Fe <sub>3</sub> B	Fe <sub>3</sub> B
		(6) 0.24	238	0.39	{ Fe-Si (5nn)	N.O.
				Fe <sub>2</sub> B (avg.)	Fe <sub>2</sub> B	
	(7) 0.11	229	0.39	t-Fe <sub>3</sub> B	Fe <sub>3</sub> B	
	(8) 0.18	200	0.39	Fe-Si (4nn)	N.O.	
450	37	(1) 0.02	334	0.29	$\alpha$ -Fe	$\alpha$ -Fe
		(2) 0.03	331	0.41	Fe-Si (8nn)	N.O.
		(3) 0.06	313	0.41	Fe-Si (7nn)	N.O.
		(4) 0.18	283	0.39	{ Fe-Si (6nn)	N.O.
				t-Fe <sub>3</sub> B	Fe <sub>3</sub> B	
		(5) 0.07	268	0.39	t-Fe <sub>3</sub> B	Fe <sub>3</sub> B
		(6) 0.24	238	0.39	{ Fe-Si (5nn)	N.O.
				Fe <sub>2</sub> B (avg.)	Fe <sub>2</sub> B	
	(7) 0.11	229	0.39	t-Fe <sub>3</sub> B	Fe <sub>3</sub> B	
	(8) 0.18	200	0.39	Fe-Si (4nn)	N.O.	
475	1	(1) 0.14	334	0.29	$\alpha$ -Fe	$\alpha$ -Fe
		(2) 0.03	327	0.39	Fe-Si (8nn)	N.O.
		(3) 0.12	311	0.39	Fe-Si (7nn)	N.O.
		(4) 0.11	288	0.39	{ Fe-Si (6nn)	N.O.
				t-Fe <sub>3</sub> B	Fe <sub>3</sub> B	
		(5) 0.07	266	0.43	t-Fe <sub>3</sub> B	Fe <sub>3</sub> B
		(6) 0.08	242	0.43	{ Fe-Si (5nn)	N.O.
				Fe <sub>2</sub> B (avg.)	Fe <sub>2</sub> B	
	(7) 0.14	226	0.39	t-Fe <sub>3</sub> B	Fe <sub>3</sub> B	
	(8) 0.21	196	0.39	Fe-Si (4nn)	N.O.	

A, B, C, D : as defined in beginning of table.

MÖSSBAUER PARAMETERS, OBTAINED FROM COMPUTER ANALYSIS FOR METALLIC  
GLASS  $\text{Fe}_{79}\text{B}_{16}\text{Si}_5$  AFTER VARIOUS HEAT TREATMENTS (contd.)

ANNEALING TEMP(°C)	TIME(hr)	IS (mm/s)	H (kOe)	$\Gamma$ (mm/s)	ASSIGNMENT	
					Mössbauer	X.B.D.
475	2	(1) 0.07	331	0.30	$\alpha$ -Fe	$\alpha$ -Fe
		(2) 0.11	327	0.48	Fe-Si (8nn)	N.O.
		(3) 0.14	310	0.33	Fe-Si (7nn)	N.O.
		(4) 0.21	286	0.30	{ Fe-Si (6nn)	N.O.
						Fe <sub>3</sub> B
		(5) 0.27	269	0.54	t-Fe <sub>3</sub> B	Fe <sub>3</sub> B
		(6) 0.16	239	0.42	{ Fe-Si (5nn)	N.O.
						Fe <sub>2</sub> B
475	4	(1)-0.02	334	0.30	$\alpha$ -Fe	$\alpha$ -Fe
		(2) 0.08	327	0.40	Fe-Si (8nn)	N.O.
		(3) 0.04	311	0.40	Fe-Si (7nn)	N.O.
		(4) 0.08	288	0.40	{ Fe-Si (6nn)	N.O.
						Fe <sub>3</sub> B
		(5) 0.01	269	0.40	t-Fe <sub>3</sub> B	Fe <sub>3</sub> B
		(6) 0.14	239	0.40	{ Fe-Si (5nn)	N.O.
						Fe <sub>2</sub> B
475	6	(1)-0.03	335	0.38	$\alpha$ -Fe	$\alpha$ -Fe
		(2) 0.10	329	0.40	Fe-Si (8nn)	N.O.
		(3) 0.03	311	0.32	Fe-Si (7nn)	N.O.
		(4) 0.15	290	0.48	{ Fe-Si (6nn)	N.O.
						Fe <sub>3</sub> B
		(5)-0.02	263	0.40	t-Fe <sub>3</sub> B	Fe <sub>3</sub> B
		(6) 0.10	235	0.32	{ Fe-Si (5nn)	N.O.
						Fe <sub>2</sub> B
475	8	(1) 0.08	334	0.29	$\alpha$ -Fe	$\alpha$ -Fe
		(2) 0.10	329	0.31	Fe-Si (8nn)	N.O.
		(3) 0.13	313	0.41	Fe-Si (7nn)	N.O.
		(4) 0.24	286	0.34	{ Fe-Si (6nn)	N.O.
						Fe <sub>3</sub> B
		(5) 0.25	265	0.30	t-Fe <sub>3</sub> B	Fe <sub>3</sub> B
		(6) 0.20	238	0.31	{ Fe-Si (5nn)	N.O.
						Fe <sub>2</sub> B
475		(7) 0.13	227	0.30	t-Fe <sub>3</sub> B	Fe <sub>3</sub> B
		(8) 0.26	202	0.49	Fe-Si (4nn)	N.O.

A, B, C, D : as defined in beginning of table.



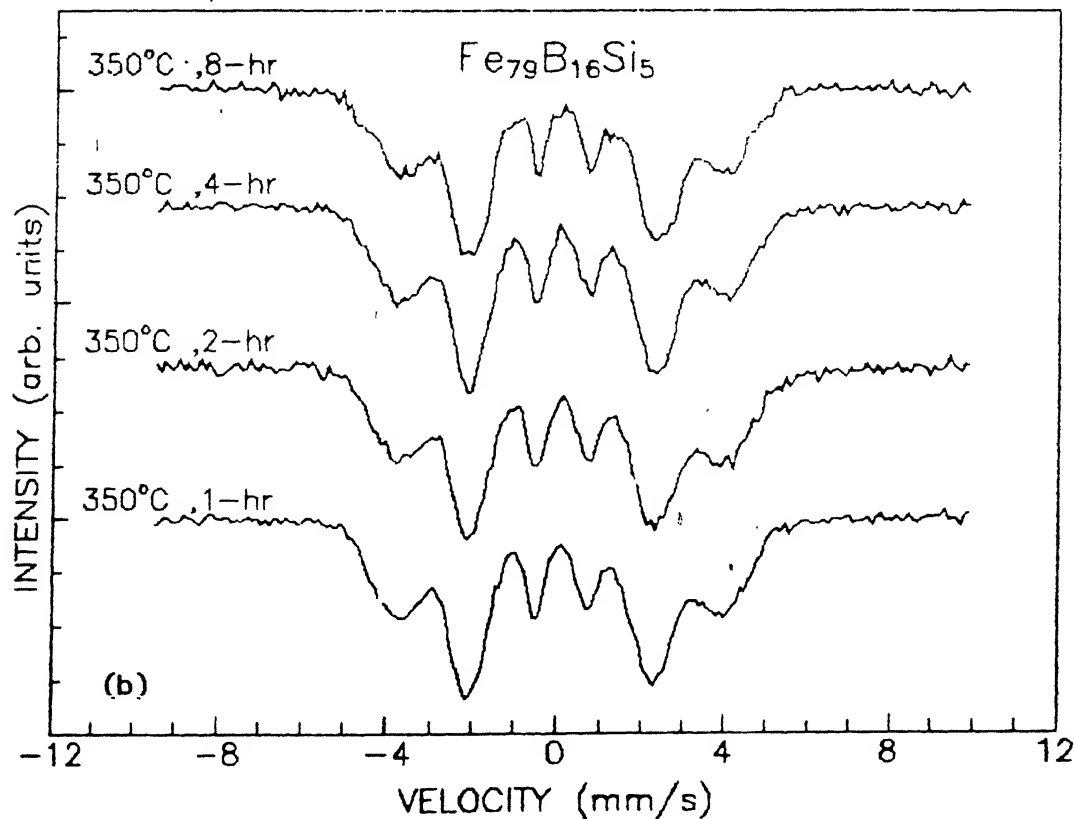
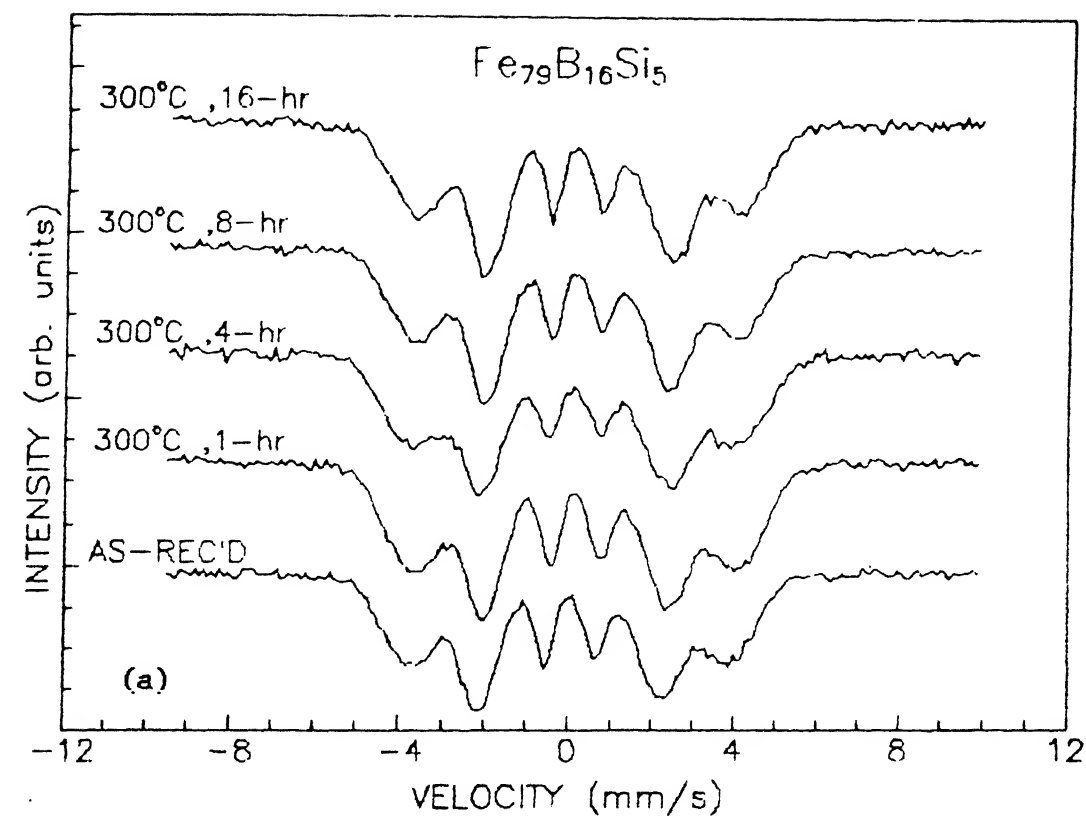


**FIGURE 4.5** Mössbauer (RT) spectra of  $\text{Fe}_{79}\text{B}_{16}\text{Si}_5$ .  
 (a) heat-treated at  $300^\circ\text{C}$  for various time periods.  
 (b) heat-treated at  $350^\circ\text{C}$  for various time periods.

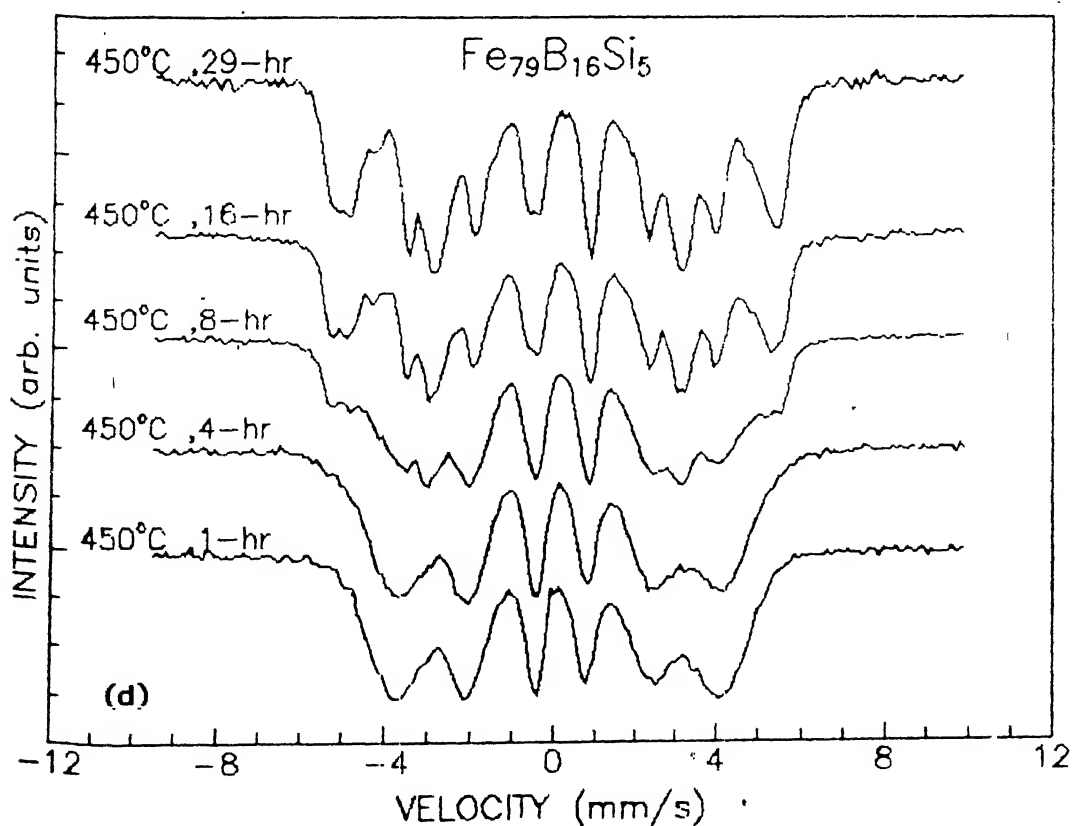
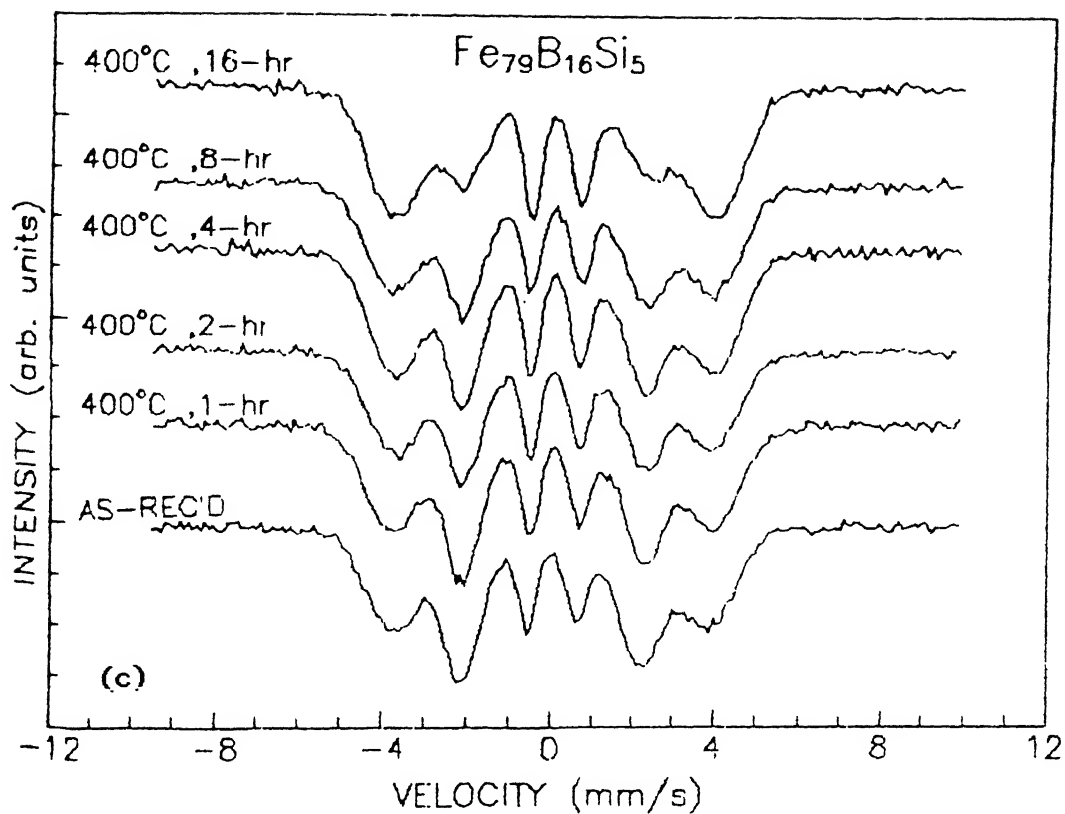


**FIGURE 4.5** Mössbauer (RT) spectra of  $\text{Fe}_{79}\text{B}_{16}\text{Si}_5$ .  
 (c) heat-treated at  $400^\circ\text{C}$  for various time periods.  
 (d) heat-treated at  $450^\circ\text{C}$  for various time periods.

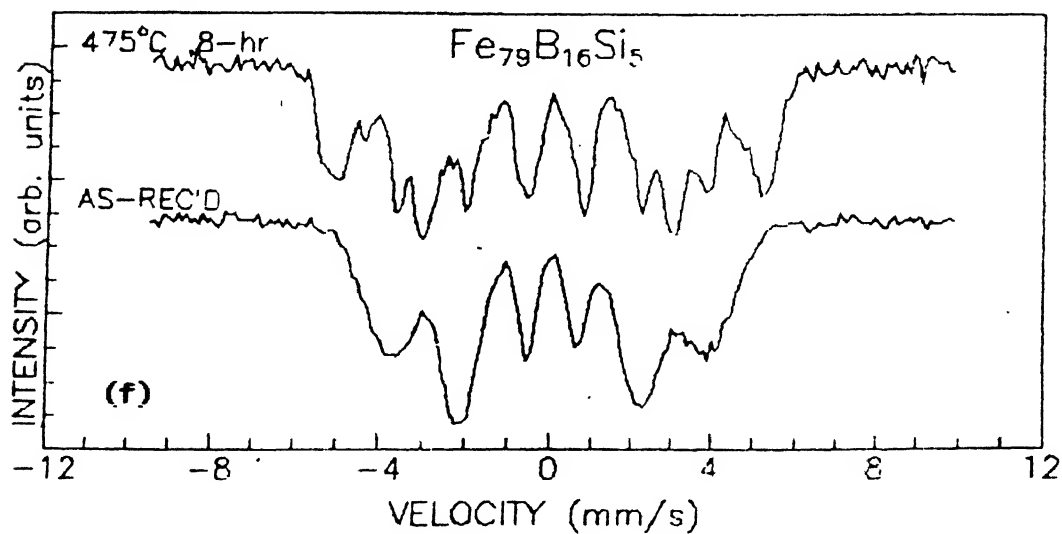
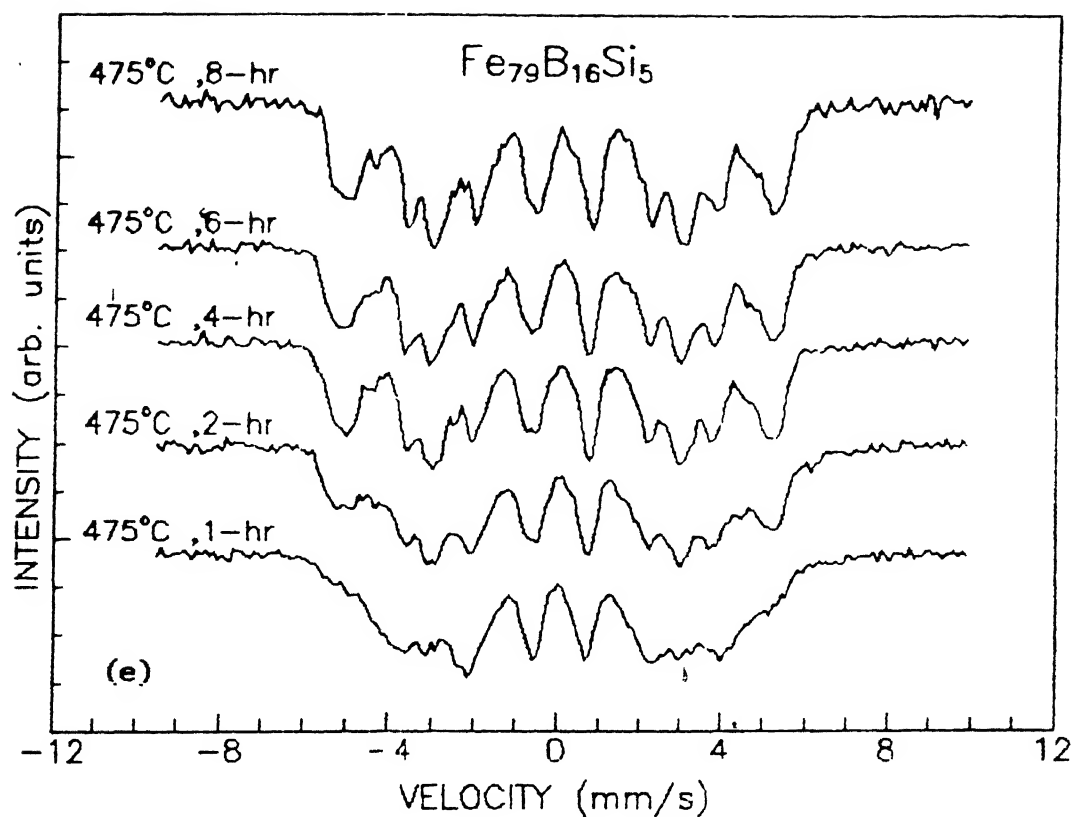


FIGURE 4.5 Mössbauer (ET) spectra of  $\text{Fe}_{79}\text{B}_{16}\text{Si}_5$ .

(e) heat-treated at 475°C for various time periods.

(f) comparison of as-recieved and 475°C (8 hr) spectra.

Results shown in Figure 4.5 indicate that samples heat-treated at (i) 300°C for 1, 4, 8, and 16 hr, (ii) 350°C for 1, 2, 4, and 8 hr, and (iii) 400°C for 1, 4, and 8 hr, show Mössbauer spectra which are similar in shape with the six-finger pattern (with broad lines) shown by the as-received sample. This behaviour suggests that the samples of  $\text{Fe}_{79}\text{B}_{16}\text{Si}_5$  heat-treated at these temperatures (for the time period mentioned) are still amorphous in nature. This conclusion is also supported by the X-ray diffraction studies. Heat treatment given at 400°C for 16 hr appears to usher changes in the nature of the Mössbauer spectrum and these changes (Figure 4.5) appear to develop quickly as the sample is heat-treated at 450°C for 1, 4, 8, and 16 hr. The broad six-finger pattern of Mössbauer spectrum changes into a more complicated spectrum composed of several lines, and this behaviour indicates the onset of crystallization process in this metallic glass. By the time the sample is heat-treated for 2 hr at 475°C, the crystallization process appears to have advanced and is perhaps more stable for the heat-treatment at 475°C at 8 hr (Figure 4.5).

In order to identify the phases precipitated, one has to examine the Mössbauer parameters obtained by computer analysis. The results of the computer analysis for samples heat-treated at 450°C (4 hr), 450°C (16 hr), 475°C (1 hr), 475°C (8hr) and 450°C (37 hr), shown in Figures 4.6 to 4.10 respectively, bring out the complicated nature of the computer analysis.

The values of the Mössbauer parameters obtained for these subspectra (Figures 4.6 to 4.10) are already shown in Table 4.3. These values indicate that  $\text{Fe}_3\text{B}$  is formed in the tetragonal phase at three Fe-sites, while only an average value of H (of the two Fe-sites) is observed for  $\text{Fe}_2\text{B}$ . Actually *Takacs et al.* [1975], have obtained H values corresponding to two Fe-sites in  $\text{Fe}_2\text{B}$ , which are very close i.e., 242 and 231.7 kOe. In our case this could not be restored, most probably due to the presence of the amorphous phase. The atomic percent of Si in Fe-Si solid solution appears to have been formed at 8, 7, 6, 5 and 4 nearest

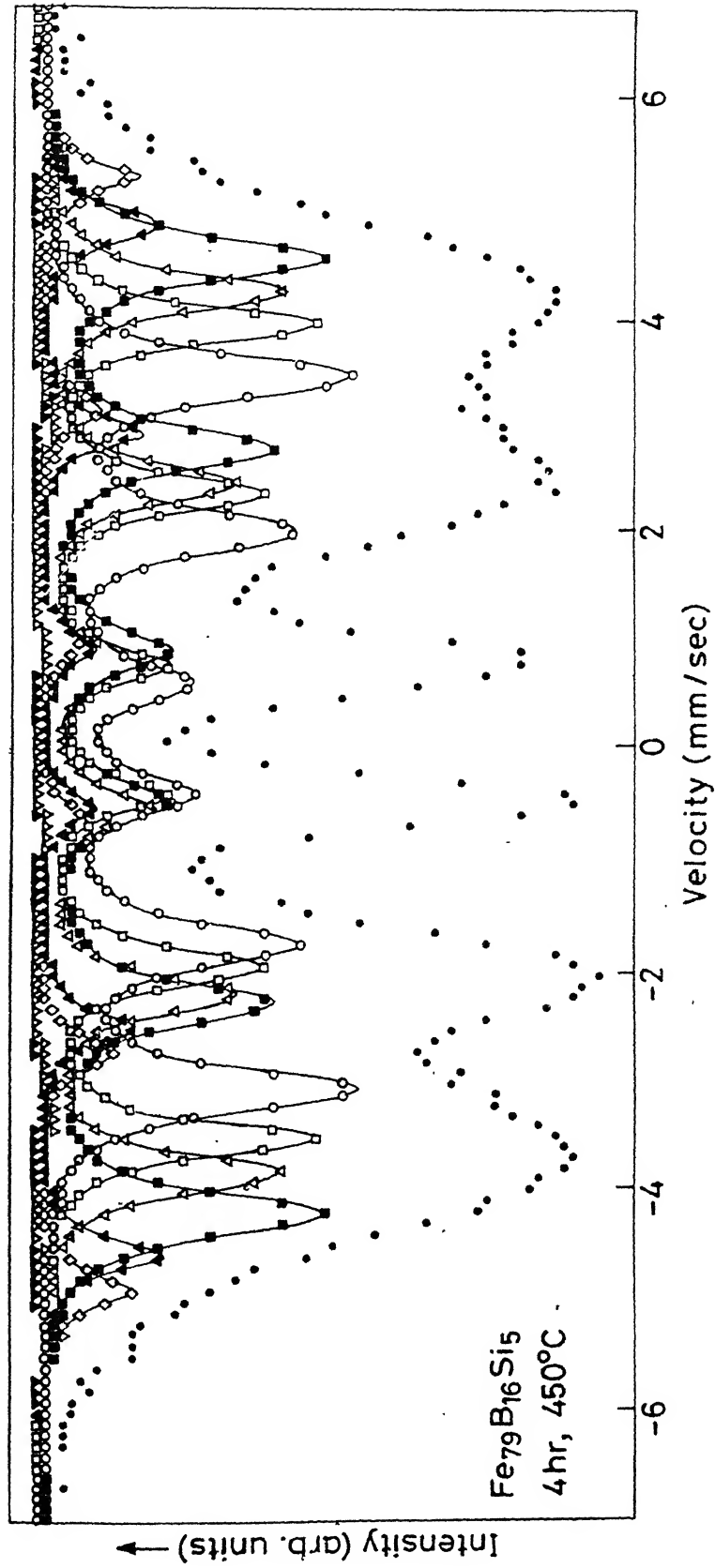


**FIGURE 4.6** Analyzed (RT) Mössbauer spectrum of heat-treated sample indicating the various phases precipitated. The symbols refer to the phases as mentioned below.

$\blacktriangledown$  -  $\alpha$ -Fe,  $\nabla$  - Fe-Si(8nn),  $\diamond$  - Fe-Si(7nn),  $\blacktriangle$  - Fe-Si(6nn) + t-Fe<sub>3</sub>B,  $\blacksquare$  - t-Fe<sub>3</sub>B,  $\triangle$  - Fe-Si(5nn) + t-Fe<sub>2</sub>B(avg),  $\square$  - t-Fe<sub>3</sub>B,  $\circ$  - Fe-Si(4nn).

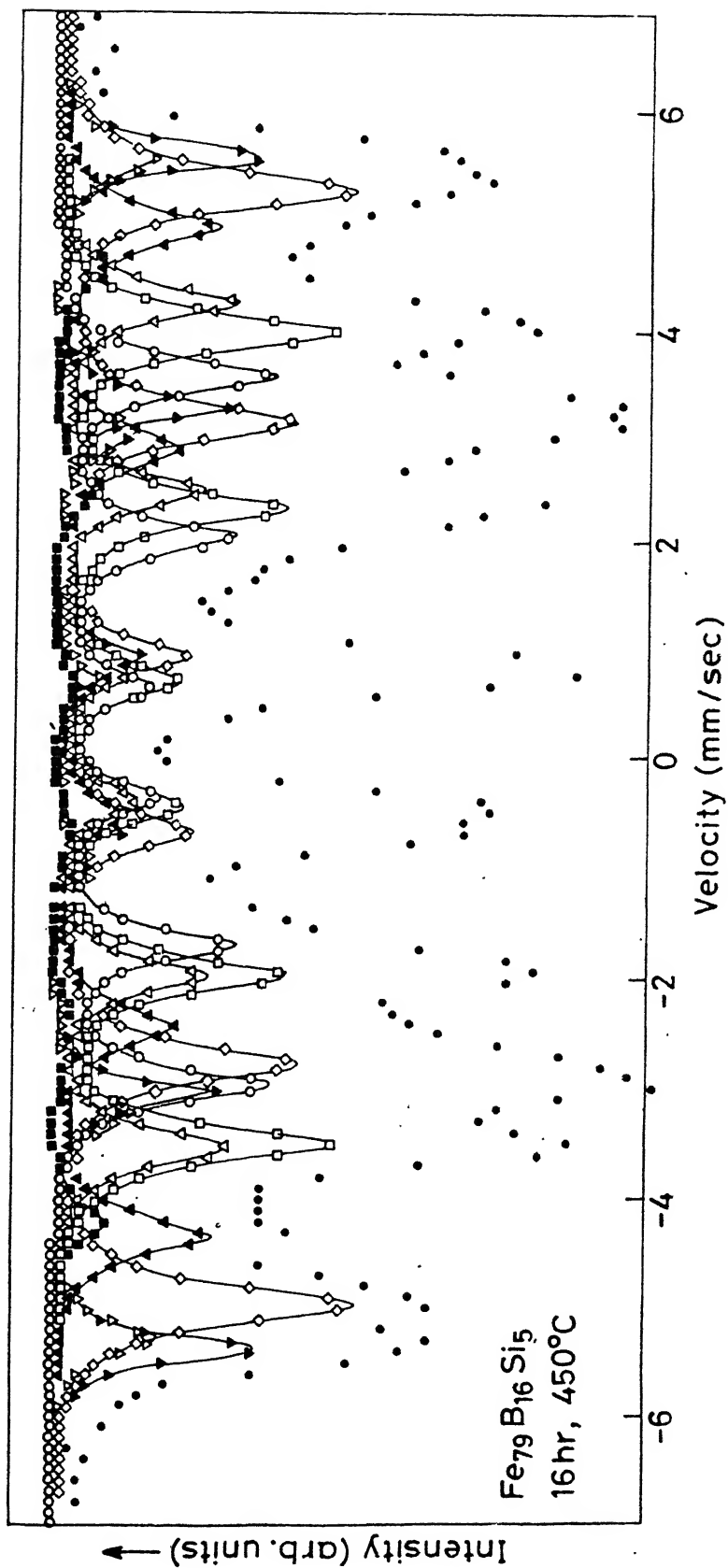


**FIGURE 4.7** Analyzed (RT) Mössbauer spectrum of heat-treated sample indicating the various phases precipitated. The symbols refer to the phases as mentioned in figure 4.6.

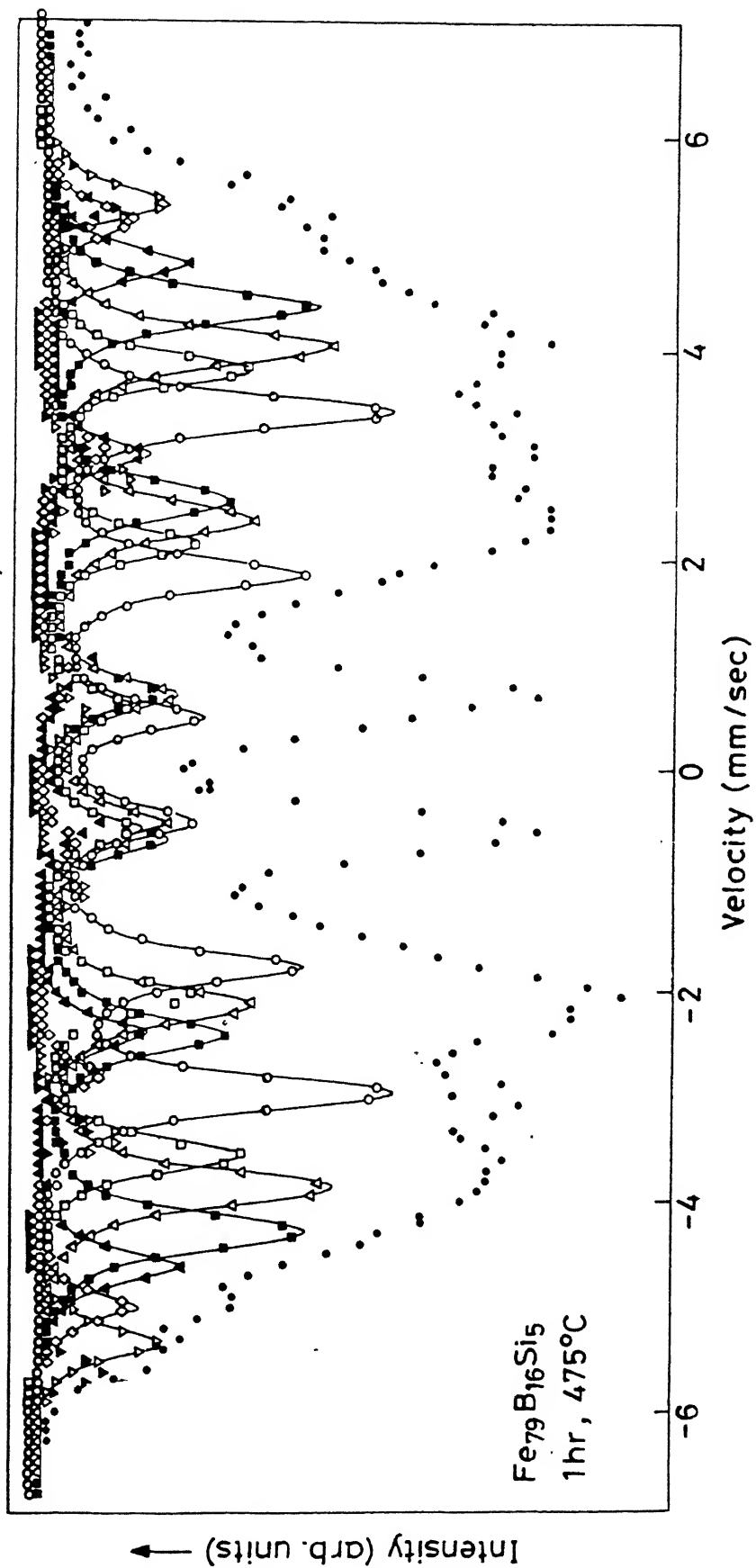


**FIGURE 4.8** Analyzed (RT) Mössbauer spectrum of heat-treated sample indicating the various phases precipitated. The symbols refer to the phases as mentioned in figure 4.6.

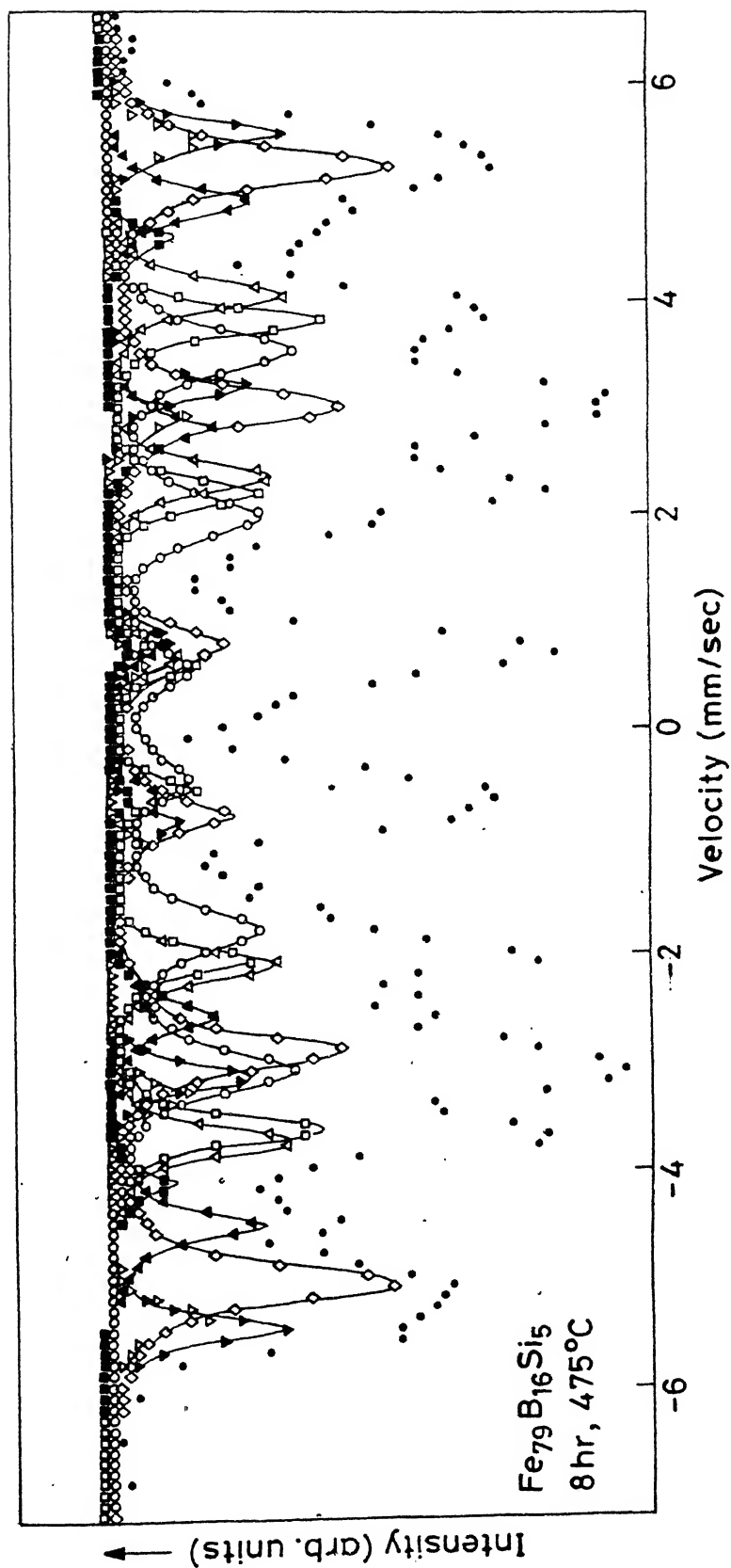


**FIGURE 4.9** Analyzed (RT) Mössbauer spectrum of heat-treated sample indicating the various phases precipitated. The symbols refer to the phases as mentioned in figure 4.6.



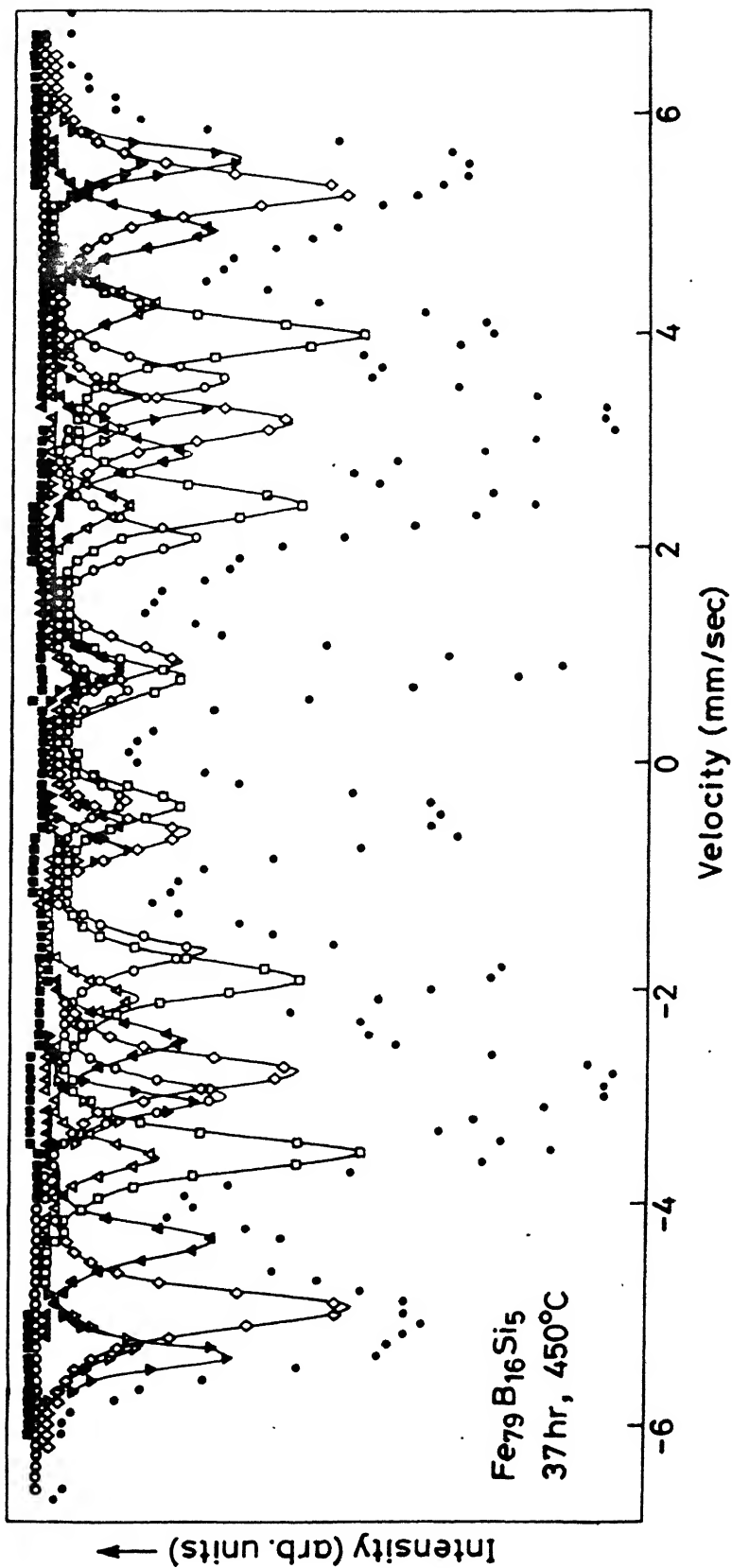
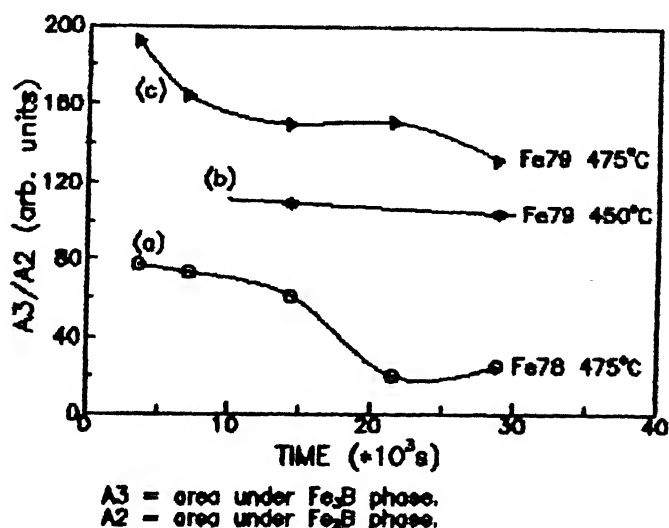


FIGURE 4.10 Analyzed (RT) Mössbauer spectrum of heat-treated sample indicating the various phases precipitated. The symbols refer to the phases as mentioned in figure 4.6.

neighbour (nn) Fe atom sites. It is well known that values of H in the Fe-Si solid solution depend on the nearest neighbour distributions [Haggstrom et al. 1973, Nagarajan et al. 1988].

These results (Table 4.3) indicate the formation of  $\alpha$ -Fe,  $\text{Fe}_3\text{B}$ ,  $\text{Fe}_2\text{B}$ , as well as Fe-Si. Previous studies of  $\text{Fe}_x\text{B}_{100-x}$  ( $72 \leq x \leq 86$ ) and crystalline  $\text{Fe}_3\text{B}$  by Chien et al. [1979] have shown that the crystalline  $\text{Fe}_3\text{B}$  is a metastable phase (not a stable one) which decomposes according to  $\text{Fe}_3\text{B} \rightarrow \text{Fe}_2\text{B} + \alpha\text{-Fe}$ , at higher temperatures [Kemeny et al. 1979, Cusido 1985]. And hence, as the crystallization is not complete in the heat-treated samples, these show the precipitation of  $\text{Fe}_3\text{B}$  and  $\text{Fe}_2\text{B}$  phases along with the  $\alpha$ -Fe phase.

In order to throw further light on this aspect we determined the ratio,  $A_3/A_2$ , of the areas under the sextets of  $\text{Fe}_3\text{B}$  and  $\text{Fe}_2\text{B}$  obtained from the computer fitting of the Mössbauer spectrum. Variation of the ratio  $A_3/A_2$  (for  $\text{Fe}_{79}\text{B}_{16}\text{Si}_5$ , heated at  $450^\circ\text{C}$  and  $475^\circ\text{C}$ , and  $\text{Fe}_{78}\text{B}_{13}\text{Si}_9$  at  $475^\circ\text{C}$ ), with the time period of heat-treatment is shown in Figure 4.11. These results, particularly for  $475^\circ\text{C}$ , support the argument that as the time period of heat-treatment is increased from 1 hr to 8 hr, the amount of  $\text{Fe}_2\text{B}$  (and  $\alpha$ -Fe) increases at the cost



**FIGURE 4.11** Variation in the ratios of the area under the  $\text{Fe}_3\text{B}$  and  $\text{Fe}_2\text{B}$  sextets obtained from the computer analysis of:  
 (a)  $\text{Fe}_{78}\text{B}_{13}\text{Si}_9$  ( $475^\circ\text{C}$ ), (b)  $\text{Fe}_{79}\text{B}_{16}\text{Si}_5$  ( $450^\circ\text{C}$ ), (c)  $\text{Fe}_{79}\text{B}_{16}\text{Si}_5$  ( $475^\circ\text{C}$ ).

of  $\text{Fe}_3\text{B}$ . It is further pointed out that *Bhatnagar and Ravi* [1983], using Mössbauer spectroscopic studies, have determined the crystallization temperature of the metallic glass  $\text{Fe}_{79}\text{B}_{16}\text{Si}_5$  to be  $546^\circ\text{C}$ . This result further suggests that the crystallization of the present samples is not complete even when the samples are heat-treated at  $475^\circ\text{C}$  for 8 hr. This conclusion can explain the presence of  $\text{Fe}_3\text{B}$ ,  $\text{Fe}_2\text{B}$ , and  $\alpha\text{-Fe}$  all the way in the samples heated at  $450^\circ\text{C}$  (for 4 hr) to  $475^\circ\text{C}$  (for 8 hr). Interestingly, *Quivy et al.* [1985] have observed the formation of  $\alpha\text{-Fe}$  and  $\text{Fe}_3\text{B}$  phases in metallic glass  $\text{Fe}_{79}\text{B}_{16}\text{Si}_5$  (heat-treated at  $475^\circ\text{C}$  for 1/2 hr) by X-ray diffraction and transmission electron microscopic studies.

It may be pointed out that during the computer analysis of the Mössbauer spectra of the Fe-B-Si metallic glasses heat-treated at  $450^\circ\text{C}$  and  $475^\circ\text{C}$ , we have used the values of H for  $\alpha\text{-Fe}$ , t- $\text{Fe}_3\text{B}$ ,  $\text{Fe}_2\text{B}$  and Fe-Si as given in Table 4.4, which were compiled from the values reported in literature. These values helped us to build subspectra for obtaining the best fit. Since the Mössbauer spectra for  $\text{Fe}_{79}\text{B}_{16}\text{Si}_5$ , reported by *Bhatnagar and Ravi* [1983] were recorded at higher temperatures, their values of H could not be used.

**TABLE 4.4**  
REPORTED VALUES OF INTERNAL MAGNETIC FIELD (H)  
OF PHASES OBSERVED IN THE METALLIC GLASSES.

PHASE OBSERVED	SITE	H (kOe)	Ref.	PHASE OBSERVED	SITE	H (kOe)	Ref.
$\alpha\text{-Fe}$		330	<i>Sanchez et al. 1989</i>	Fe-18.1at%Si (bcc)	8nn	325	<i>Ok et al. 1981</i>
					7nn	306	
					6nn	284	
t- $\text{Fe}_2\text{B}$	1	232	<i>Takacs et al. 1975</i>		5nn	244	
	2	242			4nn	192	
	avg.	237					
t- $\text{Fe}_3\text{B}$	1	226	<i>Caer et al. 1981</i>	Fe-14.8at%Si (bcc)	8nn	328	<i>Nagarajan et al. 1988</i>
	2	265			7nn	313	
	3	288			6nn	285	
	avg.	259			5nn	239	
					4nn	201	
Fe-8.6at%Si (bcc)	8nn	331	<i>Ok and Morrish 1980</i>				
	7nn	308					
	6nn	277					

Present results indicate precipitation of Fe-Si phase during the crystallization of  $\text{Fe}_{79}\text{B}_{16}\text{Si}_5$  (Table 4.3). Evidence for the formation of Fe-Si has been shown in the literature for other metallic glasses. Thus *Nowik et al.* [1988] who studied Mössbauer spectra of  $\text{Fe}_{83}\text{B}_{12}\text{Si}_5$ , found that the final products of crystallization occurring above  $500^\circ\text{C}$ , were  $\alpha\text{-Fe}$ ,  $\text{Fe}_2\text{B}$ , and Fe-Si. Similarly studies by *Ok and Morrish* [1980] by Mössbauer spectroscopy, X-ray diffraction and density measurements showed that the heat-treatment of  $\text{Fe}_{82}\text{B}_{12}\text{Si}_6$  gives rise to a transformation involving several stages, with the final products (showing absence of  $\alpha\text{-Fe}$ ) being  $\text{Fe}_2\text{B}$  and Fe-9 atom%Si.

In the case of  $\text{Fe}_{75.4}\text{B}_{14.2}\text{Si}_{10.4}$  [*Ok et al.* 1981], the final products of crystallization were  $\text{Fe}_2\text{B}$  and Fe-18.1at.%Si alloy. *Nagarajan et al.* [1988] investigated the crystallization of  $\text{Fe}_{78}\text{B}_{13}\text{Si}_9$  by Mössbauer spectroscopy and X-ray diffraction, and concluded that Fe-14.8at.%Si and  $\text{Fe}_2\text{B}$  were the final products.

During the computer analysis of the Mössbauer spectra of  $\text{Fe}_{79}\text{B}_{16}\text{Si}_5$  the best computer fit provided the set of H values in the ranges 331-335, 327-331, 310-313, 283-288, 263-269, 238-247, 225-229, and 196-200 kOe. As shown in Table 4.3, these values were assigned to t- $\text{Fe}_3\text{B}$  (283-288, 263-269 and 225-229 kOe),  $\alpha\text{-Fe}$  (331-335 kOe),  $\text{Fe}_2\text{B}$  ((average) 238-247 kOe), and Fe-Si ((8nn)327-331, (7nn)310-313, (6nn)283-288, (5nn)238-247 and (4nn)196-200 kOe). Such an analysis involved considerable overlap between different sextets making the job of computer fit complicated. In the case of  $\text{Fe}_2\text{B}$ , there was overlapping with the Fe-Si (5nn) line, whereas t- $\text{Fe}_3\text{B}$  at one site, overlapped with the Fe-Si(6nn) line.

#### 4.5 MOSSBAUER ANALYSIS OF HEAT-TREATED SAMPLES OF $\text{Fe}_{78}\text{B}_{13}\text{Si}_9$

The as-received samples of  $\text{Fe}_{78}\text{B}_{13}\text{Si}_9$  were heat-treated at different temperatures in the range  $300^\circ\text{C}$  to  $475^\circ\text{C}$  for different time periods in the range 1 hr to 37 hr as described in Table 4.5. Mössbauer spectra of the samples heat-

TABLE 4.5

MÖSSBAUER PARAMETERS OBTAINED FROM COMPUTER ANALYSIS FOR METALLIC  
GLASS  $\text{Fe}_{78}\text{B}_{13}\text{Si}_9$  AFTER VARIOUS HEAT TREATMENTS

ANNEALING TEMP(°C)	TIME(hr)	IS (mm/s)	H (kOe)	$\Gamma$ (mm/s)	ASSIGNMENT	
					Mössbauer	X.R.D.
300	1	0.12	252	0.94	amorphous	amorphous
	4	0.01	255	0.97	amorphous	amorphous
	8	0.14	252	0.91	amorphous	amorphous
	16	0.12	254	0.91	amorphous	amorphous
350	1	0.03	250	0.90	amorphous	amorphous
	2	0.06	252	0.96	amorphous	amorphous
	4	0.05	253	0.91	amorphous	amorphous
	8	0.04	254	0.90	amorphous	amorphous
	16	0.04	254	0.93	amorphous	amorphous
400	1	0.04	252	0.93	amorphous	amorphous
	2	0.07	254	1.01	amorphous	amorphous
	4	0.04	251	0.98	amorphous	amorphous
	8	0.06	255	0.94	amorphous	amorphous
	16	0.04	255	0.97	amorphous	amorphous
450	1	0.10	261	0.92	amorphous	amorphous
	4	0.12	258	1.06	amorphous	amorphous
	8	0.22	255	1.29	amorphous	amorphous
	16	0.19	253	1.12	amorphous	amorphous
450	29	(1) 0.01	332	0.29	$\alpha$ -Fe	$\alpha$ -Fe
		(2) 0.08	330	0.29	Fe-Si (8nn)	N.O.
		(3) 0.06	311	0.39	Fe-Si (7nn)	N.O.
		(4) 0.05	284	0.39	Fe-Si (6nn)	N.O.
		(5) 0.13	267	0.39	t-Fe <sub>3</sub> B (avg.)	Fe <sub>3</sub> B
		(6) 0.12	250	0.39	Fe-Si (5nn)	N.O.
		(7) 0.14	235	0.39	Fe <sub>2</sub> B (avg.)	Fe <sub>2</sub> B
		(8) 0.60	202	0.39	Fe-Si (4nn)	N.O.
450	37	(1) 0.01	332	0.29	$\alpha$ -Fe	$\alpha$ -Fe
		(2) 0.08	330	0.29	Fe-Si (8nn)	N.O.
		(3) 0.06	311	0.39	Fe-Si (7nn)	N.O.
		(4) 0.05	284	0.39	Fe-Si (6nn)	N.O.
		(5) 0.13	267	0.39	t-Fe <sub>3</sub> B (avg.)	Fe <sub>3</sub> B
		(6) 0.12	250	0.37	Fe-Si (5nn)	N.O.
		(7) 0.14	235	0.37	Fe <sub>2</sub> B (avg.)	Fe <sub>2</sub> B
		(8) 0.06	202	0.39	Fe-Si (4nn)	N.O.

A, B, C, D : are defined below:

- A = Isomer Shift measured with respect to  $\alpha$ -Fe: typical error  $\pm 0.01$   
 B = Internal Magnetic Field at 57-Fe nuclues : typical error  $\pm 5.00$   
 C = Width of the spectral line : typical error  $\pm 0.01$   
 D : N.O. = Not Observed

MÖSSBAUER PARAMETERS OBTAINED FROM COMPUTER ANALYSIS FOR METALLIC  
GLASS  $\text{Fe}_{78}\text{B}_{13}\text{Si}_9$  AFTER VARIOUS HEAT TREATMENTS (contd..)

ANNEALING TEMP(°C)	TIME(hr)	IS (mm/s)	H (kOe)	$\Gamma$ (mm/s)	ASSIGNMENT	
					Mössbauer	X.R.D.
475	1	(1) 0.13	334	0.29	$\alpha$ -Fe	$\alpha$ -Fe
		(2) 0.18	331	0.29	Fe-Si (8nn)	N.O.
		(3) 0.28	314	0.45	Fe-Si (7nn)	N.O.
		(4) 0.15	286	0.45	Fe-Si (6nn)	N.O.
		(5) 0.17	266	0.43	t-Fe <sub>3</sub> B (avg.)	N.O.
		(6) 0.16	250	0.64	Fe-Si (5nn)	N.O.
		(7) 0.22	235	0.57	Fe <sub>2</sub> B (avg.)	N.O.
		(8) 0.11	203	0.68	Fe-Si (4nn)	N.O.
475	2	(1) 0.13	334	0.58	$\alpha$ -Fe	$\alpha$ -Fe
		(2) 0.18	331	0.58	Fe-Si (8nn)	N.O.
		(3) 0.28	314	0.78	Fe-Si (7nn)	N.O.
		(4) 0.15	286	0.86	Fe-Si (6nn)	N.O.
		(5) 0.17	266	0.86	t-Fe <sub>3</sub> B (avg.)	Fe <sub>3</sub> B
		(6) 0.16	250	1.15	Fe-Si (5nn)	N.O.
		(7) 0.22	235	1.14	Fe <sub>2</sub> B (avg.)	Fe <sub>2</sub> B
		(8) 0.11	203	1.36	Fe-Si (4nn)	N.O.
	4	(1) 0.08	334	0.58	$\alpha$ -Fe	$\alpha$ -Fe
		(2) 0.13	331	0.58	Fe-Si (8nn)	N.O.
		(3) 0.08	309	0.58	Fe-Si (7nn)	N.O.
		(4) 0.07	286	0.58	Fe-Si (6nn)	N.O.
		(5) 0.06	267	0.78	t-Fe <sub>3</sub> B (avg.)	Fe <sub>3</sub> B
		(6) 0.05	253	1.10	Fe-Si (5nn)	N.O.
		(7) 0.06	235	1.14	Fe <sub>2</sub> B (avg.)	Fe <sub>2</sub> B
		(8) 0.01	203	1.44	Fe-Si (4nn)	N.O.
475	6	(1) 0.08	334	0.58	$\alpha$ -Fe	$\alpha$ -Fe
		(2) 0.13	331	0.58	Fe-Si (8nn)	N.O.
		(3) 0.06	318	0.91	Fe-Si (7nn)	N.O.
		(4) 0.08	289	0.90	Fe-Si (6nn)	N.O.
		(5) 0.02	265	0.78	t-Fe <sub>3</sub> B (avg.)	Fe <sub>3</sub> B
		(6) 0.22	242	0.78	Fe-Si (5nn)	N.O.
		(7) 0.11	235	0.72	Fe <sub>2</sub> B (avg.)	Fe <sub>2</sub> B
		(8) 0.29	196	0.78	Fe-Si (4nn)	N.O.
475	8	(1) 0.09	334	0.58	$\alpha$ -Fe	$\alpha$ -Fe
		(2) 0.15	330	0.58	Fe-Si (8nn)	N.O.
		(3) 0.13	314	0.78	Fe-Si (7nn)	N.O.
		(4) 0.11	286	0.78	Fe-Si (6nn)	N.O.
		(5) 0.07	268	0.72	t-Fe <sub>3</sub> B (avg.)	Fe <sub>3</sub> B
		(6) 0.25	243	0.78	Fe-Si (5nn)	N.O.
		(7) 0.11	235	0.72	Fe <sub>2</sub> B (avg.)	Fe <sub>2</sub> B
		(8) 0.20	196	0.78	Fe-Si (4nn)	N.O.

A, B, C, D : as in earlier page.

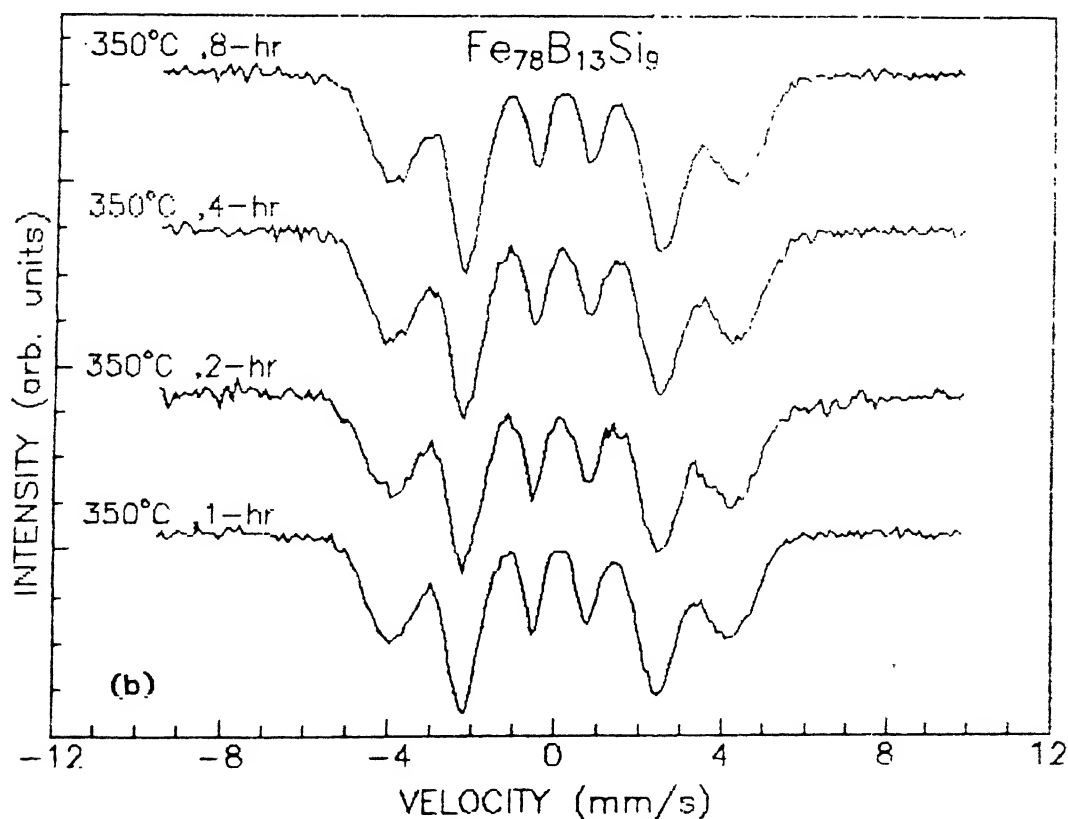
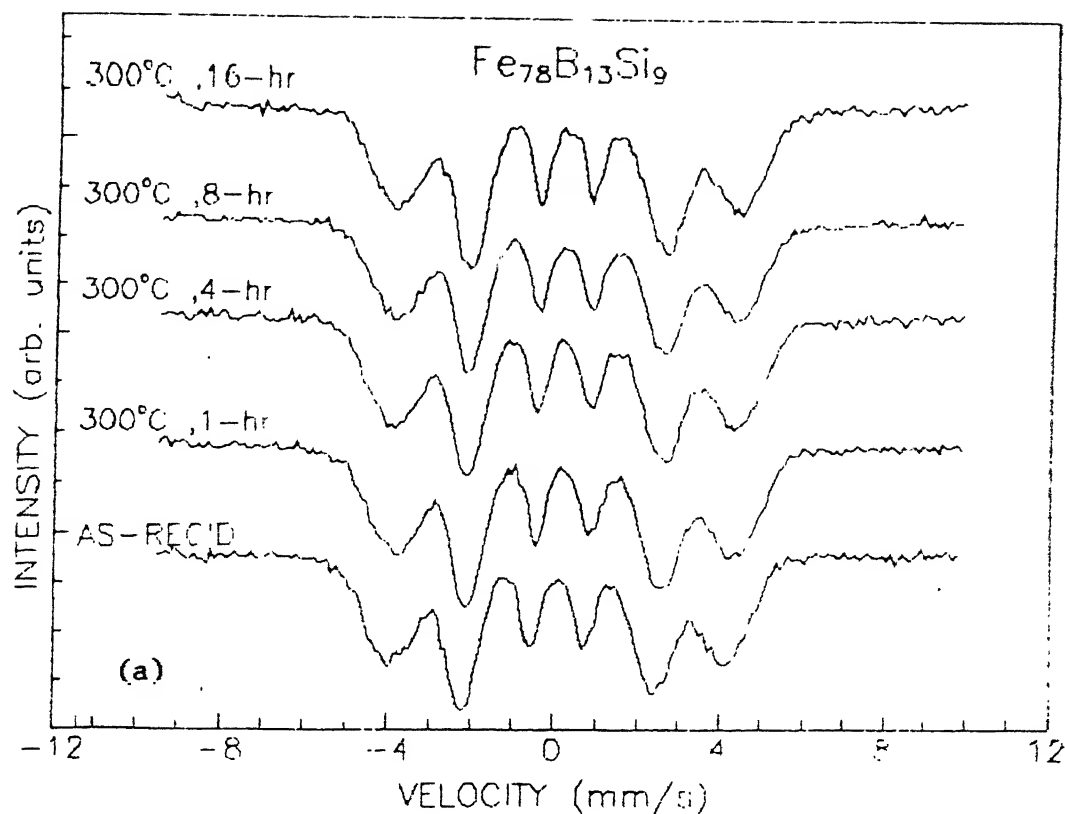


**FIGURE 4.12** Mössbauer (RT) spectra of  $\text{Fe}_{78}\text{B}_{13}\text{Si}_9$ .

(a) heat-treated at  $300^\circ\text{C}$  for various time periods.

(b) heat-treated at  $350^\circ\text{C}$  for various time periods.

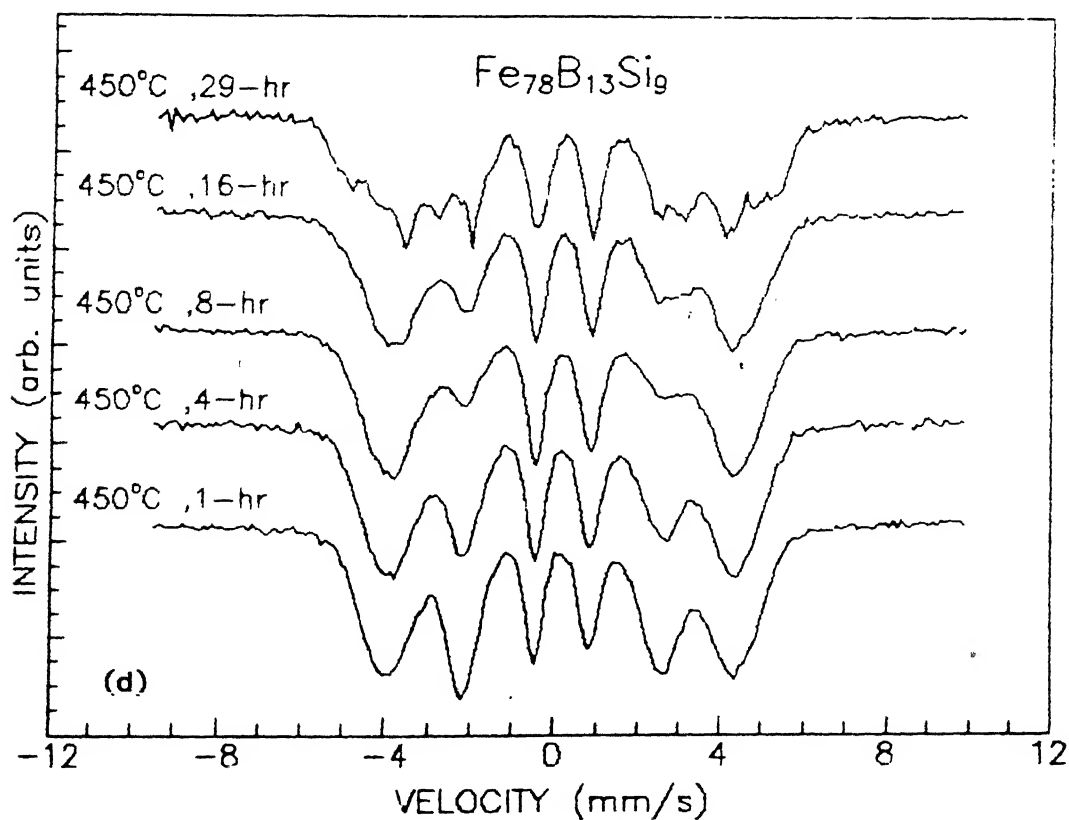
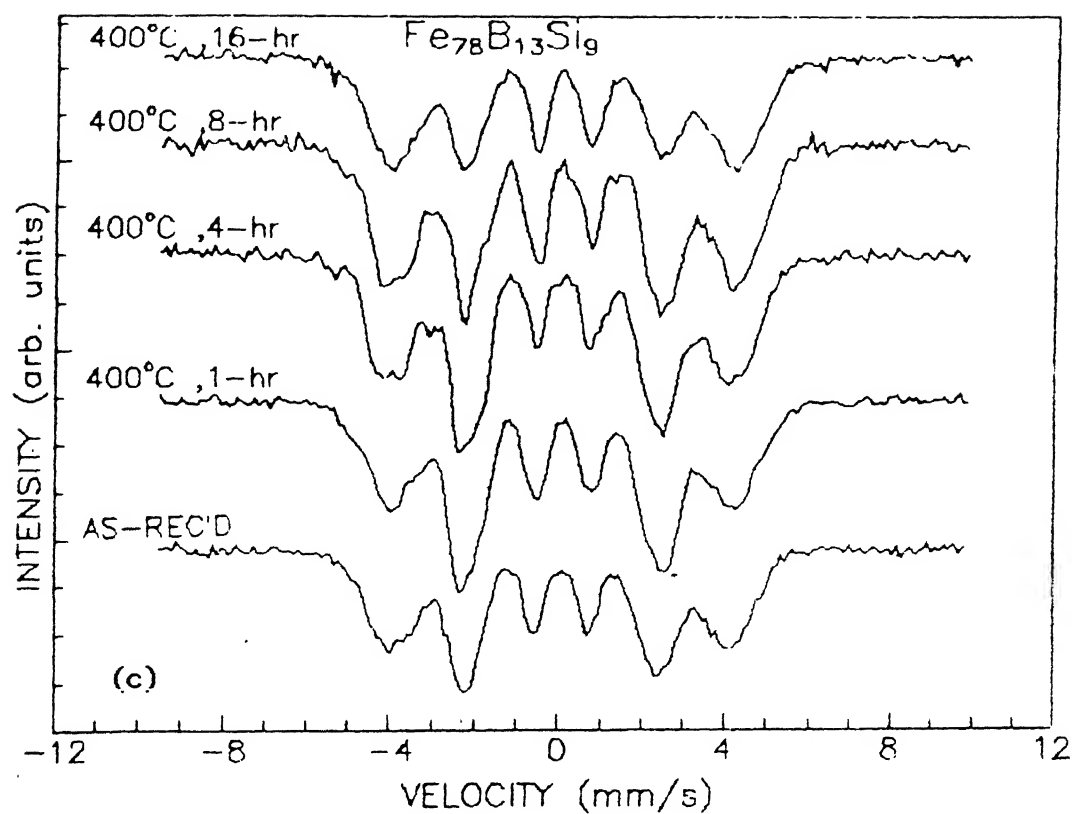


**FIGURE 4.12** Mössbauer (RT) spectra of  $\text{Fe}_{78}\text{B}_{13}\text{Si}_9$ .  
 (c) heat-treated at  $400^\circ\text{C}$  for various time periods.  
 (d) heat-treated at  $450^\circ\text{C}$  for various time periods.



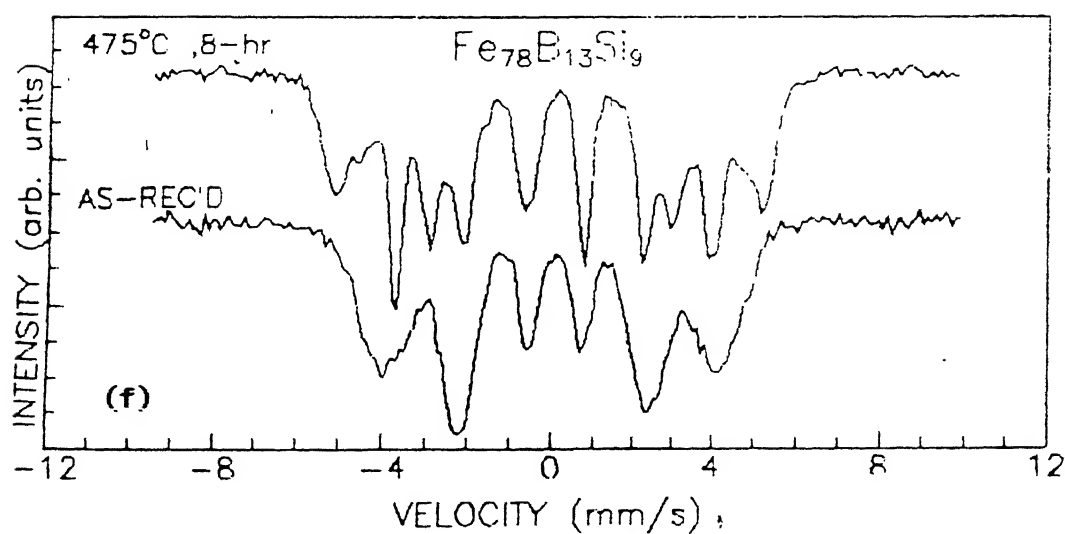
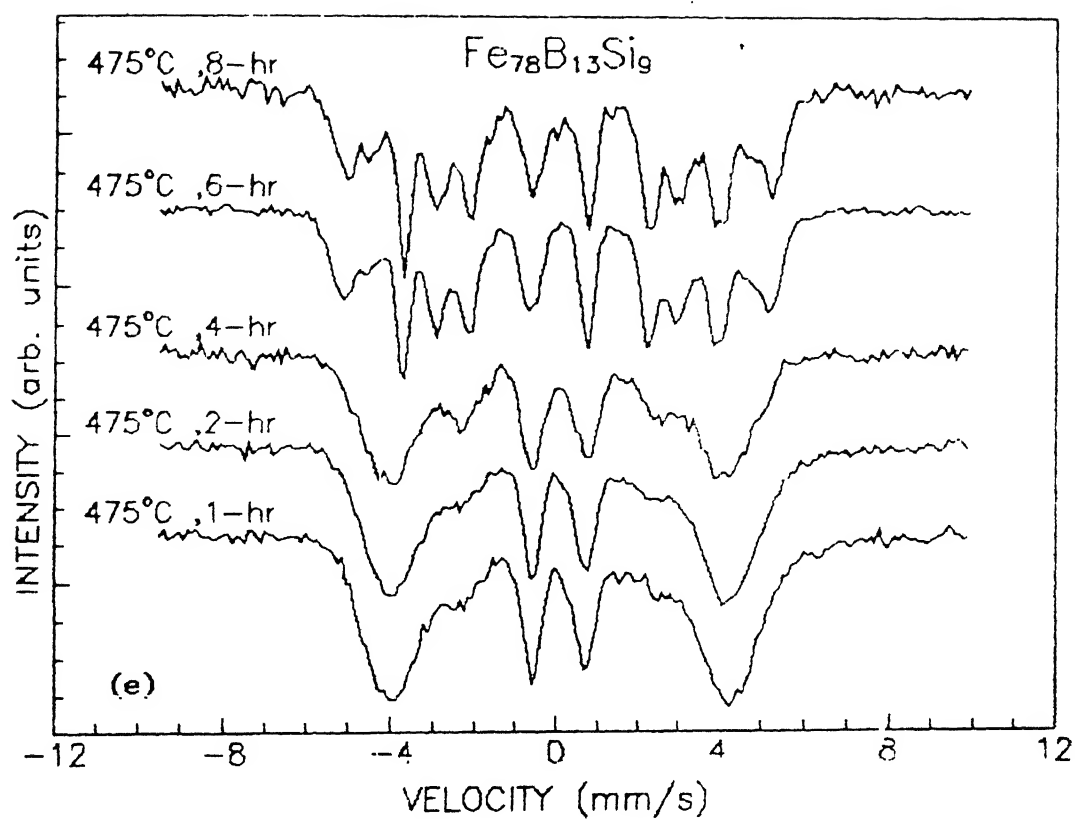


FIGURE 4.12 Mössbauer (RT) spectra of  $\text{Fe}_{78}\text{B}_{13}\text{Si}_9$ .

(e) heat-treated at 475°C for various time periods.

(f) comparison of as-recieved with heat-treated at 475°C (8 hr).

treated at 300°C, 350°C and 400°C (for different time periods as mentioned in the table) are presented in the Figure 4.12. and these consist of six broad lines (of line-widths ranging from  $0.9 \pm 0.01$  to  $1.0 \pm 0.01$  mm/s) which are typical of the amorphous phase. This behaviour continues for samples heat-treated at 450°C for 1, 4, 8, and 16 hr.

Changes in the shape of the Mössbauer spectra are observed for the samples heat-treated at 450°C for 29 and 37 hr and at 475°C for 6 and 8 hr, indicating the onset of crystallization process. It is interesting to note from Figure 4.12 that the lines in the Mössbauer spectra of the sample heat-treated at 475°C for 1 and 2 hr are not so well resolved although the computer analysis (see Table 4.5) provides phase assignments same as the samples heated at 450°C (for 29 and 37 hr) and 475°C (for 6 and 8 hr).

A general comparison of these results with those for  $\text{Fe}_{79}\text{B}_{16}\text{Si}_5$  samples indicate that the addition of Si has improved the thermal stability of these metallic glasses. Similar behaviour has been observed by several other workers.

As in the case of  $\text{Fe}_{79}\text{B}_{16}\text{Si}_5$ , the Mössbauer spectra of the samples of  $\text{Fe}_{78}\text{B}_{13}\text{Si}_9$  heat-treated at 450°C (for 29 and 37 hr) and 475°C (for 1, 2, 4, 6 and 8 hr) were complicated in nature and could be best fitted with the sub-spectra characteristic of  $\text{Fe}_3\text{B}$ ,  $\alpha\text{-Fe}$ ,  $\text{Fe}_2\text{B}$  and Fe-Si. The values of the Mössbauer parameters and assignment of phases are listed in Table 4.5, and they indicate a general similarity between the two metallic glasses. Plots of the computer-fitted sub-spectra (Figures 4.13 to 4.17) were analyzed for the ratio of the amount of  $\text{Fe}_3\text{B}$  to  $\text{Fe}_2\text{B}$  phases and these results (Figure 4.11) show that the amount of  $\text{Fe}_3\text{B}$  decreases (and that of  $\alpha\text{-Fe}$  and  $\text{Fe}_2\text{B}$  increases) as the temperature and time period of heat-treatment is increased beyond 450°C (16 hr).

The present results (Figures 4.13 to 4.17 and Table 4.5) indicate that the crystallization of the metallic glass  $\text{Fe}_{78}\text{B}_{13}\text{Si}_9$  was not complete even after an heat-treatment of 8 hr at 475°C. This result is in agreement with the observa-

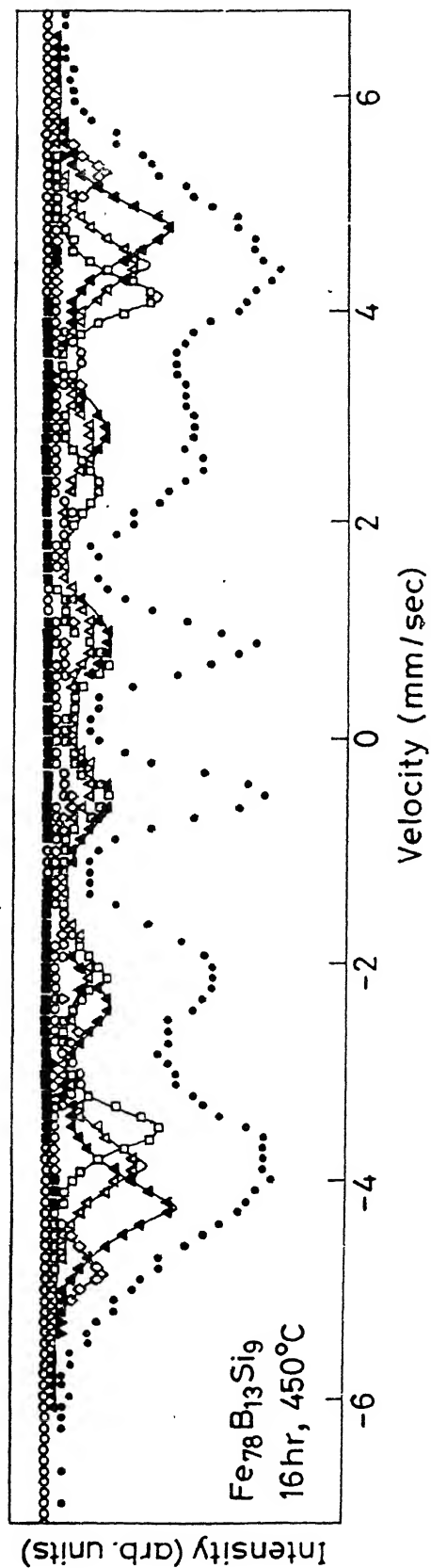
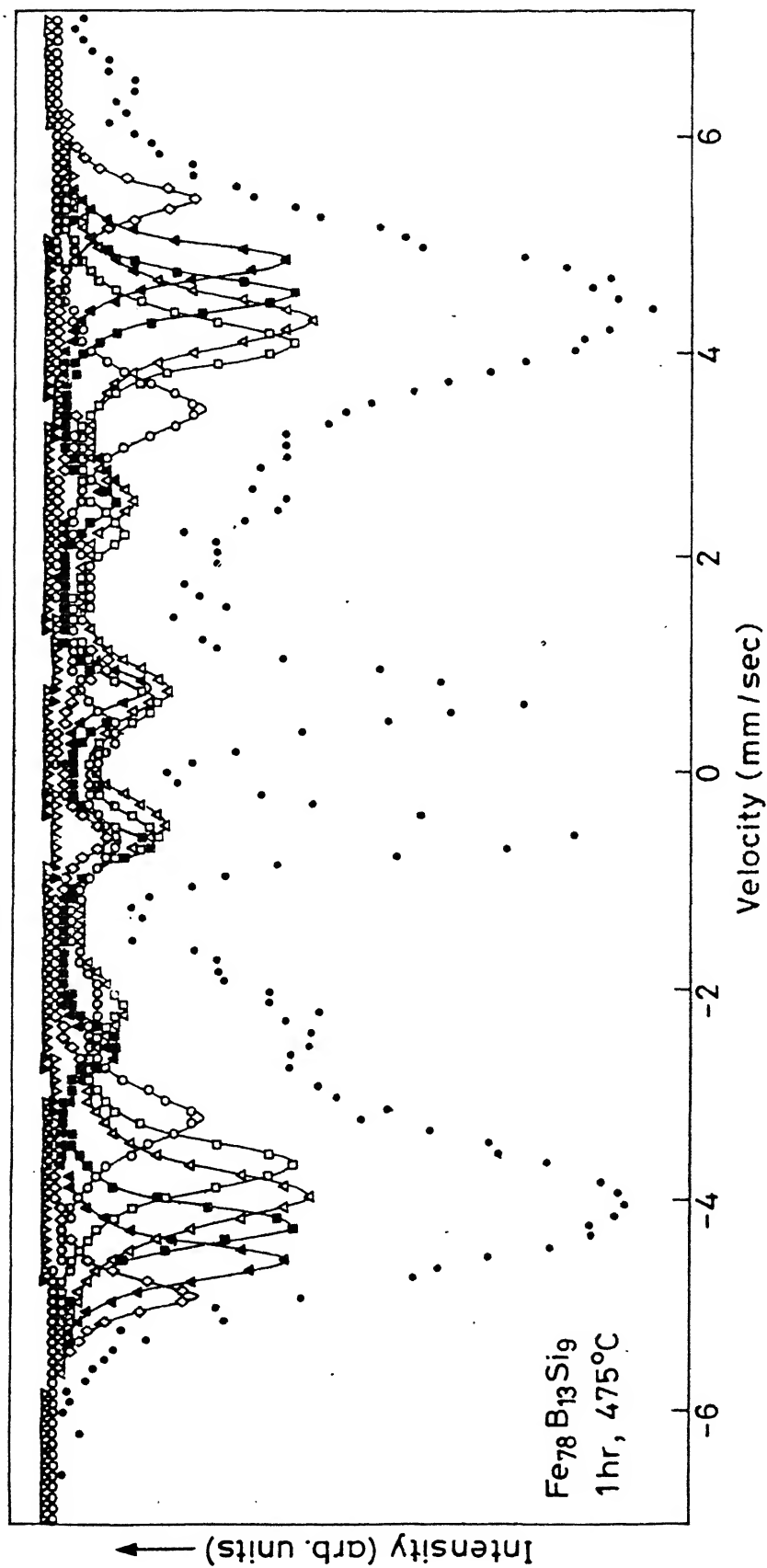
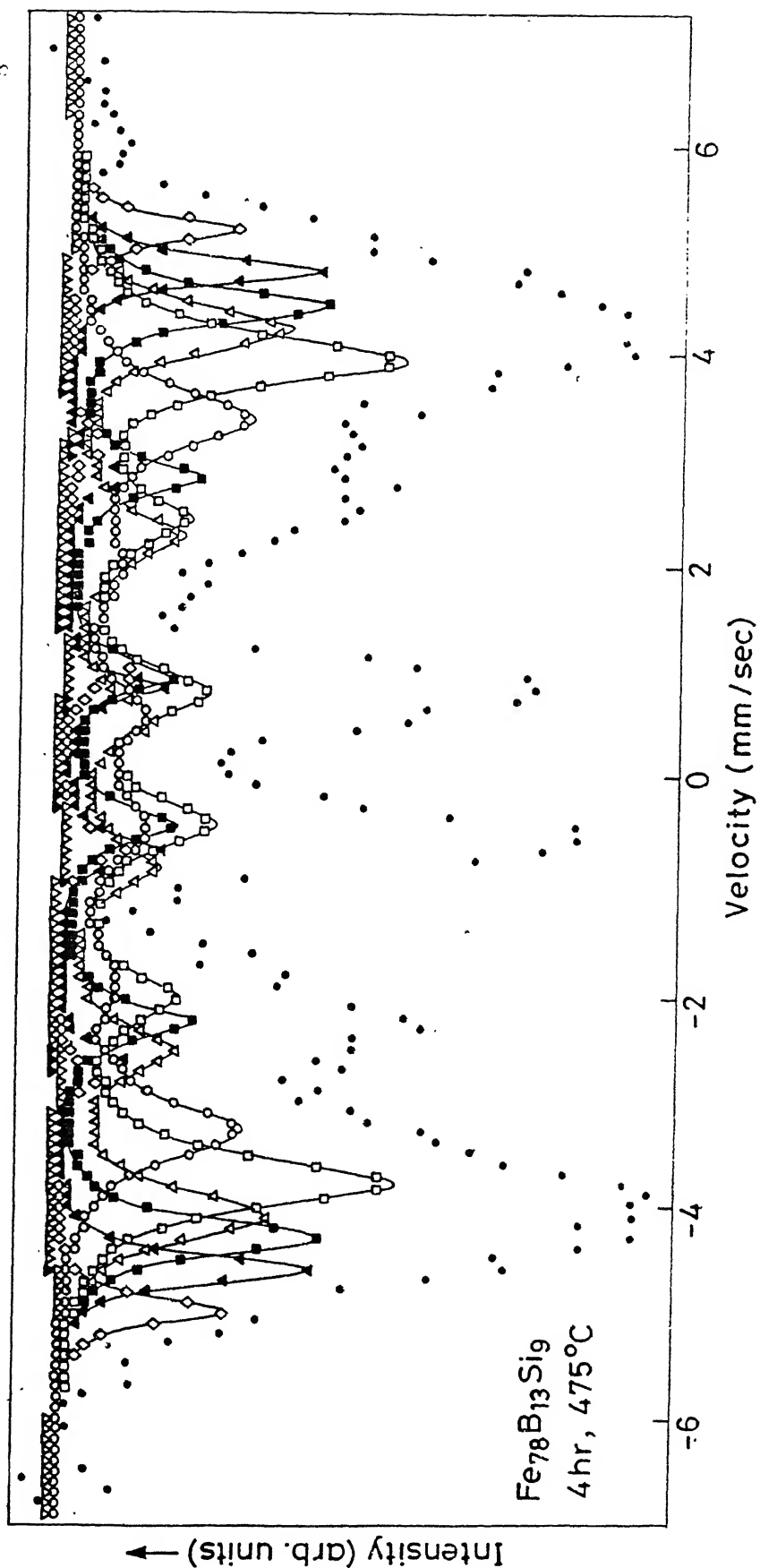


FIGURE 4.13 Analyzed (RT) Mössbauer spectrum of heat-treated sample indicating the various phases precipitated. The symbols refer to the phases as mentioned below.

$\nabla$ - $\alpha$ -Fe,  $\nabla$ -Fe-Si(8nn),  $\diamond$ -Fe-Si(7nn),  $\blacktriangle$ -Fe-Si(6nn),  $\blacksquare$ -t-Fe<sub>3</sub>B(avg),  $\triangle$ -Fe-Si(5nn),  $\square$ -t-Fe<sub>2</sub>B(avg),  $\circ$ -Fe-Si(4nn).



**FIGURE 4.14** Analyzed (RT) Mössbauer spectrum of heat-treated sample indicating the various phases precipitated. The symbols refer to the phases as mentioned in figure 4.13.



**FIGURE 4.15** Analyzed (RT) Mössbauer spectrum of heat-treated sample indicating the various phases precipitated. The symbols refer to the phases as mentioned in figure 4.13.

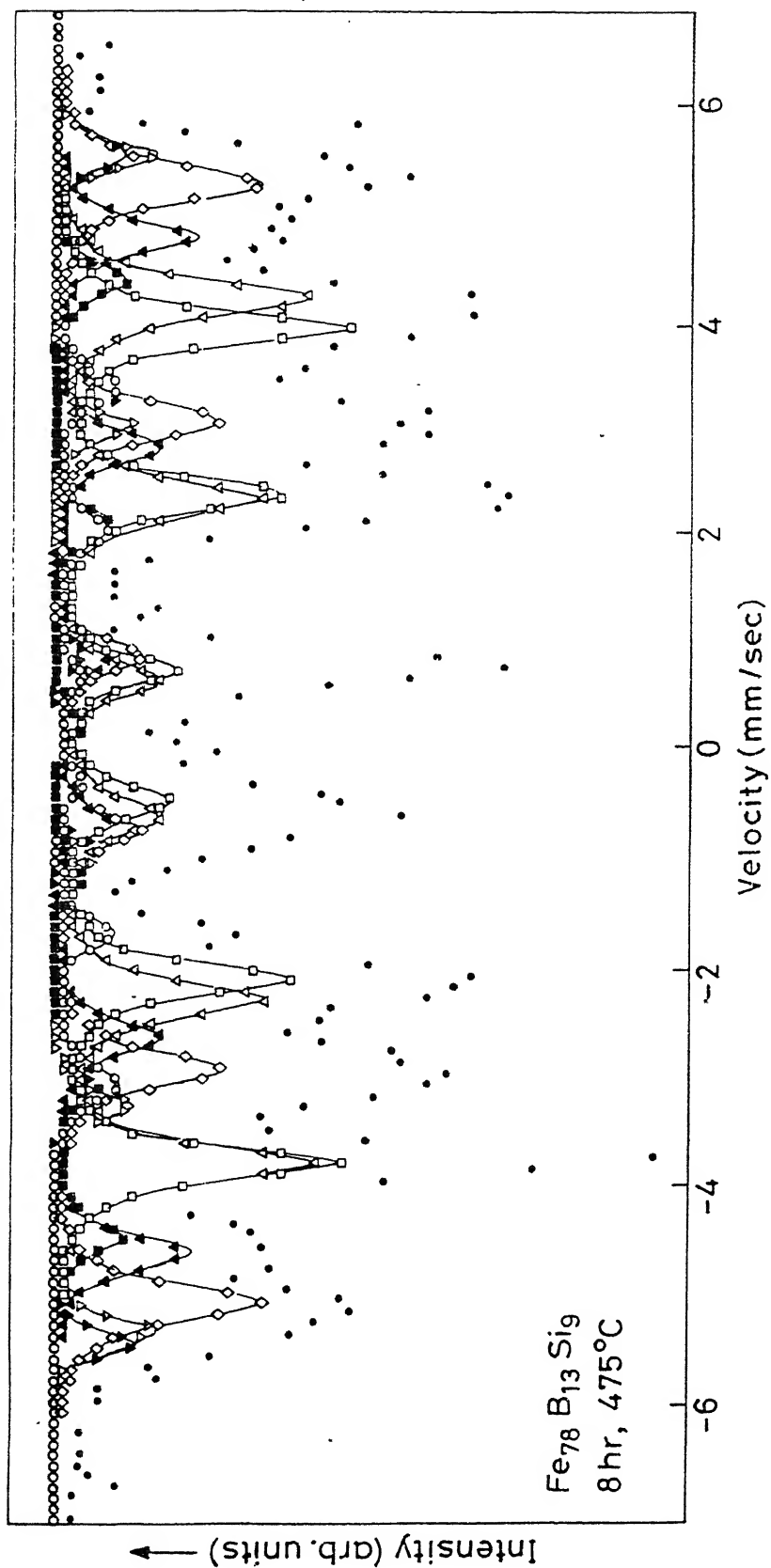


**FIGURE 4.16** Analyzed (RT) Mössbauer spectrum of heat-treated sample indicating the various phases precipitated. The symbols refer to the phases as mentioned in figure 4.13.

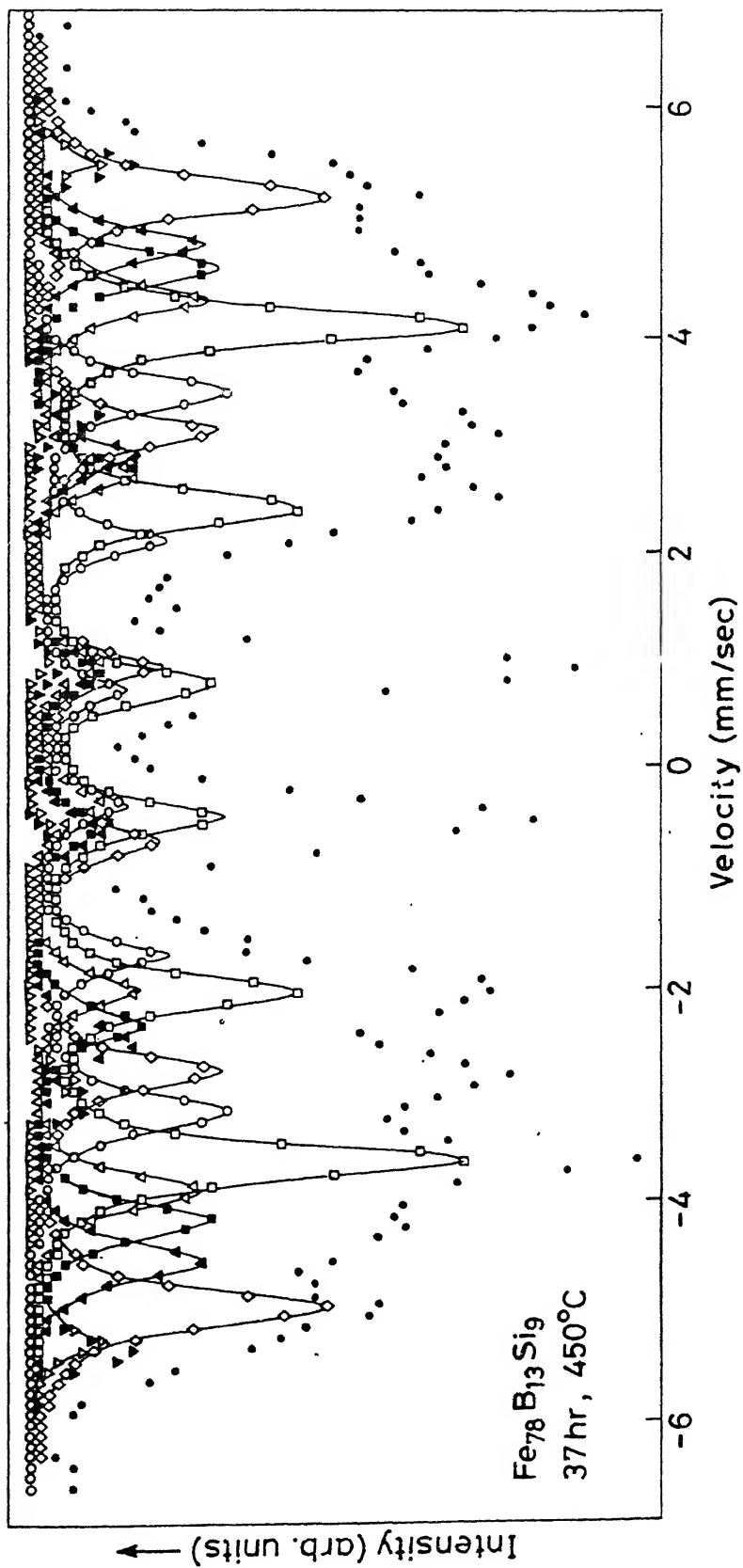


FIGURE 4.17 Analyzed (RT) Mössbauer spectrum of heat-treated sample indicating the various phases precipitated. The symbols refer to the phases as mentioned in figure 4.13.

tions by *Bhatnagar and Ravi* [1983] and that of *Nagaraajan et al.* [1988] for the crystallization temperature of  $\text{Fe}_{78}\text{B}_{13}\text{Si}_9$  to be  $563^\circ\text{C}$  and  $559^\circ\text{C}$  respectively.

General similarities in the values of Mössbauer parameters obtained at  $475^\circ\text{C}$  for  $\text{Fe}_{79}\text{B}_{16}\text{Si}_5$  and  $\text{Fe}_{78}\text{B}_{13}\text{Si}_9$  samples (Table 4.3 and 4.5) indicate that a decrease in the B content, while an increase in the Si content does not bring large changes as long as the B+Si content remains approximately the same. A minor change observed by us is that the amount of  $\text{Fe}_3\text{B}$  precipitated in  $\text{Fe}_{79}\text{B}_{16}\text{Si}_5$  is more than that in  $\text{Fe}_{78}\text{B}_{13}\text{Si}_9$ . In fact, we had obtained an average value of H for t- $\text{Fe}_3\text{B}$  in order to obtain a best fit to the Mössbauer spectra and this could be due to the smaller amount of  $\text{Fe}_3\text{B}$ . This behaviour could imply that the precipitation of  $\text{Fe}_3\text{B}$  is inhibited by the addition of Si [*Nagaraajan et al.* 1988].

We found it interesting to examine the changes in the line widths of the Mössbauer lines characteristic of  $\text{Fe}_3\text{B}$  and  $\text{Fe}_2\text{B}$  phases with the increase in the time period of heat-treatment. Results of such an analysis for the two metallic glasses are shown in Figure 4.18, and these indicate that in the case of  $\text{Fe}_2\text{B}$  phase (for both the glasses) the line width decreases with the time period of heating. This is an interesting observation and more systematic studies are necessary before it can be termed as a logical behaviour in the kinetics of crystallization.

To complete the comparison between the two metallic glasses we have shown in the Figures 4.5 (f) and 4.12 (f) the Mössbauer spectra of the as-received samples along with the spectra of the same samples heat-treated at  $475^\circ\text{C}$  for 8 hr. Similarly the as-observed Mössbauer spectra (at RT) of the two glasses after heat-treatment at  $475^\circ\text{C}$  for 8 hr, are compared in Figure 4.19.



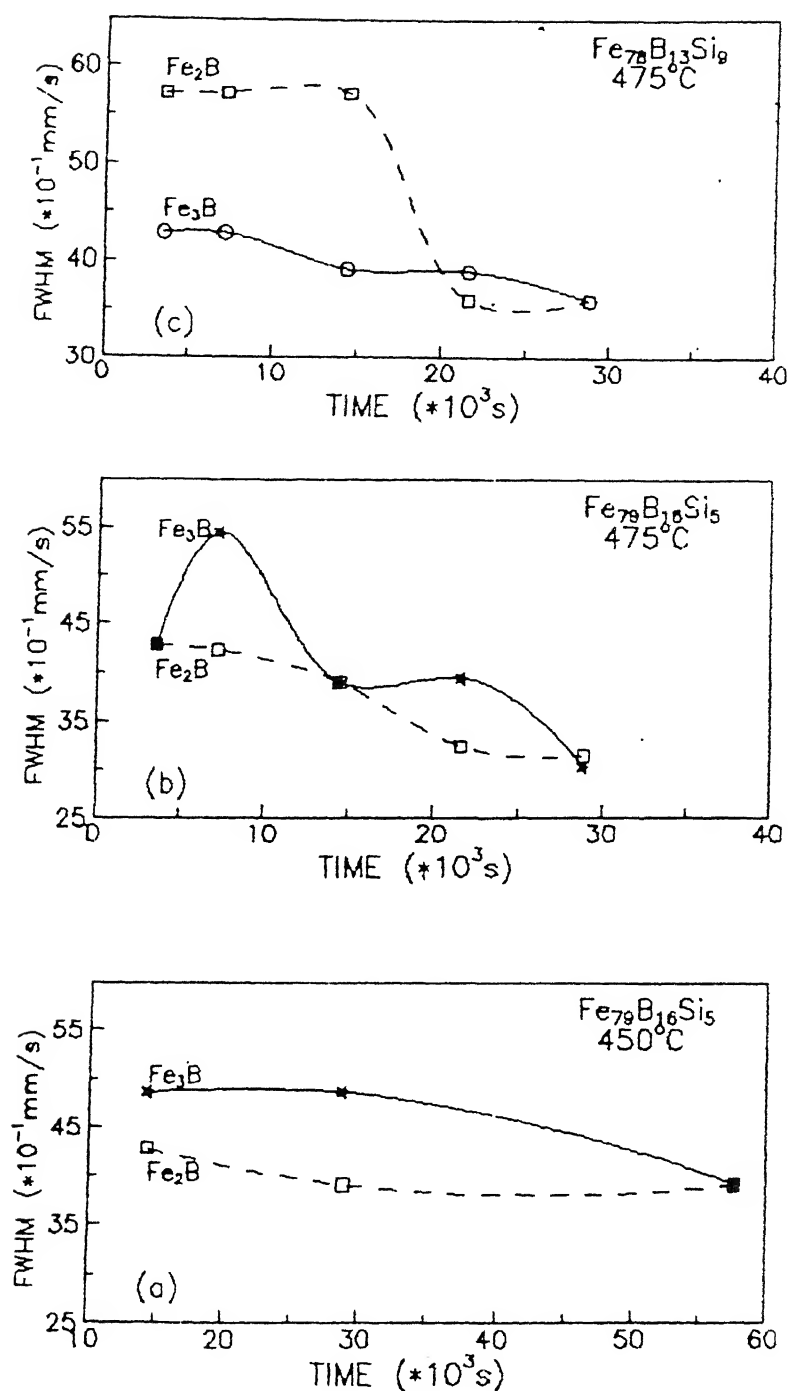


**FIGURE 4.18** Variation in the line-width (FWHM) of  $\text{Fe}_2\text{B}$  and  $\text{Fe}_3\text{B}$  lines with time period of heat-treatment, in:

- (a)  $\text{Fe}_{79}\text{B}_{16}\text{Si}_5$ , heat-treated at  $450^\circ\text{C}$ ,
- (b)  $\text{Fe}_{79}\text{B}_{16}\text{Si}_5$ , heat-treated at  $475^\circ\text{C}$ ,
- (c)  $\text{Fe}_{78}\text{B}_{13}\text{Si}_9$ , heat-treated at  $450^\circ\text{C}$ .

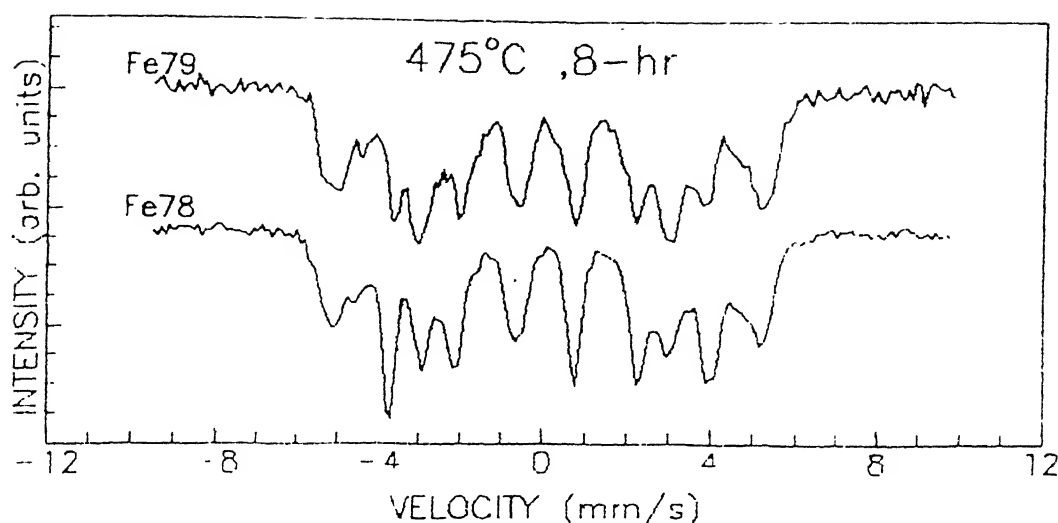


FIGURE 4.19 Comparison of spectra heat-treated at 475°C for 8 hr.  
(a)  $\text{Fe}_{79}\text{B}_{16}\text{Si}_5$ , (b)  $\text{Fe}_{78}\text{B}_{13}\text{Si}_9$ .

## 4.6 MAGNETIC ORDERING

Glassy alloys (rich in Fe content) possess long range magnetic ordering, although there is no long range structural ordering in them. Some information on the direction of the magnetic moments in these alloys can be obtained from the measurements of the relative hyperfine line intensities. For the 14.4 keV  $\gamma$ -ray from the  $^{57}\text{Fe}$  state, the ratio of the intensities of the second to the first lines is denoted by  $b$ , and is defined as:

$$b = (4\sin^2\theta)/(3(1+\cos^2\theta)) \quad (4.1)$$

where  $\theta$  is the angle between the magnetization direction and the  $\gamma$ -ray propagation direction. For a powdered sample (having randomly oriented moments) the value of  $b$  is equal to 2/3.

Metallic glasses being amorphous in nature give rise to broad spectral lines (Figure 4.4) and hence the ratio of the area under the peaks, and not the intensity of the peaks are taken into consideration. Clamping the samples affect the direction of the moments. Amorphous alloys are apparently more susceptible to external stresses than crystalline solids, probably due to the disordered

atomic arrangements. These results suggest that the direction of the magnetic moment in the as-received samples are affected by the strain frozen in the alloy during the rapid quenching process. Annealing at high temperatures releases these stresses which in turn changes the moment directions. However the internal magnetic field  $H$  is not affected by the directional changes in magnetic moments.

Because of the mounting of the samples on copper holders there was a considerable amount of out-of-plane magnetization due to the induced stresses. It has been observed that annealing at high temperatures changes the direction of the moments away from the plane of the ribbon.

The areal ratios of the Mössbauer spectra of the samples have been found to change considerably on annealing the samples as is observed in Figures 4.5 and 4.12. For the as-received sample of amorphous  $\text{Fe}_{79}\text{B}_{16}\text{Si}_5$ ,  $b$  is equal to 1.33 i.e.,  $\theta$  is equal to  $90^\circ$ , whereas in the case of  $\text{Fe}_{78}\text{B}_{13}\text{Si}_9$ ,  $\theta$  is equal to  $68^\circ$ . It is clear that, with increase in the Si concentration, the value of  $\theta$  has decreased. Similar metalloid dependence of the magnetic anisotropy (decreasing  $\theta$  with Si concentration) has also been reported in literature for other Fe-B-Si [Lubrosky *et al.* 1979, Lin *et al.* 1981] alloys. As the time-period of heat treatment, or the temperature is increased the magnetization direction rotates out of the plane. Similar results of out of the plane rotation of the magnetization axis on annealing has also been observed in  $\text{Fe}_{80}\text{B}_{20}$  [Chien 1978],  $\text{Fe}_{82}\text{B}_{18}$  [Ruckman *et al.* 1980],  $\text{Fe}_{40}\text{Ni}_{38}\text{B}_{18}\text{Mo}_4$  [Kamal *et al.* 1981],  $\text{Fe}_{67}\text{Co}_{18}\text{B}_{14}\text{Si}_1$  [Bhatnagar *et al.* 1985], etc.. The results indicate that annealing does relieve internal stresses in the sample which are invariably present in the rapidly quenched alloys. Since the direction of magnetization is stress sensitive, this relief in the internal stress gets reflected in the directional change of the magnetization axis. The effects of annealing are usually interpreted in terms of a reduction of the number of vacancies and an increase in the topological order approaching a relaxed, ideal glass.

## 4.7 INFERENCES FOR DIFFUSION STUDIES

The amorphous nature of the as-received samples of  $\text{Fe}_{79}\text{B}_{16}\text{Si}_5$  and  $\text{Fe}_{78}\text{B}_{13}\text{Si}_9$  is maintained even when the glasses are heated upto  $400^\circ\text{C}$  for different time periods not exceeding 16 hr.

In the case of amorphous  $\text{Fe}_{79}\text{B}_{16}\text{Si}_5$  glass the crystallization process appears to commence when the sample is heated at  $450^\circ$  for 4 hr or more. Thus the diffusion studies of this metallic glass, while annealing upto  $450^\circ\text{C}$  (4 hr) corresponds to the diffusion process in the amorphous phase.

For the  $\text{Fe}_{78}\text{B}_{13}\text{Si}_9$  samples, the crystallization process starts after heat-treatment at  $475^\circ\text{C}$  for 1 hr. Thus, in this metallic glass the diffusion data obtained upto  $475^\circ\text{C}$  (1 hr) belongs to the diffusion process in the amorphous phase.

Since we found that the crystallization process of these glasses was not complete even when heated upto  $475^\circ\text{C}$  for 8 hr, the diffusion data obtained in this temperature region will neither belong to the amorphous phase nor to the crystalline phase.

The magnetization direction in the Fe-B-Si glasses have been found to change their direction on annealing.

Against this background of extensive investigation of structural changes occurring in these metallic glasses for long annealing durations below the reported crystallization temperature, we present our results of diffusion studies in these glasses, in the next chapter. The investigations reported in this chapter have helped us to identify the range of temperature and time period of heat-treatment which can be employed for investigating diffusion coefficients in the amorphous structure of these metallic glasses.

## CHAPTER 5

### DIFFUSION STUDIES

#### 5.1 INTRODUCTION

The results of the diffusion measurements of Ge, Pd, Ag and Au in the metallic glasses  $\text{Fe}_{79}\text{B}_{16}\text{Si}_5$ ,  $\text{Fe}_{78}\text{B}_{13}\text{Si}_9$ , and  $\text{Fe}_{40}\text{Ni}_{38}\text{B}_{18}\text{Mo}_4$ , are presented in this chapter. The experimental set-up for the diffusion studies using Rutherford backscattering spectrometry (RBS), has been explained in Chapter 3. The procedure of determining the diffusion coefficients from a given RBS spectrum of the annealed sample (diffusion couple) has been illustrated in section 3.5, for the case of diffusion of Pd in  $\text{Fe}_{79}\text{B}_{16}\text{Si}_5$ . The RBS spectra, the simulations and the diffusion data are presented in sections 5.2 to 5.10 of this chapter. The time dependence of the diffusion coefficients has been presented for each diffusion couple, which is followed by the determination of the activation energy ( $Q$ ) and the pre-exponential factor ( $D_0$ ) in the relaxed amorphous state. In order to clarify the figures and make each section self-explanatory, a repetition in presenting the diffusion results for the various diffusion couples became unavoidable. A discussion on the observed diffusion data is given in sections 5.11 to 5.14. The changes occurring in the diffusion coefficients, before relaxation, during relaxation and in the relaxed state have been exemplified in these sections. Important correlations have been presented between the radii of the diffusing elements and the diffusion coefficients. The last section 5.15, brings out the possible diffusion mechanisms in the metallic glasses inferred from the available diffusion data, on the basis of the theoretical formalism presented by *Nachtrieb and Handler [1954]*, *Seeger and Chik [1968]*, *Bokshteyn et al. [1980]*.

## 5.2 DIFFUSION OF Ge IN METALLIC GLASS $\text{Fe}_{79}\text{B}_{16}\text{Si}_5$

The metallic glass  $\text{Fe}_{79}\text{B}_{16}\text{Si}_5$  - Ge diffusion couples were annealed at temperatures and time periods mentioned in Table 5.1.

**TABLE 5.1**  
SAMPLE IDENTIFICATION FOR  $\text{Fe}_{79}\text{B}_{16}\text{Si}_5$  - Ge DIFFUSION COUPLE

SAMPLE NUMBER	FILM ( $\text{\AA}$ ) THICKNESS	ANNEAL TEMP( $^{\circ}\text{C}$ )	ANNEAL TIME(hr)
MG252/Ge	345	300	1, 2, 4, 8, 12, 16
MG248/Ge	320	350	1, 2, 4, 8, 12, 16
MG247/Ge	300	400	1, 2, 4, 8, 12, 16
MG253/Ge	330	450	1, 2, 4, 8, 12, 16
MG254/Ge	315	475	1, 2, 4, 8, 12, 16

The backscattering spectrum obtained from the as-evaporated film of Ge on the metallic glass  $\text{Fe}_{79}\text{B}_{16}\text{Si}_5$  is shown in Figure 5.1, along with the spectra obtained after the heat-treatment of the sample for 2 hr, and 8 hr at  $400^{\circ}\text{C}$ . The normalized yields have been plotted in order to make these spectra directly comparable, as described earlier in (sec.3.5). The experimental parameters of the backscattering measurements for this sample are also mentioned in the figure. The thickness of the as-evaporated Ge film (calculated from the RBS spectrum) for this diffusion couple is  $300 \text{ \AA}$  (see Table 5.1). The surface positions for Ge and Fe are indicated in the figure. The surface position for boron appears at channel number 66 (energy 327 keV) and that for silicon at channel number 281 (energy 819.5 keV). These signals cannot be distinguished because of the background formed by the thick target yield and hence are not depicted in the figure. The expanded form (from channel number 360 to 430) of the spectrum has been presented so that the changes occurring in the spectrum around the interface of the metallic glass and Ge film can be clearly observed. The diffusion of Ge in the metallic glass after annealing at  $400^{\circ}\text{C}$  is indicated

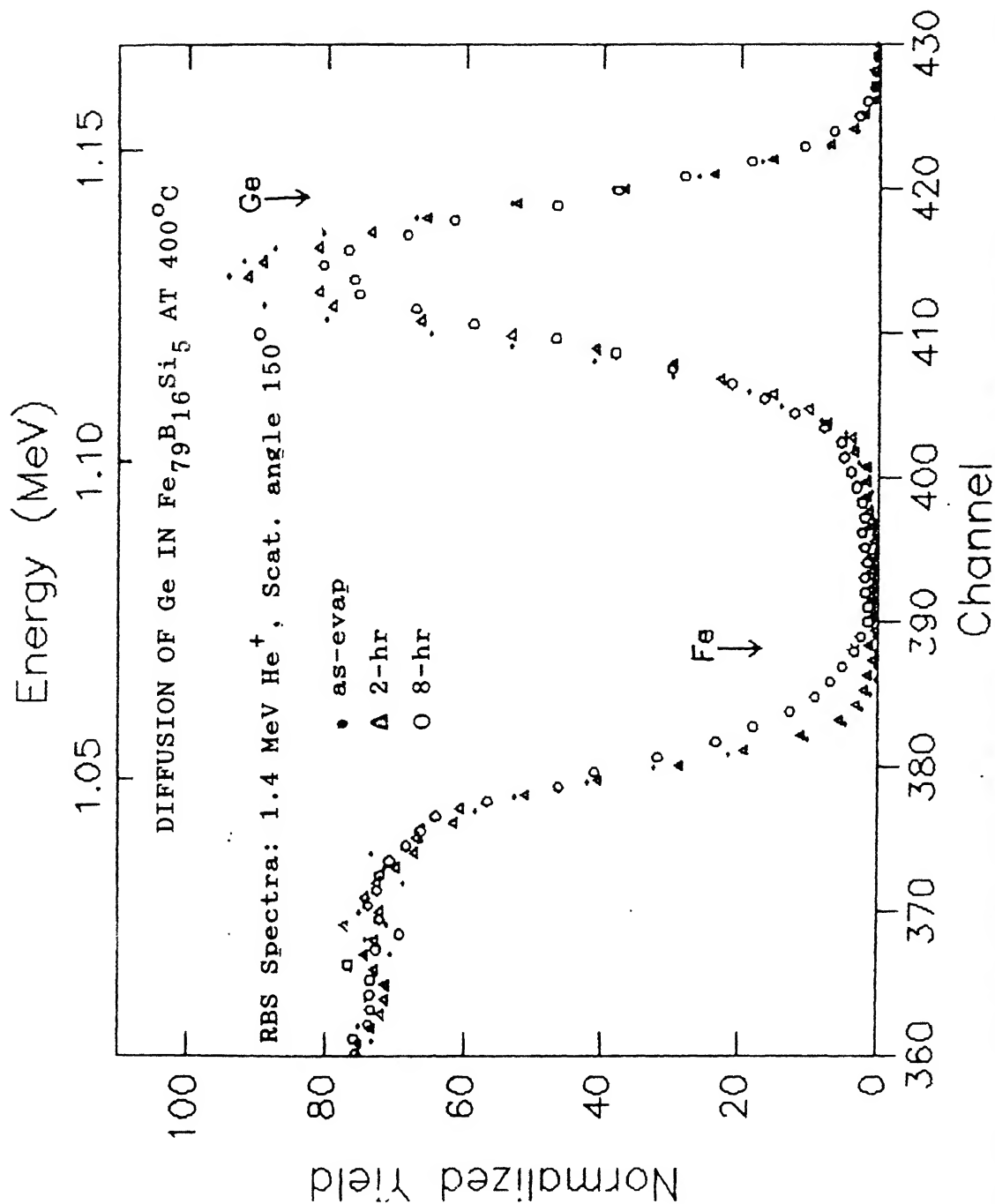


FIGURE 5.1 Normalised RBS spectra of  $\text{Fe}_{79}\text{B}_{16}\text{Si}_5$ -Ge diffusion couple before and after annealing at  $400^\circ\text{C}$  for 2 hr and 8 hr respectively. The thickness of the as-evaporated film is  $300 \text{ \AA}$ . The arrow indicates the surface position.

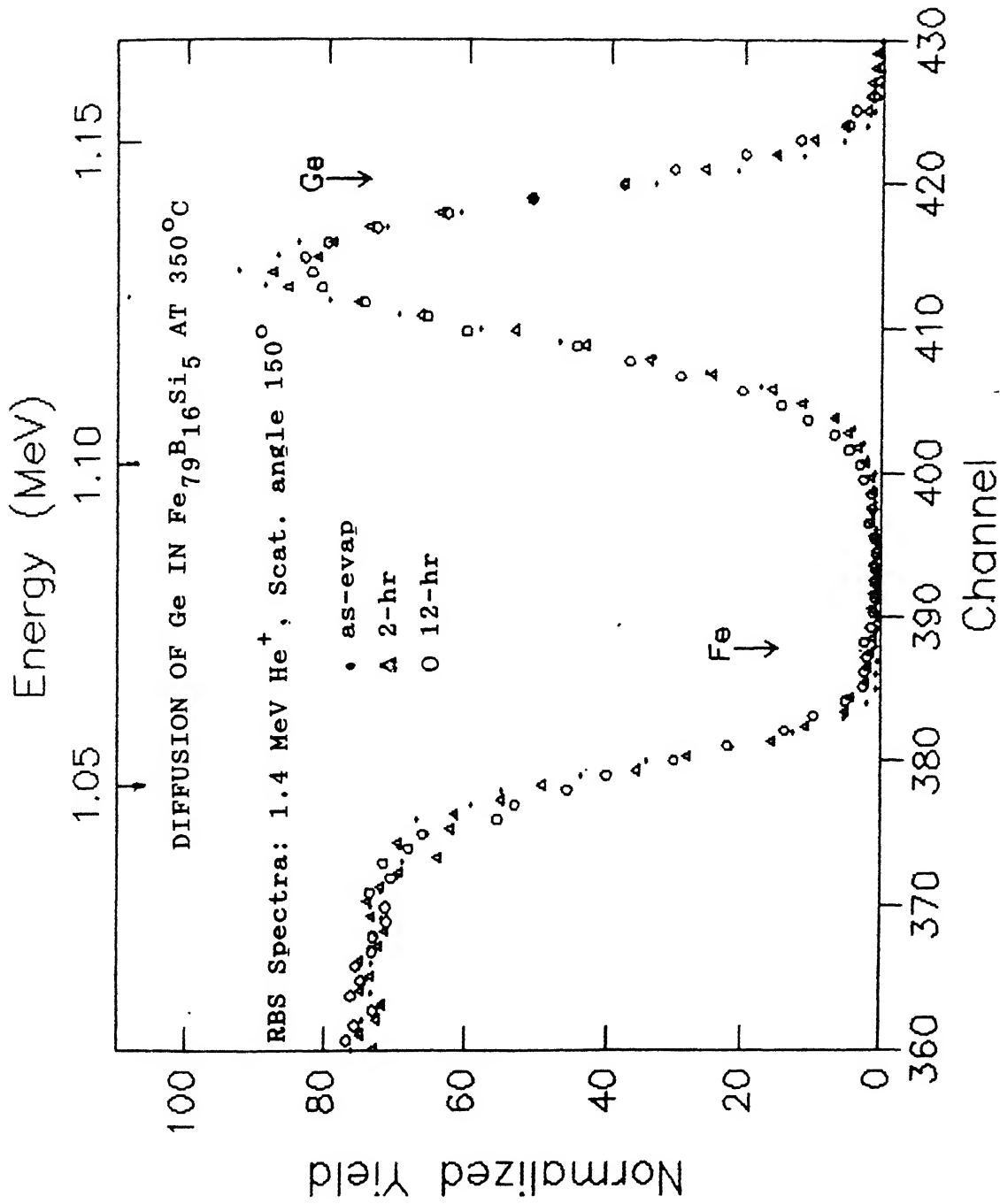
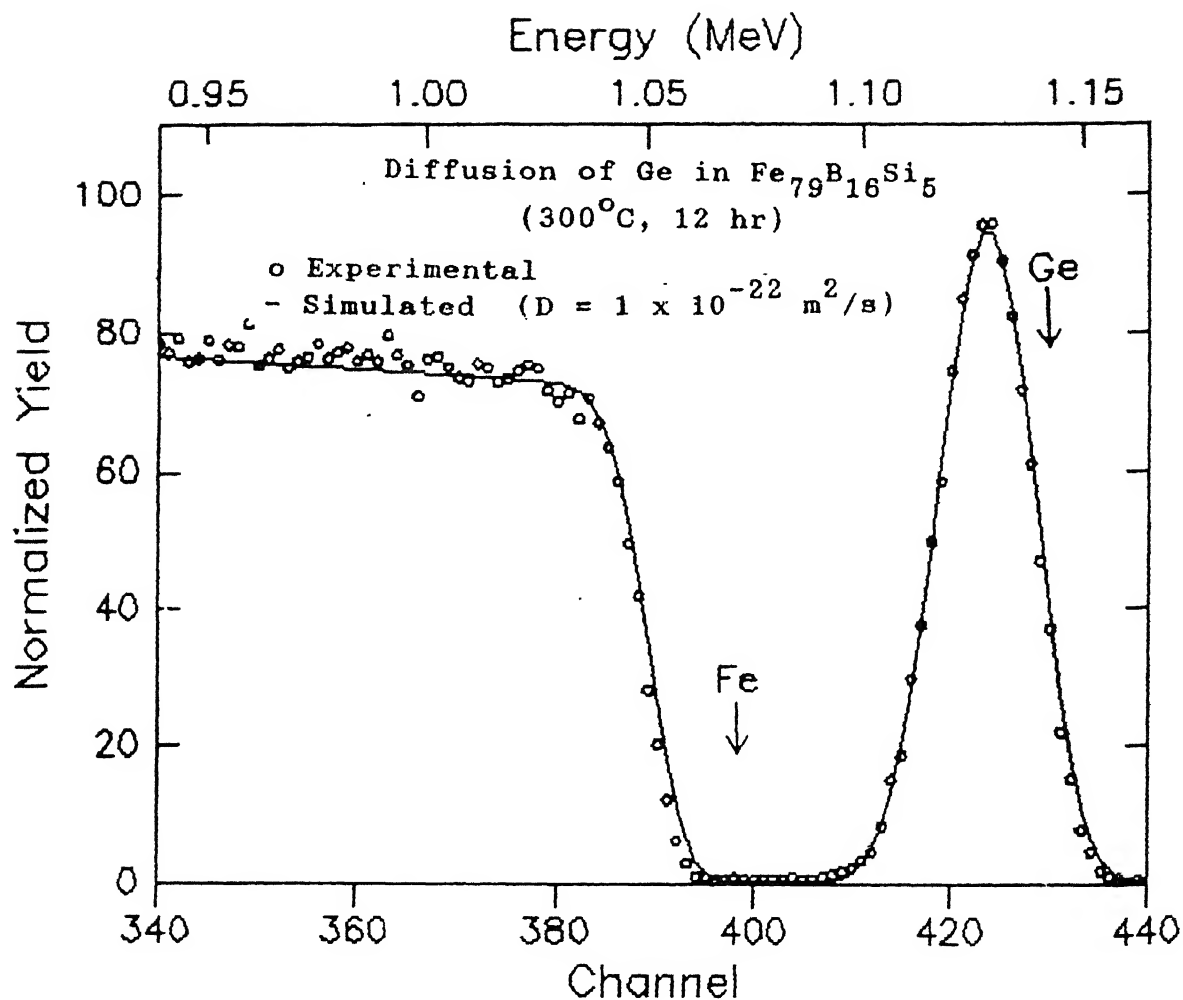
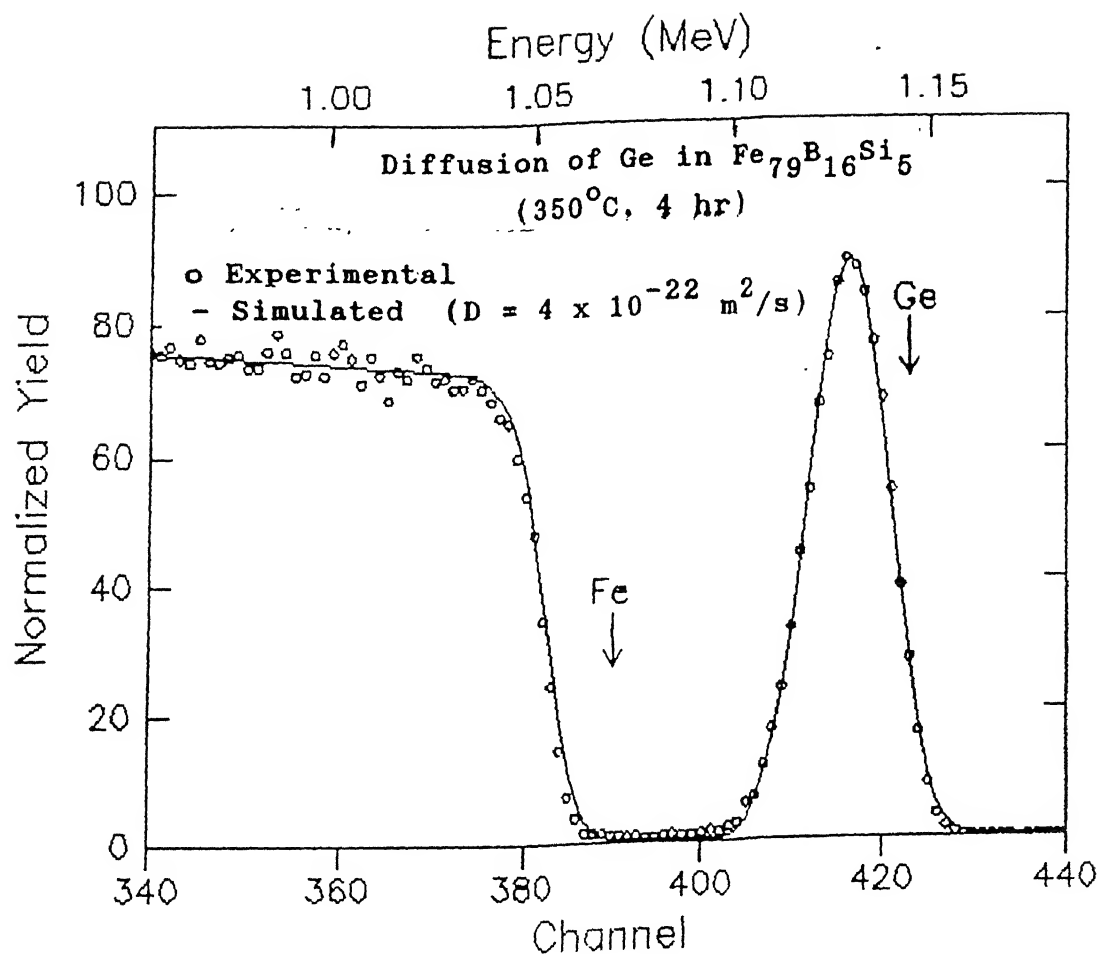


FIGURE 5.2 Normalised RBS spectra of Fe<sub>79</sub>B<sub>16</sub>Si<sub>5</sub>-Ge diffusion couple before and after annealing at 350°C for 2 hr and 12 hr respectively. The thickness of the as-evaporated film is 320 Å. The arrow indicates the surface position.





**FIGURE 5.3** Comparison of experimental (1.4 MeV  $\text{He}^+$ , scattering angle  $150^\circ$ ) and simulated RBS spectra to determine the D-value of Ge in  $\text{Fe}_{79}\text{B}_{16}\text{Si}_5$  at 300°C (12 hr). The simulation was performed using the error function solution of the diffusion equation (refer section 1.4.3).



**FIGURE 5.4** Comparison of experimental (1.4 MeV  $\text{He}^+$ , scattering angle  $150^\circ$ ) and simulated RBS spectra to determine the  $D$ -value of Ge in  $\text{Fe}_{79}\text{B}_{16}\text{Si}_5$  at 350°C (4 hr). The simulation was performed using the error function solution of the diffusion equation (refer section 1.4.3).

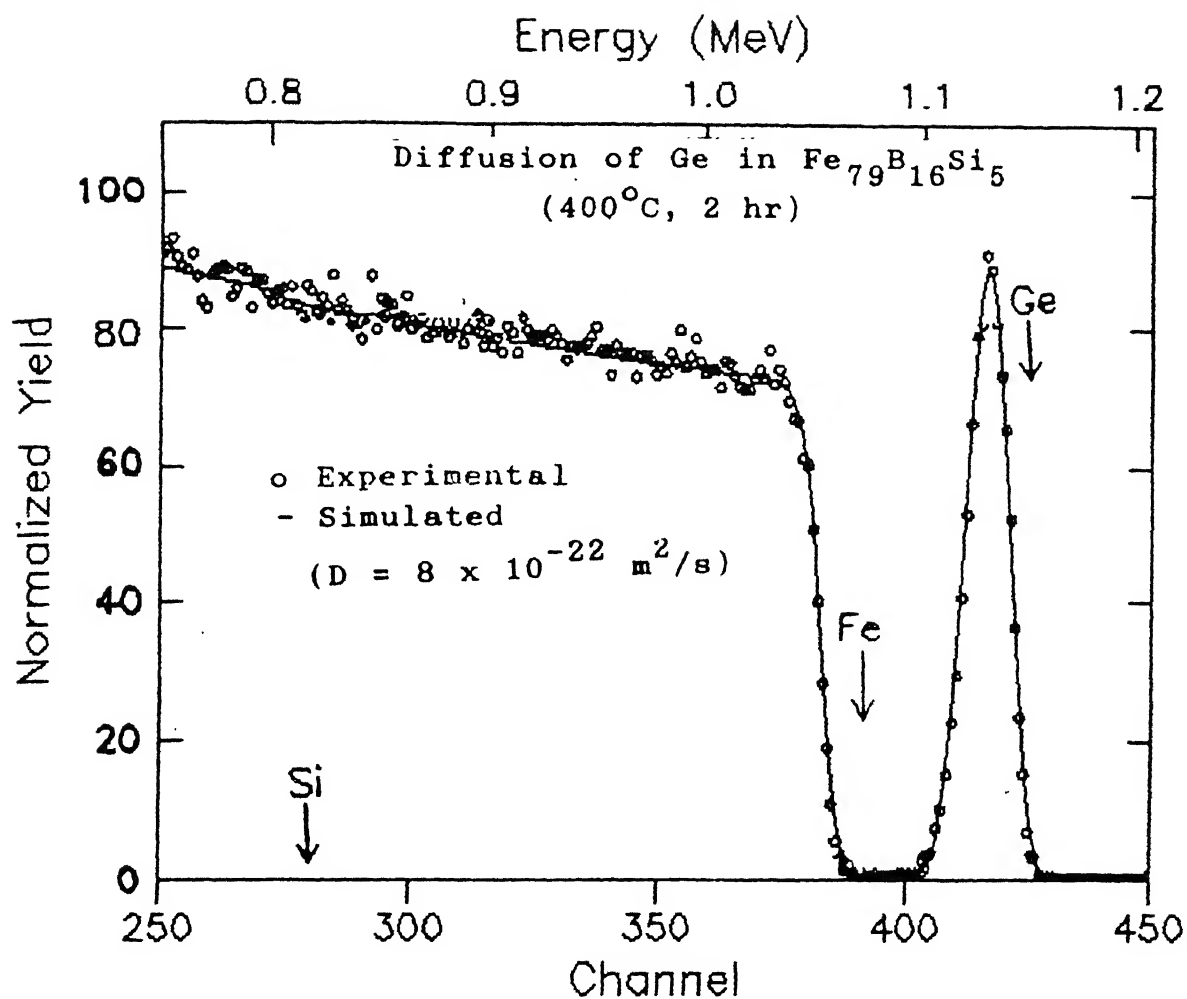


**FIGURE 5.5** Comparison of experimental (1.4 MeV  $\text{He}^+$ , scattering angle  $150^\circ$ ) and simulated RBS spectra to determine the D-value of Ge in  $\text{Fe}_{79}\text{B}_{16}\text{Si}_5$  at 400°C (2 hr). The simulation was performed using the error function solution of the diffusion equation (refer section 1.4.3).

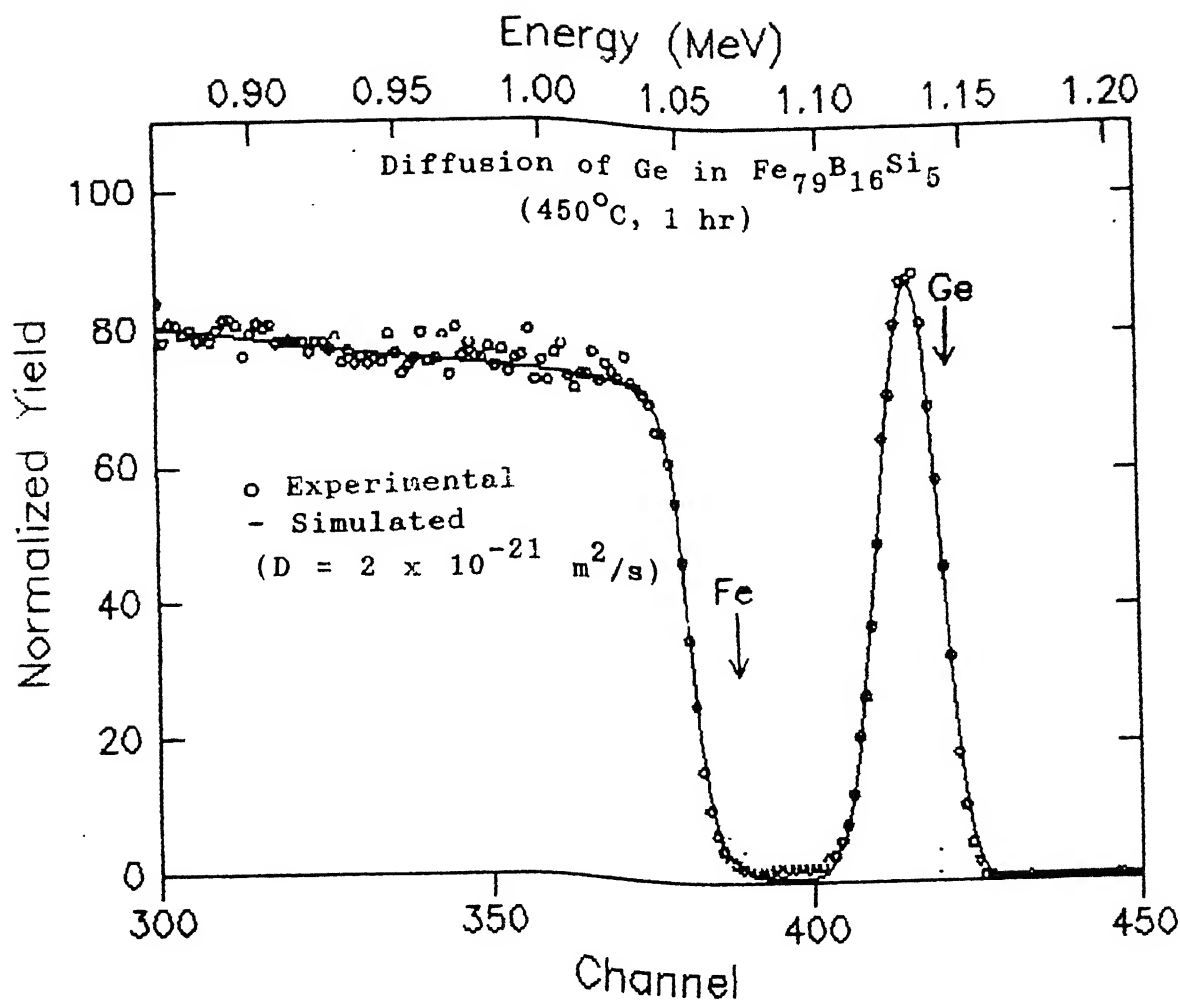


**FIGURE 5.6** Comparison of experimental (1.4 MeV  $\text{He}^+$ , scattering angle  $150^\circ$ ) and simulated RBS spectra to determine the D-value of Ge in  $\text{Fe}_{79}\text{B}_{16}\text{Si}_5$  at 450°C (1 hr). The simulation was performed using the error function solution of the diffusion equation (refer section 1.4.3).

by (i) the broadening of the FWHM of the Ge peak; and (ii) the appearance of the RBS signals from Ge at lower energies.

Another set of RBS spectra obtained from a similar diffusion couple isothermally annealed at  $350^{\circ}\text{C}$  is shown in Figure 5.2, for the annealing durations as indicated in the figure. The spectra in the Figures 5.1 and 5.2 illustrate the changes occurring in the RBS profile as a function of anneal time.

Each RBS spectrum was analyzed to obtain the diffusion coefficient for a particular annealing temperature and duration (refer Table 5.1), following the procedure of the diffusion analysis by simulation described earlier in Chapter 3. The results of the simulations for a few typical cases  $\{300^{\circ}\text{C}$  (12 hr),  $350^{\circ}\text{C}$  (4 hr),  $400^{\circ}\text{C}$  (2 hr), and  $450^{\circ}\text{C}$  (1 hr) $\}$  are shown in Figures 5.3 to 5.6, where the experimental spectrum has been compared in each case with the simulated one. The diffusion coefficients obtained from this analysis are denoted by  $D(t)$ , where  $t$  is the annealing time, and are given in Table 5.2 for each annealing temperature and time period.

These diffusion coefficients are then utilized to study the dependence of the  $D(t)$ -values on the annealing time and the dependence of diffusivity on the reciprocal of the annealing temperature, in order to obtain information regarding the relaxation behaviour and the activation energies. The error in the  $D(t)$  values is  $\pm 30\%$ .

### 5.2.1 Dependence of $D(t)$ on annealing time

The diffusion coefficient of Ge in  $\text{Fe}_{79}\text{B}_{16}\text{Si}_5$  evaluated at various annealing periods at the annealing temperature of  $300^{\circ}\text{C}$ ,  $350^{\circ}\text{C}$ ,  $400^{\circ}\text{C}$ ,  $450^{\circ}\text{C}$  and  $475^{\circ}\text{C}$  are plotted in Figures 5.7 (a)-(e), respectively. These figures depict the changes occurring in the  $D(t)$  values as a function of annealing time ( $t$ ). There are not many studies of the dependence of the diffusion coefficient on the annealing time ( $t$ ) in metallic glasses. The studies reported so far have

TABLE 5.2  
THE D-VALUES FOR THE DIFFUSION OF  
Ge IN METALLIC GLASS  $\text{Fe}_{79}\text{B}_{16}\text{Si}_5$

ANNEALING TEMP ( $^{\circ}\text{C}$ )	ANNEALING TIME (s)	$D(t), \text{m}^2/\text{s}$ *
300	3600	$1.00 \times 10^{-21}$
300	7200	$7.50 \times 10^{-22}$
300	14400	$3.50 \times 10^{-22}$
300	28800	$2.00 \times 10^{-22}$
300	43200	$1.00 \times 10^{-22}$
300	57600	$1.00 \times 10^{-22}$
350	3600	$8.00 \times 10^{-22}$
350	7200	$5.00 \times 10^{-22}$
350	14400	$4.00 \times 10^{-22}$
350	28800	$3.00 \times 10^{-22}$
350	43200	$2.80 \times 10^{-22}$
350	57600	$2.00 \times 10^{-22}$
400	3600	$1.00 \times 10^{-21}$
400	7200	$8.00 \times 10^{-22}$
400	14400	$8.00 \times 10^{-22}$
400	28800	$8.00 \times 10^{-22}$
400	43200	$5.00 \times 10^{-22}$
400	57600	$4.50 \times 10^{-22}$
450	3600	$2.00 \times 10^{-21}$
450	7200	$1.80 \times 10^{-21}$
450	14400	$9.00 \times 10^{-22}$
450	28800	$5.00 \times 10^{-22}$
450	43200	$4.00 \times 10^{-22}$
450	57600	$2.20 \times 10^{-22}$
475	3600	$3.00 \times 10^{-21}$
475	7200	$3.00 \times 10^{-21}$
475	14400	$8.00 \times 10^{-22}$
475	28800	$4.00 \times 10^{-22}$
475	43200	$3.00 \times 10^{-22}$
475	57600	$1.80 \times 10^{-22}$

\*The error in D is  $\pm 30\%$

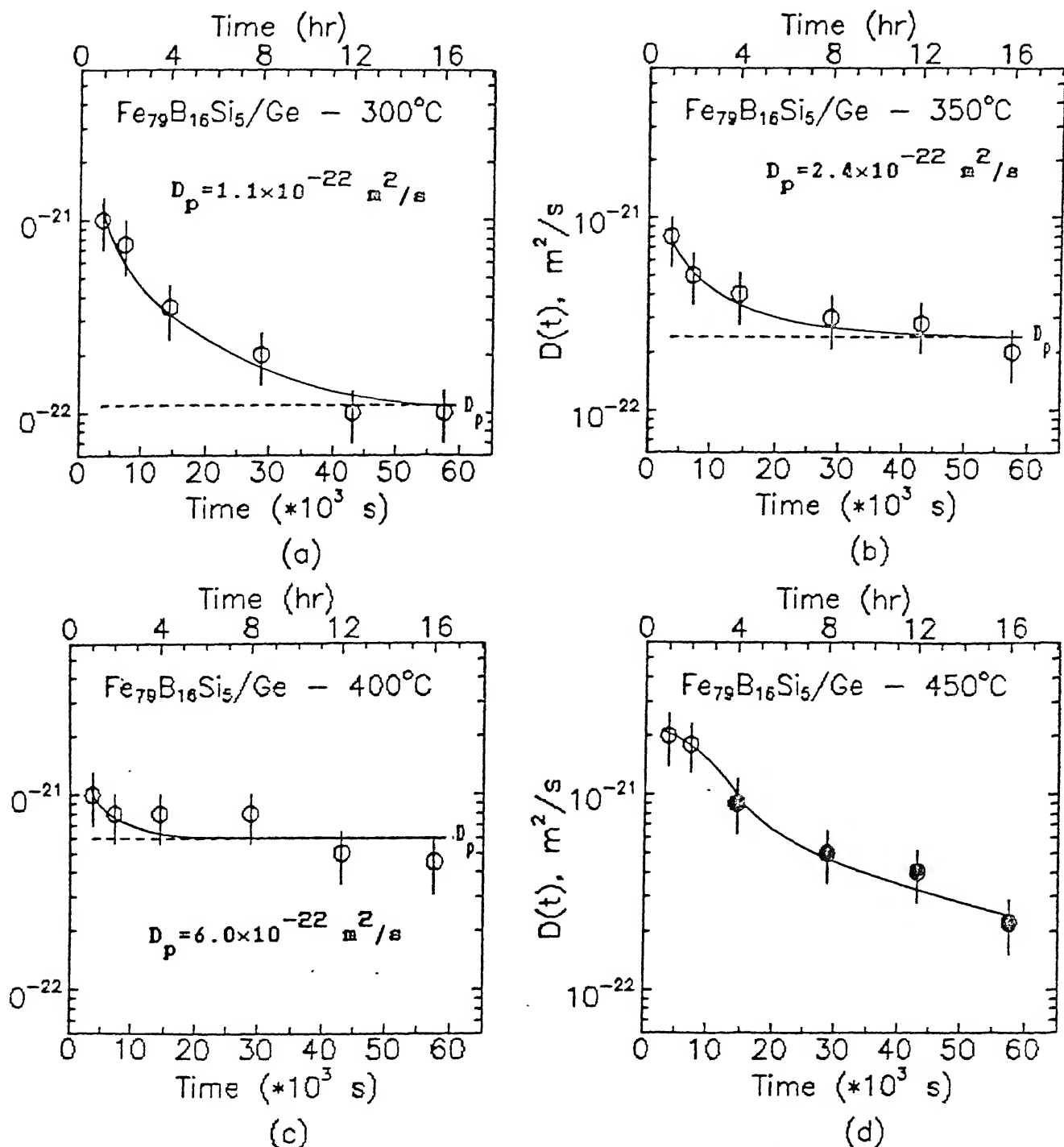


FIGURE 5.7(a)-(d) Diagrams showing variation of the diffusion coefficient  $D(t)$  as a function of annealing time  $t$ , for diffusion of Ge in  $\text{Fe}_{79}\text{B}_{16}\text{Si}_5$ . The vertical bars on the data points indicate error in the diffusion coefficients. The solid circles indicate that the crystallization of the metallic glass is observed by us using X-ray and Mössbauer techniques for these data points. The solid line, drawn as a best visual fit to the data points, asymptotically approaches a plateau value ( $D_p$ ) shown by the dashed line (except for  $450^\circ\text{C}$ , see text).

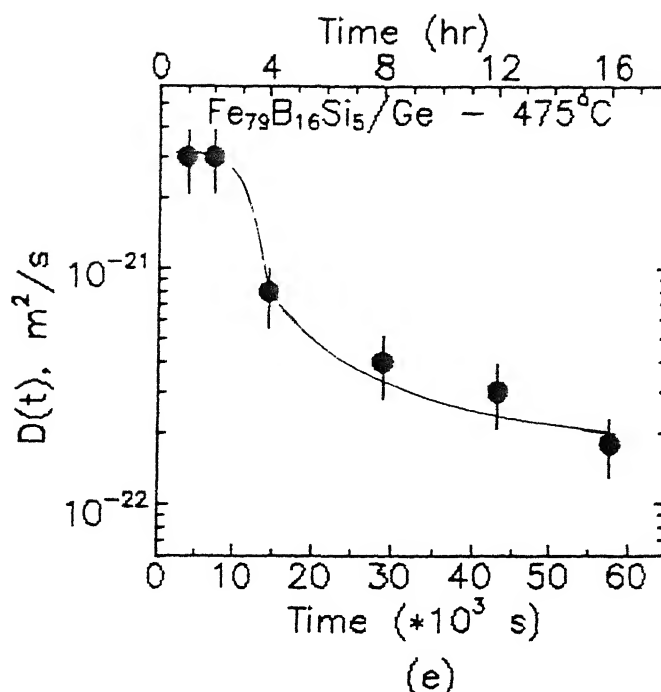


FIGURE 5.7(e) Diagram showing variation of the diffusion coefficient  $D(t)$  as a function of annealing time  $t$ , for diffusion of Ge in  $\text{Fe}_{79}\text{B}_{16}\text{Si}_5$  at  $475^\circ\text{C}$ . In this case crystallization has been observed by us using X-ray and Mössbauer techniques for all the data points. The solid line indicates a best visual fit to the data points.

employed the tracer technique for studying the behaviour of  $D(t)$  in Fe-Ni-B [Pfahler et al. 1985, Horvath et al. 1985], Fe-Si-B [Horvath et al. 1988], Fe-Zr [Horvath et al. 1988], and Co-Zr [Mehrer and Dorner 1989]. The behaviour of  $D(t)$  versus  $t$  observed by us for the diffusion of Ge in  $\text{Fe}_{79}\text{B}_{16}\text{Si}_5$  (Figures 5.7 (a) to (e)) is similar to that reported by the above workers in that for a given temperature  $T$ ,  $D(t)$  decreases smoothly with  $t$  and reaches an almost flat plateau at large  $t$ . We consider these solid lines as best visual fits to the data points taking into account the error bars on the  $D(t)$  values. The results in Figure 5.7 also show that  $D(t)$  falls by a factor of 2 to 15 (depending on the temperature of annealing) between  $t=0$  and  $t=16$  hr. Similar decrease has been observed previously [Pfahler et al. 1985, Horvath and Mehrer 1986, Horvath et al. 1988,



and Mehrer and Dorner 1989] and it has been attributed to the structural relaxation in the amorphous host material. The  $D(t)$  versus  $t$  curves for the annealing temperatures of  $300^{\circ}\text{C}$ ,  $350^{\circ}\text{C}$  and  $400^{\circ}\text{C}$ , asymptotically approach a plateau value  $D(t)=D_p$  and the horizontal dashed lines in Figures 5.7 (a), (b) and (c) indicate the line  $D(t)=D_p$ . These  $D_p$  values represent the diffusion process in the 'relaxed' amorphous phase of the metallic glass. When the annealing temperature is raised to  $450^{\circ}\text{C}$  or  $475^{\circ}\text{C}$ , the nature of the  $D(t)$  versus  $t$  curve changes. It is also observed from Figures 5.7 (c), (d) and (e), that in the range  $t \leq 2$  hr the  $D(t)$  values observed for  $450^{\circ}\text{C}$  and  $475^{\circ}\text{C}$  anneal are higher than the corresponding values of  $D(t)$  for  $400^{\circ}\text{C}$ . However this trend is reversed at higher values of  $t$ , and the value of  $D(t)$  at  $t=16$  hr is lower for  $450^{\circ}\text{C}$  and  $475^{\circ}\text{C}$  anneal compared to  $400^{\circ}\text{C}$ . An explanation of this behaviour is found in the crystallization kinetics in the host metallic glasses. Previous studies [Cahn et al. 1980, Horvath and Mehrer 1986, Horvath et al. 1988, Bohac et al. 1989], have shown that the diffusion coefficient in the crystalline phase of metallic glass can be lower than that observed in the amorphous phase by almost a factor of 10 or so. The above explanation can be checked against our results obtained by X-ray diffraction technique and Mössbauer spectroscopy reported in Chapter 4. These measurements clearly indicate that the crystallization of the metallic glass  $\text{Fe}_{79}\text{B}_{16}\text{Si}_5$  has commenced when it is annealed at  $450^{\circ}\text{C}$  for 4 hr, and is not yet complete even when annealed at  $475^{\circ}\text{C}$  for 16 hr. In view of these results the behaviour observed in Figures 5.7 (d) and (e) is attributed to the process of crystallization occurring at  $450^{\circ}\text{C}$  ( $t \geq 4$  hr) and  $475^{\circ}\text{C}$  ( $t=1$  to 16 hr). We, therefore, assumed that the diffusion coefficients obtained by us for samples annealed at  $450^{\circ}\text{C}$  ( $t \geq 4$  hr) and  $475^{\circ}\text{C}$  ( $t=1$  to 16 hr) do not represent diffusion in the amorphous phase of the host metallic glass. These data points are, therefore, shown as solid circles in Figures 5.7 (d) and (e). On the other hand the data points which represent diffusion in the amorphous phase of the host

metallic glass are shown as open circles (Figures 5.7 (a) - (d)). It is obvious that a plateau value representing diffusion in the relaxed amorphous phase could not be assigned for the 450°C and 475°C anneal. Although the  $D(t)$  values for  $t < 4$  hr at 450°C anneal, belong to the diffusion process in the amorphous phase, it cannot be stated with certainty whether these  $D(t)$  values represent diffusion in a completely 'relaxed' amorphous host material.

### 5.2.2 Dependence of $D$ on annealing temperature

In diffusion measurements, it is necessary to study the temperature dependence of diffusivity in order to examine the Arrhenius type behaviour given by the equation

$$D = D_0 \exp\left(-\frac{Q}{kT}\right) \quad (5.1)$$

where  $D_0$  is the pre-exponential factor,  $Q$  is the activation energy,  $k$  is the Boltzmann constant and  $T$  is the annealing temperature (in °K). This is done by plotting a graph of the diffusion coefficients against the reciprocal of the respective annealing temperatures, and the values of  $Q$  and  $D_0$  are determined. The evaluation of  $Q$  and  $D_0$  values and its systematic analysis helps in understanding the microscopic mechanism of the diffusion process in the host material. In crystalline materials, the diffusion coefficient is a function of the annealing temperature only and is independent of the annealing time. On the other hand, for metallic glasses, as mentioned above, the diffusion coefficient, for a particular temperature, depends on the annealing time as well. As a matter of fact such explicit time dependence has not been studied in most of the diffusion measurements in metallic glasses reported in the literature so far. Thus in most of the cases the problem regarding the choice of the diffusion coefficient value for a particular annealing temperature did not arise. As mentioned earlier in Sec. 5.2.1 explicit time dependence was first studied by Horvath *et al.* [1988], and these authors have used the plateau value  $D_p$

(obtained from tracer technique) for examining the Arrhenius type behaviour of diffusion in metallic glasses. The reason given for this choice is that this plateau value truly represents the diffusion in the relaxed amorphous phase. We decided to follow the approach of *Horvath et al.* [1988].

A plot of  $D_p$  vs.  $1/T$  is shown in Figure 5.8 and the straight line drawn therein is a least square fit to these data points. In Figure 5.8 the open circles refer to the data points corresponding to the amorphous phase of the host metallic glass, and the open squares correspond to the  $D(t)$  values annealed at  $450^\circ\text{C}$ , at those  $t$ -values for which crystallization was ruled out by the present X-ray diffraction and Mössbauer spectroscopic studies. As mentioned in Sec. 5.2.1, these values (open squares) at  $450^\circ\text{C}$ , belong to the diffusion process in the amorphous state but do not represent diffusion in a completely relaxed condition. Therefore, the data points for  $450^\circ\text{C}$  are not used in the least square fit and subsequent determination of the activation energy and pre-exponential factor. A comparative discussion of the diffusion behaviour at  $450^\circ\text{C}$  for this and all other diffusion couples described in the succeeding sections is presented in Sec. 5.12. It is pointed out that Figure 5.8 does not include any  $D(t)$  values for  $475^\circ\text{C}$  because our studies (Chapter 4) indicate onset of crystallization in the metallic glass at  $T=475^\circ\text{C}$ .

The values of  $Q$  and  $D_0$  obtained from a linear regression analysis [Bevington 1982, Sharma 1986] of the data (Figure 5.8) are

$$Q = 0.56 \pm 0.05 \text{ eV}$$

$$D_0 = 9.1^{+15}_{-5.7} \times 10^{-18} \text{ m}^2/\text{s}$$

with an error in  $Q$  being 9% and that in  $\log(D_0)$  being about 2.5%. These errors are of the same order as those generally reported in the literature [Sharma et al. 1988b]. A computer program used for the calculation of  $Q$  and  $D_0$  and their errors is given in Appendix 1.

### 5.3 DIFFUSION OF Ge IN METALLIC GLASS $\text{Fe}_{78}\text{B}_{13}\text{Si}_9$

The samples of the  $\text{Fe}_{78}\text{B}_{13}\text{Si}_9$  / Ge diffusion-couples were annealed at the temperature and time periods shown in Table 5.3.

TABLE 5.3  
SAMPLE IDENTIFICATION FOR  $\text{Fe}_{78}\text{B}_{13}\text{Si}_9$  - Ge DIFFUSION COUPLE

SAMPLE NUMBER	FILM ( $\text{\AA}$ ) THICKNESS	ANNEAL TEMP( $^{\circ}\text{C}$ )	ANNEAL TIME(hr)
MG249/Ge	260	300	1, 2, 4, 8, 12, 16
MG246/Ge	230	350	1, 2, 4, 8, 12, 16
MG245/Ge	280	400	1, 2, 4, 8, 12, 16
MG250/Ge	250	450	1, 2, 4, 8, 12, 16
MG251/Ge	210	475	1, 2, 4, 8, 12, 16

The presence of diffusion in this diffusion couple has been illustrated by comparing the RBS as-evaporated spectrum with the after-annealed spectra in Figures 5.9 and 5.10. The simulations for some typical cases are shown in Figures 5.11 to 5.13 for  $400^{\circ}\text{C}$  (1hr),  $350^{\circ}\text{C}$  (8hr) and  $300^{\circ}\text{C}$  (4hr) respectively. The experimental parameters and the sample layer description are tabulated below the figures in each case. The diffusion coefficients  $D(t)$  obtained from the simulations of each spectrum are given in Table 5.4 above. The error in the  $D(t)$  values is  $\pm 30\%$ .

#### 5.3.1 Dependence of $D(t)$ on annealing time

The diffusion coefficients (see Table 5.4) of this system are plotted as a function of annealing time in Figure 5.14(a)-(e) for the isothermal annealing temperatures of  $300^{\circ}\text{C}$ ,  $350^{\circ}\text{C}$ ,  $400^{\circ}\text{C}$ ,  $450^{\circ}\text{C}$  and  $475^{\circ}\text{C}$  respectively. The solid circles indicate that crystallization has been observed by X-ray diffraction and Mössbauer studies for these data points. And the open circles represent the diffusion process in the amorphous phase of the metallic glass. The features of

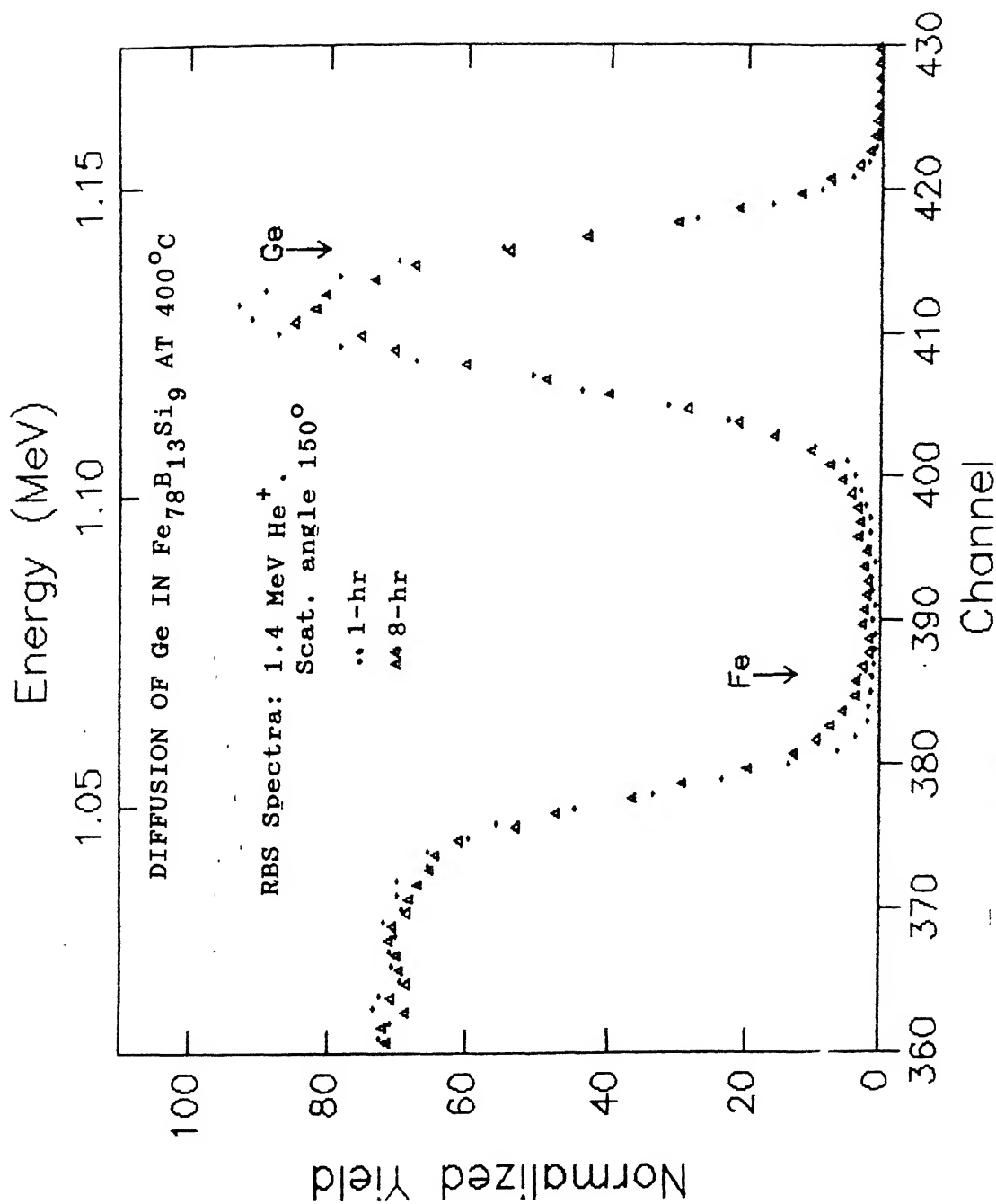


FIGURE 5.9 Normalised RBS spectra of  $\text{Fe}_{78}\text{B}_{13}\text{Si}_9$ -Ge diffusion couple before and after annealing at  $400^\circ\text{C}$  for 1 hr and 8 hr respectively. The thickness of the as-evaporated film is  $280 \text{ \AA}$ . The arrow indicates the surface position.

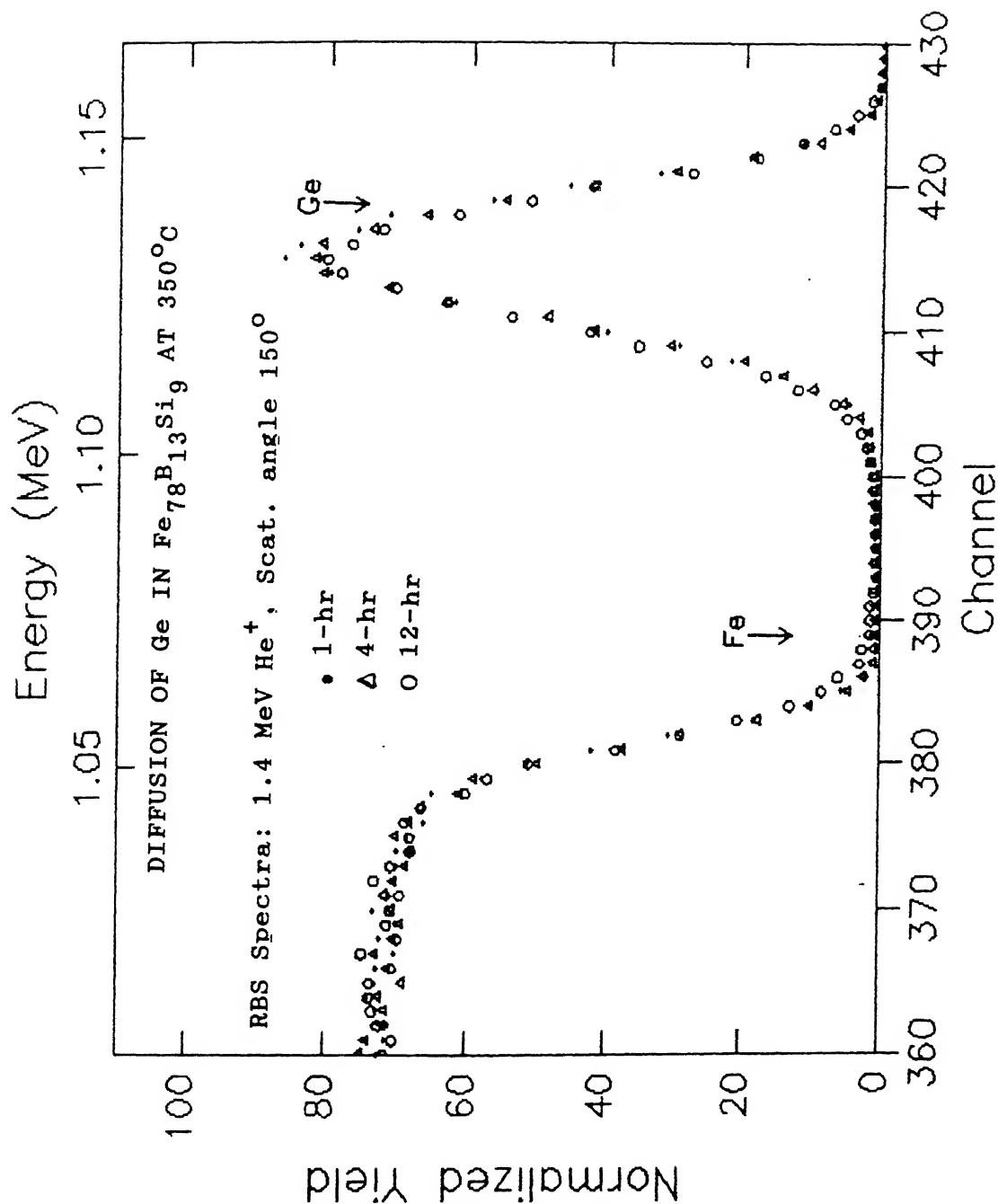


FIGURE 5.10 Normalised RBS spectra of  $\text{Fe}_{78}\text{B}_{13}\text{Si}_9$ -Ge diffusion couple before and after annealing at  $350^\circ\text{C}$  for 1 hr, 4 hr and 12 hr respectively. The thickness of the as-evaporated film is  $230 \text{ \AA}$ . The arrow indicates the surface position.

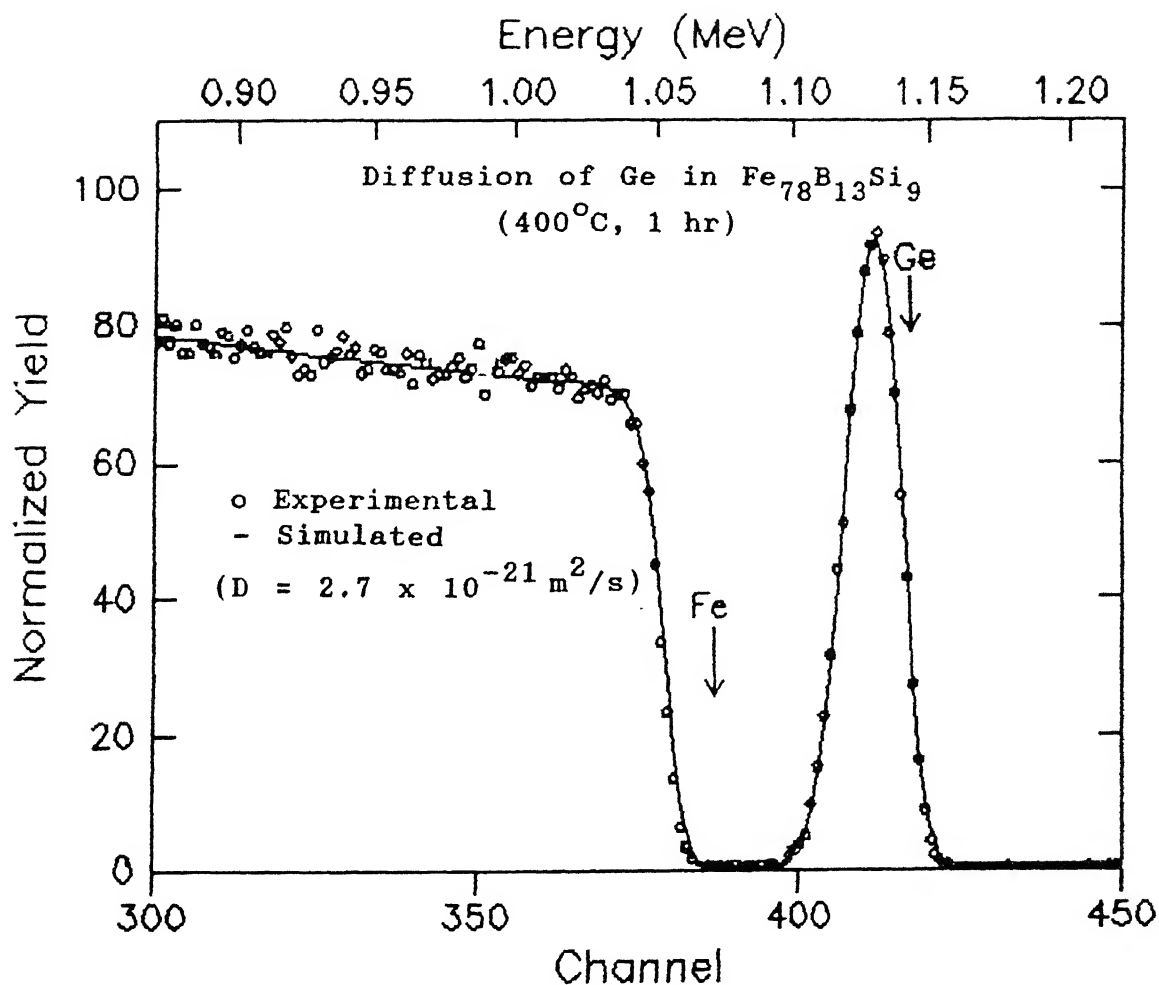
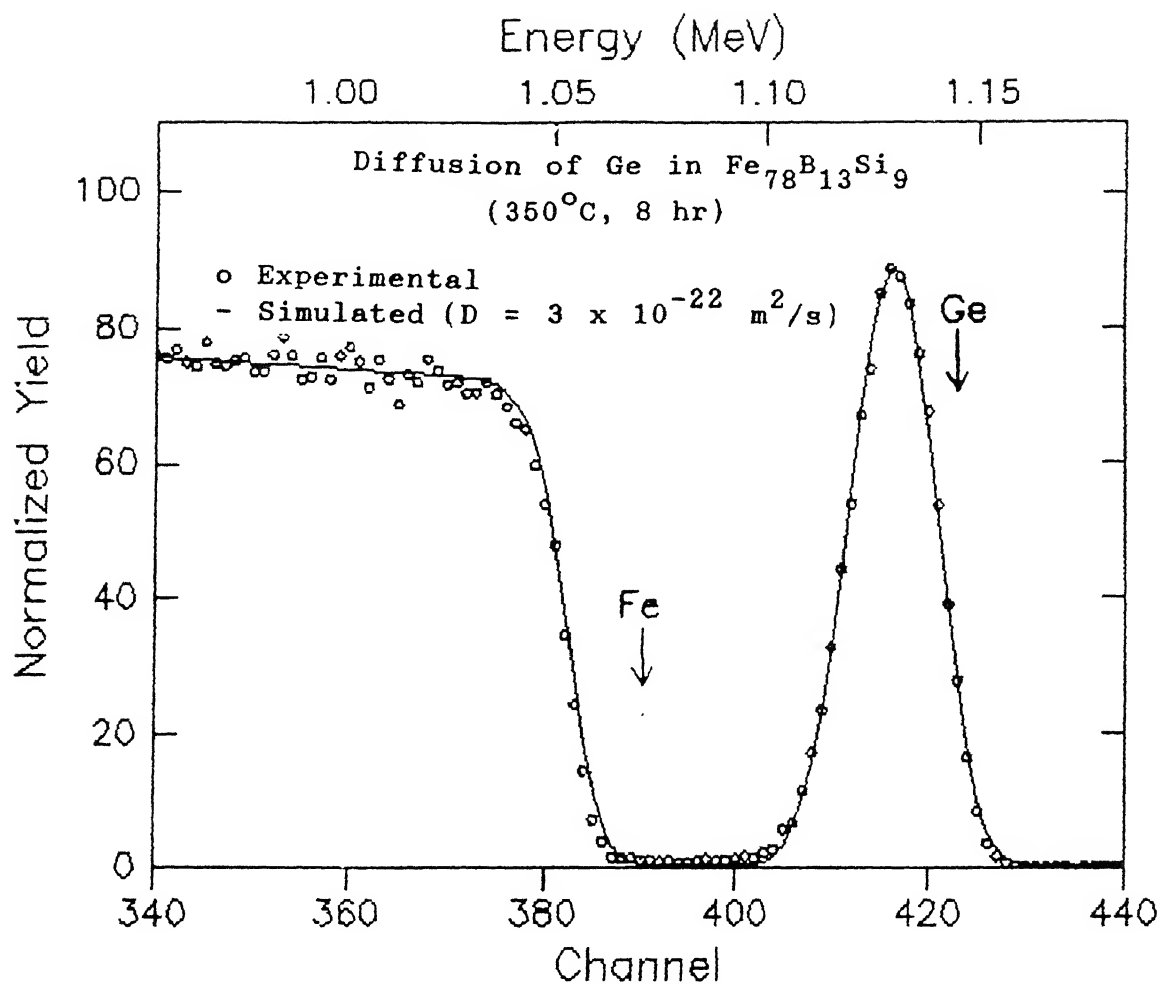
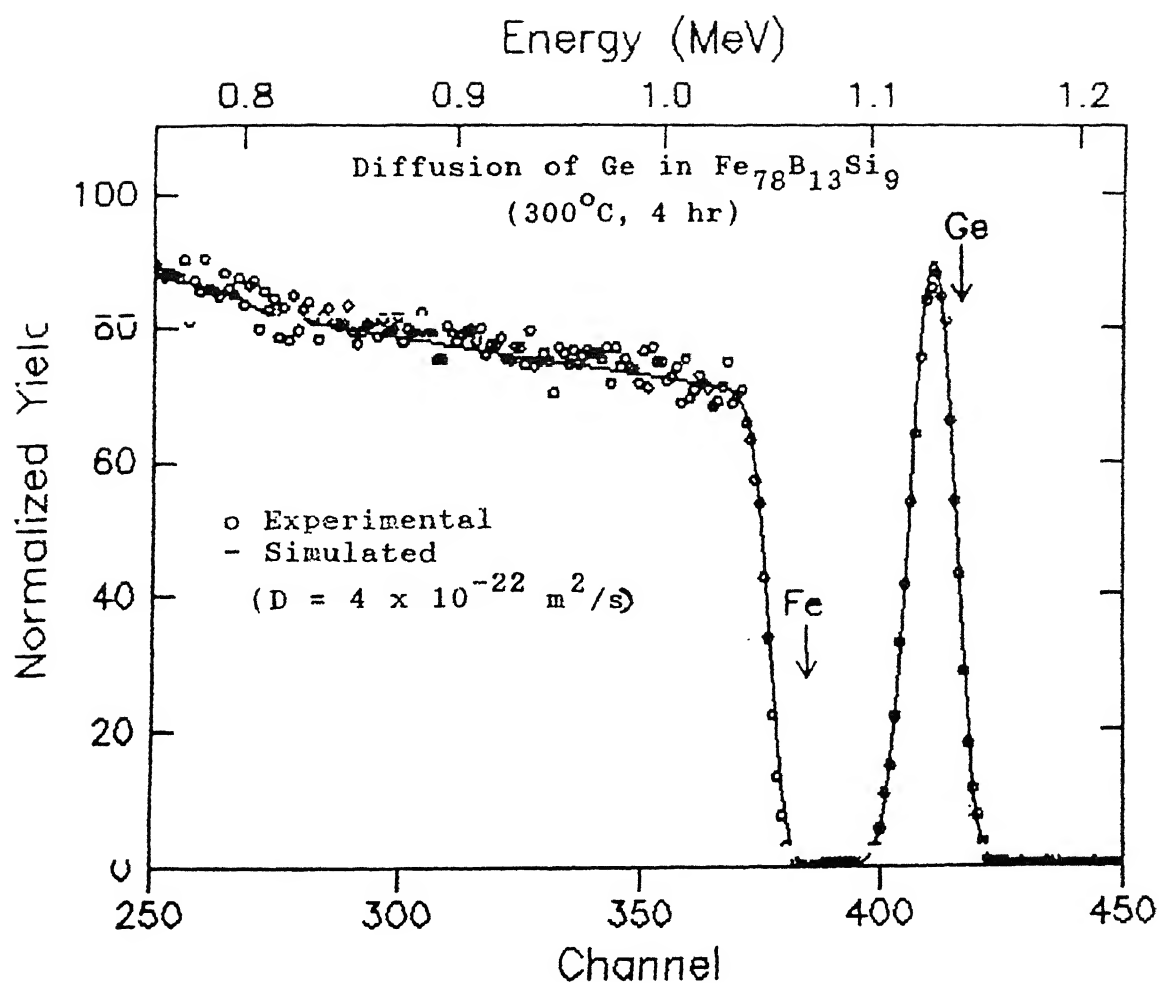


FIGURE 5.11 Comparison of experimental (1.4 MeV  $\text{He}^+$ , scattering angle  $150^\circ$ ) and simulated RBS spectra to determine the D-value of Ge in  $\text{Fe}_{78}\text{B}_{13}\text{Si}_9$  at 400°C (1 hr). The simulation was performed using the error function solution of the diffusion equation (refer section 1.4.3).



**FIGURE 5.12** Comparison of experimental (1.4 MeV  $\text{He}^+$ , scattering angle  $150^\circ$ ) and simulated RBS spectra to determine the D-value of Ge in  $\text{Fe}_{78}\text{B}_{13}\text{Si}_9$  at 350°C (8 hr). The simulation was performed using the error function solution of the diffusion equation (refer section 1.4.3).





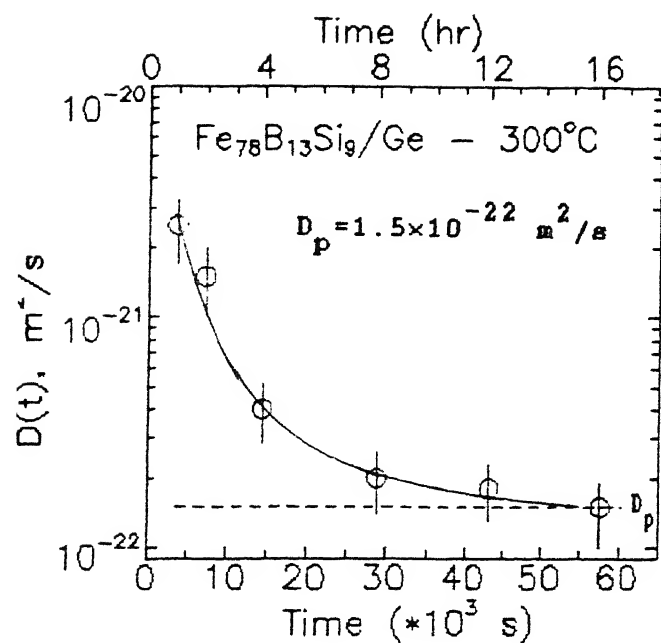
**FIGURE 5.13** Comparison of experimental (1.4 MeV  $\text{He}^+$ , scattering angle  $150^\circ$ ) and simulated RBS spectra to determine the D-value of Ge in  $\text{Fe}_{78}\text{B}_{13}\text{Si}_9$  at 300°C (4 hr). The simulation was performed using the error function solution of the diffusion equation (refer section 1.4.3).

TABLE 5.4

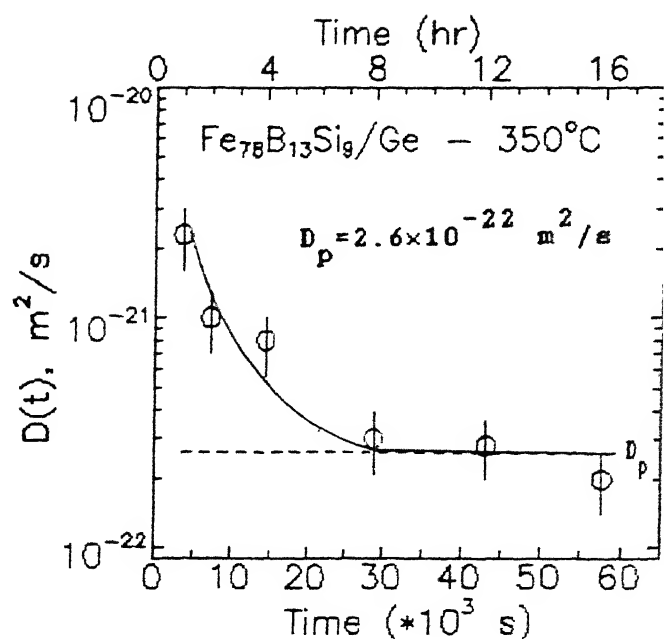
THE D-VALUES FOR THE DIFFUSION OF  
Ge IN METALLIC GLASS  $\text{Fe}_{78}\text{B}_{13}\text{Si}_9$

ANNEALING TEMP(°C)	ANNEALING TIME (s)	D(t), $\text{m}^2/\text{s}$ *
300	3600	$2.50 \times 10^{-21}$
300	7200	$1.50 \times 10^{-21}$
300	14400	$4.00 \times 10^{-22}$
300	28800	$2.00 \times 10^{-22}$
300	43200	$1.80 \times 10^{-22}$
300	57600	$1.50 \times 10^{-22}$
350	3600	$2.30 \times 10^{-21}$
350	7200	$1.00 \times 10^{-21}$
350	14400	$8.00 \times 10^{-22}$
350	28800	$3.00 \times 10^{-22}$
350	43200	$2.80 \times 10^{-22}$
350	57600	$2.00 \times 10^{-22}$
400	3600	$2.70 \times 10^{-21}$
400	7200	$1.00 \times 10^{-21}$
400	14400	$1.00 \times 10^{-21}$
400	28800	$1.00 \times 10^{-21}$
400	43200	$5.50 \times 10^{-22}$
400	57600	$1.00 \times 10^{-21}$
450	3600	$3.00 \times 10^{-21}$
450	7200	$1.75 \times 10^{-21}$
450	14400	$1.50 \times 10^{-21}$
450	28800	$5.00 \times 10^{-22}$
450	43200	$3.50 \times 10^{-22}$
450	57600	$2.00 \times 10^{-22}$
475	3600	$5.80 \times 10^{-21}$
475	7200	$3.20 \times 10^{-21}$
475	14400	$1.50 \times 10^{-21}$
475	28800	$8.50 \times 10^{-22}$
475	43200	$4.90 \times 10^{-22}$
475	57600	$4.00 \times 10^{-22}$

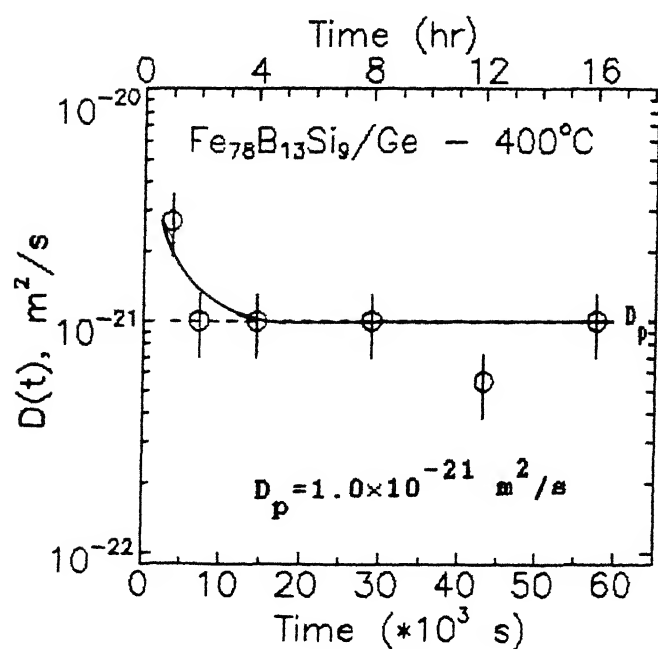
\*The error in D is  $\pm 30\%$



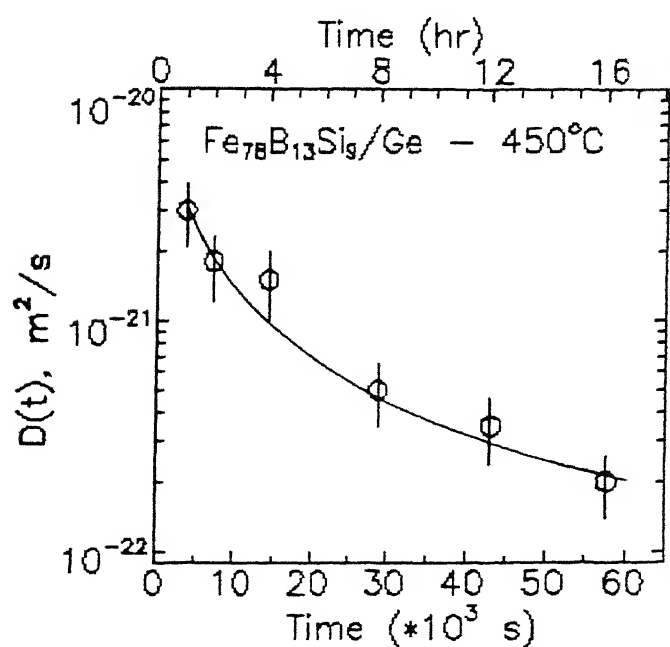
(a)



(b)



(c)



(d)

FIGURE 5.14 (a)-(d) Diagrams showing variation of the diffusion coefficient  $D(t)$  as a function of annealing time  $t$ , for diffusion of Ge in  $\text{Fe}_{78}\text{B}_{13}\text{Si}_9$ . The vertical bars on the data points indicate error in the diffusion coefficient. The solid line, drawn as a best visual fit to the data points, asymptotically approach a plateau value ( $D_p$ ) shown by the dashed line (except for  $450^\circ\text{C}$ , see text).

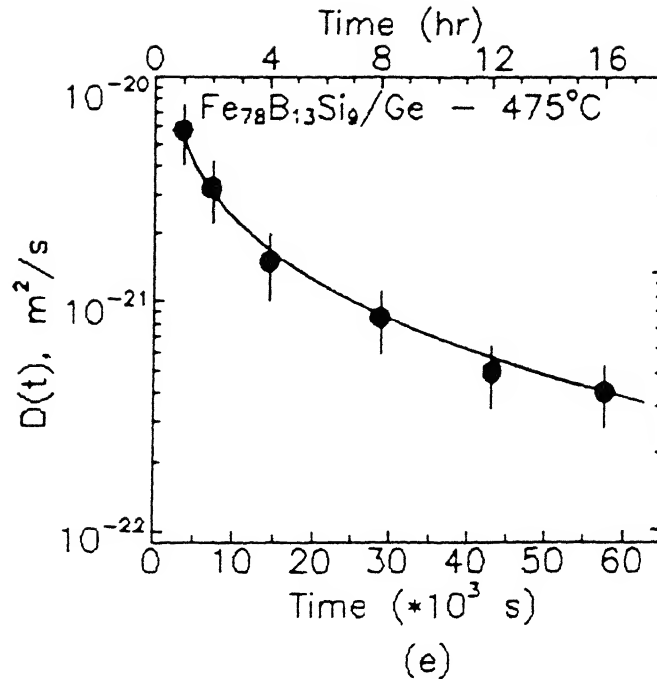


FIGURE 5.14 (e) Diagram showing variation of the diffusion coefficient  $D(t)$  as a function of annealing time  $t$ , for diffusion of Ge in  $\text{Fe}_{78}\text{B}_{13}\text{Si}_9$  at  $475^\circ\text{C}$ . In this case crystallization has been observed by us using X-ray and Mössbauer techniques for all the data points. The solid line indicates a best visual fit to the data points.

these plots are similar to that of Ge diffusion in  $\text{Fe}_{79}\text{B}_{16}\text{Si}_5$ , namely: (i) for a given temperature,  $D(t)$  decreases smoothly with  $t$  and reaches an almost flat plateau at large  $t$ . (ii) the  $D(t)$  values decrease by factor of 3 to 20 depending on the annealing temperature between  $t = 1$  hr and  $t = 16$  hr, (iii) for annealing temperatures of  $300^\circ\text{C}$ ,  $350^\circ\text{C}$  and  $400^\circ\text{C}$ ,  $D(t)$  asymptotically approaches a plateau value  $D(t)=D_p$  shown by the horizontal dashed lines in Figures 5.14 (a), (b) and (c), which represents the diffusion process in the 'relaxed' amorphous phase of the metallic glass.

The Mössbauer and X-ray diffraction results (mentioned in Chapter 4) indicate that in the metallic glass  $\text{Fe}_{78}\text{B}_{13}\text{Si}_9$  the amorphous to crystalline

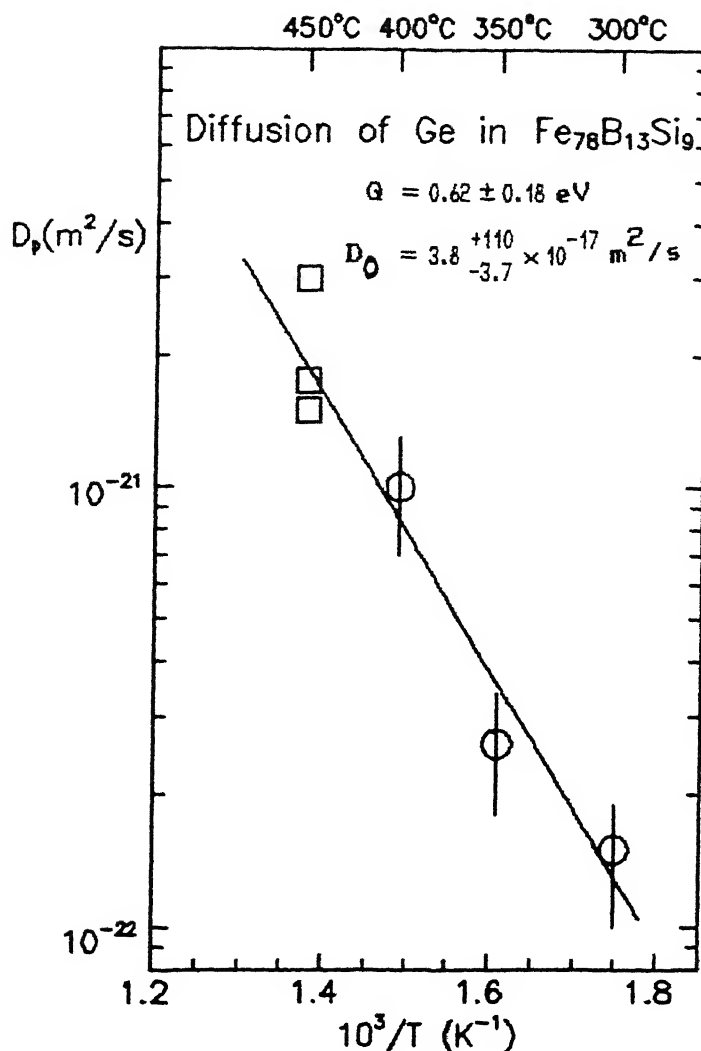


FIGURE 5.15 Temperature dependence of diffusivity of Ge in metallic glass  $\text{Fe}_{78}\text{B}_{13}\text{Si}_9$  (Arrhenius plot). The open circles indicate the plateau values ( $D_p$ ) obtained from the  $D(t)$  vs. annealing time diagrams (Figs. 5.14 (a),(b),(c)), and the solid line is a least square fitting to these data points. The values of  $Q$  and  $D_0$  obtained from the fit is also mentioned. The open squares depict the  $D(t)$  values at  $450^\circ\text{C}$  for  $t \leq 4$  hr. The  $D(t)$  values for  $475^\circ\text{C}$  are not shown because crystallization is observed at this temperature even for the lowest annealing duration.

transformation at 450°C annealing occurs for  $t > 16$  hr. However it may be noted that for this system the  $D(t)$  values at 450°C for  $t \geq 8$  hr are lower than the plateau value  $D_p$  at 400°C, suggesting occurrence of crystallization of this metallic glass at 450°C for  $t \geq 8$  hr due to the presence of Ge. Therefore a plateau value could not be assigned at this temperature.

### 5.3.2 Dependence of $D$ on annealing temperature

The Arrhenius plot of  $D_p$  versus  $1/T$  is shown in Figure 5.15 for diffusion of Ge in  $\text{Fe}_{78}\text{B}_{13}\text{Si}_9$ . The least square fitting has been done using the  $D_p$  values obtained for the annealing temperatures of 300°C, 350°C and 400°C. For reasons mentioned above a plateau value could not be obtained for 450°C. However the  $D(t)$  values at 450°C for  $t < 8$  hr are shown by open squares for the sake of comparison. The activation energy and pre-exponential factor obtained from the Arrhenius plot are:

$$Q = 0.62 \pm 0.18 \text{ eV}$$

$$D_0 = 3.8^{+110}_{-3.7} \times 10^{-17} \text{ m}^2/\text{s}$$

with an error in  $Q$  being 29% and that in  $\log(D_0)$  being 9%.

## 5.4 DIFFUSION OF Pd IN METALLIC GLASS $\text{Fe}_{79}\text{B}_{16}\text{Si}_5$

Diffusion couples of metallic glass  $\text{Fe}_{79}\text{B}_{16}\text{Si}_5$  - Pd film, were annealed at temperatures and time periods mentioned in Table 5.5 below. The thickness of the

TABLE 5.5  
SAMPLE IDENTIFICATION FOR  $\text{Fe}_{79}\text{B}_{16}\text{Si}_5$  - Pd DIFFUSION COUPLE

SAMPLE NUMBER	FILM (A) THICKNESS	ANNEAL TEMP(°C)	ANNEAL TIME(hr)
MG272/Pd	250	300	1, 2, 4, 8, 12, 16
MG273/Pd	200	350	1, 2, 4, 8, 12, 16
MG258/Pd	250	400	1, 2, 4, 8, 12, 16
MG257/Pd	230	450	1, 2, 4, 8, 12, 16

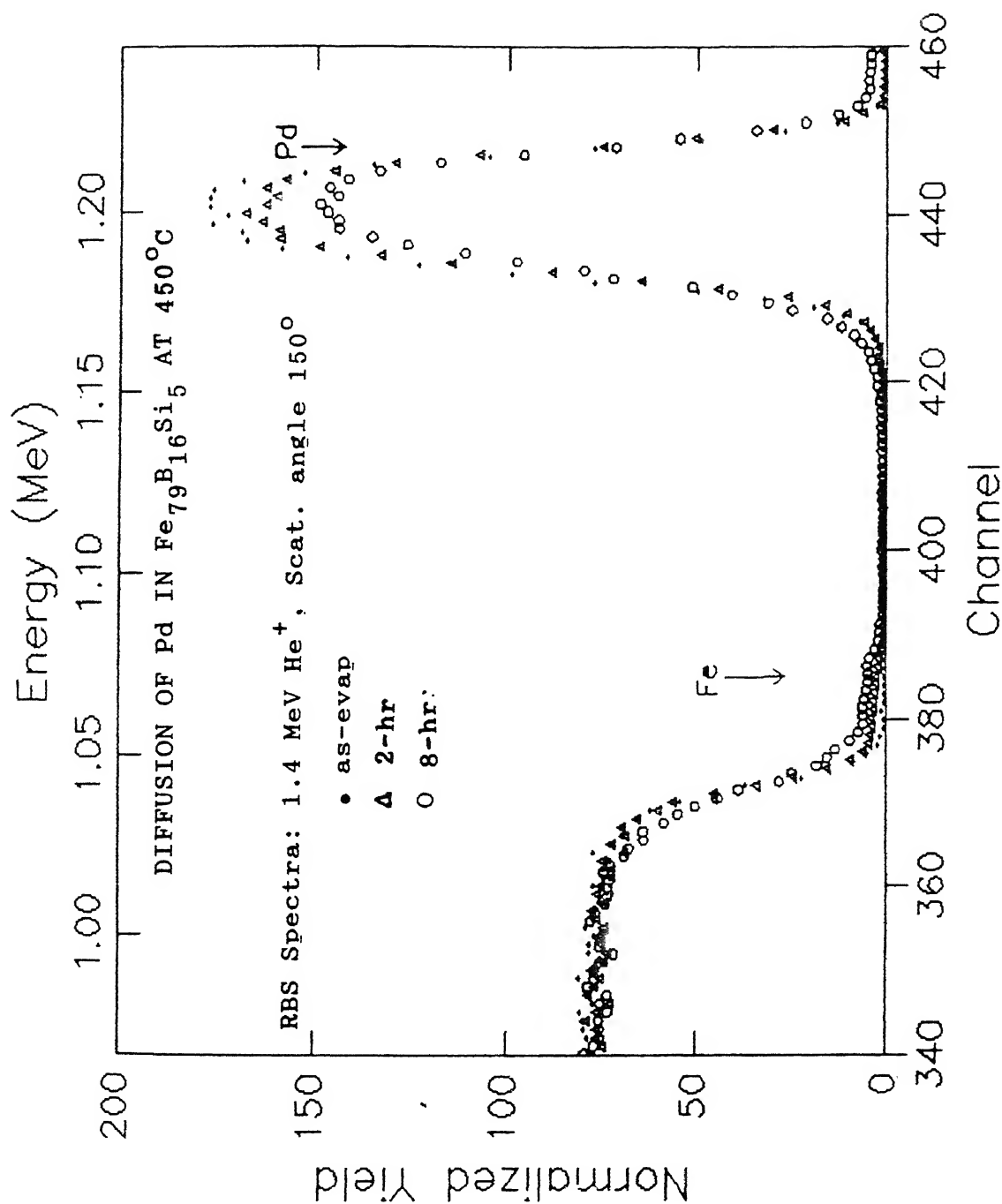


FIGURE 5.16 Normalised RBS spectra of  $\text{Fe}_{79}\text{B}_{16}\text{Si}_5$ -Pd diffusion couple before and after annealing at  $450^\circ\text{C}$  for 2 hr and 8 hr respectively. The thickness of the as-evaporated film is 230 Å. The arrow indicates the surface position.

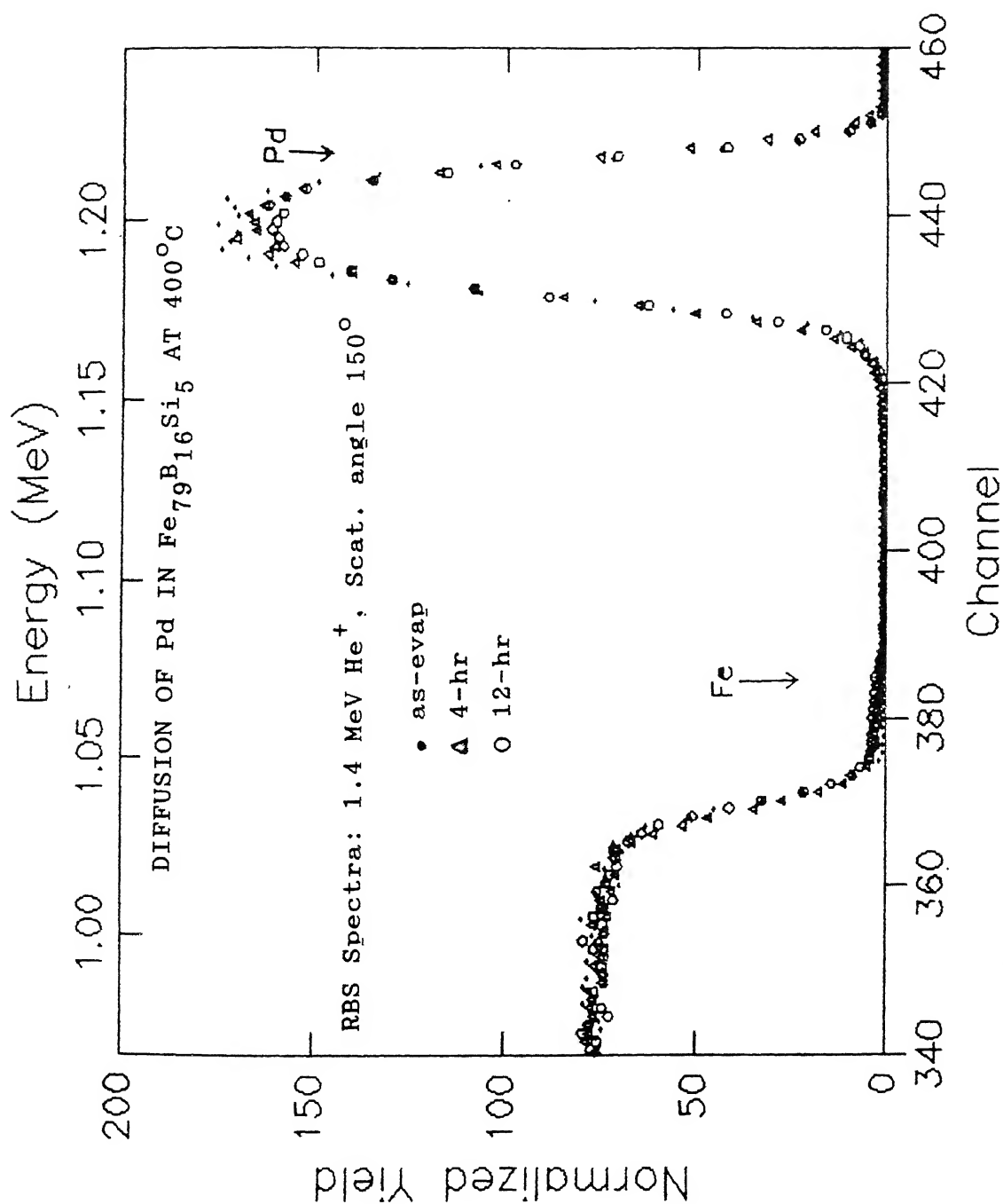
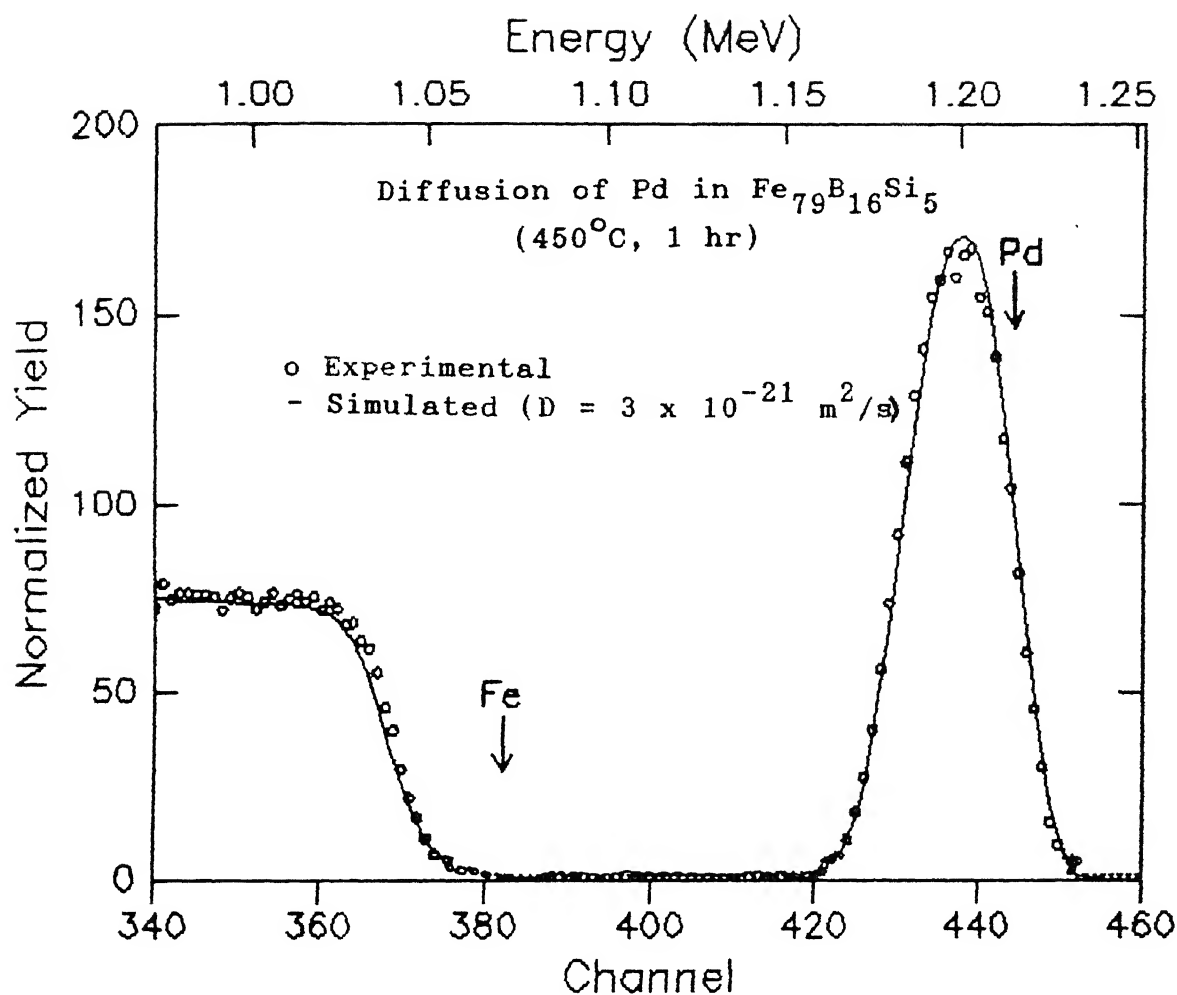


FIGURE 5.17 Normalised RBS spectra of  $\text{Fe}_{79}\text{B}_{16}\text{Si}_5$ -Pd diffusion couple before and after annealing at  $400^\circ\text{C}$  for 4 hr and 12 hr respectively. The thickness of the as-evaporated film is  $250 \text{ \AA}$ . The arrow indicates the surface position.





**FIGURE 5.18** Comparison of experimental (1.4 MeV  $\text{He}^+$ , scattering angle  $150^\circ$ ) and simulated RBS spectra to determine the D-value of Pd in  $\text{Fe}_{79}\text{B}_{16}\text{Si}_5$  at 450°C (1 hr). The simulation was performed using the error function solution of the diffusion equation (refer section 1.4.3).

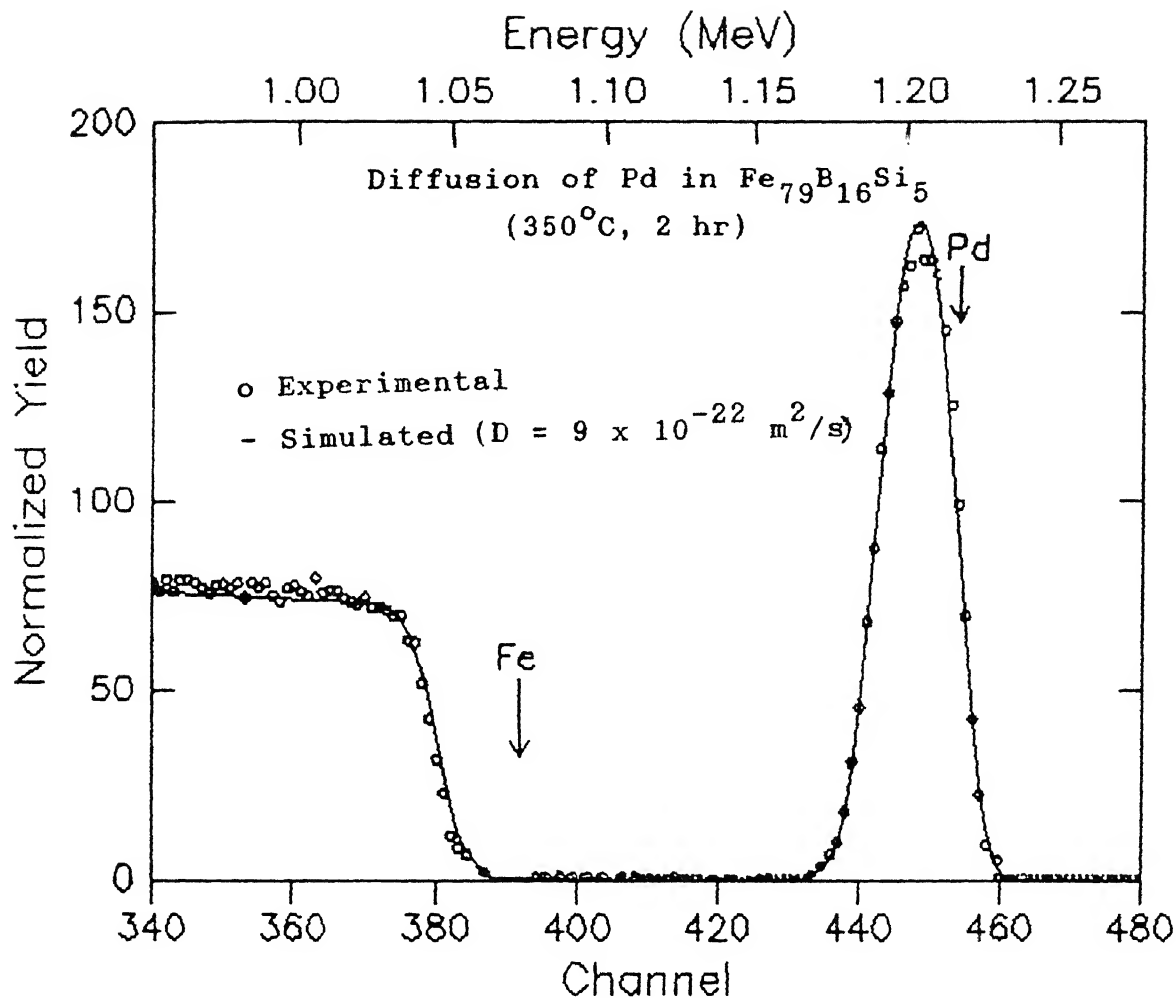


FIGURE 5.19 Comparison of experimental (1.4 MeV  $\text{He}^+$ , scattering angle  $150^\circ$ ) and simulated RBS spectra to determine the D-value of Pd in  $\text{Fe}_{79}\text{B}_{16}\text{Si}_5$  at 350°C (2 hr). The simulation was performed using the error function solution of the diffusion equation (refer section 1.4.3).

TABLE 5.6

THE D-VALUES FOR THE DIFFUSION OF  
Pd IN METALLIC GLASS  $\text{Fe}_{79}\text{B}_{16}\text{Si}_5$

ANNEALING TEMP ( $^{\circ}\text{C}$ )	ANNEALING TIME (s)	$D(t), \text{m}^2/\text{s}$ *
300	3600	$2.20 \times 10^{-21}$
300	7200	$1.50 \times 10^{-21}$
300	14400	$9.00 \times 10^{-22}$
300	28800	$2.00 \times 10^{-22}$
300	43200	$1.00 \times 10^{-22}$
300	57600	$8.00 \times 10^{-23}$
350	3600	$2.60 \times 10^{-21}$
350	7200	$9.00 \times 10^{-22}$
350	14400	$4.00 \times 10^{-22}$
350	28800	$3.00 \times 10^{-22}$
350	43200	$1.40 \times 10^{-22}$
350	57600	$1.60 \times 10^{-22}$
400	3600	$3.00 \times 10^{-21}$
400	7200	$1.30 \times 10^{-21}$
400	14400	$7.00 \times 10^{-22}$
400	28800	$4.00 \times 10^{-22}$
400	43200	$2.40 \times 10^{-22}$
400	57600	$2.00 \times 10^{-22}$
450	3600	$3.00 \times 10^{-21}$
450	7200	$9.00 \times 10^{-22}$
450	14400	$8.20 \times 10^{-22}$
450	28800	$8.80 \times 10^{-22}$
450	43200	$8.80 \times 10^{-22}$
450	57600	$8.00 \times 10^{-22}$

\*The error in D is  $\pm 30\%$

Pd films in the various samples are also specified. The spectra of the as-evaporated samples are shown in Figures 5.16 and 5.17 overlapped with a few of those obtained after annealing the samples at 450°C and 400°C respectively. As mentioned earlier only few spectra are plotted for the sake of clarity to observe the changes occurring at the interface of the metallic glass  $\text{Fe}_{79}\text{B}_{16}\text{Si}_5$ -Pd film couple.

A few of the simulated spectra along with the experimentally observed spectra of the same samples at a particular annealing temperature and time period are shown in Figures 5.18 (450°C, 1 hr) and 5.19 (350°C, 2 hr). The error function solution of the diffusion equation has been utilized for the determination of the diffusion coefficients of these samples. The diffusion coefficients obtained from the simulations are tabulated for each annealing temperature and time period in Table 5.6. The error in the  $D(t)$  values is  $\pm 30\%$ .

#### 5.4.1 Dependence of $D(t)$ on annealing time

The diffusion coefficients of Pd in  $\text{Fe}_{79}\text{B}_{16}\text{Si}_5$  (Table 5.6) evaluated for the annealing temperatures of 300°C, 350°C, 400°C and 450°C at various annealing durations are plotted in Figure 5.20 (a)-(d), respectively. Here also the solid circles indicate that crystallization has been observed by X-ray diffraction and Mössbauer studies for these data points. And the open circles represent the diffusion process in the amorphous phase of the metallic glass. The features of the plots at 300°C, 350°C and 400°C, are similar to that of Ge diffusion in this metallic glass (Sec. 5.2.1). As mentioned in Chapter 4, the metallic glass  $\text{Fe}_{79}\text{B}_{16}\text{Si}_5$  shows indication of crystallization at 450°C for  $t \geq 4$  hr. However the data points of Figure 5.20 (d), indicate a plateau value equal to  $8.7 \times 10^{-22} \text{ m}^2/\text{s}$  for the 450°C anneal, which is greater than the  $D_p$  value obtained at 400°C. This observation is indicative of the fact that the metallic glass has

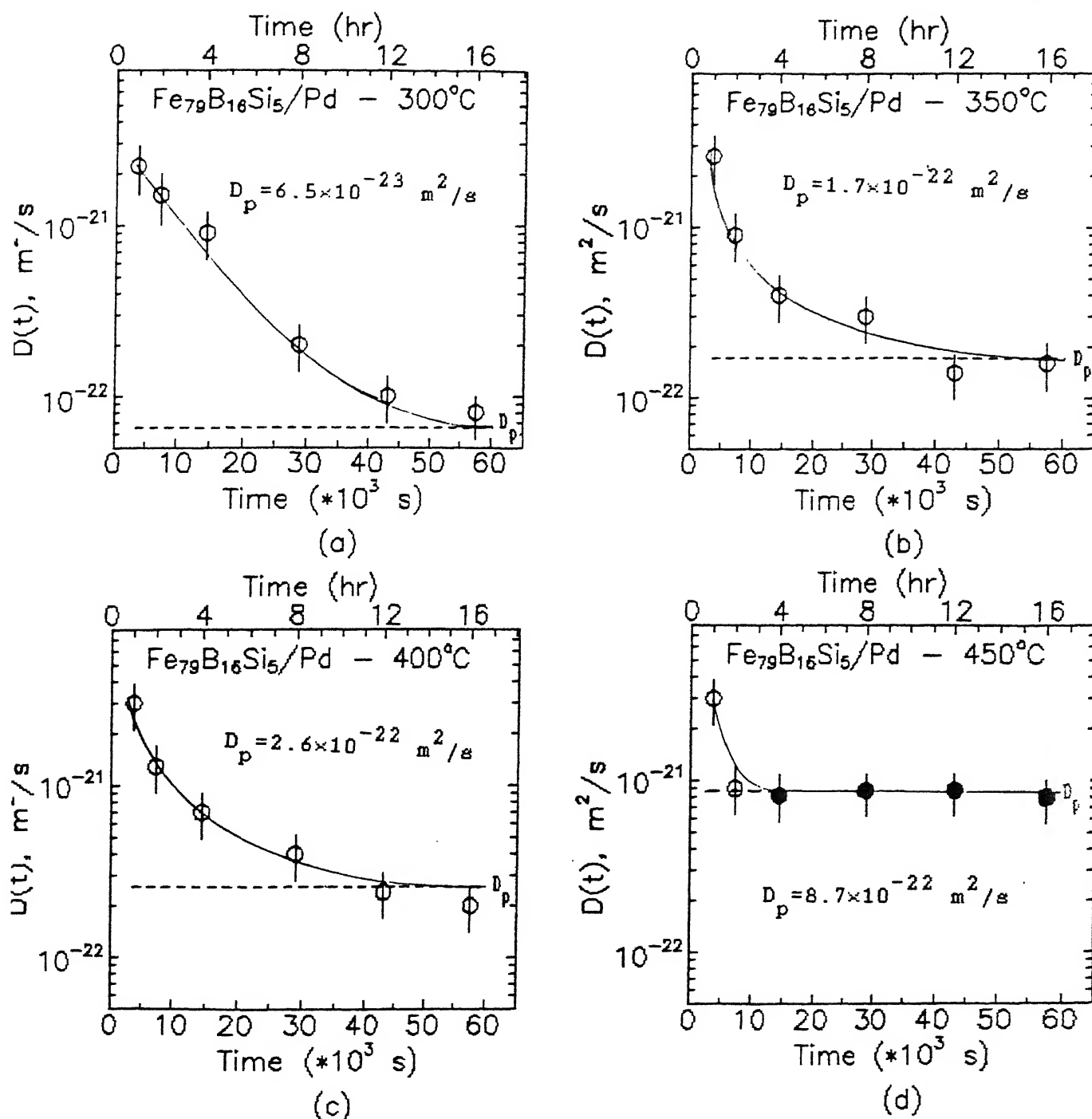


FIGURE 5.20 (a)-(d) Diagrams showing variation of the diffusion coefficient  $D(t)$  as a function of annealing time  $t$ , for diffusion of Pd in  $\text{Fe}_{79}\text{B}_{16}\text{Si}_5$ . The vertical bars on the data points indicate error in the diffusion coefficient. The solid circles indicate that the crystallization of the metallic glass is observed by us using X-ray and Mössbauer techniques for these data points. The solid line, drawn as a best visual fit to the data points, asymptotically approaches a plateau value ( $D_p$ ) shown by the dashed line.

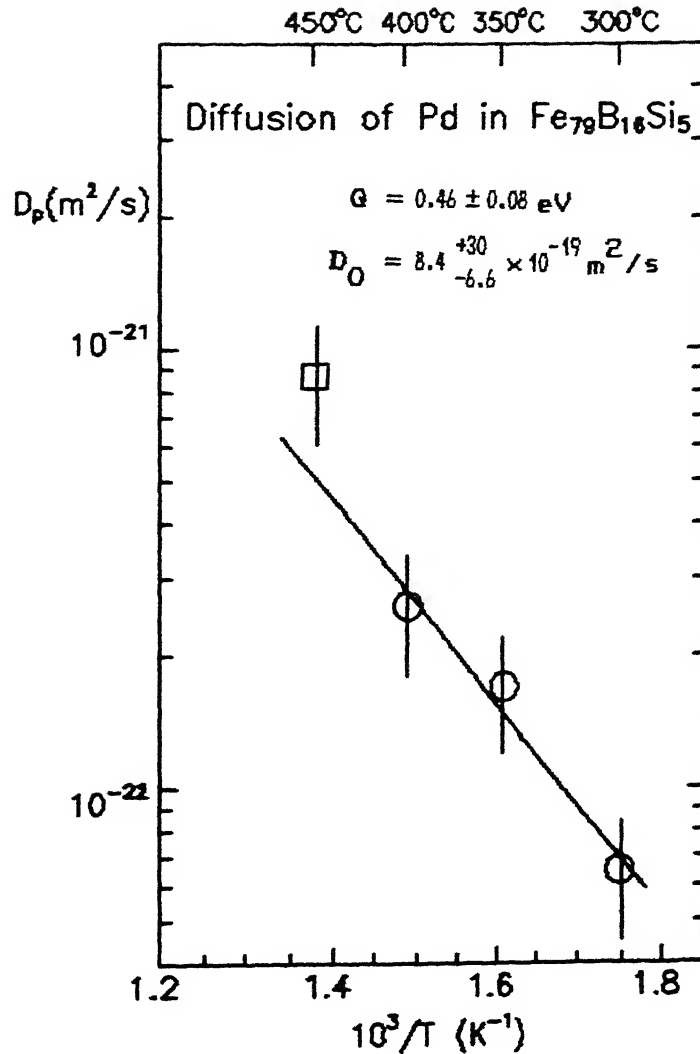


FIGURE 5.21 Temperature dependence of diffusivity of Pd in metallic glass Fe<sub>79</sub>B<sub>16</sub>Si<sub>5</sub> (Arrhenius plot). The open circles indicate the plateau values ( $D_p$ ) obtained from the  $D(t)$  vs annealing time diagrams (Figs. 5.20 (a),(b),(c)), and the solid line is a least square fitting to these data points. The values of  $Q$  and  $D_0$  obtained from the fit are also mentioned. The open square depicts the plateau value at 450°C, and is shown for the sake of comparison.

not yet crystallized at 450°C even after annealing for 16 hr, perhaps due to the presence of Pd in the diffused metallic glass sample.

#### 5.4.2 Dependence of D on annealing temperature

The Arrhenius plot of  $D_p$  versus  $1/T$  for this system is shown in Figure 5.21. The solid line is a least square fit to the data points for 300°C, 350°C and 400°C. The plateau value at 450°C is shown by the open square for the sake of comparison. The values of  $Q$  and  $D_0$  obtained are

$$Q = 0.46 \pm 0.08 \text{ eV}$$

$$D_0 = 8.4^{+30}_{-6.6} \times 10^{-19} \text{ m}^2/\text{s}$$

with an error in  $Q$  being 18% and that in  $\log(D_0)$  being 4%.

### 5.5 DIFFUSION OF Pd IN METALLIC GLASS $\text{Fe}_{78}\text{B}_{13}\text{Si}_9$

The samples of the metallic glass  $\text{Fe}_{78}\text{B}_{13}\text{Si}_9$  / Pd film, diffusion couples have been annealed at temperatures for time periods mentioned in Table 5.7.

**TABLE 5.7**  
**SAMPLE IDENTIFICATION FOR  $\text{Fe}_{78}\text{B}_{13}\text{Si}_9$  - Pd DIFFUSION COUPLES**

SAMPLE NUMBER	FILM ( $\text{\AA}$ ) THICKNESS	ANNEAL TEMP(°C)	ANNEAL TIME(hr)
MG267/Pd	220	300	1, 2, 4, 8, 12, 16
MG268/Pd	240	350	1, 2, 4, 8, 12, 16
MG255/Pd	190	400	1, 2, 4, 8, 12, 16
MG256/Pd	165	450	1, 2, 4, 8, 12, 16

The RBS spectra of the sample annealed at 450°C (2 hr) and 400°C (12 hr) are shown in Figures 5.22 and 5.23 respectively. Some of the results of simulation are shown in Figures 5.24 and 5.25, while the diffusion data obtained from the simulations are reported in Table 5.8.

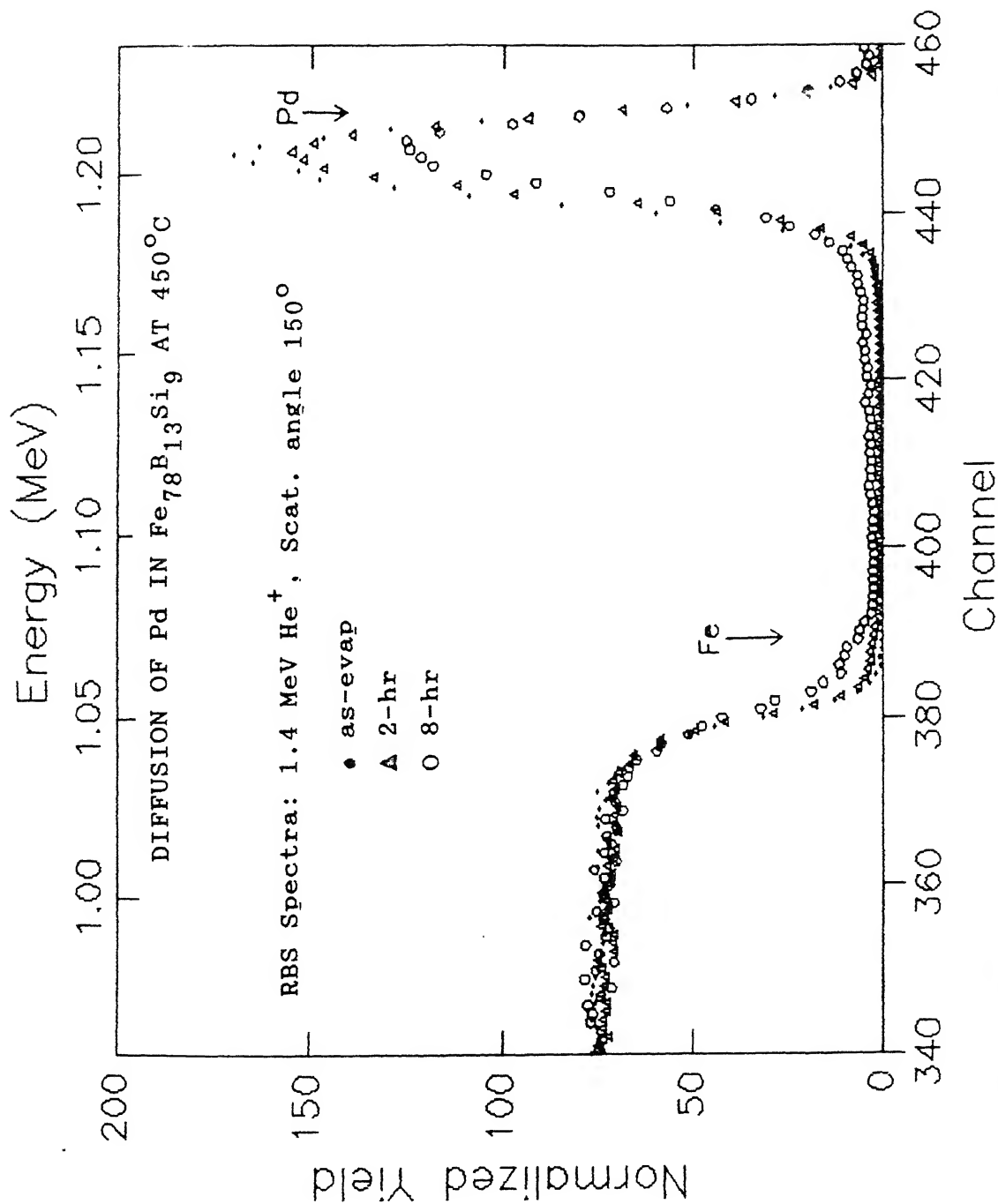


FIGURE 5.22 Normalised RBS spectra of  $\text{Fe}_{78}\text{B}_{13}\text{Si}_9$ -Pd diffusion couple before and after annealing at  $450^\circ\text{C}$  for 2 hr and 8 hr respectively. The thickness of the as-evaporated film is  $165 \text{ \AA}$ . The arrow indicates the surface position.



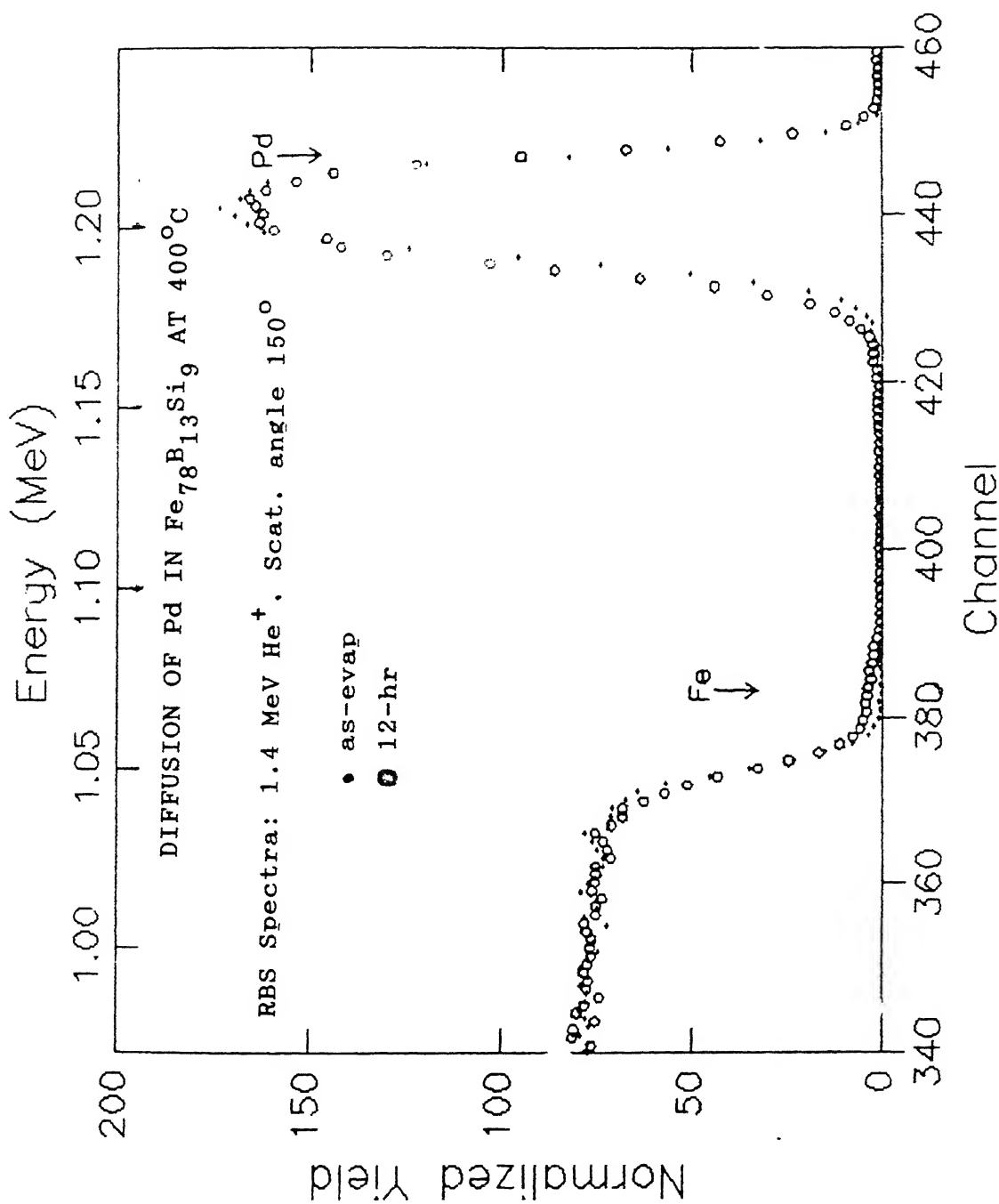
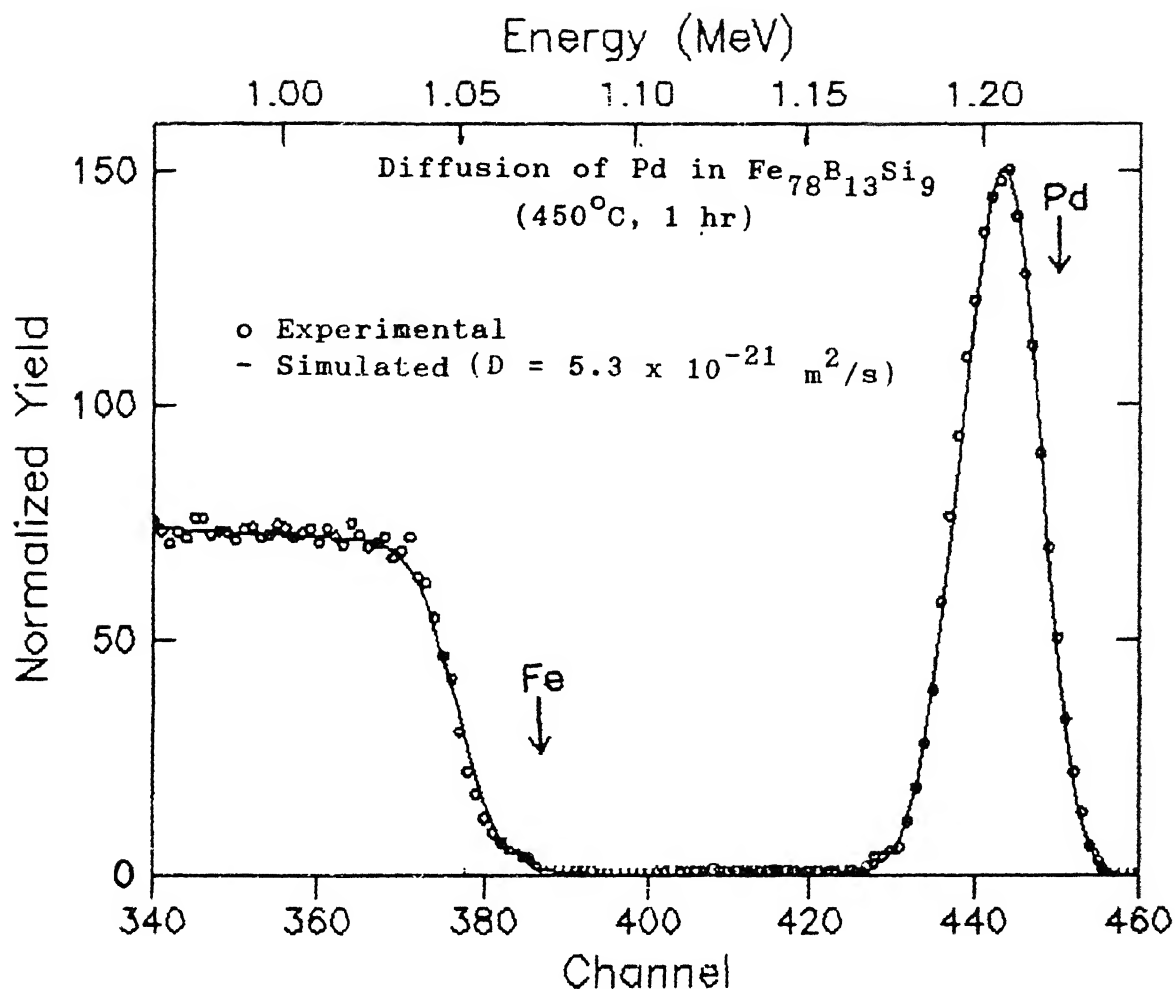
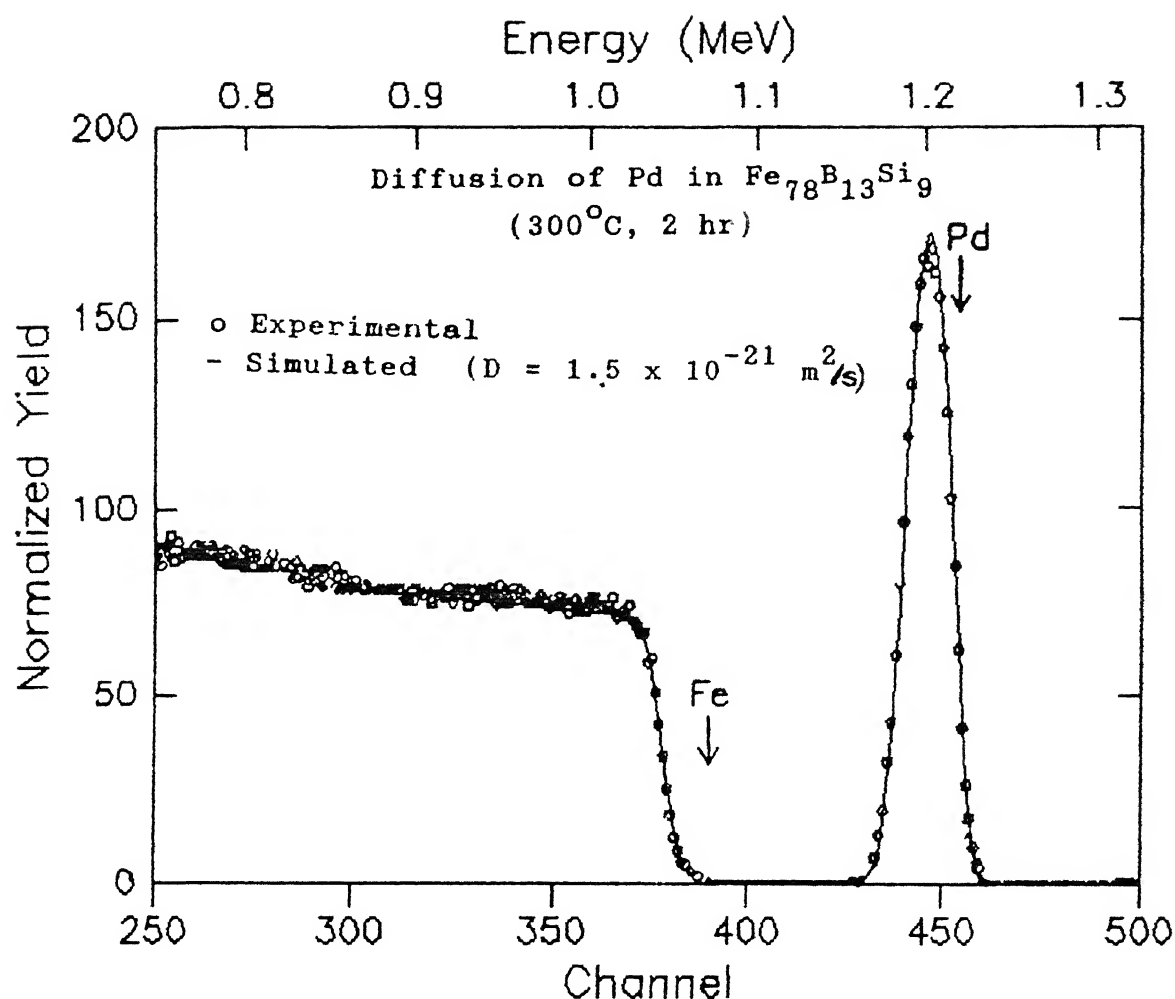


FIGURE 5.23 Normalised RBS spectra of  $\text{Fe}_{78}\text{B}_{13}\text{Si}_9$ -Pd diffusion couple before and after annealing at  $400^\circ\text{C}$  for 12 hr. The thickness of the as-evaporated film is  $190 \text{ \AA}$ . The arrow indicates the surface position.



**FIGURE 5.24** Comparison of experimental (1.4 MeV  $\text{He}^+$ , scattering angle  $150^\circ$ ) and simulated RBS spectra to determine the D-value of Pd in  $\text{Fe}_{78}\text{B}_{13}\text{Si}_9$  at 450°C (1 hr). The simulation was performed using the error function solution of the diffusion equation (refer section 1.4.3).



**FIGURE 5.25** Comparison of experimental (1.4 MeV  $\text{He}^+$ , scattering angle  $150^\circ$ ) and simulated RBS spectra to determine the D-value of Pd in  $\text{Fe}_{78}\text{B}_{13}\text{Si}_9$  at 300°C (2 hr). The simulation was performed using the error function solution of the diffusion equation (refer section 1.4.3).

TABLE 5.8  
THE D-VALUES FOR THE DIFFUSION OF  
Pd IN METALLIC GLASS  $\text{Fe}_{78}\text{B}_{13}\text{Si}_9$

ANNEALING TEMP( $^{\circ}\text{C}$ )	ANNEALING TIME (s)	$D(t), \text{m}^2/\text{s}$ *
300	3600	$2.30 \times 10^{-21}$
300	7200	$1.50 \times 10^{-21}$
300	14400	$8.00 \times 10^{-22}$
300	28800	$3.00 \times 10^{-22}$
300	43200	$1.70 \times 10^{-22}$
300	57600	$1.50 \times 10^{-22}$
350	3600	$5.00 \times 10^{-21}$
350	7200	$1.70 \times 10^{-21}$
350	14400	$9.00 \times 10^{-22}$
350	28800	$4.50 \times 10^{-22}$
350	43200	$2.50 \times 10^{-22}$
350	57600	$2.00 \times 10^{-22}$
400	3600	$4.00 \times 10^{-21}$
400	7200	$1.50 \times 10^{-21}$
400	14400	$9.50 \times 10^{-22}$
400	28800	$5.00 \times 10^{-22}$
400	43200	$3.50 \times 10^{-22}$
400	57600	$3.20 \times 10^{-22}$
450	3600	$5.30 \times 10^{-21}$
450	7200	$2.70 \times 10^{-21}$
450	14400	$1.80 \times 10^{-21}$
450	28800	$9.00 \times 10^{-22}$
450	43200	$5.00 \times 10^{-22}$
450	57600	$4.50 \times 10^{-22}$

\*The error in D is  $\pm 30\%$

### 5.5.1 Dependence of $D(t)$ on annealing time

The diffusion coefficients (see Table 5.8) obtained for the diffusion of Pd in  $\text{Fe}_{78}\text{B}_{13}\text{Si}_9$  are plotted as a function of annealing time in Figures 5.26(a)-(d) for the isothermal annealing temperatures of 300°C, 350°C, 400°C and 450°C respectively. The features of these plots are: (i) the function  $D(t)$  falls by a factor of 10 to 20 (depending on the temperature of annealing) between  $t = 1$  hr and  $t = 16$  hr, (ii) for a given temperature,  $D(t)$  asymptotically approaches a plateau value  $D_p$  shown by the horizontal dashed lines in Figures 5.26 (a)-(d), which represents the diffusion process in the 'relaxed' amorphous state of the metallic glass.

### 5.5.2 Dependence of $D$ on annealing temperature

The Arrhenius plot of  $D_p$  values (obtained from Figures 5.26 (a)-(d)) versus  $1/T$  for this system is shown in Figure 5.27 and the straight line drawn therein is a least square fit to these data points.

The activation energy  $Q$  and pre-exponential factor  $D_0$  obtained are

$$Q = 0.31 \pm 0.02 \text{ eV}$$

$$D_0 = 6.9^{+2.6}_{-1.9} \times 10^{-20} \text{ m}^2/\text{s}$$

with an error in  $Q$  being 6% and that in  $\log(D_0)$  being 0.7%. Errors of the same order are generally reported in literature [Sharma et al. 1988, Hoshino et al. 1988, Horvath and Mehrer 1986, Cantor 1985].

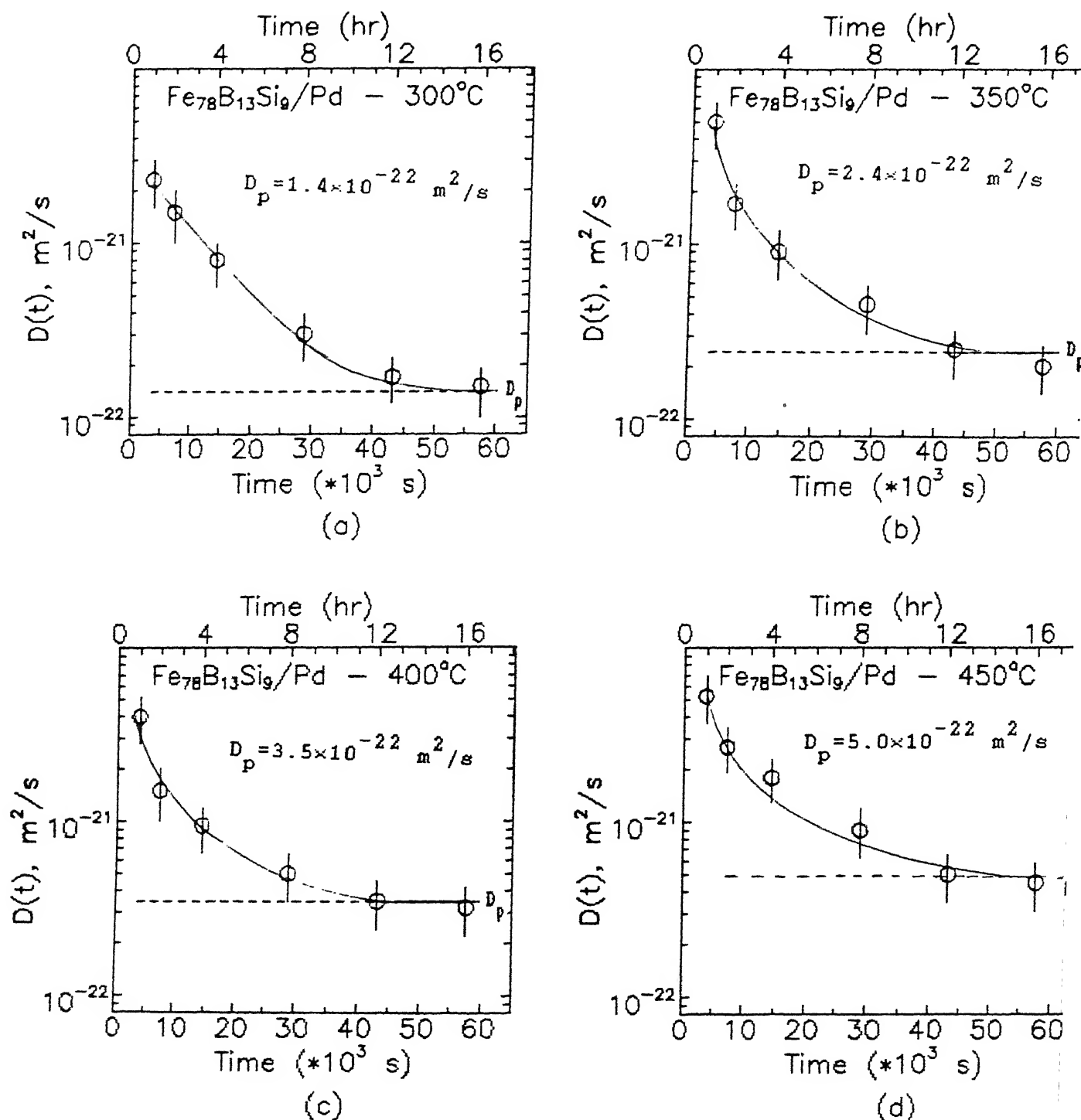


FIGURE 5.26 (a)-(d) Diagrams showing variation of the diffusion coefficient  $D(t)$  as a function of annealing time  $t$ , for diffusion of Pd in  $\text{Fe}_{78}\text{B}_{13}\text{Si}_9$ . The vertical bars on the data points indicate error in the diffusion coefficient. The solid line, drawn as a best visual fit to the data points, asymptotically approaches a plateau value ( $D_p$ ) as shown by the dashed line.

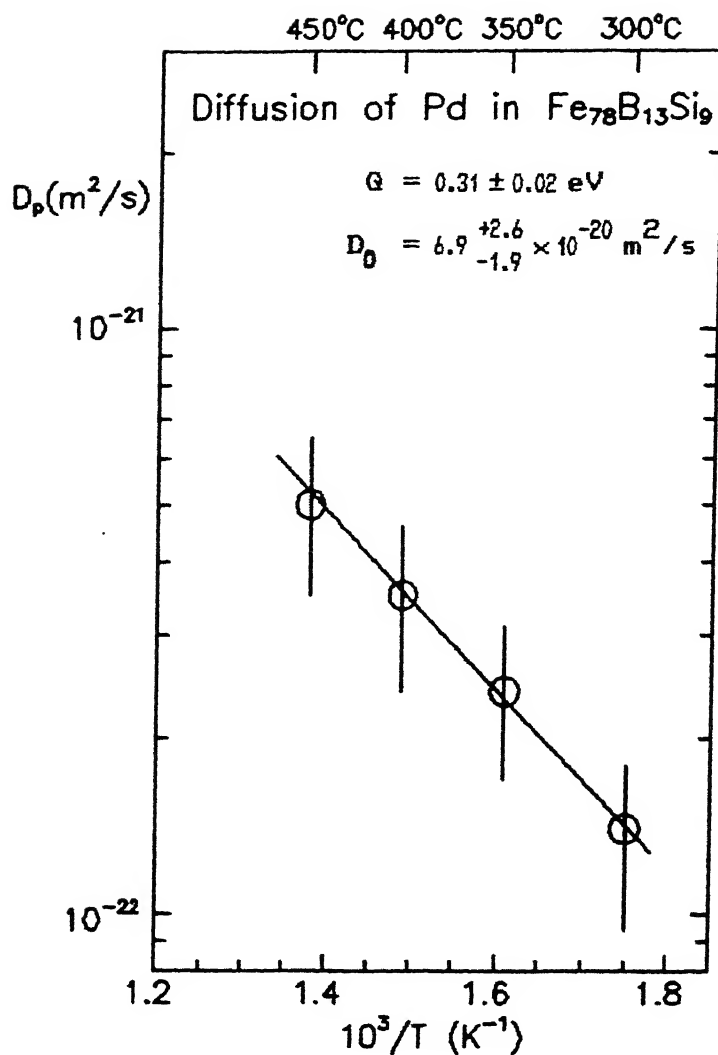


FIGURE 5.27 Temperature dependence of diffusivity of Pd in metallic glass  $\text{Fe}_{78}\text{B}_{13}\text{Si}_9$  (Arrhenius plot). The open circles indicate the plateau values ( $D_p$ ) obtained from the  $D(t)$  vs. annealing time diagrams (Figs. 5.26 (a) to (d)), and the solid line is a least square fitting to these data points. The values of  $Q$  and  $D_0$  obtained from the fit are also mentioned.

## 5.6 DIFFUSION OF AU IN METALLIC GLASS $\text{Fe}_{79}\text{B}_{16}\text{Si}_5$

The diffusion couples of the metallic glass  $\text{Fe}_{79}\text{B}_{16}\text{Si}_5$  - Au film were annealed at the temperatures for the annealing durations mentioned in Table 5.9.

**TABLE 5.9**  
SAMPLE IDENTIFICATION FOR  $\text{Fe}_{79}\text{B}_{16}\text{Si}_5$  - Au DIFFUSION COUPLES

SAMPLE NUMBER	FILM ( $\text{\AA}$ ) THICKNESS	ANNEAL TEMP( $^{\circ}\text{C}$ )	ANNEAL TIME(hr)
MG149/Au	50	300	16
MG180/Au	130	350	8
MG183/Au	165	400	1, 2, 4, 8, 16
MG150/Au	45	450	1, 2, 4, 8, 16
MG181/Au	140	475	1, 2, 4, 8, 16

The diffusion process for this system is illustrated in Figure 5.28. In this figure the as-evaporated spectrum of the same sample is shown along with the one obtained after annealing the sample at  $350^{\circ}\text{C}$  for 8 hr. The results of the simulations for this case is shown in Figure 5.29. All other spectra were analyzed in a similar manner to obtain the diffusion coefficients. The samples MG149/Au and MG150/Au were analyzed using the thin film solution of the diffusion equation as the film thickness in these were comparable to the diffusion length. The other samples MG180/Au, MG181/Au and MG183/Au were analyzed using the error function solution to the diffusion equation. The diffusion coefficients or  $D(t)$  values obtained from the simulations for each annealing temperature and time period are given in Table 5.10.

### 5.6.1 Dependence of $D(t)$ on annealing time

The detailed diffusion study as a function of annealing time for diffusion of Au in  $\text{Fe}_{79}\text{B}_{16}\text{Si}_5$  was done at  $400^{\circ}\text{C}$ ,  $450^{\circ}\text{C}$  and  $475^{\circ}\text{C}$ . The plots of  $D(t)$  versus anneal time ( $t$ ) for these temperatures are shown in Figures 5.30 (a)-(c). The



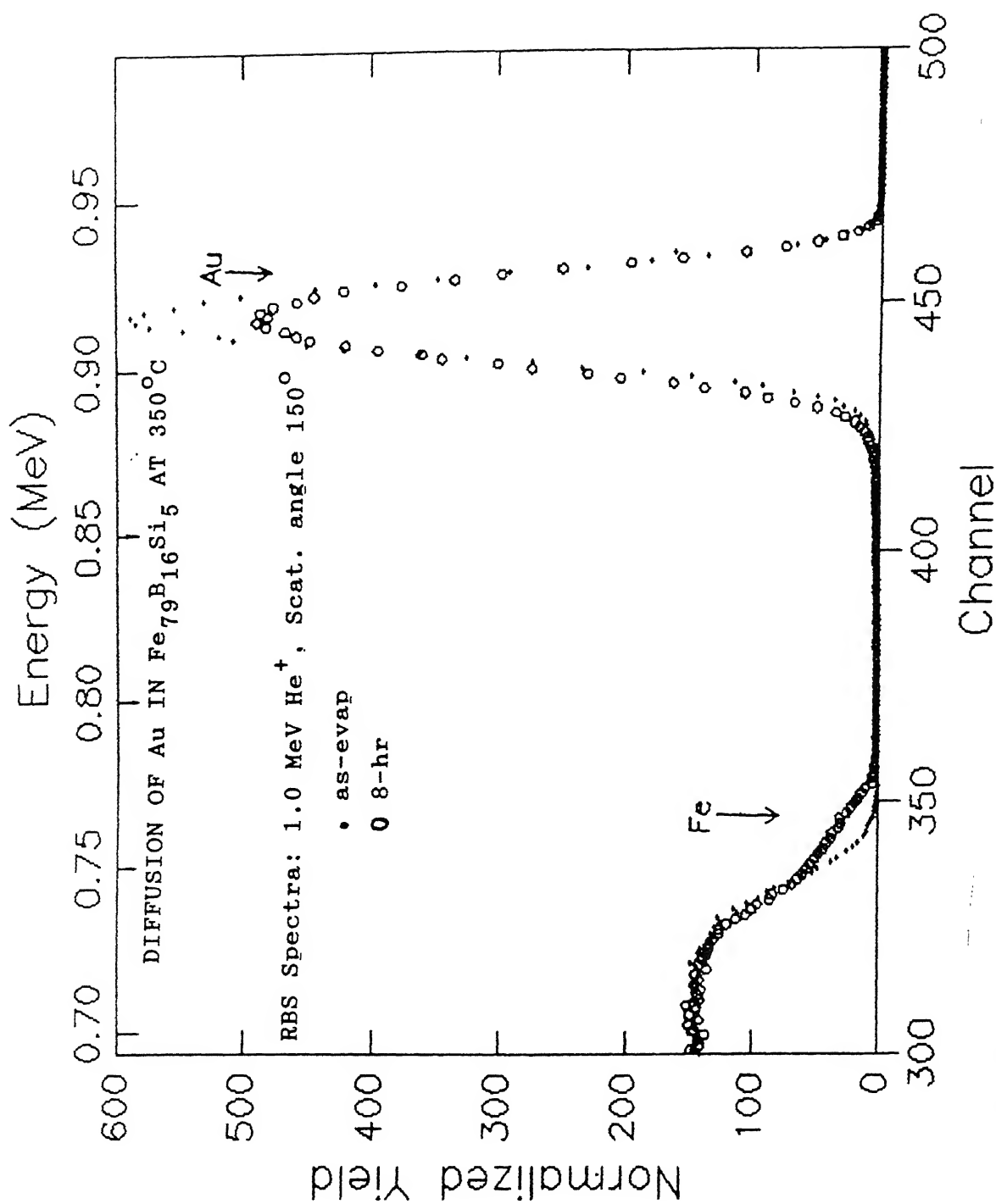


FIGURE 5.28 Normalised RBS spectra of  $\text{Fe}_{79}\text{B}_{16}\text{Si}_5$ -Au diffusion couple before and after annealing at  $350^\circ\text{C}$  for 8 hr. The thickness of the as-evaporated film is 130 Å. The arrow indicates the surface position.

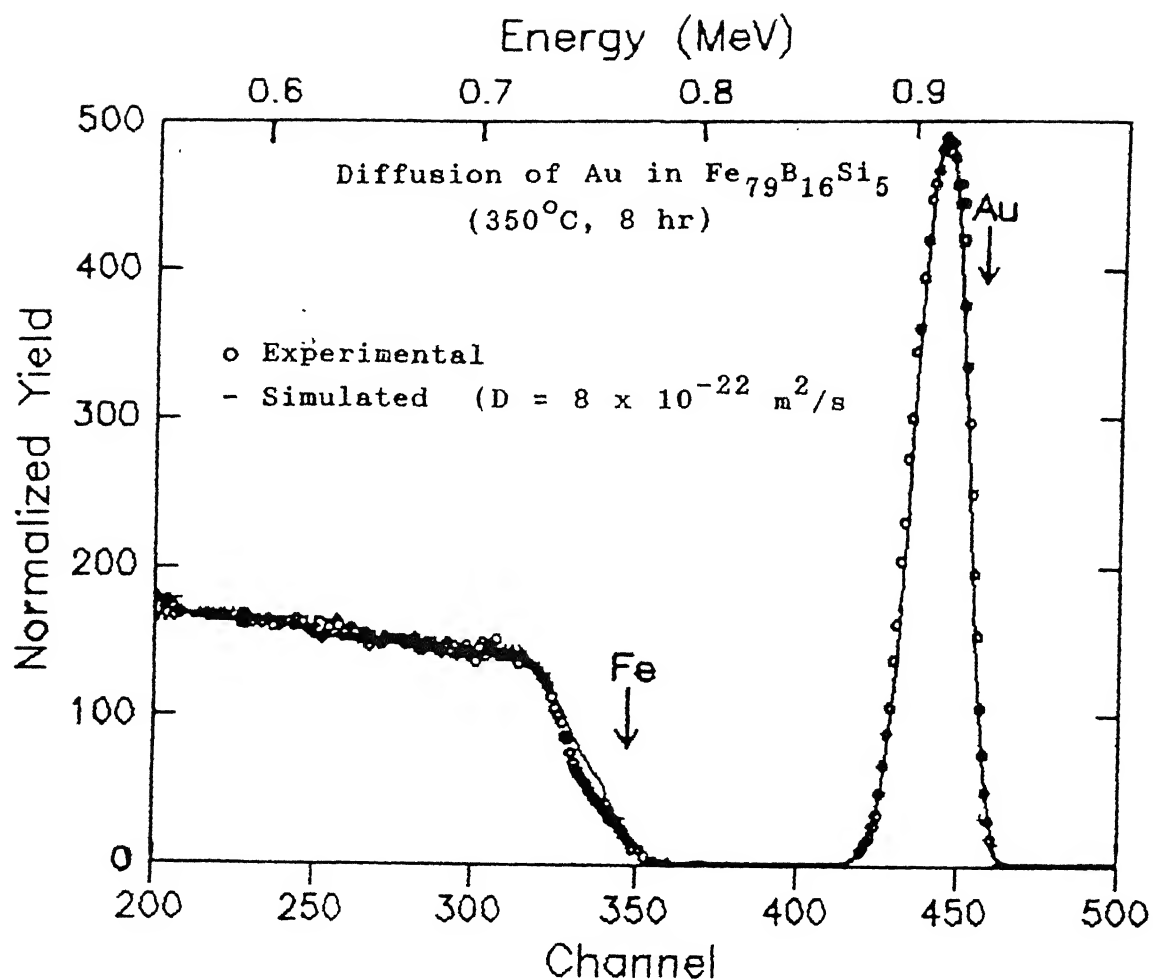


FIGURE 5.29 Comparison of experimental (1.0 MeV  $\text{He}^+$ , scattering angle  $150^\circ$ ) and simulated RBS spectra to determine the D-value of Au in  $\text{Fe}_{79}\text{B}_{16}\text{Si}_5$  at 350°C (8 hr). The simulation was performed using the error function solution of the diffusion equation (refer section 1.4.3).

TABLE 5.10

THE D-VALUES FOR THE DIFFUSION OF  
Au IN METALLIC GLASS  $\text{Fe}_{79}\text{B}_{16}\text{Si}_5$

Annealing Temp. ( $^{\circ}\text{C}$ )	Annealing Time (s)	$D(t)$ , $\text{m}^2/\text{s}$ *
300	57600	$8.00 \times 10^{-22}$
350	28800	$8.00 \times 10^{-22}$
400	3600	$4.00 \times 10^{-21}$
400	7200	$8.00 \times 10^{-22}$
400	14400	$6.50 \times 10^{-22}$
400	28800	$4.00 \times 10^{-22}$
400	57600	$3.00 \times 10^{-22}$
450	3600	$1.30 \times 10^{-20}$
450	14400	$3.50 \times 10^{-21}$
450	28800	$1.60 \times 10^{-21}$
450	57600	$8.00 \times 10^{-22}$
475	3600	$6.00 \times 10^{-21}$
475	7200	$4.00 \times 10^{-21}$
475	14400	$1.20 \times 10^{-21}$
475	28800	$7.00 \times 10^{-22}$
475	57600	$3.50 \times 10^{-22}$

\*The error in D is  $\pm 30\%$

open circle data points indicate that the nature of the metallic glass was amorphous as observed by X-ray and Mössbauer studies. On the other hand those data points shown as solid circles indicate the occurrence of crystallization. The  $D(t)$  values decrease by factor of 10 to 20 (depending on the temperature of annealing) between  $t = 1$  hr and  $t = 16$  hr. As reported in literature, the  $D(t)$  values decrease as the metallic glass transforms from amorphous to crystalline phase. Thus the observation of low  $D(t)$  values at  $400^{\circ}\text{C}$ , as compared to the ones at  $300^{\circ}\text{C}$  and  $350^{\circ}\text{C}$ , implies that the metallic glass starts crystallizing at  $400^{\circ}\text{C}$  due to the presence of Au atoms in the host matrix. In other words the crystallization kinetics is probably changing due to the presence of Au atoms which influence the diffusion process. Although a plateau value is assigned in the  $D(t)$  vs  $t$  plot for  $400^{\circ}\text{C}$ , we are not certain that it definitely indicates diffusion in the amorphous state.

#### 5.6.2 Dependence of $D$ on annealing temperature

For this system the Arrhenius behaviour could be observed (see Figure 5.31) by choosing the diffusion coefficients obtained at lower annealing durations for higher temperatures and vice-versa. The  $D$  values obtained for annealing durations of 16 hr, 8 hr, 1 hr, and 1 hr at the annealing temperatures of  $300^{\circ}\text{C}$ ,  $350^{\circ}\text{C}$ ,  $400^{\circ}\text{C}$ , and  $450^{\circ}\text{C}$  respectively have been chosen for the  $D$  vs  $1/T$  plot. As a matter of fact the Au diffusion does not show as clean a systematic behaviour as is observed for Ge and Pd at annealing temperatures  $\leq 400^{\circ}\text{C}$ . At present we cannot completely understand this anomalous behaviour of diffusion of Au in this metallic glass. As mentioned in the previous section, probably Au diffusion influences the crystallization kinetics more strongly and this in turn affects the diffusion process.

The values of activation energy and pre-exponential factor obtained from the fit are

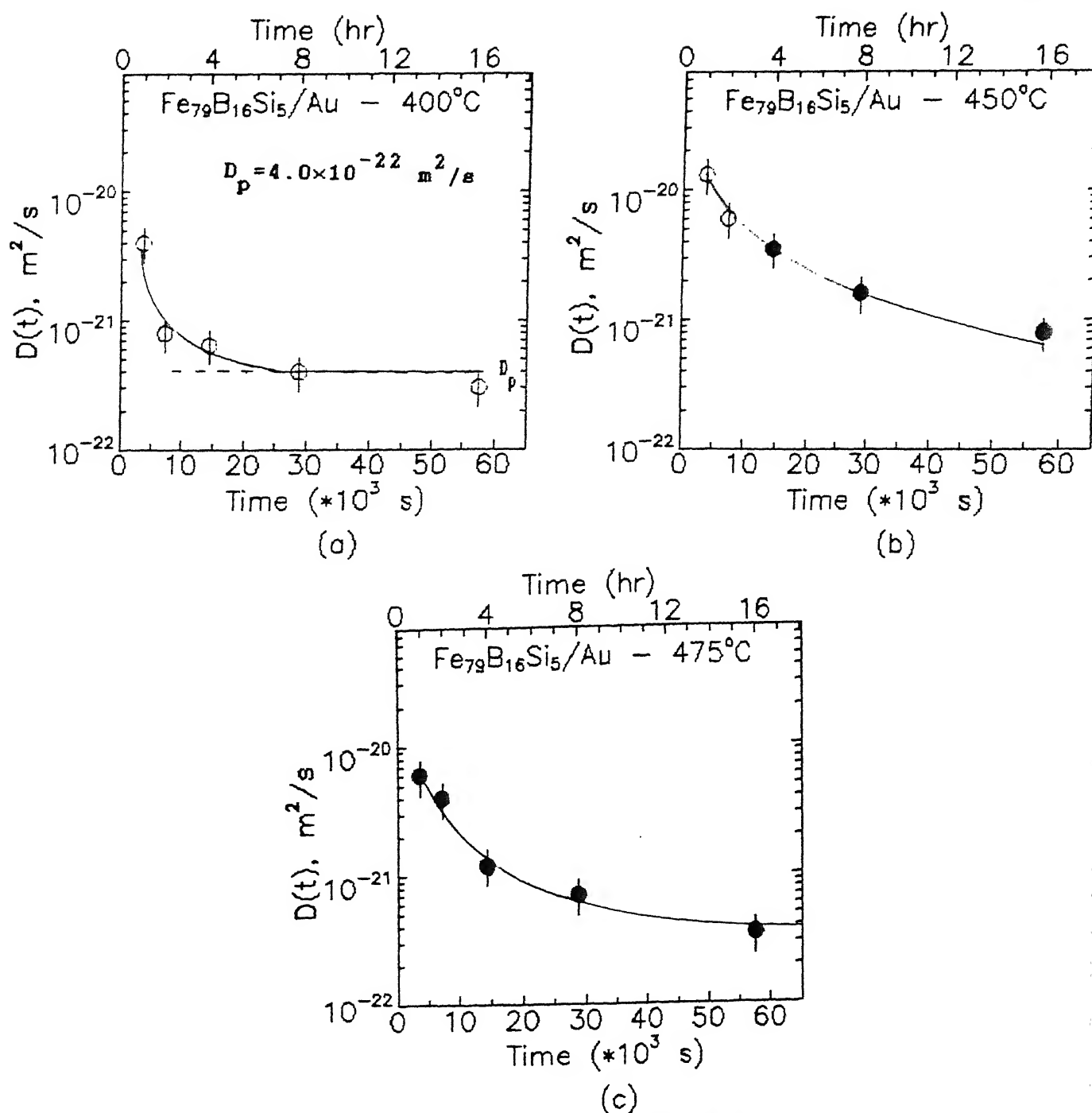


FIGURE 5.30 (a)-(c) Diagrams showing variation of the diffusion coefficient  $D(t)$  as a function of annealing time  $t$ , for diffusion of Au in  $\text{Fe}_{79}\text{B}_{16}\text{Si}_5$ . The vertical bars on the data points indicate error in the diffusion coefficient. The solid circles indicate that the crystallization of the metallic glass is observed by us using X-ray and Mössbauer techniques for these data points. The solid line, drawn as a best visual fit to the data points, asymptotically approaches a plateau value ( $D_p$ ) shown by the dashed line (for  $400^\circ\text{C}$ ).

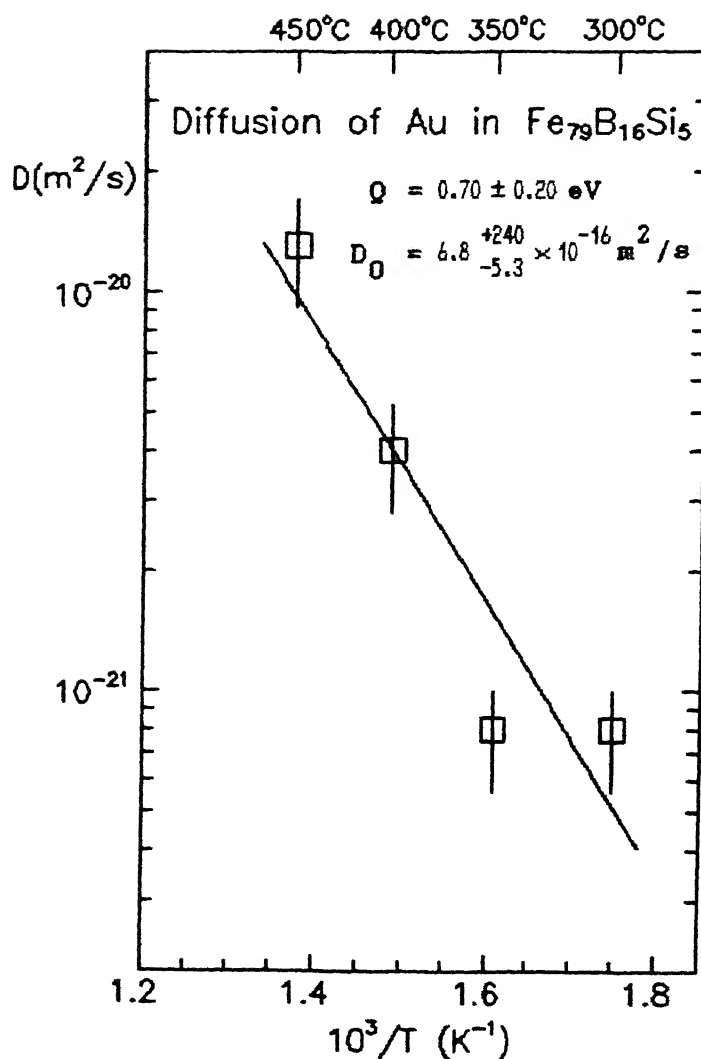


FIGURE 5.31 Temperature dependence of diffusivity of Au in metallic glass  $\text{Fe}_{79}\text{B}_{16}\text{Si}_5$  (Arrhenius plot). The solid line is a least square fitting to the data points at 300°C (16 hr), 350°C (8 hr), 400°C (1 hr) and 450°C (1 hr), (see text Sec. 5.6.2). The values of  $Q$  and  $D_0$  obtained from the fit are also mentioned.

$$Q = 0.70 \pm 0.20 \text{ eV}$$

$$D_0 = 6.8 \begin{matrix} +240 \\ -5.3 \end{matrix} \times 10^{-16} \text{ m}^2/\text{s}$$

with an error in  $Q$  being 28% and that in  $\log(D_0)$  being 10%. We assume, that the large errors observed in the  $Q$  and  $D_0$  values have occurred due to the spread in the data points (in the  $D$  vs  $1/T$  plot) at  $300^\circ\text{C}$  and  $350^\circ\text{C}$ . This spread may have occurred because of the following reasons; (i) at  $300^\circ\text{C}$  the  $D$  values have not attained the plateau values after 16 hr of annealing. It might occur at a later stage with the  $D_p$  value in that case being lower than the present value at  $300^\circ\text{C}$  (16 hr). (ii) Partial crystallization may have commenced at  $350^\circ\text{C}$  (8 hr) due to the presence of the Au atoms. In that case a higher  $D$  value obtained at  $t < 8$  hr might represent the relaxed amorphous state. In both the cases the data points would get closer to the solid line used in the fitting. Hence detailed measurements of  $D$  values at  $300^\circ\text{C}$  and  $350^\circ\text{C}$  along with the conversion electron Mössbauer spectroscopic measurements will help in confirming these facts.

## 5.7 DIFFUSION OF Au IN METALLIC GLASS $\text{Fe}_{78}\text{B}_{13}\text{Si}_9$

The diffusivity of Au in the metallic glass  $\text{Fe}_{78}\text{B}_{13}\text{Si}_9$  was studied by isothermally annealing the diffusion couples at the temperatures and time periods mentioned in Table 5.11.

TABLE 5.11  
SAMPLE IDENTIFICATION FOR  $\text{Fe}_{78}\text{B}_{13}\text{Si}_9$  - Au DIFFUSION COUPLES

SAMPLE NUMBER	FILM ( $\text{\AA}$ ) THICKNESS	ANNEAL TEMP( $^\circ\text{C}$ )	ANNEAL TIME(hr)
MG148/Au	55	300	16
MG174/Au	100	350	8
MG177/Au	170	400	1, 2, 4, 8, 16
MG146/Au	45	450	1, 2, 4, 8, 16
MG175/Au	110	475	1, 2, 4, 8, 16

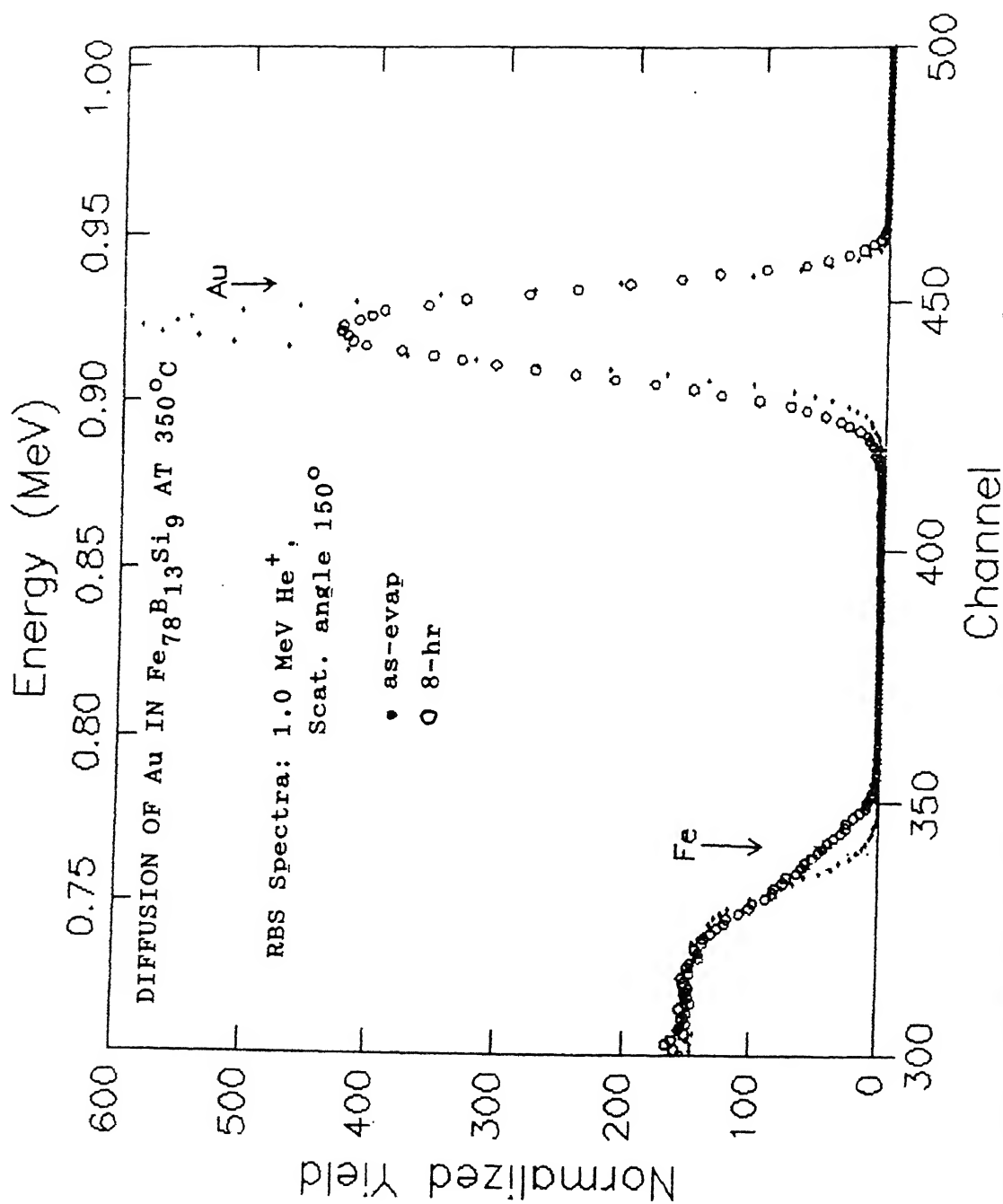


FIGURE 5.32 Normalised RBS spectra of  $\text{Fe}_{78}\text{B}_{13}\text{Si}_9$ -Au diffusion couple before and after annealing at  $350^\circ\text{C}$  for 8 hr. The thickness of the as-evaporated film is 100 Å. The arrow indicates the surface position.



**TABLE 5.12**  
**THE D-VALUES FOR THE DIFFUSION OF**  
**Au IN METALLIC GLASS Fe<sub>78</sub>B<sub>13</sub>Si<sub>9</sub>**

ANNEALING TEMP. (°C)	ANNEALING TIME (s)	D(t), m <sup>2</sup> /s *
300	57600	7.80×10 <sup>-22</sup>
350	28800	8.50×10 <sup>-22</sup>
400	3600	5.50×10 <sup>-21</sup>
400	7200	9.50×10 <sup>-22</sup>
400	14400	8.50×10 <sup>-22</sup>
400	28800	5.50×10 <sup>-22</sup>
400	57600	4.00×10 <sup>-22</sup>
450	3600	1.60×10 <sup>-20</sup>
450	7200	8.00×10 <sup>-21</sup>
450	14400	4.00×10 <sup>-21</sup>
450	28800	2.20×10 <sup>-21</sup>
450	57600	1.50×10 <sup>-21</sup>
475	3600	7.50×10 <sup>-21</sup>
475	7200	2.00×10 <sup>-21</sup>
475	14400	9.50×10 <sup>-22</sup>
475	28800	8.00×10 <sup>-22</sup>
475	57600	2.50×10 <sup>-22</sup>

\* The error in D is ±30%

The RBS spectra of the as-evaporated sample MG174/Au and that obtained after annealing at 350°C (8 hr) is shown in Figure 5.32. The simulated and the experimental spectrum for the same sample and for the same annealing parameters is shown in Figure 5.33. The samples MG146/Au and MG148/Au were analyzed using the thin film solution of the diffusion equation as the film thickness in these were comparable to the diffusion lengths. The other samples MG174/Au, MG175/Au and MG177/Au were analyzed using the error function solution to the diffusion equation. The diffusion coefficients obtained from these simulations are given in Table 5.12.

#### 5.7.1 Dependence of $D(t)$ on annealing time

The  $D(t)$  values obtained for the metallic glass  $\text{Fe}_{79}\text{B}_{16}\text{Si}_5$ -Au diffusion couple for the isothermal annealing temperatures of 400°C, 450°C and 475°C have been plotted against the annealing duration ( $t$ ) and are shown in Figures 5.34 (a), (b) and (c). The  $D(t)$  values decrease by factor of 10 to 30 (depending on the temperature of annealing) between  $t = 1$  hr and  $t = 16$  hr. For the annealing temperature of 400°C,  $D(t)$  asymptotically approaches a plateau value  $D(t) = D_p$  shown by the horizontal dashed line in Figure 5.34 (a). The  $D_p$  value at 400°C is less than the  $D(t)$  value for the largest annealing time at 300°C and 350°C, suggesting onset of crystallization in this metallic glass at 400°C, rather than at 450°C for  $t > 16$  hr or at 475°C for  $t > 1$  hr, as indicated by the X-ray diffraction and Mössbauer results (Chapter 4). The data points which represent diffusion in the amorphous phase of the host metallic glass are shown as open circles (Figures 5.30 (a) and (b)). On the other hand the data points representing diffusion in the crystalline phase (as per results of Chapter 4) are shown as solid circles in Figure 5.34 (c).

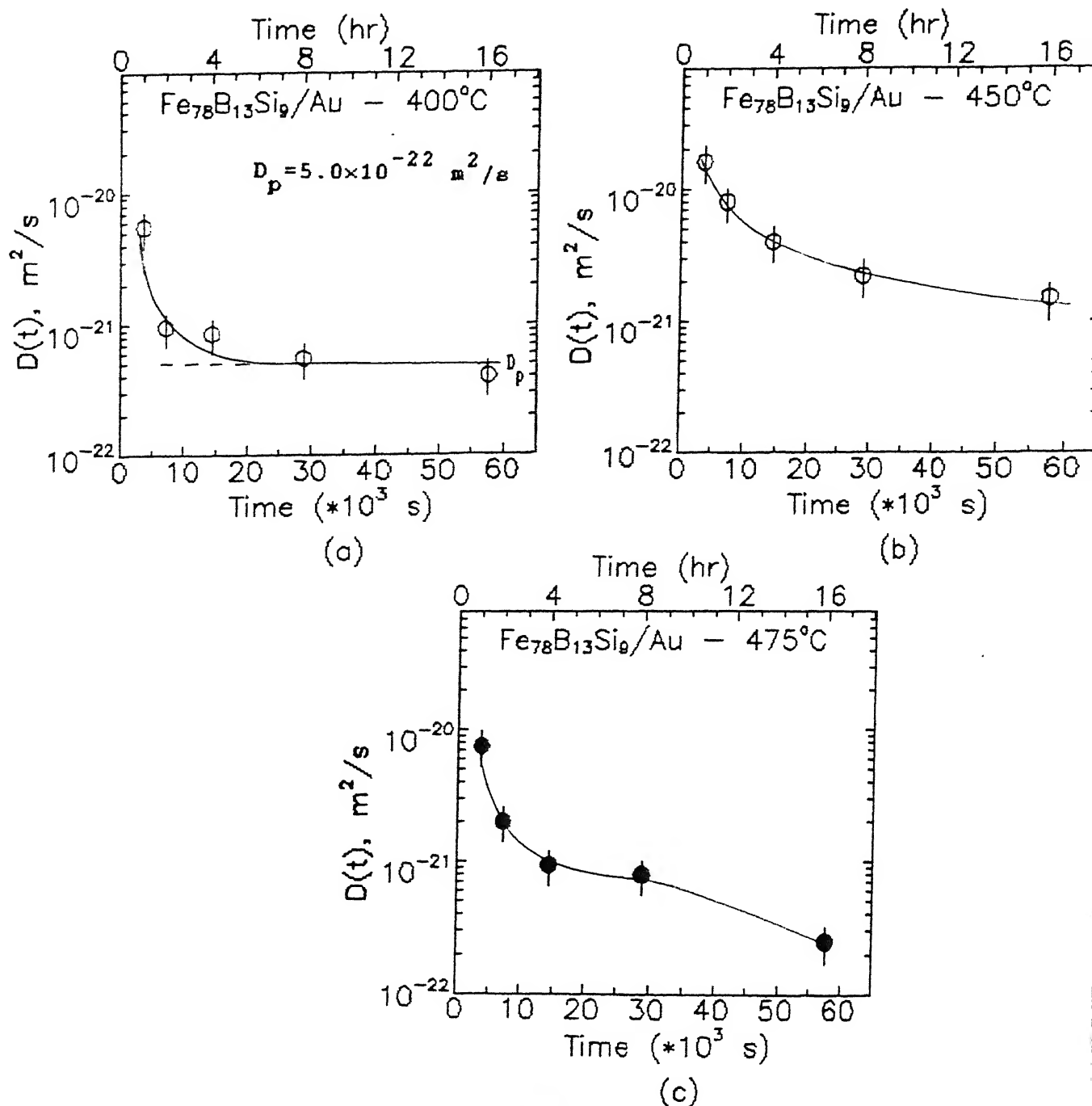


FIGURE 5.34 (a)-(c) Diagrams showing variation of the diffusion coefficient  $D(t)$  as a function of annealing time  $t$ , for diffusion of Au in  $\text{Fe}_{78}\text{B}_{13}\text{Si}_9$ . The vertical bars on the data points indicate error in the diffusion coefficients. The solid circles indicate that the crystallization of the metallic glass is observed by us using X-ray and Mössbauer techniques for these data points. The solid line, drawn as a best visual fit to the data points, asymptotically approaches a plateau value ( $D_p$ ) shown by the dashed line (for  $400^\circ\text{C}$ , see text).

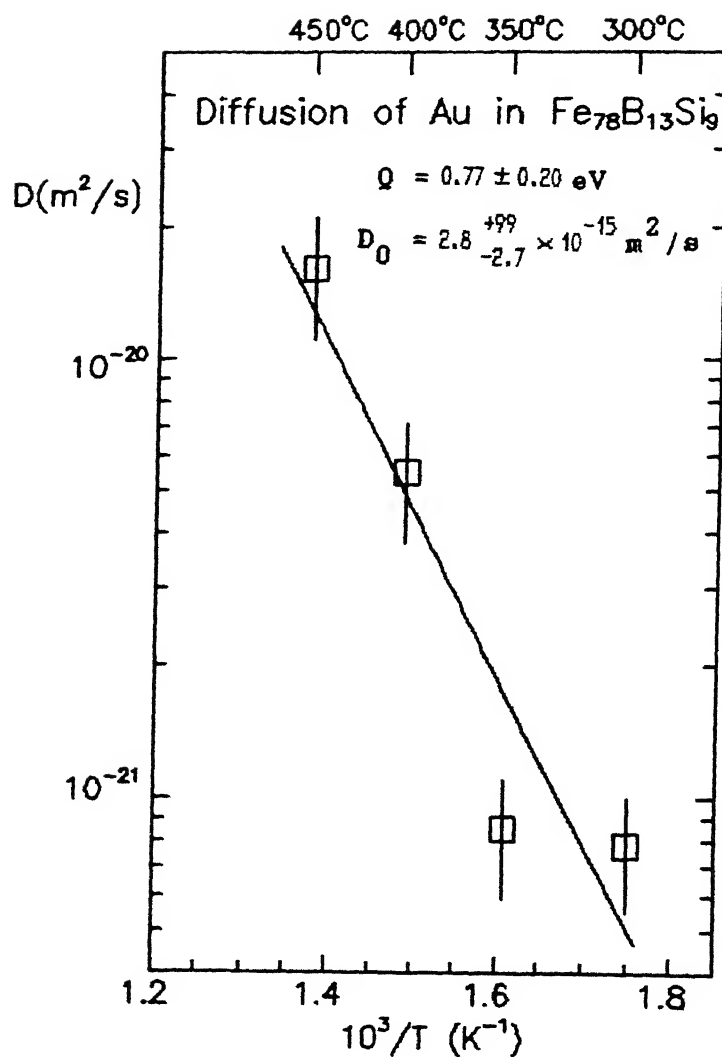


FIGURE 5.35 Temperature dependence of diffusivity of Au in metallic glass  $\text{Fe}_{78}\text{B}_{13}\text{Si}_9$  (Arrhenius plot). The solid line is a least square fitting to the data points at 300°C (16 hr), 350°C (8 hr), 400°C (1 hr) and 450°C (1 hr), (see text Sec. 5.7.2). The values of  $Q$  and  $D_0$  obtained from the fit are also mentioned.

### 5.7.2 Dependence of D on annealing temperature

The temperature dependence of the  $D(t)$  values for the diffusion of Au in  $\text{Fe}_{78}\text{B}_{13}\text{Si}_9$  is shown in Figure 5.35. Similar to that of Au diffusion in  $\text{Fe}_{79}\text{B}_{16}\text{Si}_5$ , here also the Arrhenius behaviour is observed if the  $D(t)$  values at  $300^\circ\text{C}$  (16 hr),  $350^\circ\text{C}$  (8 hr),  $400^\circ\text{C}$  (1 hr) and  $450^\circ\text{C}$  (1 hr) are utilized, and the straight line drawn therein is a least square fit to these data points. A comparative discussion of the anomalous diffusion behaviour at  $400^\circ\text{C}$  and  $450^\circ\text{C}$  for this diffusion couple is presented in Sec. 5.12. The activation energy  $Q$  and pre-exponential factor  $D_0$  obtained from the fit (of Figure 5.35) are:

$$Q = 0.77 \pm 0.20 \text{ eV}$$

$$D_0 = 2.8^{+99}_{-2.7} \times 10^{-15} \text{ m}^2/\text{s}$$

with an error in  $Q$  being 26% and that in  $\log(D_0)$  being 11%. The large errors obtained for the  $Q$  and  $D_0$  values is due to the spread in the data at  $350^\circ\text{C}$  and  $300^\circ\text{C}$  (see Figure 5.35) about the fitted solid line.

## 5.8 DIFFUSION OF AG IN METALLIC GLASS $\text{Fe}_{79}\text{B}_{16}\text{Si}_5$

The metallic glass/Ag diffusion couple (or sample) was annealed at  $350^\circ\text{C}$  for durations given in Table 5.13.

TABLE 5.13  
SAMPLE IDENTIFICATION FOR  $\text{Fe}_{79}\text{B}_{16}\text{Si}_5$ - Ag DIFFUSION COUPLE

SAMPLE NUMBER	FILM ( $\text{\AA}$ ) THICKNESS	ANNEAL TEMP( $^\circ\text{C}$ )	ANNEAL TIME(hr)
MG102/Ag	230	350	1, 4, 8, 16

The RBS spectra of this couple for the as-evaporated case as well as after annealing for 8 hr, is depicted in Figure 5.36. The simulations of these RBS spectra were done by using the error function solution to the diffusion equation and a particular case of simulation is shown in Figure 5.37. The results of the diffusion analysis for the annealing durations are shown in Table 5.14.

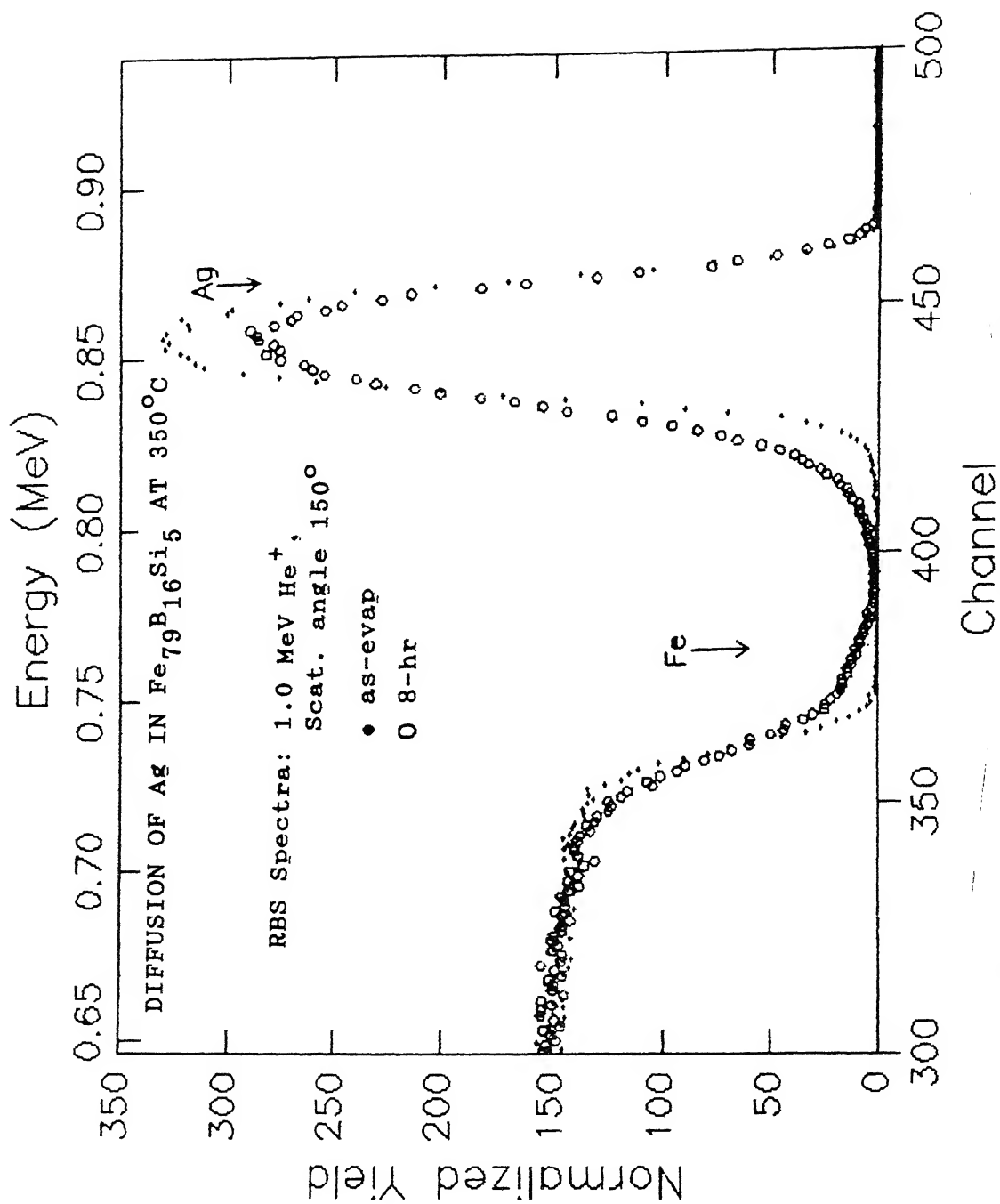


FIGURE 5.36 Normalised RBS spectra of  $\text{Fe}_{79}\text{B}_{16}\text{Si}_5$ -Ag diffusion couple before and after annealing at  $350^\circ\text{C}$  for 8 hr. The thickness of the as-evaporated film is  $230 \text{ \AA}$ . The arrow indicates the surface position.

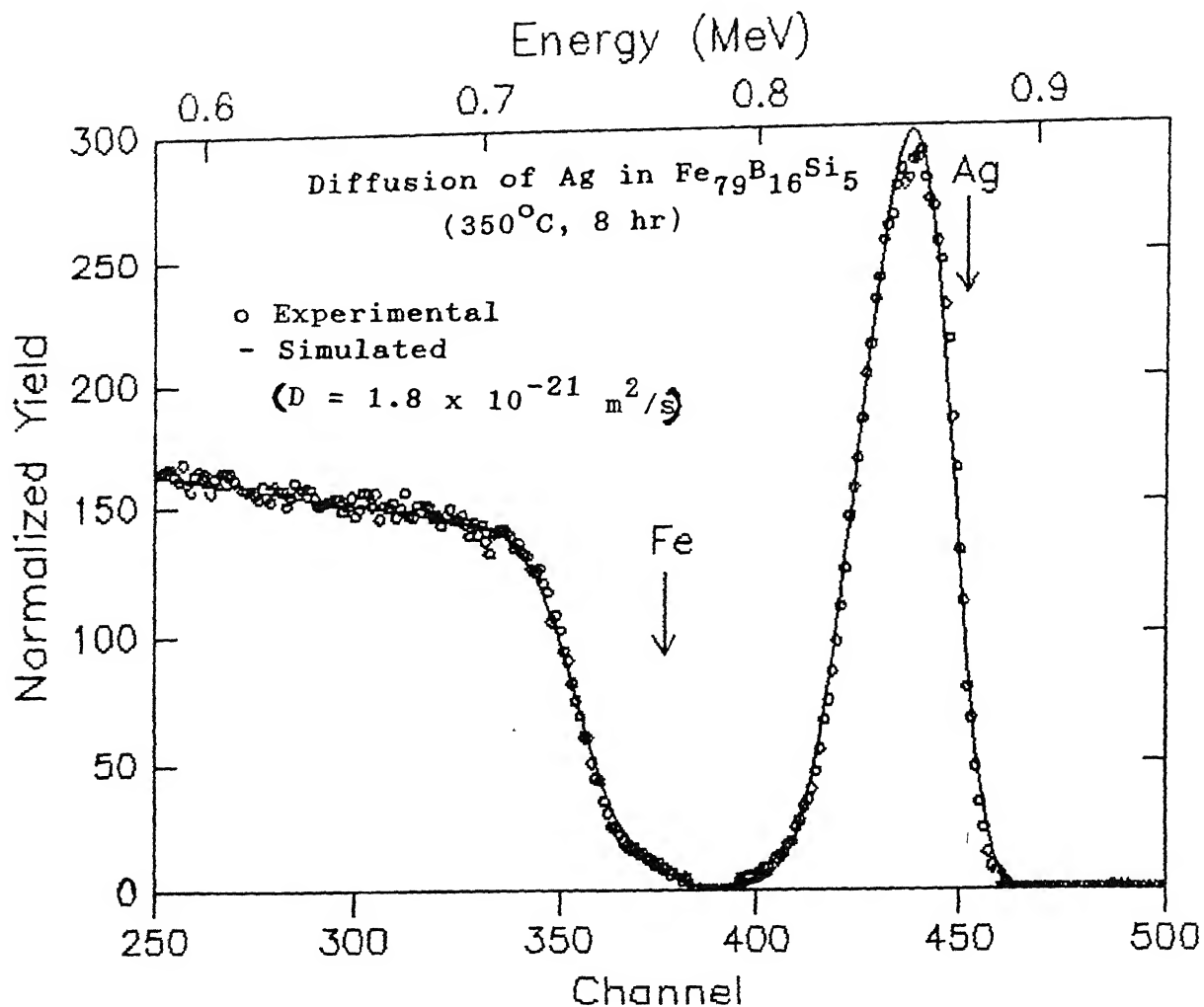


FIGURE 5.37 Comparison of experimental (1.0 MeV  $\text{He}^+$ , scattering angle  $150^\circ$ ) and simulated RBS spectra to determine the D-value of Ag in  $\text{Fe}_{79}\text{B}_{16}\text{Si}_5$  at 350°C (8 hr). The simulation was performed using the error function solution of the diffusion equation (refer section 1.4.3).

**TABLE 5.14**  
D values for Ag in  $\text{Fe}_{79}\text{B}_{16}\text{Si}_5$

Annealing Temp. ( $^{\circ}\text{C}$ )	Time (s)	D(t), $\text{m}^2/\text{s}$ *
350	1	$8.00 \times 10^{-21}$
	4	$3.20 \times 10^{-21}$
	8	$1.75 \times 10^{-21}$
	16	$1.00 \times 10^{-21}$

\* The error in D is  $\pm 30\%$

#### 5.8.1 Dependence of D(t) on annealing time

The diffusion coefficients of Ag in  $\text{Fe}_{79}\text{B}_{16}\text{Si}_5$  obtained at  $350^{\circ}\text{C}$  for various annealing periods is plotted in Figure 5.38. These data points representing diffusion in the amorphous phase of the host metallic glass are shown as open circles. The result in Figure 5.38 shows that D(t) falls by a

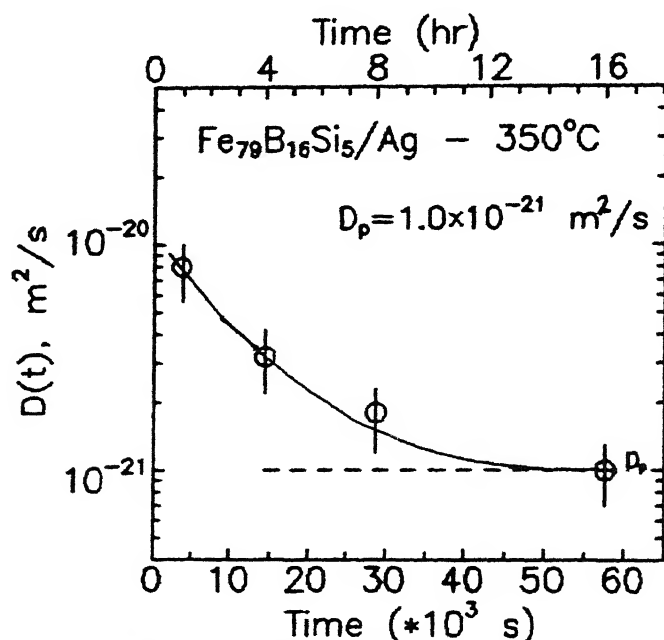


**FIGURE 5.38** Diagram showing variation of the diffusion coefficient D(t) as a function of annealing time t, at  $350^{\circ}\text{C}$ , for diffusion of Ag in  $\text{Fe}_{79}\text{B}_{16}\text{Si}_5$ . The vertical bars on the data points indicate error in the diffusion coefficient. The solid line, drawn as a best visual fit to the data points, asymptotically approaches a plateau value ( $D_p$ ) shown by the dashed line.



factor of 8 between  $t = 1$  hr and  $t = 16$  hr. The  $D(t)$  vs.  $t$  curve asymptotically approaches a plateau value  $D_p$  (as shown by the horizontal dashed line  $D(t) = D_p$ ) representing diffusion in the 'relaxed' amorphous phase of the metallic glass.

## 5.9 DIFFUSION OF AG IN METALLIC GLASS $\text{Fe}_{78}\text{B}_{13}\text{Si}_9$

Diffusion couples made from the metallic glass  $\text{Fe}_{78}\text{B}_{13}\text{Si}_9$  and Ag film were annealed at  $350^\circ\text{C}$  for the various durations mentioned in Table 5.15 below.

TABLE 5.15  
SAMPLE IDENTIFICATION FOR  $\text{Fe}_{78}\text{B}_{13}\text{Si}_9$ - Ag DIFFUSION COUPLE

SAMPLE NUMBER	FILM ( $\text{\AA}$ ) THICKNESS	ANNEAL TEMP( $^\circ\text{C}$ )	ANNEAL TIME(hr)
MG104/Ag	220	350	1, 4, 8, 16

The RBS spectrum of the as-evaporated sample and that obtained on annealing are shown overlapped in Figure 5.39. The experimental spectra were simulated to determine the diffusion coefficient after each annealing time period. The error function solution of the diffusion equation was used for the same. A simulated spectrum along with its experimental counterpart are shown in Figure 5.40. The  $D(t)$  values obtained from the simulations of the experimental spectra are given in Table 5.16 below.

TABLE 5.16  
D values for Ag in  $\text{Fe}_{78}\text{B}_{13}\text{Si}_9$

Annealing Temp. ( $^\circ\text{C}$ )	Time(s)	$D(t)^*$ , $\text{m}^2/\text{s}$
350	1	$1.00\text{e-}20$
	4	$5.00\text{e-}21$
	8	$2.50\text{e-}21$
	16	$1.20\text{e-}21$

\* The error in D is  $\pm 30\%$

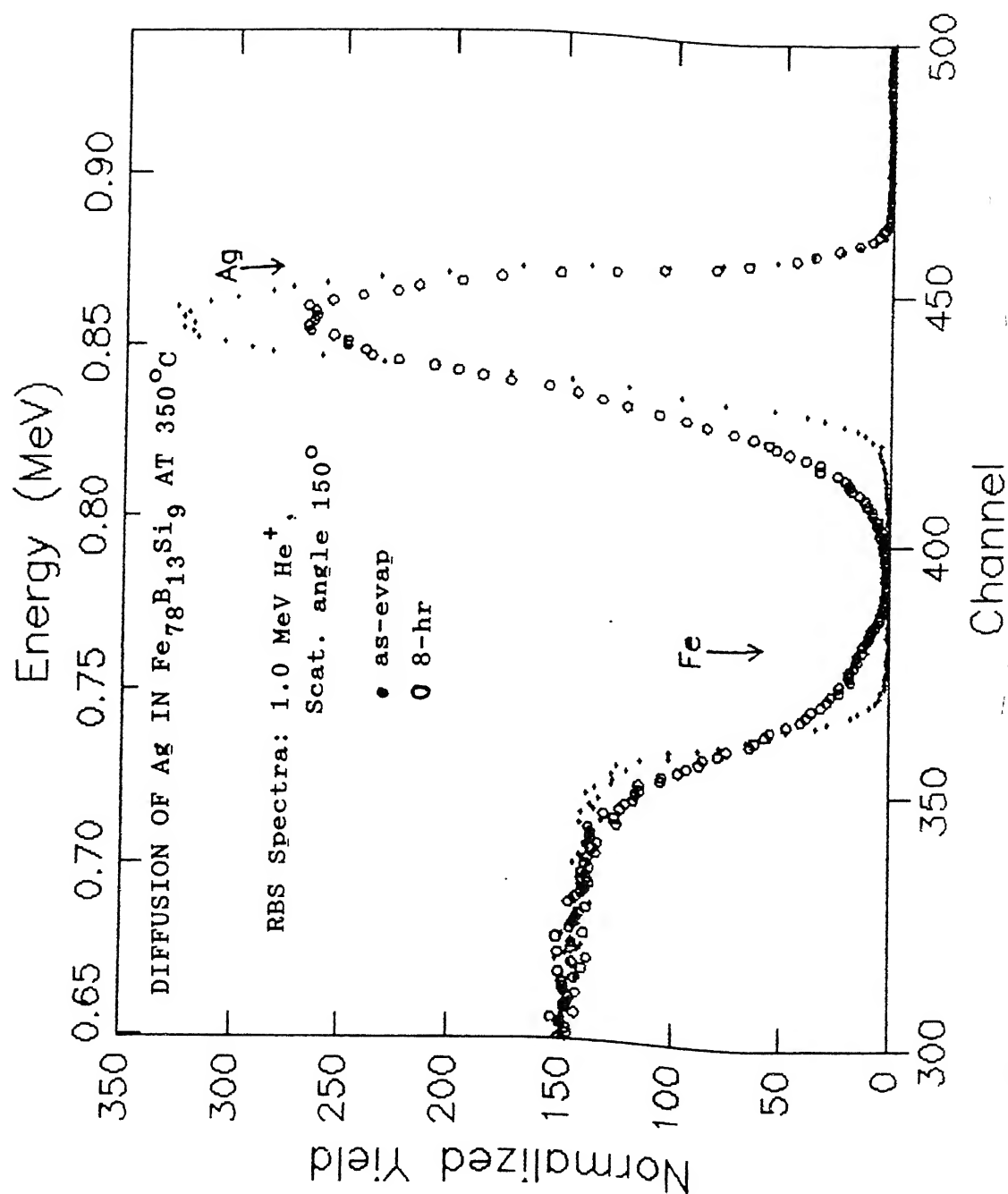
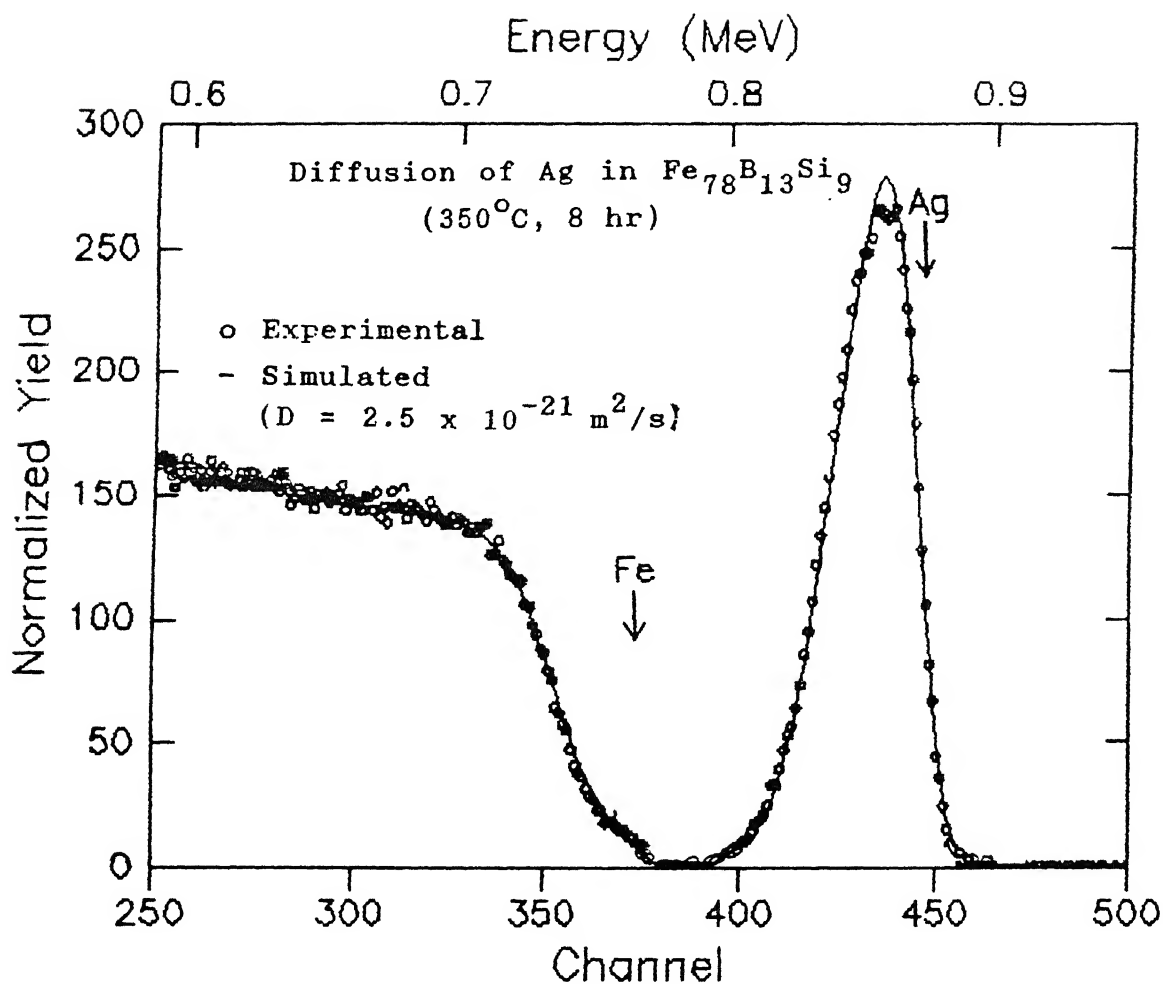


FIGURE 5.39 Normalised RBS spectra of  $\text{Fe}_{78}\text{B}_{13}\text{Si}_9$ -Ag diffusion couple before and after annealing at  $350^\circ\text{C}$  for 8 hr. The thickness of the as-evaporated film is  $220 \text{ \AA}$ . The arrow indicates the surface position.



**FIGURE 5.40** Comparison of experimental ( $1.0 \text{ MeV He}^+$ , scattering angle  $150^\circ$ ) and simulated RBS spectra to determine the D-value of Ag in  $\text{Fe}_{78}\text{B}_{13}\text{Si}_9$  at  $350^\circ\text{C}$  (8 hr). The simulation was performed using the error function solution of the diffusion equation (refer section 1.4.3).

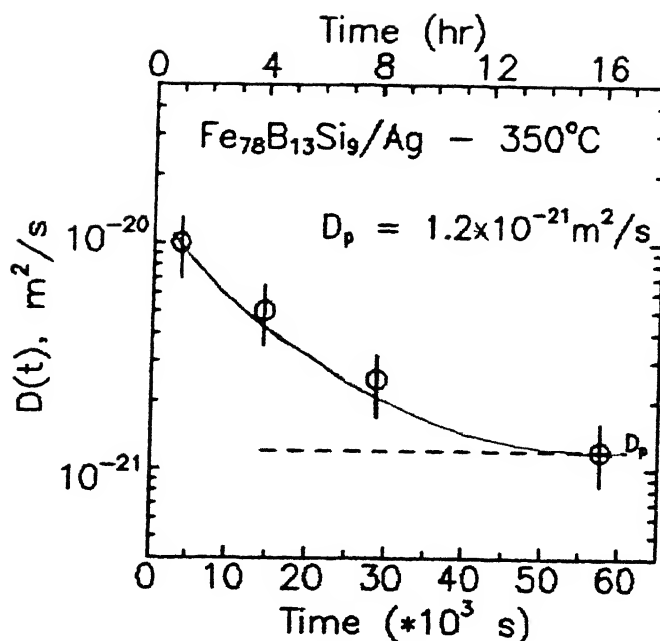


FIGURE 5.41 Diagram showing variation of the diffusion coefficient  $D(t)$  as a function of annealing time  $t$ , at  $350^\circ\text{C}$ , for diffusion of Ag in  $\text{Fe}_{78}\text{B}_{13}\text{Si}_9$ . The vertical bars on the data points indicate error in the diffusion coefficient. The solid line, is drawn as a best visual fit to the data points, asymptotically approaches a plateau value ( $D_p$ ) shown by the dashed line.

#### 5.9.1 Dependence of $D(t)$ on annealing time

The  $D(t)$  values obtained at  $350^\circ\text{C}$  for diffusion of Ag in  $\text{Fe}_{78}\text{B}_{13}\text{Si}_9$ , have been plotted in Figure 5.41 against the annealing time period ( $t$ ). It is observed that  $D(t)$  falls by a factor of 10 between  $t = 1$  hr and  $t = 16$  hr. The  $D(t)$  versus  $t$  curve drawn as a best visual fit asymptotically approaches a plateau value  $D(t) = D_p$  which is indicated by a horizontal dashed line in the figure. Similar behaviour has been observed in the diffusing couples mentioned in the earlier sections and it has been attributed to the process of structural relaxation in the amorphous host material.

## 5.10 DIFFUSION OF Pd IN METALLIC GLASS $\text{Fe}_{40}\text{Ni}_{38}\text{B}_{18}\text{Mo}_4$

The diffusion couples of the metallic glass  $\text{Fe}_{40}\text{Ni}_{38}\text{B}_{18}\text{Mo}_4$  / Pd film, were annealed at temperatures and time periods mentioned in Table 5.17.

TABLE 5.17  
SAMPLE IDENTIFICATION FOR  $\text{Fe}_{40}\text{Ni}_{38}\text{B}_{18}\text{Mo}_4$ - Pd DIFFUSION COUPLE

SAMPLE NUMBER	FILM ( $\text{\AA}$ ) THICKNESS	ANNEAL TEMP( $^{\circ}\text{C}$ )	ANNEAL TIME(hr)
MB278/Pd	250	300	1, 2, 4, 8, 12, 16
MB277/Pd	200	350	1, 2, 4, 8, 12, 16
MB259/Pd	250	400	1, 2, 4, 8, 12, 16
MB260/Pd	230	450	1, 2, 4, 8, 12, 16

The time dependence of the diffusion process at  $450^{\circ}\text{C}$  and  $400^{\circ}\text{C}$  is illustrated by the RBS spectra of the samples before and after annealing in the Figures 5.42 and 5.43. The diffusion occurring at the interface is clearly observed in the figures by (i) the decrease in the film height; (ii) signals from Pd being observed at lower energies and (iii) increase in the FWHM of the film. Simulations of the RBS spectra are illustrated in Figures 5.44 and 5.45 for a few cases. The error function solution of the diffusion equation was utilized to obtain the D values in this system and these are mentioned in Table 5.18.

### 5.10.1 Dependence of $D(t)$ on annealing time

The diffusion coefficients obtained for the diffusion of Pd in  $\text{Fe}_{40}\text{Ni}_{38}\text{B}_{18}\text{Mo}_4$  evaluated at various annealing periods for the annealing temperatures of  $300^{\circ}\text{C}$ ,  $350^{\circ}\text{C}$ ,  $400^{\circ}\text{C}$  and  $450^{\circ}\text{C}$  are plotted in Figure 5.46 (a)-(d), respectively. These figures depict the changes occurring in the  $D(t)$  values as a function of annealing time ( $t$ ). For a given temperature  $T$ ,  $D(t)$  decreases to an almost flat plateau at large  $t$ . This trend is similar to that observed earlier for diffusion in the Fe-B-Si alloys.

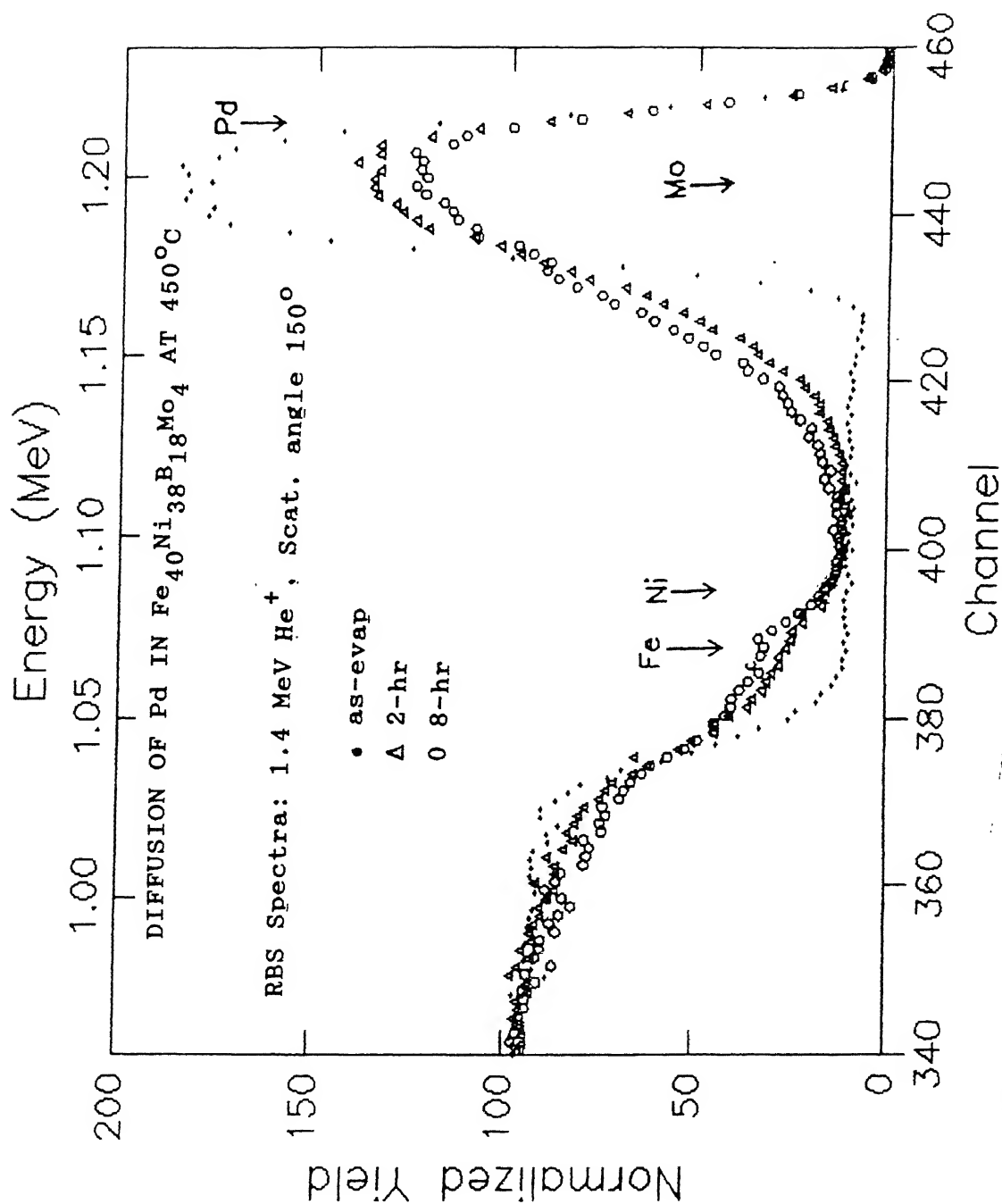


FIGURE 5.42 Normalised RBS spectra of Fe<sub>40</sub>Ni<sub>38</sub>B<sub>18</sub>Mo<sub>4</sub>-Pd diffusion couple before and after annealing at 450°C for 2 hr and 8 hr respectively. The thickness of the as-evaporated film is 230 Å. The arrow indicates the surface position.

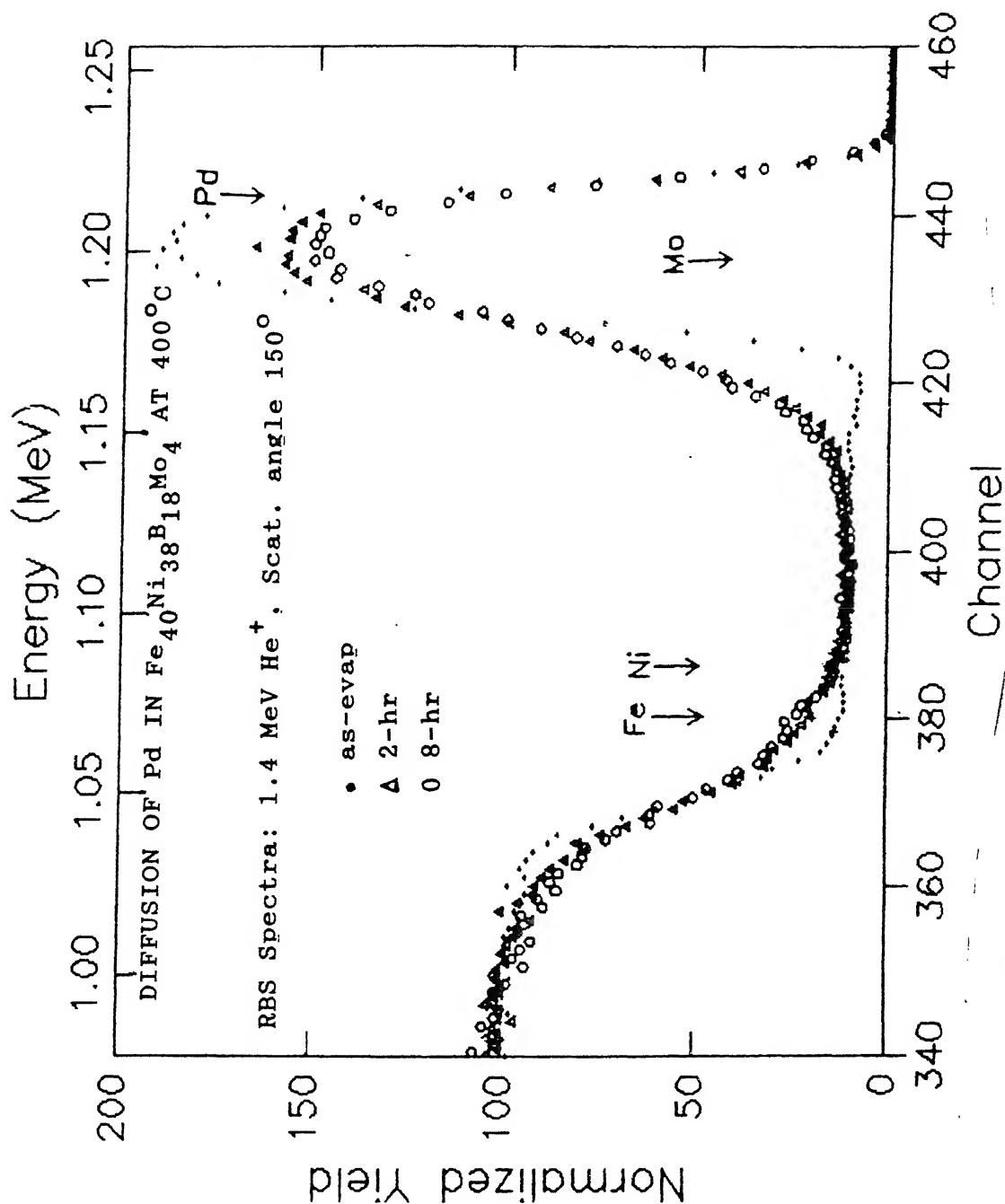
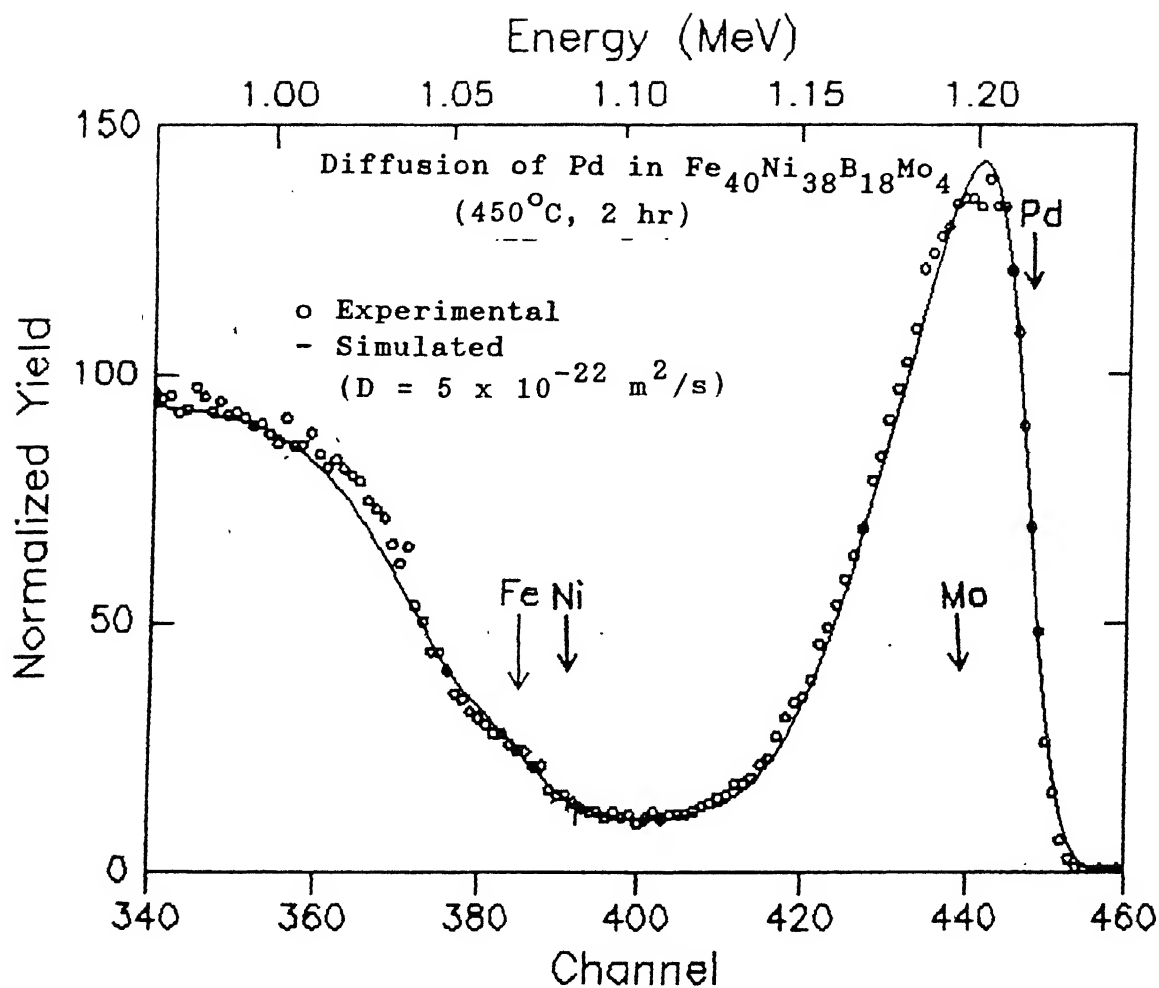


FIGURE 5.43 Normalised RBS spectra of  $\text{Fe}_{40}\text{Ni}_{38}\text{B}_{18}\text{Mo}_4$ -Pd diffusion couple before and after annealing at  $400^\circ\text{C}$  for 2 hr and 8 hr respectively. The thickness of the as-evaporated film is  $250 \text{ \AA}$ . The arrow indicates the surface position.



**FIGURE 5.44** Comparison of experimental (1.4 MeV  $\text{He}^+$ , scattering angle  $150^\circ$ ) and simulated RBS spectra to determine the D-value of Pd in  $\text{Fe}_{40}\text{Ni}_{38}\text{B}_{18}\text{Mo}_4$  at 450°C (2 hr). The simulation was performed using the error function solution of the diffusion equation (refer section 1.4.3).



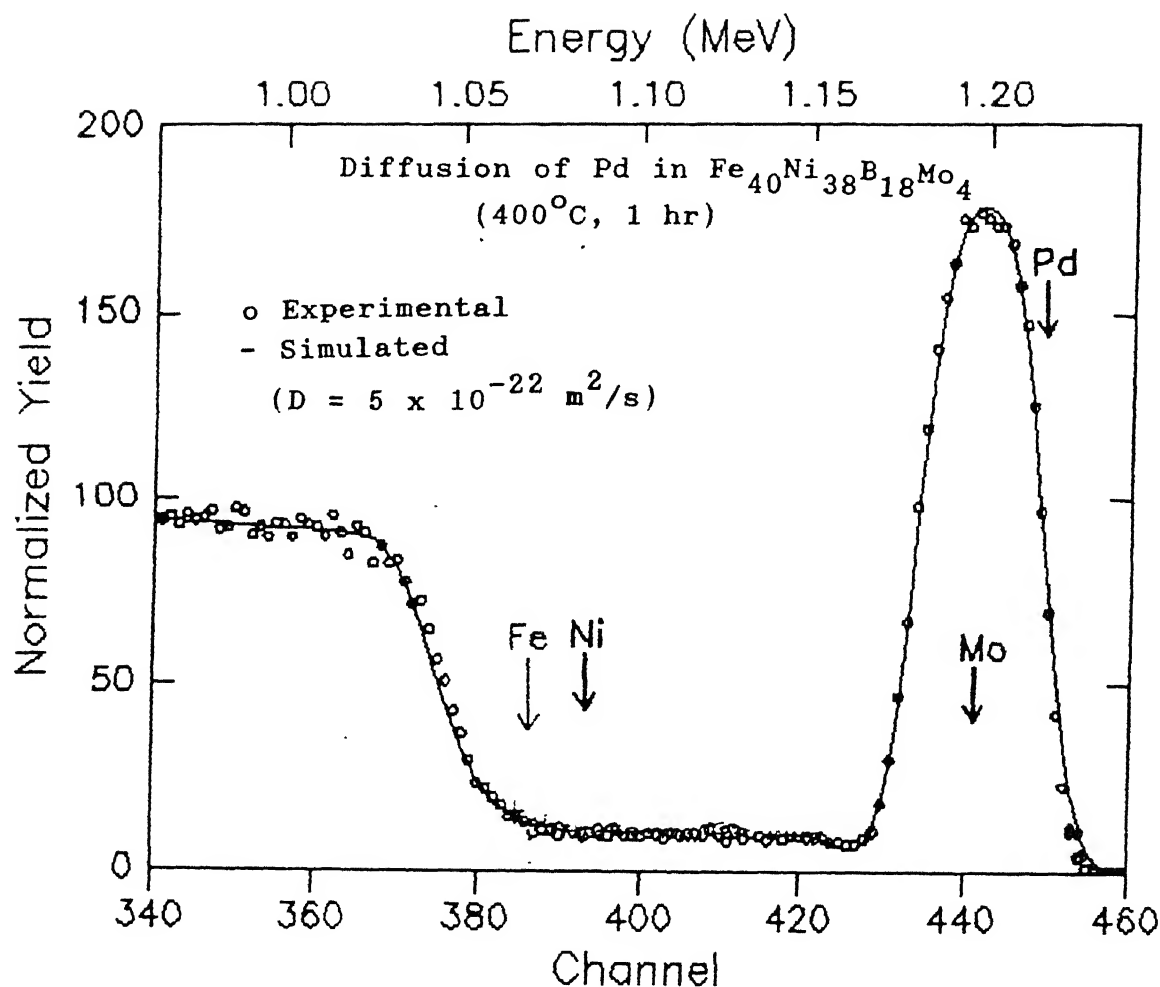


FIGURE 5.45 Comparison of experimental (1.4 MeV  $\text{He}^+$ , scattering angle  $150^\circ$ ) and simulated RBS spectra to determine the D-value of Pd in  $\text{Fe}_{40}\text{Ni}_{38}\text{B}_{18}\text{Mo}_4$  at 400°C (1 hr). The simulation was performed using the error function solution of the diffusion equation (refer section 1.4.3).

**TABLE 5.18**  
**THE D-VALUES FOR THE DIFFUSION OF**  
**Pd IN METALLIC GLASS  $\text{Fe}_{40}\text{Ni}_{38}\text{B}_{18}\text{Mo}_4$**

ANNEALING TEMP ( $^{\circ}\text{C}$ )	ANNEALING TIME (s)	$D(t), \text{m}^2/\text{s}$ *
300	3600	$2.30 \times 10^{-21}$
300	7200	$1.50 \times 10^{-21}$
300	14400	$8.00 \times 10^{-22}$
300	28800	$3.00 \times 10^{-22}$
300	43200	$1.50 \times 10^{-22}$
300	57600	$1.00 \times 10^{-22}$
350	3600	$3.00 \times 10^{-21}$
350	7200	$6.50 \times 10^{-22}$
350	14400	$6.50 \times 10^{-22}$
350	28800	$5.00 \times 10^{-22}$
350	43200	$1.80 \times 10^{-22}$
350	57600	$2.00 \times 10^{-22}$
400	7200	$1.20 \times 10^{-20}$
400	14400	$7.00 \times 10^{-21}$
400	28800	$4.00 \times 10^{-21}$
400	43200	$3.20 \times 10^{-21}$
400	57600	$2.30 \times 10^{-21}$
450	3600	$4.50 \times 10^{-20}$
450	7200	$2.50 \times 10^{-20}$
450	14400	$2.00 \times 10^{-20}$
450	28800	$9.50 \times 10^{-21}$
450	43200	$7.00 \times 10^{-21}$
450	57600	$7.00 \times 10^{-21}$

\* The error in D is  $\pm 30\%$

We consider these curves as best visual fits to the data points taking into account the error bars on the  $D(t)$  values. The results in Figure 5.46 show that  $D(t)$  falls by factor of 5 to 20 (depending on the temperature of annealing) between  $t = 1$  hr and  $t = 16$  hr. The asymptotic decrease in  $D(t)$  to a plateau value  $D_p$  at  $300^\circ\text{C}$  for  $1 \leq t \leq 16$  hr and at  $350^\circ\text{C}$  for  $t \leq 4$  hr. has been attributed to the structural relaxation in the amorphous host material. The plateau values have been indicated in Figures 5.46 (a) and (b) by the horizontal dashed lines  $D(t) = D_p$ . These  $D_p$  values represent the diffusion process in the 'relaxed' amorphous phase of the metallic glass. For  $350^\circ\text{C}$  (Figure 5.46(b)), the decrease in  $D(t)$  at  $t > 8$  hr has been attributed to the effect of crystallization in the alloy. Similar behaviour of  $D(t)$  has been reported by Pfahler and co-workers [Pfahler et al. 1985] for the tracer diffusion of  $^{59}\text{Fe}$  in  $\text{Fe}_{41}\text{Ni}_{41}\text{B}_{18}$ . These authors have reported a crystallization temperature of  $370^\circ\text{C}$  for this metallic glass, and the sudden drop observed at  $340^\circ\text{C}$  (25 hr) has been attributed to the crystallization of the metallic glass. It is known from the literature [Goodfellow metals catalogue 1990/91] that the crystallization temperature of  $\text{Fe}_{40}\text{Ni}_{38}\text{B}_{18}\text{Mo}_4$  metallic glass is  $410^\circ\text{C}$ . We, therefore, assumed that the diffusion coefficients obtained by us for samples annealed at  $400^\circ\text{C}$  for  $t > 1$  hr and  $450^\circ\text{C}$  for  $1 \text{ hr} \leq t \leq 16$  hr obviously do not represent diffusion in the amorphous phase of the host metallic glass. These data points are shown as solid circles in Figures 5.46 (c) and (d). On the other hand the data points which represent diffusion in the amorphous phase of the host metallic glass are shown as open circles.

### 5.10.2 Dependence of $D$ on annealing temperature

The temperature dependence of the  $D(t)$  values for the diffusion of Pd in  $\text{Fe}_{40}\text{Ni}_{38}\text{B}_{18}\text{Mo}_4$  has been plotted in Figure 5.47 against the inverse of the annealing temperature  $T$ . In the figure the open circles refer to the plateau

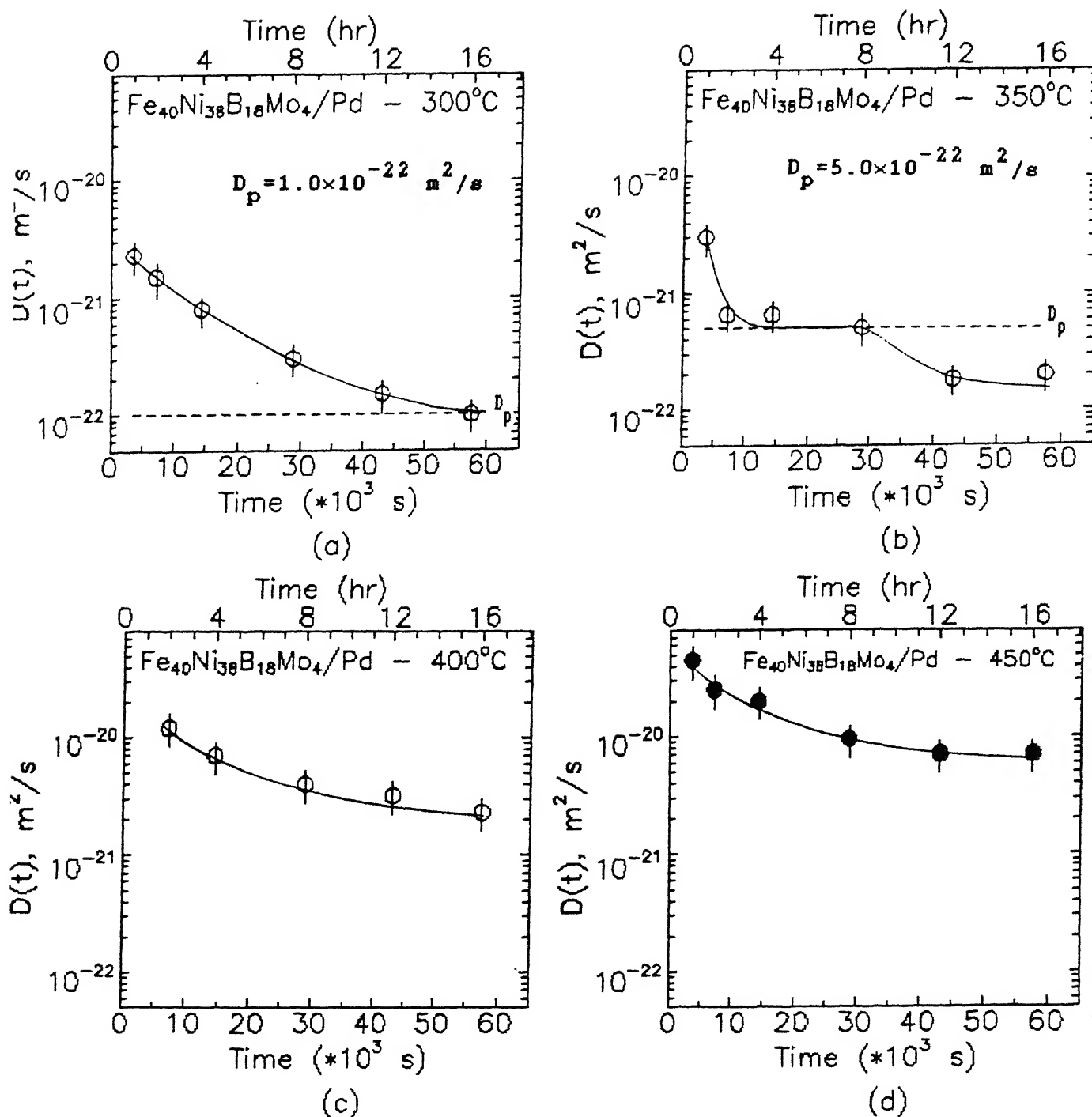


FIGURE 5.46 (a)-(d) Diagrams showing variation of the diffusion coefficient  $D(t)$  as a function of annealing time  $t$ , for diffusion of Pd in  $\text{Fe}_{40}\text{Ni}_{38}\text{B}_{18}\text{Mo}_4$ . The vertical bars on the data points indicate error in the diffusion coefficient. The solid circles indicate crystallization of the metallic glass for these data points. The solid line, drawn as a best visual fit to the data points, asymptotically approaches (for  $300^\circ\text{C}$  and  $350^\circ\text{C}$ ) a plateau value ( $D_p$ ) shown by the dashed line.

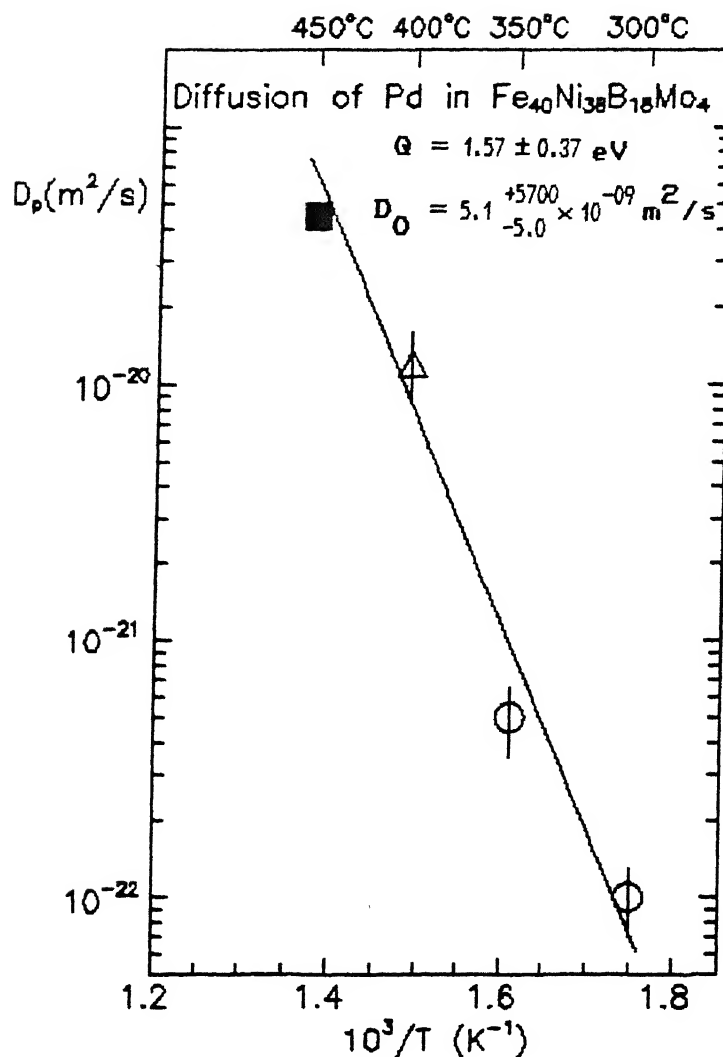


FIGURE 5.47 Temperature dependence of diffusivity of Pd in metallic glass  $\text{Fe}_{40}\text{Ni}_{38}\text{B}_{18}\text{Mo}_4$  (Arrhenius plot). The open circles indicate the plateau values ( $D_p$ ) obtained from the  $D(t)$  vs. annealing time diagrams (Figs. 5.46 (a),(b)), and the solid line is a least square fitting to these data points alongwith the  $D(t)$  value at 400°C (1 hr). The values of  $Q$  and  $D_0$  obtained from the fit are also mentioned. The solid square indicates the  $D(t)$  value at 450°C (1 hr) which represents diffusion in crystallized  $\text{Fe}_{40}\text{Ni}_{38}\text{B}_{18}\text{Mo}_4$ .

values corresponding to the diffusion in the relaxed state, and the open triangle corresponds to the  $D(t)$  value at  $400^{\circ}\text{C}$  (1 hr) which represents diffusion in the amorphous state of the metallic glass (see Sec. 5.10.1). The straight line drawn therein is a least square fit to these data points. The  $D(t)$  value at  $450^{\circ}\text{C}$  for  $t = 1$  hr, representing diffusion in crystallized sample of  $\text{Fe}_{40}\text{Ni}_{38}\text{B}_{18}\text{Mo}_4$  is also shown in the figure (by closed square symbol) for the sake of comparison, but it has not been used for the fitting.

The values of  $Q$  and  $D_0$  obtained from the least square fit to the data are

$$Q = 1.57 \pm 0.37 \text{ eV}$$

$$D_0 = 5.1_{-5.0}^{+5700} \times 10^{-9} \text{ m}^2/\text{s}$$

with an error in  $Q$  being 24% and that in  $\log(D_0)$  being 37%. The large errors in the  $Q$  and  $D_0$  values is most probably due to the spread in the data of Figure 5.47, about the fitted line.

## 5.11 TIME DEPENDENCE OF DIFFUSIVITY AND RELAXATION

The plots of  $D(t)$  versus annealing time indicate interesting features where the diffusion coefficient values decrease by a factor of 5 to 10 during the first few hours of isothermal annealing. As a matter of fact, in most of the previously reported diffusion data on metallic glasses such dependence of the diffusion coefficient values on the annealing duration had not been considered except in the case of diffusion of B in amorphous metallic glass  $\text{Ni}_x\text{Nb}_{100-x}$  [Kijek 1982], and more recently that of the diffusion of  $^{59}\text{Fe}$ ,  $^{57}\text{Co}$ ,  $^{99}\text{Zr}$  in amorphous Fe-B and Fe-Zr metallic glasses [Horvath et al. 1988].

In the present work the time dependence of the  $D(t)$  values has been observed for all the amorphous metallic glass / metal or metalloid diffusion couples undertaken for diffusion studies. The  $D(t)$  values obtained in each case are tabulated in the earlier sections in the Tables 5.2, 5.4, 5.6, 5.8, 5.10, 5.12, 5.14, 5.16 and 5.18; and the results of the time dependence of the

$D(t)$ -values are depicted earlier in Figures 5.7, 5.14, 5.20, 5.26, 5.30, 5.34, 5.38, 5.41 and 5.46. Following the arguments given by *Frank et al.* [1988] and *Mehrer and Dorner* [1989] such decrease in the  $D(t)$  values as a function of annealing time ( $t$ ), towards a plateau value  $D_p$  can be attributed to the effect of structural relaxation occurring in the metallic glass samples.

The effect of structural relaxation has also been shown to occur in the volume density [*Komatsu et al.* 1986a] and electrical resistivity [*Komatsu et al.* 1986b] measurements. The measurements on volume density have shown that structural relaxation always leads to an increase in the volume density. In general the structural relaxation can be considered as occurring due to (i) higher Gibb's free energy of the quenched alloy [*Mehrer and Dorner* 1989] and (ii) the presence of excess free volume [*Frank et al.* 1988] which lead to the decrease of the diffusion coefficient. Structural relaxation of the viscosity of metallic glasses has been reported by *Tsao and Spaepen* [1984].

During relaxation, units of free volume which Horvath and collaborators have termed as "quasi-vacancies", disappear via thermally activated migration. According to these authors the enhancement in the diffusivity ( $\delta D$ ) during relaxation is due to an indirect diffusion of the diffusing species via "quasi-vacancies", and can be expressed by the relation

$$\delta D = f_v D_v \delta C_v \quad (5.2)$$

where  $f_v$  is a correlation factor.  $D_v$  is the diffusivity and  $\delta C_v$  is the concentration of the quasi-vacancies and are expressed as

$$D_v = D_{vo} \exp\left(-\frac{H_v^m}{kT}\right) \quad (5.3)$$

$$\delta C_v = \delta C_{vo} \exp\left(-\frac{t}{\tau_v}\right) \quad (5.4)$$

where  $D_{vo}$  is the pre-exponential factor for diffusivity,  $H_v^m$  is the quasi-vacancy migration enthalpy, and  $\delta C_{vo}$  is the concentration of the "defects" in the as-quenched state.  $\tau_v$  is the relaxation time and can be expressed as a function of

the quasi-vacancy migration enthalpy i.e.,

$$\tau_v = \tau_{vo} \exp\left(\frac{H_v^m}{kT}\right) \quad (5.5)$$

Based on the above formalism, we have analyzed our data of  $D(t)$  versus annealing time, obtained from the measurements of the diffusion of Ge in  $\text{Fe}_{79}\text{B}_{16}\text{Si}_5$ . The  $D(t)$  vs  $t$  diagrams for this diffusion couple is shown here again in Figure 5.48(i), with the arrows indicating the completion of the relaxation process. We have chosen the relaxation time  $\tau$  for the annealing temperatures of  $300^\circ\text{C}$ ,  $350^\circ\text{C}$  and  $400^\circ\text{C}$ , as that time where the smooth curve (drawn between the data points) reaches to 20% of the plateau value  $D_p$ . On the other hand for  $450^\circ\text{C}$  we have chosen  $\tau$  as the lowest annealing duration employed in our studies, i.e., 1 hr. The choice of the condition that  $D(t)$  approaches to within 20% of  $D_p$  for relaxation to be over, is somewhat arbitrary. Since there is no definite criterion given in the literature for choosing the relaxation time, and that the  $D$  values in the present study show  $\pm 30\%$  error, we decided to choose this condition for the present analysis. The plot of  $\tau$  vs  $1/T$  obtained for the diffusion of Ge in  $\text{Fe}_{79}\text{B}_{16}\text{Si}_5$  is shown in Figure 5.48(ii). The lower limit of the bar on the data points indicate that the  $D(t)$  values approach to within 30% of the  $D_p$  value, while the upper limit indicates that the  $D(t)$  values approach to within 10% of the plateau value. A least-square fit to these data points, gives the following equation in  $\tau$ :

$$\tau = 6.43 \times 10^{-01} \exp(6.36/T)$$

The quasi-vacancy migration enthalpy  $H_v^m$  and the pre-exponential factor  $\tau_{vo}$  obtained from this equation are:

$$\begin{aligned} H_v^m &= 0.55 \text{ eV} \\ \tau_{vo} &= 6.43 \times 10^{-01} \text{ s} \end{aligned}$$

Frank et al. [1988] have given an estimate of these values for  $\text{Fe}_{40}\text{Ni}_{40}\text{B}_{20}$  i.e.,  $H_v^m \leq 1 \text{ eV}$ , and  $\tau_{vo} \cong 10^{-05} \text{ s}$ , but the details of the analysis are not reported.



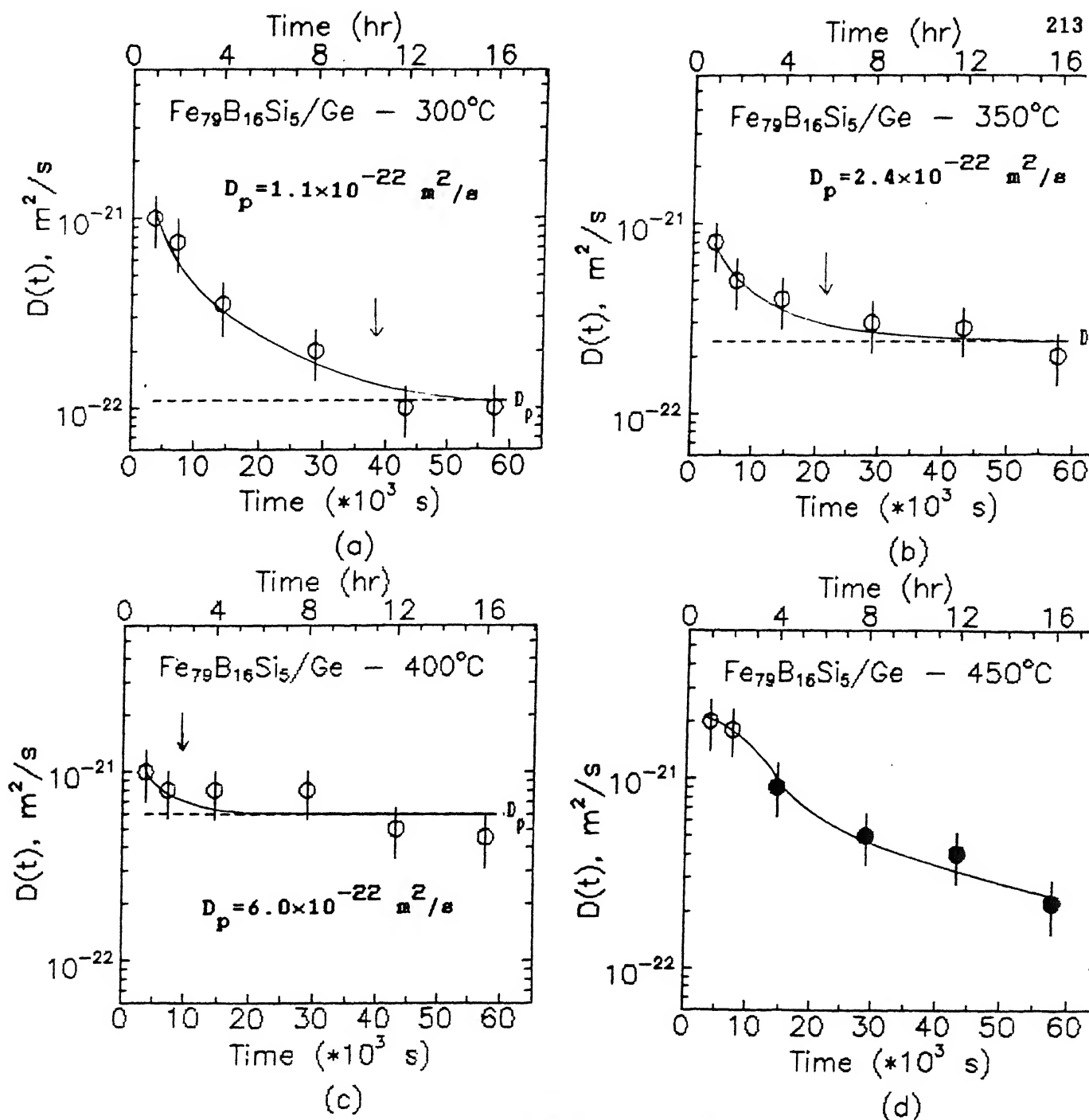


FIGURE 5.48(i), ((a)-(d)) Diagrams showing variation of the diffusion coefficient  $D(t)$  as a function of annealing time  $t$ , for diffusion of Ge in  $\text{Fe}_{79}\text{B}_{16}\text{Si}_5$ . The vertical bars on the data points indicate error in the diffusion coefficient. The solid circles indicate that crystallization of the metallic glass is observed by us using X-ray and Mössbauer techniques for these data points. The solid line, drawn as a best visual fit to the data points, asymptotically approaches a plateau value ( $D_p$ ) shown by the dashed line (except for  $450^\circ\text{C}$ ). The arrows indicate the annealing time ( $\tau$ ) at which the  $D(t)$  value approaches to within 20% of the plateau value.

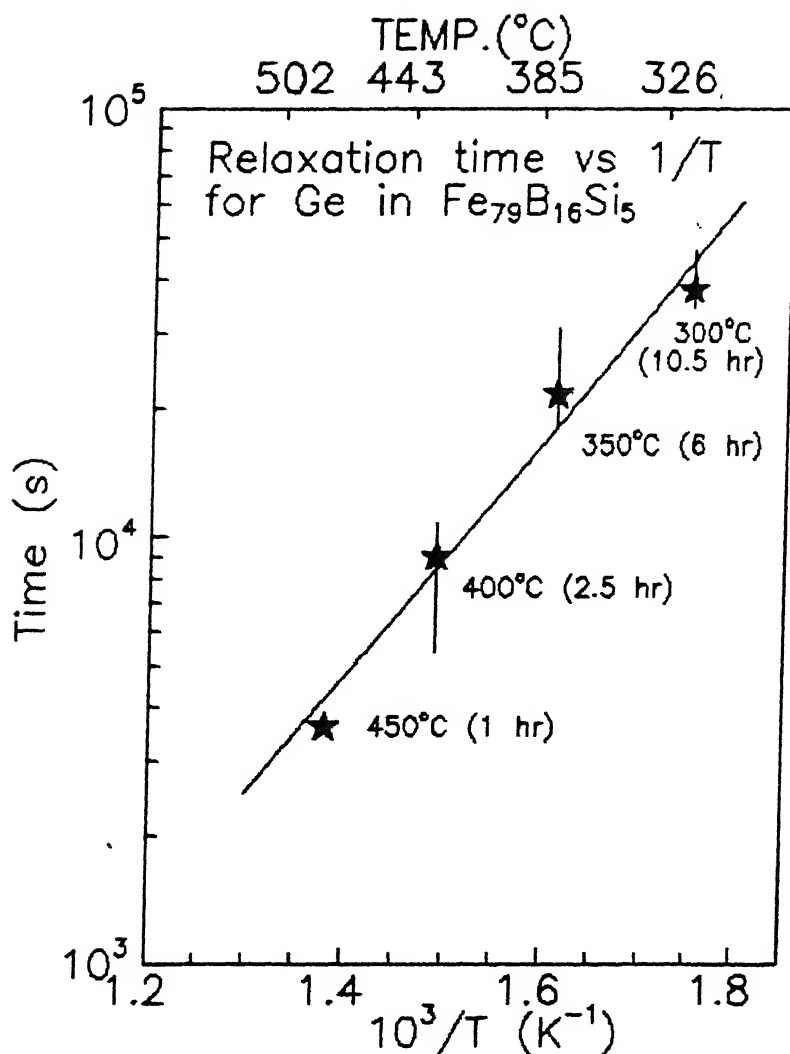


FIGURE 5.48(ii) Diagram showing the variation of the relaxation time  $\tau$  with respect to the inverse of the annealing temperature for the diffusion of Ge in the metallic glass  $\text{Fe}_{79}\text{B}_{16}\text{Si}_5$ . The value of  $\tau$  for 300°C, 350°C and 400°C is obtained from the  $D(t)$  vs. annealing time diagrams shown in Figs. 5.48(i). The value of  $\tau$  is that annealing duration for which the  $D(t)$  value approaches to within 20% of the plateau value  $D_p$  in each case. The lower end of the vertical bars on the data points indicate the annealing duration at which the  $D(t)$  approaches to within 30% of the  $D_p$  value and the upper end indicates the annealing duration at which the  $D(t)$  approaches to within 10% of  $D_p$ . For 450°C the value of  $\tau$  is taken as 1 hr (lowest annealing duration). The least square fitting to the data points gives an activation energy equal to 0.55 eV and a pre-exponential factor of value 0.64 s.

The excess quasi-vacancies can either diffuse towards the surface of the specimen or agglomerate and annihilate inside the specimen. On this basis one can infer that diffusion in the early stages of heat treatment is dominated by an elimination of "quasi-vacancy".

Greer [1984] and Adda *et al.* [1987] have compared the relaxation effect derived from viscosity vs annealing time ( $t$ ) and diffusion vs  $t$  measurements, in the same metallic glass system. The comparison indicates that as a function of time the viscosity increases while the diffusivity decreases. Thus the variation of the reciprocal of the viscosity as a function of annealing time may be related with the diffusion process. Adda *et al.* [1987] have reported that while the diffusion coefficient becomes constant after 100 hr. the viscosity measurements show gradual change even after 300 hr. In the present case, we have utilized the viscosity versus annealing time measurements at 475°C and 375°C, by Bhatti and Cantor [1988], for the metallic glass  $\text{Fe}_{78}\text{B}_{13}\text{Si}_9$ , and are plotted in Figure 5.49(a). This plot may be compared with the diffusion data for the same metallic glass at similar temperatures as plotted in Figure 5.49(b). The  $D(t)$  values at 400°C attain a plateau value after approximately 8 hr and those at 475°C show a trend of attaining a constant value above 16 hr. On the other hand the viscosity measurements indicate a rapid increasing trend at 375°C (above 12 hr) as well as 475°C (above 2 hr).

## 5.12 TEMPERATURE DEPENDENCE OF DIFFUSIVITY

The temperature dependence of the diffusion coefficients of the diffusing species Au, Ge and Pd in the two Fe-B-Si and in the Fe-Ni-B-Mo metallic glasses are summarized in Table 5.19, below. The value of  $D_0$  has been expressed in two different forms for convenience. The Arrhenius type of diffusion behaviour observed for the metallic glasses indicate that the diffusion is limited by a single activation barrier over the temperature range investigated. The

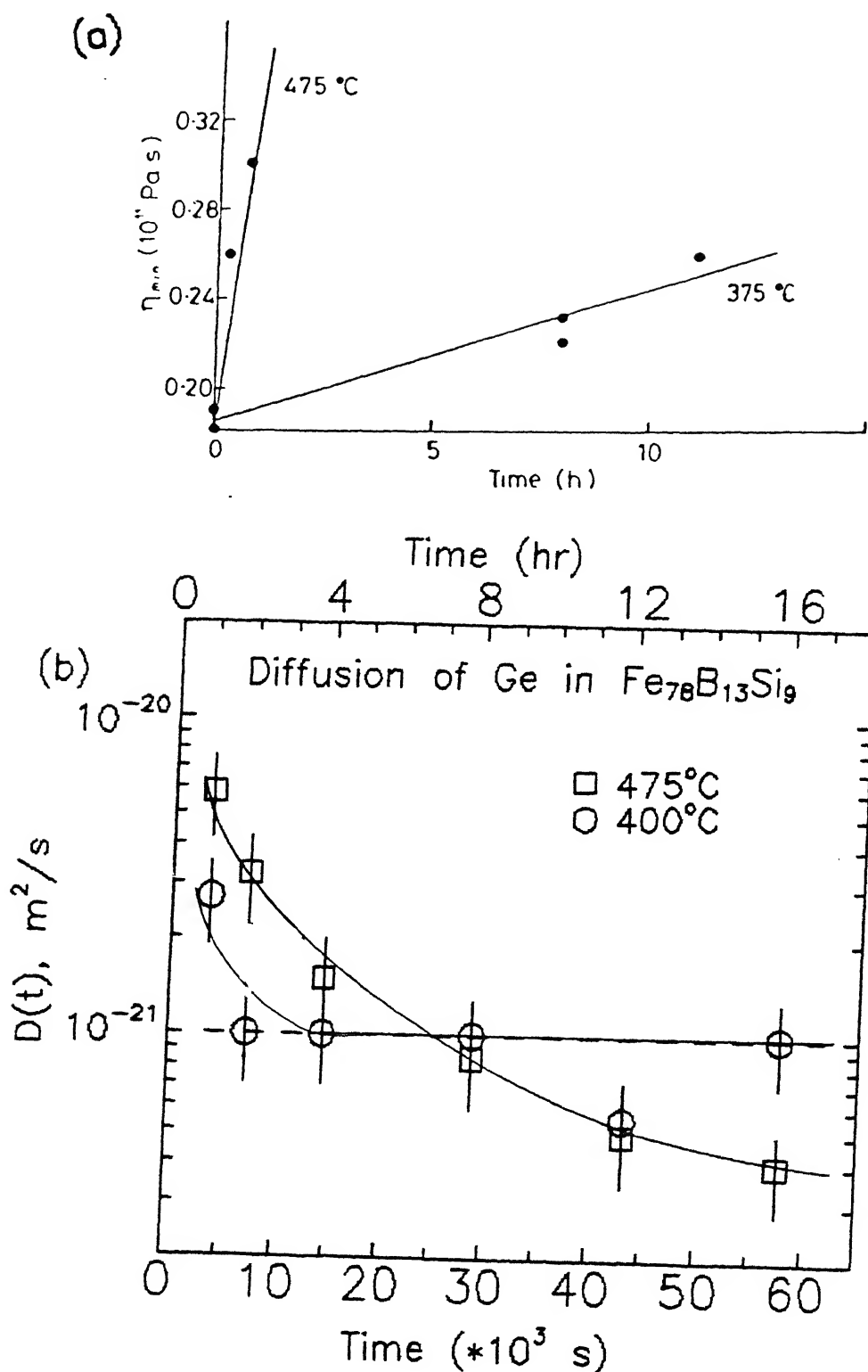


FIGURE 5.49 Comparison of variation in viscosity ( $\eta$ ) and diffusivity ( $D$ ) with respect to the annealing duration.  
 (a) Viscosity plot of  $\text{Fe}_{78}\text{B}_{13}\text{Si}_9$  [Bhatti and Cantor 1988],  
 (b) Diffusivity plot of Ge in  $\text{Fe}_{78}\text{B}_{13}\text{Si}_9$  [present study].

**TABLE 5.19**  
**VALUES OF ACTIVATION ENERGY & PRE-EXPONENTIAL FACTOR FOR**  
**DIFFUSION OF VARIOUS SPECIES IN THE METALLIC GLASSES**

Metallic glass	Diffusing species	Q (eV)	$D_0$ (m <sup>2</sup> /s)	Temperature range
Fe <sub>79</sub> B <sub>16</sub> Si <sub>5</sub>	Pd	0.46 ± 0.08	$8.4_{-6.6}^{+30} \times 10^{-19}$ ( $10^{-18.08 \pm 0.66}$ )	300°C-400°C <sup>a</sup>
	Ge	0.56 ± 0.05	$9.1_{-5.7}^{+15} \times 10^{-18}$ ( $10^{-17.04 \pm 0.43}$ )	300°C-400°C <sup>a</sup>
	Au	0.70 ± 0.20	$6.8_{-6.6}^{+240} \times 10^{-16}$ ( $10^{-15.17 \pm 1.55}$ )	300°C-400°C <sup>b</sup>
Fe <sub>78</sub> B <sub>13</sub> Si <sub>9</sub>	Pd	0.31 ± 0.02	$6.9_{-1.9}^{+2.6} \times 10^{-20}$ ( $10^{-19.16 \pm 0.14}$ )	300°C-450°C <sup>a</sup>
	Ge	0.62 ± 0.18	$3.8_{-3.7}^{+110} \times 10^{-17}$ ( $10^{-16.42 \pm 1.48}$ )	300°C-400°C <sup>a</sup>
	Au	0.77 ± 0.20	$2.8_{-2.7}^{+99} \times 10^{-15}$ ( $10^{-14.55 \pm 1.56}$ )	300°C-400°C <sup>b</sup>
Fe <sub>40</sub> Ni <sub>38</sub> B <sub>18</sub> Mo <sub>4</sub>	Pd	1.57 ± 0.37	$5.1_{-5.1}^{+5700} \times 10^{-9}$ ( $10^{-8.29 \pm 3.04}$ )	300°C-400°C <sup>c</sup>

notes: a. Plateau values used for the Arrhenius plot.

b. D(t) values at 300°C (16 hr), 350°C (8hr), 400°C (1 hr) and 450°C (1 hr) used for fitting.

c. For 400°C, D(t) value at t=1 hr was used for Arrhenius plot.

activation energies of the diffusing species in the Fe-B-Si metallic glasses have similar values (within errors), which indicate that these species have to overcome similar energy barriers in these alloys, for the diffusion process. The diffusion coefficients obtained for Au diffusion in the Fe-B-Si metallic glass and those obtained from literature for Fe-B glasses is plotted in Figure 5.50.

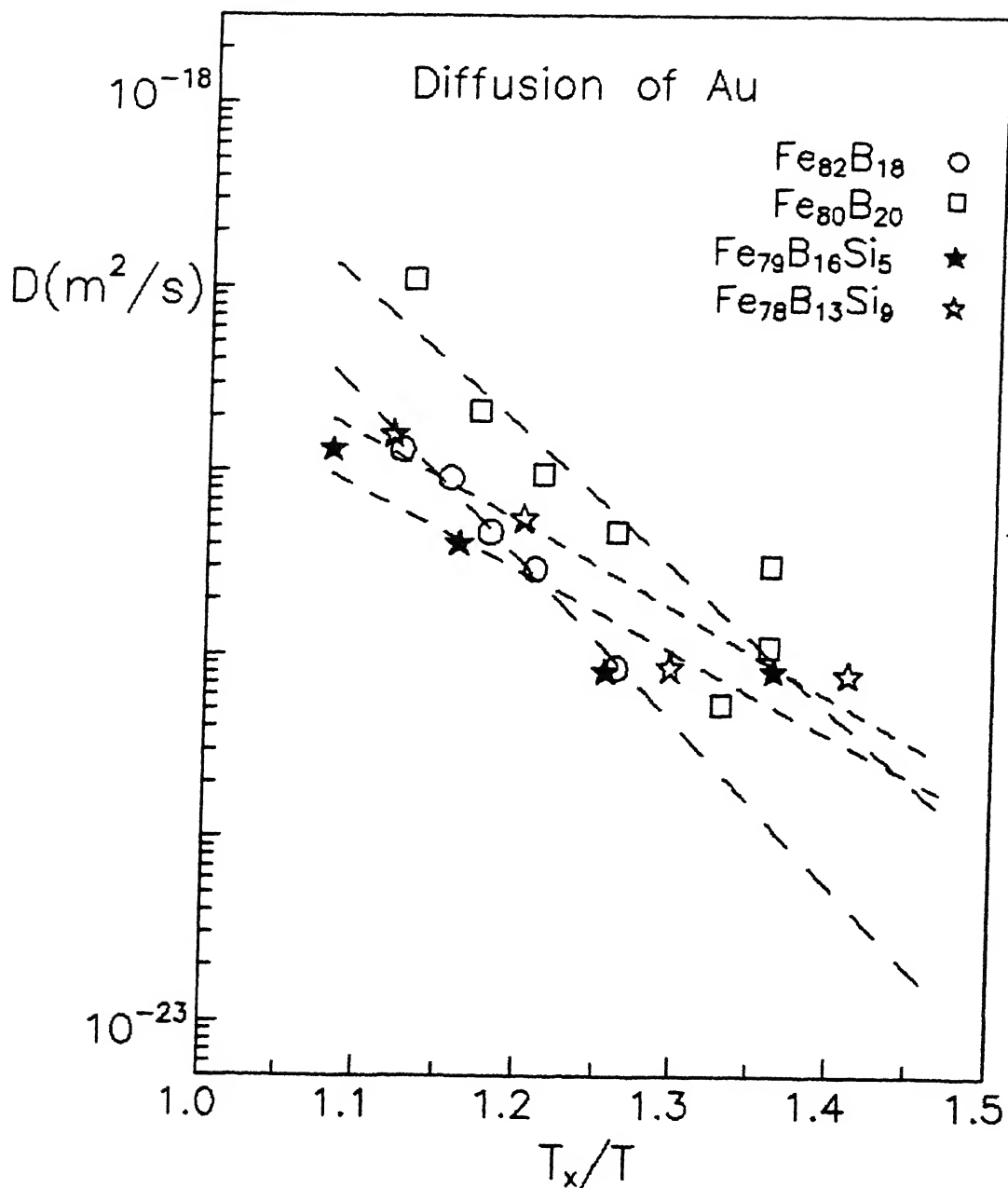


**FIGURE 5.50** Normalized  $1/T$  dependence of diffusivity of Au in Fe-B (from literature, refer Table 1.3), and Fe-B-Si amorphous alloys. ( $T_x$  is the crystallization temperature is the metallic glasses). The slope changes with the addition of Si to the Fe-B alloys.

It appears from the plot that the activation energy reduces with the addition of silicon to the Fe-B system.

As mentioned under the relevant subsections above, we have used the  $D_p$  values obtained at 300°C, 350°C and 400°C in order to infer the Arrhenius behaviour of diffusion of Pd and Ge in  $\text{Fe}_{79}\text{B}_{16}\text{Si}_5$  and  $\text{Fe}_{78}\text{B}_{13}\text{Si}_9$ . The plateau values could not be assigned for  $\text{Fe}_{79}\text{B}_{16}\text{Si}_5$  because the present X-ray diffraction and Mössbauer spectroscopy studies indicate crystallization at this temperature for the annealing time  $t > 4$  hr. For  $\text{Fe}_{78}\text{B}_{13}\text{Si}_9$  the crystallization has been observed at 450°C for  $t > 16$  hr. However the  $D(t)$  vs  $t$  diagrams for these metallic glasses for Ge showed reduction in the  $D(t)$  values at 450°C compared to the plateau values at 400°C. If we consider this decrease in the diffusion coefficients at 450°C as a result of the process of crystallization, then we can infer that the crystallization of  $\text{Fe}_{79}\text{B}_{16}\text{Si}_5$  and  $\text{Fe}_{78}\text{B}_{13}\text{Si}_9$  in the presence of Ge is taking place at 450°C at annealing durations much lower than that obtained from X-ray diffraction and Mössbauer studies. Thus the presence of Ge is probably enhancing the process of crystallization in  $\text{Fe}_{79}\text{B}_{16}\text{Si}_5$  and  $\text{Fe}_{78}\text{B}_{13}\text{Si}_9$ . Similar observations of  $D(t)$  vs  $t$  diagrams for the Pd diffusion (Figures 5.20 and 5.26) indicate that the crystallization process of these metallic glasses is inhibited by the presence of Pd. We suspect that the kinetics of crystallization is affected by the presence of the impurities, which in turn affects the diffusion process, and hence the diffusion coefficient. This probably is the reason due to which we cannot obtain Arrhenius behaviour in case of diffusion of Au in  $\text{Fe}_{79}\text{B}_{16}\text{Si}_5$  and  $\text{Fe}_{78}\text{B}_{13}\text{Si}_9$  using the plateau values of diffusion coefficients. However, at present, we cannot furnish a direct experimental evidence which can show the effect of impurity on the crystallization process in metallic glass because the X-ray and Mössbauer spectroscopy techniques presently utilized to study the kinetics of crystallization measures the bulk of the sample, while the impurity-affected

crystallization will be limited to the first few hundred to thousand angstrom of the surface. In order to observe this effect, surface sensitive techniques like transmission electron microscopy (TEM), conversion electron Mössbauer spectroscopy (CEMS) or glancing angle X-ray diffraction should be used. We plan to undertake the CEMS studies of the metallic glass - metal diffusion couples in future to confirm the effect of impurity on the kinetics of crystallization on these metallic glasses.

### 5.13 DIFFUSION DURING EARLY STAGES OF RELAXATION (COMPARISON WITH RADIATION-ENHANCED DIFFUSION)

The Arrhenius behaviour of diffusion for the various species has been shown in section 5.12, where the D-values representing the relaxed amorphous structure (when the D-values levels off as a function of time) were used. In Figure 5.51 (a) and Figures 5.51 (c) to (h) the diffusion coefficients belonging to the unrelaxed amorphous structure (i.e., the diffusion coefficients belonging to the initial region of D vs time plots of Figures 5.7, 5.14, 5.20, 5.26, 5.30, 5.34 and 5.46) are plotted as dotted lines along with the Arrhenius behaviour shown by the solid line, for diffusion of Ge, Pd and Au in the Fe-B-Si metallic glasses and of Pd in the Fe-Ni-B-Mo metallic glass.

The immediately noticeable feature of these plots is that the diffusion coefficients are almost independent of temperature for the unrelaxed amorphous state, as represented by the nearly zero value for the activation energy. There is a striking similarity between these D vs  $1/T$  plots of the unrelaxed amorphous state of the alloys with that of the radiation enhanced diffusion (RED) observed in crystalline solids. The data reported by *Dearnaley [1982]* showing the RED of Si in Fe has been reproduced in Figure 5.51(b). Here the solid line indicates thermal-diffusion, while the dashed line indicates diffusion of Si in Fe occurring under ion bombardment with 300 keV  $\text{Ar}^+$  ions at various temperatures. Thus



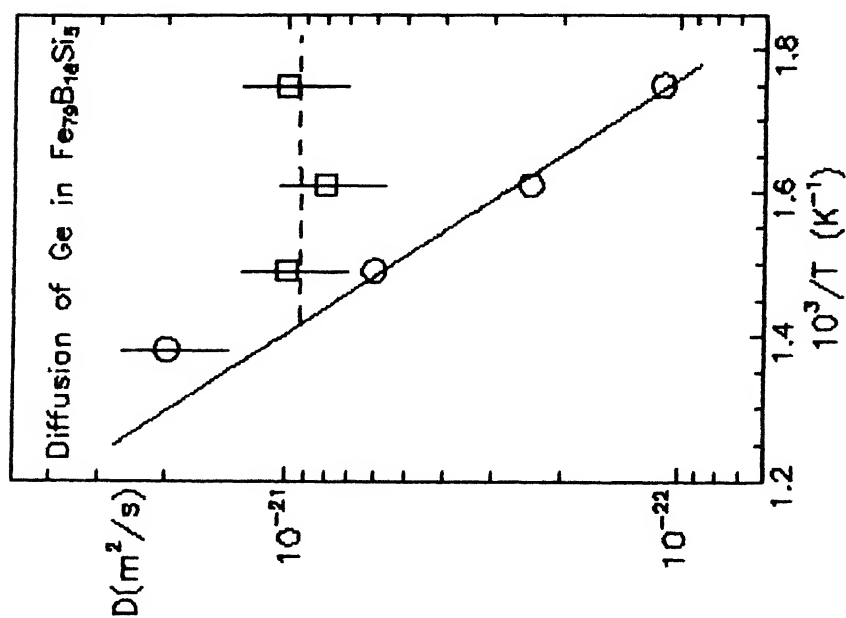


FIGURE 5.51(a) Comparison of the temperature dependence of diffusivity of Ge in  $\text{Fe}_{79}\text{B}_{16}\text{Si}_{15}$  during the early stages of relaxation (dashed line) and after relaxation (solid line). Note the similarity with the radiation enhanced diffusion shown in Figure 5.51(b) for Si in  $\alpha\text{-Fe}$ .

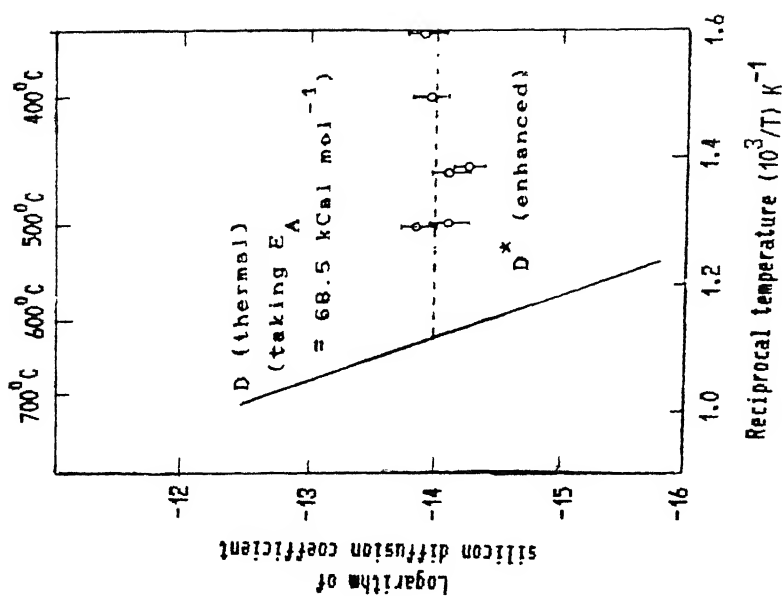


FIGURE 5.51(b) Comparison of enhanced diffusivity for Si in Fe substrate (under bombardment with 300 keV  $\text{Ar}^+$  ions) and thermal diffusivity at various temperatures (after Dearnaley 1982).

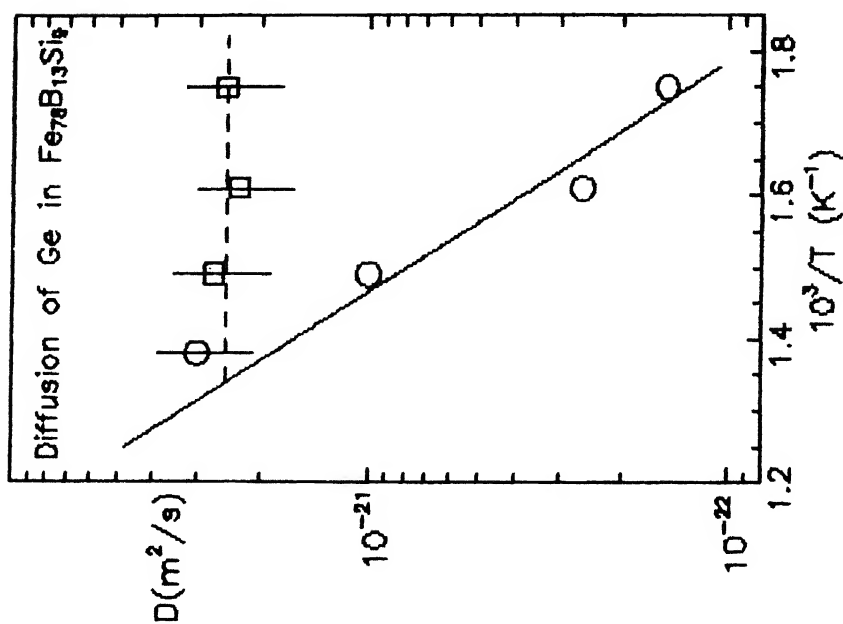


FIGURE 5.51(c) Comparison of the temperature dependence of diffusivity of Ge in Fe<sub>78</sub>B<sub>13</sub>Si<sub>9</sub> during the early stages of relaxation (dashed line) and after relaxation (bold line).

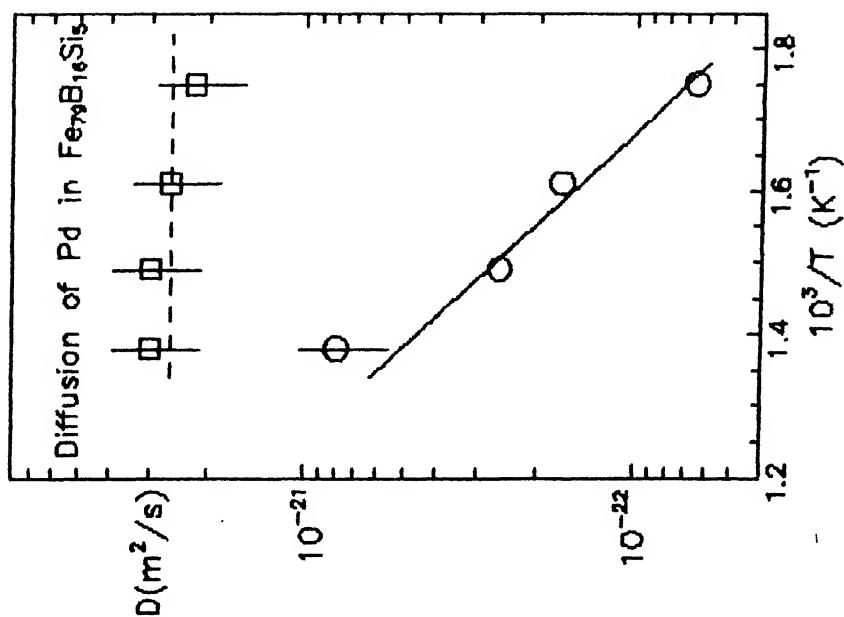


FIGURE 5.51(d) Comparison of the temperature dependence of diffusivity of Pd in Fe<sub>79</sub>B<sub>16</sub>Si<sub>5</sub> during the early stages of relaxation (dashed line) and after relaxation (bold line).

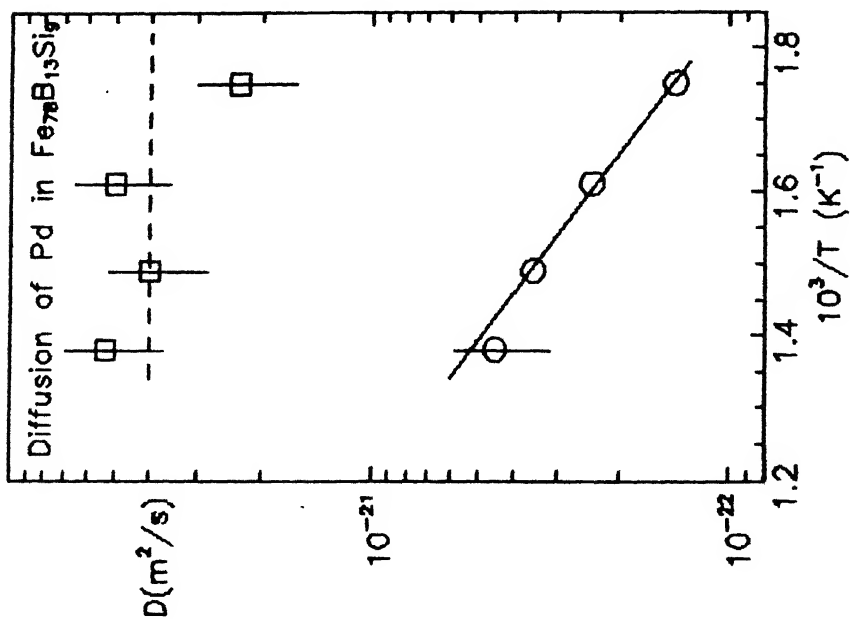


FIGURE 5.51(e) Comparison of the temperature dependence of diffusivity of Pd in  $\text{Fe}_{78}\text{B}_{13}\text{Si}_9$  during the early stages of relaxation (dashed line) and after relaxation (bold line).

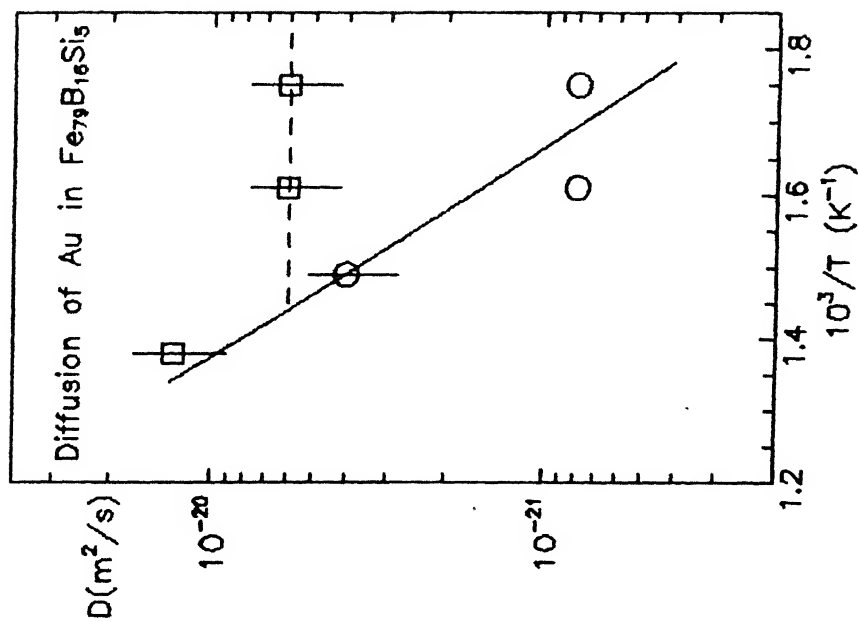


FIGURE 5.51(f) Comparison of the temperature dependence of diffusivity of Au in  $\text{Fe}_{79}\text{B}_{16}\text{Si}_5$  during the early stages of relaxation (dashed line) and after relaxation (bold line).

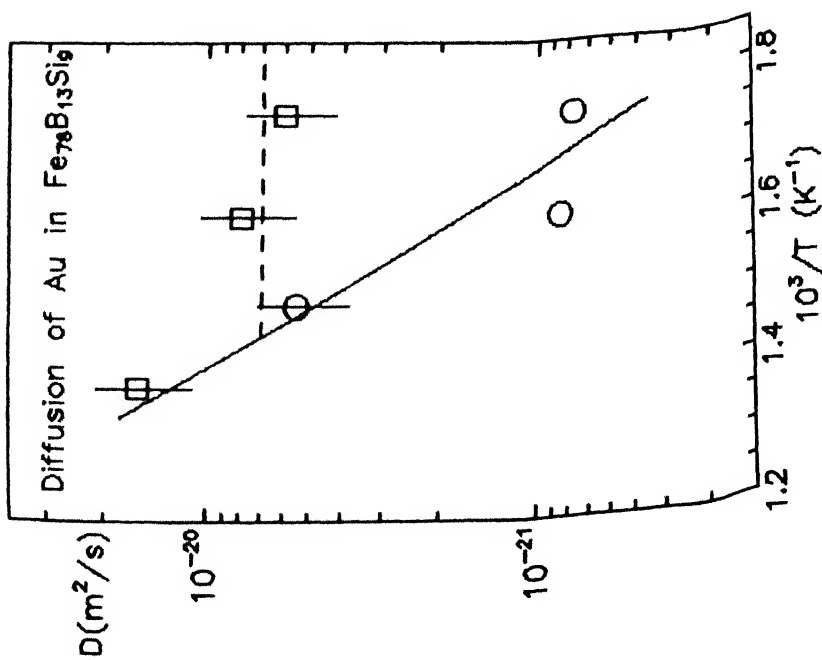


FIGURE 5.51(g) Comparison of the temperature dependence of diffusivity of Au in  $\text{Fe}_{78}\text{B}_{13}\text{Si}_9$  during the early stages of relaxation (dashed line) and after relaxation (bold line).

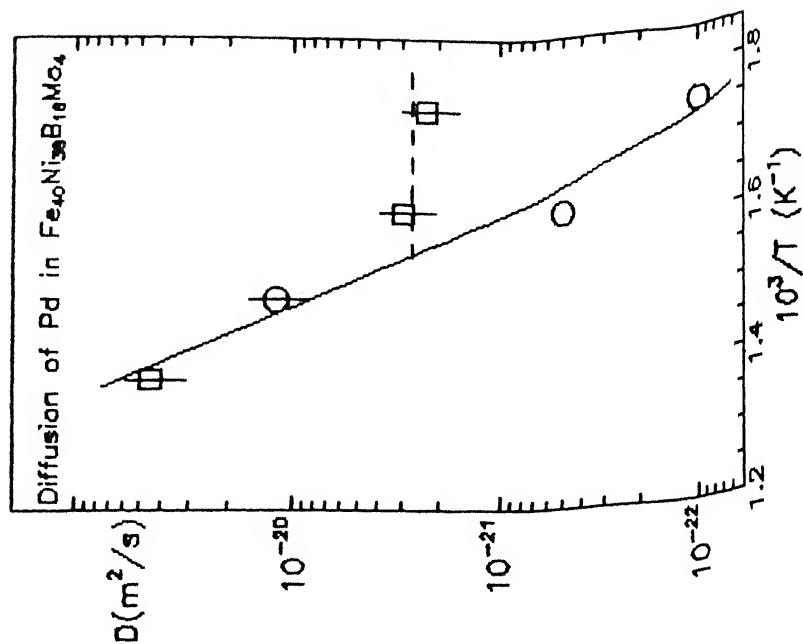


FIGURE 5.51(h) Comparison of the temperature dependence of diffusivity of Pd in  $\text{Fe}_{40}\text{Ni}_{38}\text{B}_{18}\text{Mo}_4$  during the early stages of relaxation (dashed line) and after relaxation (bold line).

under irradiation the diffusion coefficient is seen to be independent of temperature. This is the first time that such a similarity is being pointed out between RED and diffusion during relaxation in metallic glasses. When we analyzed the  $D$  vs  $1/T$  plots reported in literature for diffusion of Fe and P in amorphous  $\text{Fe}_{40}\text{Ni}_{40}\text{B}_{20}$  [Horvath et al. 1985], and that for B in  $\text{Ni}_{59.5}\text{Nb}_{40.5}$  [Kijek 1982], in the above mentioned way, the plots showed similar features with zero activation energy.

The absence of a temperature dependence of diffusion coefficient in RED has been explained by Dearnaley [1982], in the following way. During ion-irradiation there is a continuous generation of defects in the near surface region. These defects get annihilated at fixed sinks giving rise to the observed enhanced diffusion. In other words, the excess defects are responsible for the enhanced diffusion. In the case of amorphous metallic glasses there is an already existing excess free volume which gets eliminated (analogous to defect annihilation) during relaxation giving rise to the excess diffusivity. This comparison indicates a possible similarity in the diffusion mechanism occurring during irradiation of a crystalline material with the diffusion mechanism in the amorphous alloys during initial stages of relaxation.

#### 5.14 Correlations

It has been demonstrated that various properties of the metallic glasses and the diffusing species can be correlated with that of the diffusion parameters such as  $D$ ,  $Q$  and  $D_0$ . The search of correlations in the diffusion data in different metallic glasses is done broadly in the following ways:

- (i) scaling of the diffusion data of the various species to the metallic glass transition temperature  $T_g$  or the crystallization onset temperature  $T_x$  ;
- (ii) studying the dependence of diffusion coefficient  $D$  and activation energy  $Q$  on the radii of the diffusing species;

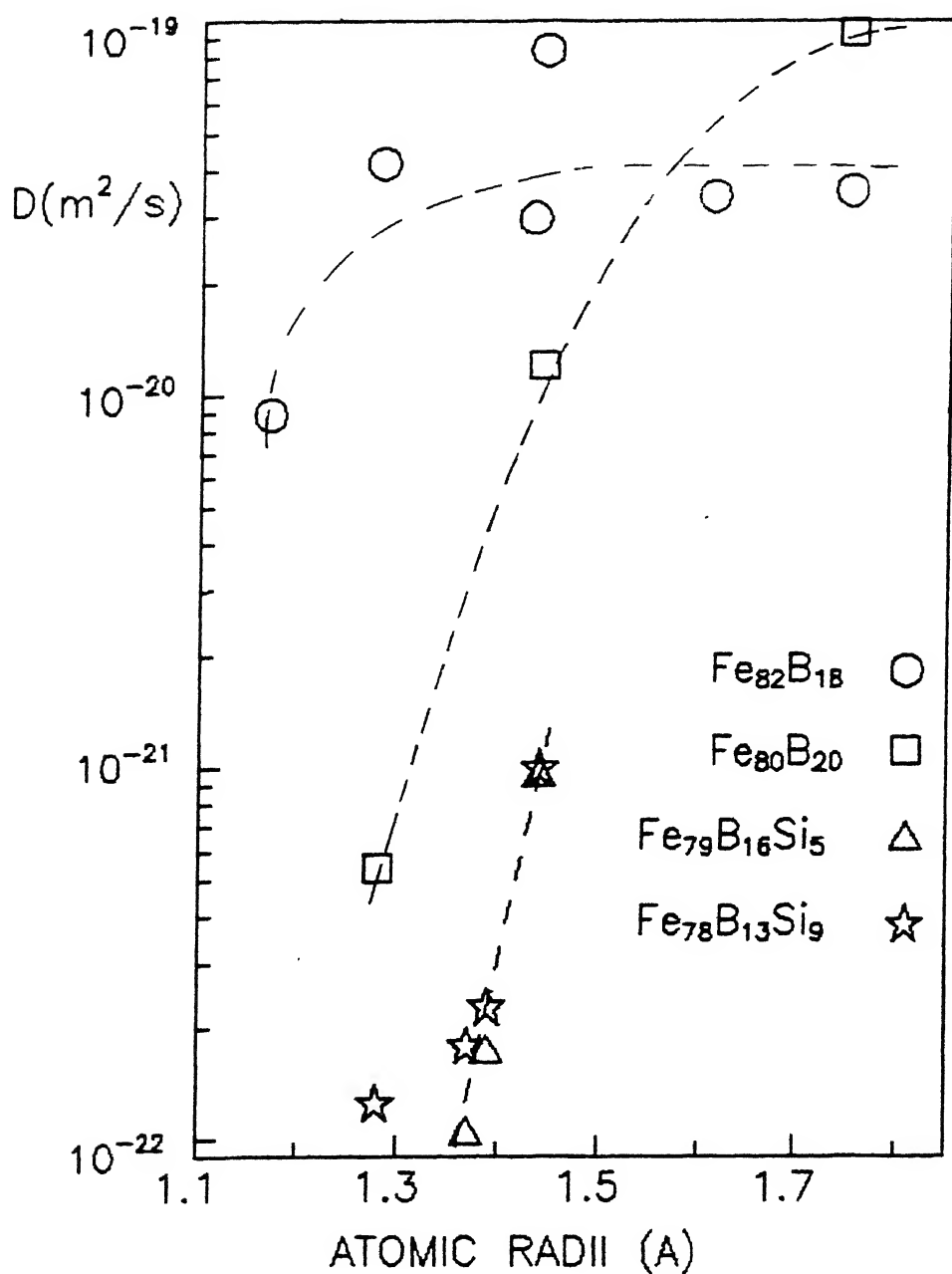


FIGURE 5.52 Correlation between diffusivity (at 600 K, calculated from the Arrhenius plot), and atomic radii of the diffusing species in Fe-B and Fe-B-Si metallic glasses. The lines have been drawn to guide the eye. Note that the radius dependence of diffusivity is similar to the one observed in crystalline Fe and Cu (as shown in Figure 5.53(a) and (b)).

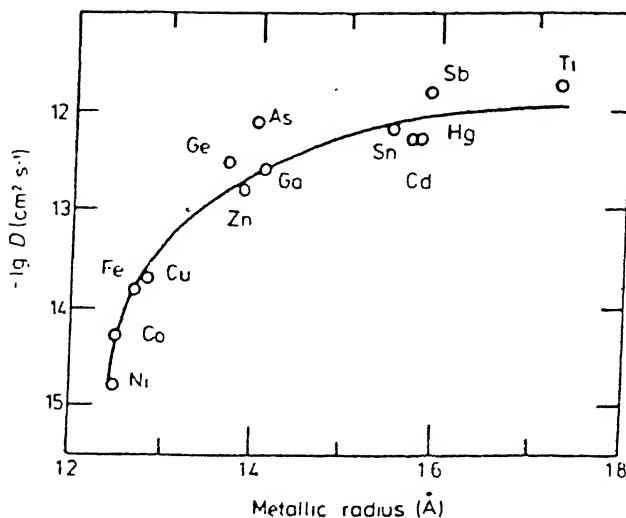


FIGURE 5.53(a) Variation of diffusivity with the atomic radii of the diffusing species in crystalline Cu [after Hood, 1978].

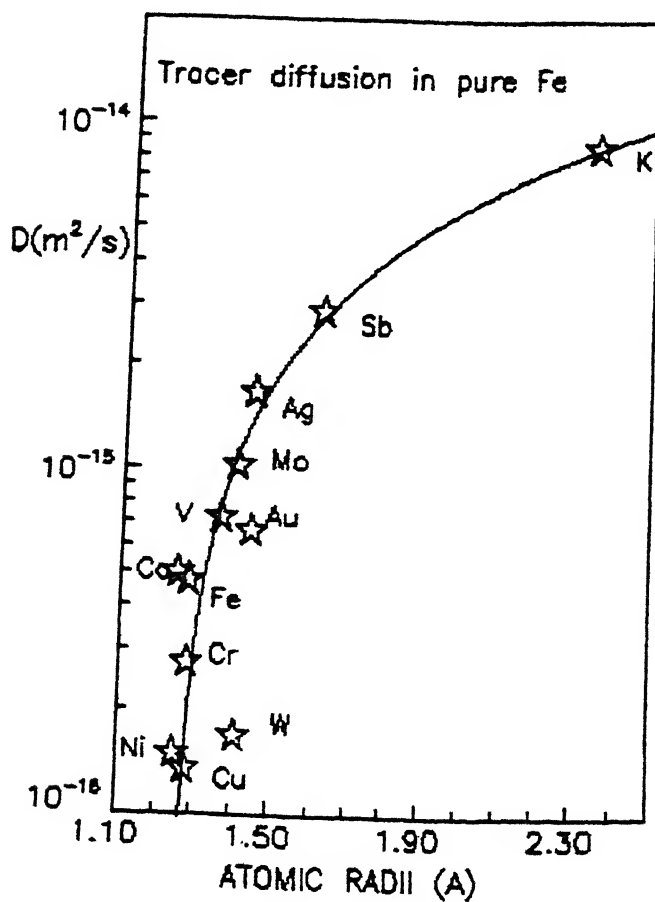


FIGURE 5.53(b) Variation of diffusivity with the atomic radii of the diffusing species in crystalline  $\alpha$ -Fe [after Askill 1979].

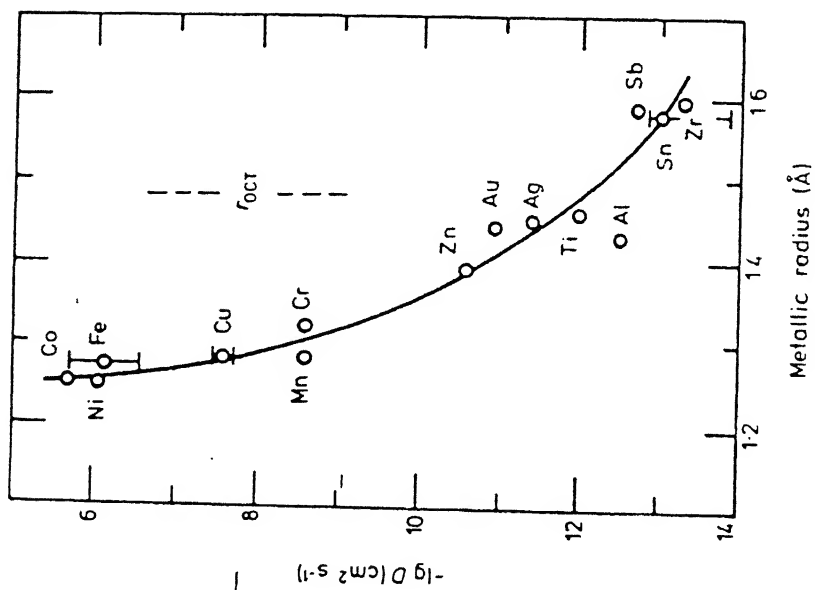


FIGURE 5.53(c) Variation of diffusivity with the atomic radii of the diffusing species in crystalline  $\alpha$ -Zr [after Hood, 1978].

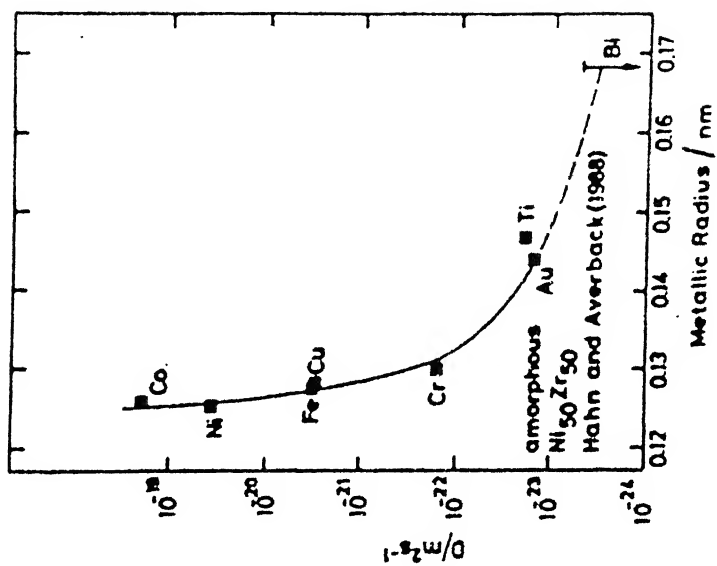


FIGURE 5.53(d) Variation of diffusivity with the atomic radii of the diffusing species in amorphous Ni-Zr alloy [Hahn and Averback 1988].



the diffusion coefficient on the radius of the diffusing species shows distinctly different trends in two cases. For diffusion in Cu there is an increase in the D-values as a function of increasing  $r$ , while for  $\alpha$ -Zr a reverse trend is observed.

The two different types of D vs  $r$  dependence in crystalline Cu and Zr metals has been categorized by Hood [1978] on the basis of the ratio of the metallic radius to the ionic radius of the host crystalline material. For Cu this ratio is close to unity and Hood has termed it as "full" metal while for Zr this ratio is large and thus is called as "open" metal. The diffusion of various species in Cu is attributed to a vacancy type diffusion only. On the other hand the diffusion in crystalline  $\alpha$ -Zr is attributed to both vacancy and interstitial type of mechanism.

The dependence between atomic size and tracer diffusivity has been reported by Hahn and Averbach [1988] for the amorphous alloy Ni-Zr and is reproduced in Figure 5.53(d). Interestingly there is a remarkable similarity in the D vs  $r$  dependence of Ni-Zr metallic glass (Figure 5.54(d)) and that of crystalline  $\alpha$ -Zr (Figure 5.53(c)). This similarity in the diffusion behaviour leads to the hypothesis that the diffusion mechanism in the two systems are alike and accordingly the local atomic structure may also be similar. Hence the diffusion in a-Ni-Zr is of interstitial type for low  $r$  diffusing species while it becomes vacancy type in diffusing species having larger radii (Bi, Ti, Zr, etc.,).

Coming back to the case of Fe-B and Fe-B-Si metallic glasses shown in Figure 5.52, we find that there is a similarity of the D vs  $r$  dependence of diffusion with metallic Fe (Figure 5.53(b)) and metallic Cu (Figure 5.53(a)). Although the data points are few, the increase in the D-values as a function of  $r$  leading to a saturation level is clearly seen for the Fe-B alloys (for which the data is taken from the literature). The D vs  $r$  dependence for amorphous Fe-B-Si alloys used in the present study also clearly shows the initial rapid

increase in D-values as a function of increase in r, for low r values. However the saturation of D-values for large r has yet to be established. This can be done by choosing diffusing species such as Sb, Ti, Sn, etc... We have not chosen these materials for the present study because these tend to form globules on the surface after heat treatment thus obscuring the diffusion profile. Such work will be undertaken in future by using Fe-B-Si metallic glasses implanted with the above mentioned species for diffusion experiments.

The similarity of D vs r dependence in the case of diffusion in Fe-B and Fe-B-Si amorphous alloys with crystalline  $\alpha$ -Fe (and Cu) suggests that the diffusion mechanism and the localized atomic structure might be similar in these materials.

#### 5.14.2 Correlation of Q with atomic species and radii

The activation energy Q for each of the diffusing species in the Fe-B-Si metallic glasses have been plotted in Figure 5.54, against the atomic radii of the diffusing species. Similar data for the Fe-B metallic glasses reported in the literature have also been plotted in the same figure. Apparently no relation between the activation energy and the radius of the diffusing species is observed in these cases.

#### 5.14.3 Correlation of Q with $D_0$

The activation energy Q and the pre-exponential factor  $D_0$  are often dependent on each other. This dependence is exhibited in two ways: (i) from results of diffusion of different diffusing species in the same matrix or substrate; and (ii) from results of diffusion of the same diffusing species in different matrices or substrates of different concentrations or defect structure. Figure 5.55 shows the relationship between  $\ln D_0$  and Q for the Fe-B and Fe-B-Si amorphous alloys. The open circles indicate the values for Fe-B glasses obtained

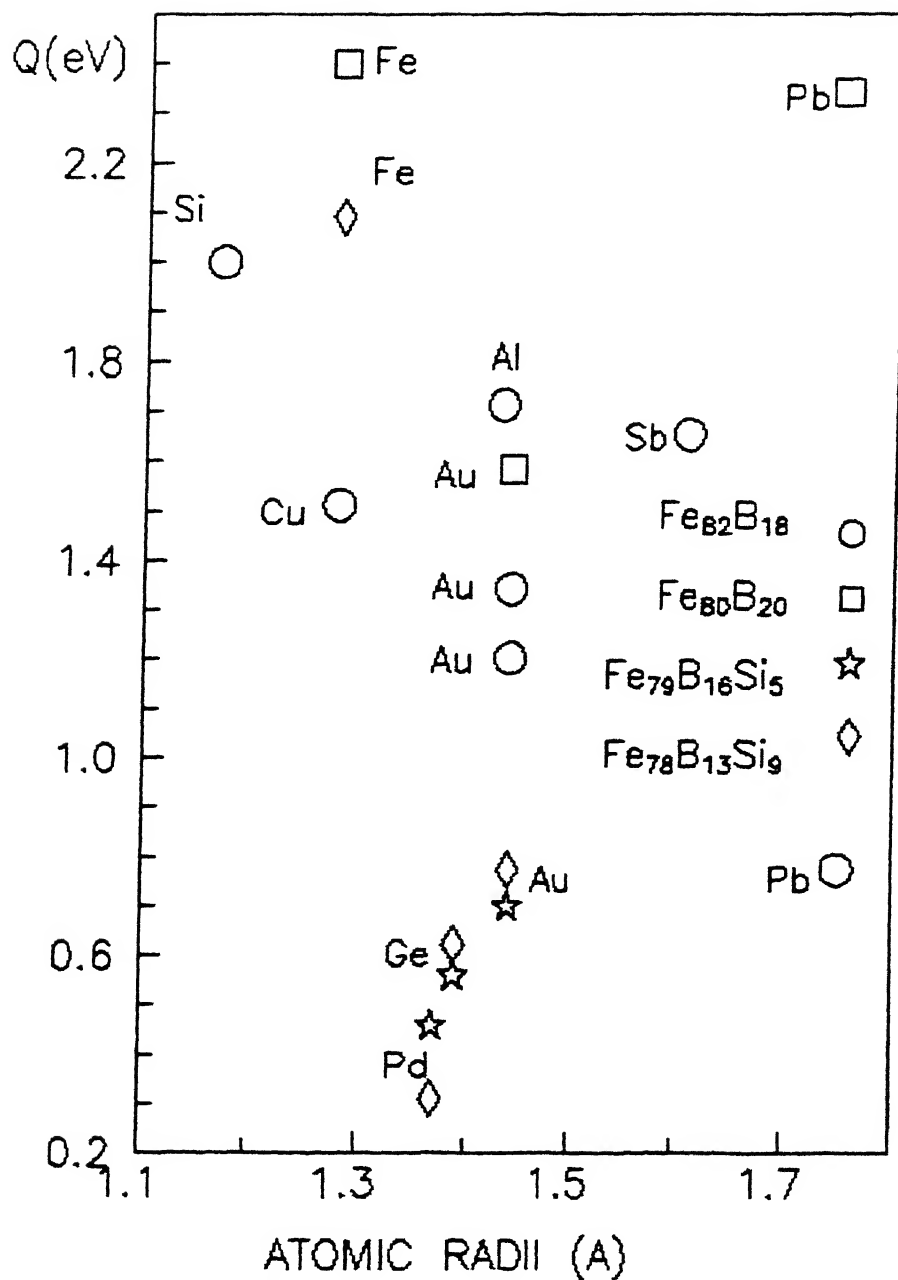
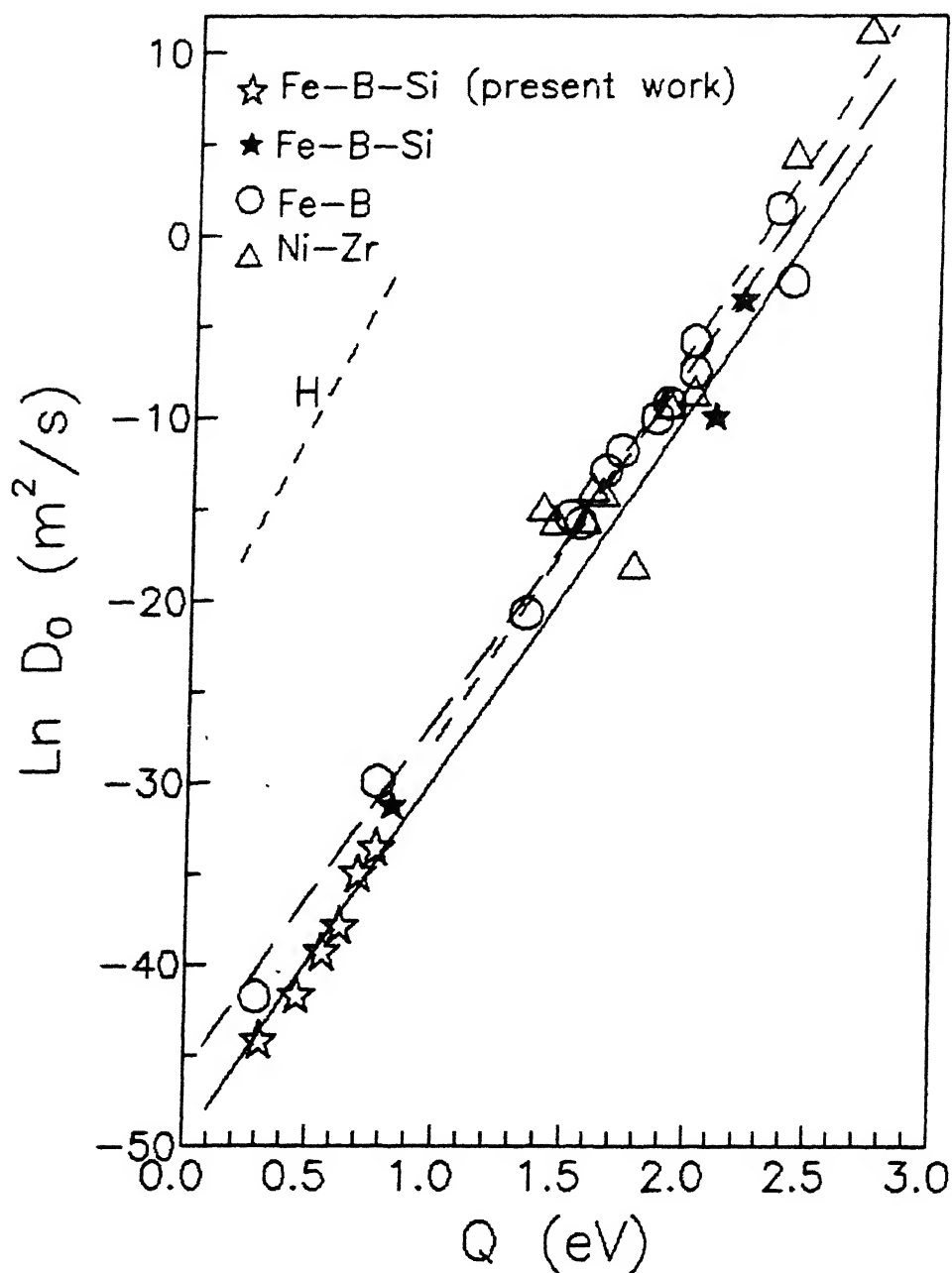


FIGURE 5.54 Correlation between activation energy ( $Q$ ) and the atomic radii ( $r$ ) of the diffusing species in Fe-B (from literature) and Fe-B-Si (present work) amorphous alloys. The plot does not show any definite trend in the variation of  $Q$  with  $r$ .



**FIGURE 5.55** Correlation between activation energy ( $Q$ ) and pre-exponential factor ( $D_0$ ) for diffusion of various elements in Fe-B and Fe-B-Si metallic glasses. The lines are least square fitting to the data points. The solid line depicts the trend in Fe-B-Si alloys, the larger dashed line represents the Fe-B alloys, the smaller dashed line represents the Ni-Zr alloy and the dashed line at the extreme left depicts hydrogen diffusion in metallic glasses.

from literature [Sharma et al. 1988a, 1988b, 1988c; Reill et al. 1985; Misse et al. 1985; Horvath et al. 1988; Edelin et al. 1981; and Luborsky 1983] and have been mentioned earlier in Table 1.3. The open squares represents the data obtained in the present work as well as those obtained from literature for diffusion of Si [Luborsky et al. 1982],  $^{59}\text{Fe}$  [Horvath et al. 1988], and N [Bokshteyn et al. 1981] in Fe-B-Si metallic glasses. The latter are the only data available in literature on diffusion in the Fe-B-Si system and have been mentioned earlier in Table 1.3. All these are fitted by a solid line, while the values for Fe-B glasses have been least-square fitted by a dashed line.

It is worth mentioning here that the reported diffusion data in ternary and other multi-component alloys also cluster along these straight lines as shown in Figure 5.55. However these data points have not been plotted for the sake of clarity. Similar linear behaviour between  $\ln D_0$  and  $Q$  has been observed for crystalline systems as well [Hood 1986; Kirchheim and Huang 1987]. The linear behaviour between  $\ln D_0$  and  $Q$  indicates a relationship of the type

$$D_0 = A \exp(Q/B)$$

The values of the constants A and B for the Fe-B and Fe-B-Si systems are almost similar and are found to be

for Fe-B system:	$A=1.08 \times 10^{-20} \text{ m}^2/\text{s}$	$B=0.051 \text{ eV/atom}$
Fe-B-Si system:	$A=2.05 \times 10^{-22} \text{ m}^2/\text{s}$	$B=0.049 \text{ eV/atom}$

The values of the constants A and B in these systems have been interpreted to represent a particular diffusion mechanism. Sharma et al. [1989] have compared the values obtained for various elements in Fe-B amorphous metallic alloys. They have reported that the data represents two distinct groups. The hydrogen data falls on a straight line giving values of A and B as  $8.9 \times 10^{-11} \text{ m}^2/\text{s}$  and 0.038 eV/atom respectively. This is shown as a dotted line in Figure 5.55. While all the other species fall on the other straight line giving values of  $8.5 \times 10^{-20} \text{ m}^2/\text{s}$  and 0.054 eV/atom for A and B respectively. The comparison of

these with those in crystalline system shows that the values for hydrogen diffusion in amorphous alloys are closer to those for interstitial type of diffusion in crystalline metals. Thus on this basis *Sharma et al.* [1989] have argued that the diffusion of hydrogen is categorized by interstitial mechanism while all other species which can be termed as larger atoms and which include B, Si, Li, Cu, Au, Sn, etc., are governed by a single diffusion mechanism.

Our data plotted in Figure 5.55 is in agreement with the generally observed linear dependence of  $\ln D_0$  vs  $Q$ . However in our opinion this linear relationship cannot give any clue to the underlying diffusion mechanism. In support of this argument we have plotted the  $\ln D_0$  vs  $Q$  values reported for a-Ni-Zr alloys. The points are shown in Figure 5.55. It is clearly seen that the least-square fitting follows a similar line as obtained for Fe-B and Fe-B-Si alloys yielding similar values for A and B. i.e., for the amorphous Ni-Zr system:

$$A = 3.64 \times 10^{-22} \text{ m}^2/\text{s} \qquad B = 0.0461 \text{ eV/atom}$$

Actually all the data points of Fe-B, Fe-B-Si and Ni-Zr systems can be fitted by a single line giving similar values for A and B as compared to the systems considered separately, i.e.,

$$A = 3.46 \times 10^{-22} \text{ m}^2/\text{s} \qquad B = 0.0471 \text{ eV/atom}$$

We have seen in the section 5.14.1 that the  $D$  versus  $r$  dependence for a-Ni-Zr alloys is entirely different as compared with that observed for a-Fe-B and a-Fe-B-Si alloys; representing clearly the different diffusion mechanisms. Thus only from the linear relationship between  $\ln D_0$  and  $Q$  it is not possible to infer the mechanism of diffusion. The linear dependence between  $\ln D_0$  and  $Q$  is actually a manifestation of the Arrhenius type of behaviour of the diffusion coefficients. This point has been clearly brought out by *Kircheim and Huang* [1987] with illustrations for crystalline materials.

### 5.15 Diffusion Defect and Mechanisms

In the foregoing sections we have inferred, from the experimental data obtained in the present investigations and the data published in the literature, the empirical relationship with which the mass transport is governed in metallic glasses. Actually in case of the problems of mass transport a researcher generally wishes to find out the details of the mechanisms of mass transport or diffusion on an atomic level. In this last section we will present a discussion on the mechanisms of atomic diffusion in amorphous alloys.

Diffusion in a substrate takes place because of the atoms and defects in it. This movement or jumps of defects and/or atoms are due to thermal vibrations of very high frequencies. This means that once in several thermal fluctuations, a vibration appears sufficiently large for an atom to overcome the energy barrier separating it from the next stable position. This energy barrier which must be overcome to reach another stable position is called the activation energy ( $Q$ ) of diffusion. In a crystalline lattice the individual diffusion jumps are equivalent in nature. In general the diffusion coefficient for a crystalline lattice is given as

$$D = \alpha a^2 w N_d \gamma \quad (5.2)$$

where,  $\alpha$  is a geometrical factor;  $a$  is the diffusion jump distance;  $w$  is the jump frequency;  $N_d$  is the mole fraction of defects in the substrate; and  $\gamma$  is the correlation factor and is equal to one in most cases. Expanding  $w$  and  $N_d$  in their respective exponential form and inserting in Equation 5.2 gives,

$$D = \alpha a^2 \gamma \eta \exp\left(\frac{(\Delta S_f + \Delta S_m)}{k}\right) \times \exp\left(\frac{(-\Delta H_f - \Delta H_m)}{kT}\right) \quad (5.3)$$

where  $\Delta S_f$  and  $\Delta H_f$  are the entropy and enthalpy of formation of defects;  $\Delta S_m$  and  $\Delta H_m$  are the entropy and enthalpy of motion of diffusing species; and  $\eta$  is the vibration frequency of a diffusing atom. Comparing Equation 5.3 with the Arrhenius law of Equation 5.1, i.e.,  $D = D_0 \exp(-Q/kT)$ , we get;

$$D_0 = \alpha a^2 \gamma \eta \exp\left(\frac{(\Delta S_m + \Delta S_f)}{k}\right) \quad (5.4)$$

$$\text{and} \quad Q = (\Delta H_m + \Delta H_f) \quad (5.5)$$

For an amorphous alloy (unlike a crystalline lattice), the values of  $\alpha$ ,  $a$ ,  $\gamma$ ,  $\Delta S$  and  $\Delta H$  vary between each energy barrier and the localized atomic structure is also differing in nature. This indicates that over an average of the whole structure, the activation energy would be quite high, which is not observed practically. Therefore it implies that with the given geometrical factors, the diffusion mechanism is quite specific for the individual diffusion jumps.

In almost all the studies of diffusion in amorphous alloys, reported in the literature and in the present work, the diffusion coefficients have been found to obey an Arrhenius law similar to that in crystalline solids. As a consequence of this similarity, it is natural to extend the approach a bit further and utilize the existing information about diffusion mechanisms in crystalline solids in order to understand the diffusion mechanism in amorphous alloys.

#### 5.15.1 Defects

In crystalline solids diffusion occurs via defect mechanisms namely vacancy and interstitial. In crystal lattice, a vacancy defect is defined as an unoccupied lattice site while an interstitial defect is one where the atom takes up regular positions upon certain energetically favoured interstices. Whereas in an amorphous structure a vacancy can be defined only as a space of atomic dimension. In the dense random packing (DRP) model of the amorphous structure, a number of polyhedral holes (or cavities) are contained, and these holes can be supposed to be a kind of interstitial site (or in a sense, a kind of vacancy) like in crystalline materials. For amorphous structures, computer modeling studies (molecular dynamics) [Bennett 1978] have indicated that when a vacancy is created artificially by removing one atom in a DRP computer model, the excess of space thus created is quickly redistributed over a large volume by atomic vibrations. This indicates that the vacancies are unstable in amorphous alloys.



Also, the stability of the artificial vacancy thus created depends upon which atom is removed. On the other hand, computer modeling studies by *Finney and Wallace [1981]*, indicate definite presence of interstitial sites surrounded by distorted tetrahedral and octahedral groups of atoms. The size of a tetrahedral interstitial comes out to be about 0.3 times the atomic diameter while an octahedral interstitial size is about 0.7 times the atomic diameter. These sizes are comparable to the regular tetrahedral and octahedral interstitial sizes in close packed crystals. *Cantor and Ramachandrarao [1981]*, have suggested that small atomic movements can change this local interstitial structure as a consequence of which grouping of the tetrahedral interstices results into a single octahedral interstice. Such grouping of local interstitial structure leads to an interstitial site which becomes comparable to atomic size. In short, according to *Cantor and Cahn [1983]* and many others, vacancy in an amorphous structure is not characterized by absence of an atom because a space created in this way is unstable, but a large interstitial position can be called as a vacancy.

*Bennet et al. [1979]* have put forth a different view point concerning vacancies in amorphous structure. According to these authors, the stability of a vacancy (created artificially in an amorphous structure by removing an atom) is very much sensitive to the type of potential used in the molecular dynamic simulations. Instead of a Lennard-Jones potential, if a Keating potential is used in the simulation of the amorphous structure, the vacancy remains stable. According to *Chaudhari [1980]*, this is related strongly to the directional covalent bond which preserves the local symmetry in the amorphous structure.

The experimental investigations of the defects in metallic glasses have been performed by various researchers using positron annihilation methods. The experimental data on a variety of metallic glasses have been reviewed by *Gopinathan and Sunder [1984]*. These experiments suggest that (i) there are quenched-in cavities having a void volume which is less than one atom in size,

(ii) there are low density dilated regions with a spatial extent of about 0.5 nm. These observations relate well with the definition of vacancy in amorphous structures as given by *Cantor and Cahn [1983]*, and with the excess free volume existing in the as-quenched state respectively.

In addition to the possibility of the existence of the point defects in amorphous alloys discussed above, the existence of spread-out defects have also been suggested. The concept of spread out defect has its origin in the relaxed vacancy model for diffusion suggested by *Nachtrieb and Handler [1954]*, and was first used by *Seeger and Chik [1968]* to explain the self diffusion in silicon and germanium near their melting points.

The spread-out vacancy can be defined in the following way. Suppose eleven atoms occupy a certain volume in a disordered alloy. When one atom is removed and the remaining ten atoms distribute themselves over the same volume, then the free space so created is called as the spread-out vacancy. The spread-out interstitials can also be explained in a similar way.

There are no direct experimental observations which can confirm the presence of spread-out defects, but their existence have been attributed to the large enthalpy of formation obtained from the pre-exponential factor  $D_0$ .

Having discussed the possible defects in the amorphous metallic alloys, we will now see how the possible diffusion mechanisms can be inferred from the experimental diffusion data.

#### 5.15.2 Mechanisms

The diffusion mechanisms discussed in the literature are analogous to the ones which are well established for crystalline materials, namely interstitial and vacancy mechanisms. The discussion of diffusion mechanism in the literature has always been qualitative in nature.

In the interstitial type of mechanism the impurity solute atoms are assumed

to migrate through the interstitial sites described in the amorphous matrix. *Ahmadzadeh and Cantor [1981]* have discussed the interstitial type of mechanism very extensively. In the diffusion of Si in amorphous Fe-B glass, *Luborsky [1983]*, has observed a similarity in the diffusion data with that of B diffusion in metallic glasses, and hence has proposed an interstitial type of mechanism similar to that for B diffusion. *Hahn and Averbach [1988]*, have observed a similarity of their diffusion data of small atoms (Ni and Co) in amorphous Ni-Zr alloy with that of diffusion in  $\alpha$ -Zr, and have proposed that diffusion of small atoms in a-Ni-Zr alloys takes place via an interstitial type of mechanism.

*Hahn and Averbach*, have further proposed that impurity atoms with large radii like Au, Ti, Zr, etc., diffuse via vacancy like mechanism using the quenched in excess free volume of the amorphous structure, the large atoms using these vacancies or excess volume as jump sites. Since this process requires only a rearrangement of the excess free volume into voids or vacancies by a coordinated motion of many atoms, the enthalpy of formation of a vacancy and hence the activation energy of the amorphous metallic glasses are much less than in the crystalline materials. *Baer et al. [1981]*, have also observed that the diffusion parameters for the diffusion of P in the metallic glasses Fe-Ni-P-B and Fe-Ni-P-B-Cr, are similar to that for P diffusion in crystalline  $\alpha$ -Fe, in which the diffusion is controlled by vacancy formation and motion. They suggest that if quenched-in defects, similar to vacancies in crystals, are present in the amorphous alloys (as proposed in the literature) then the  $Q$ -values would be in the range 0.5 to 1 eV. Hence they suggest that quenched in defects probably do not control phosphorus diffusion in the amorphous alloys. *Bohac et al. [1989a]* have obtained diffusion parameters of Ti in amorphous Ni-Si-B alloys, which are very close to those known for crystalline nickel, where the vacancy mechanism is assumed to operate. Hence they propose that the atomic diffusion in these Ni-Si-B alloys is via the quasi-vacancies present in it. *Horvath et al.*

[1985,1988], and Frank et al [1988], have determined the diffusion parameters of P, Fe and Zr in various Fe and Zr based alloys. They propose that diffusion in these alloys takes place via mobile spread-out quasi-vacancies present in them.

The variation of D-values with radii of the diffusing elements observed in the present work for the Fe-B-Si glasses, has been found to be similar to that of diffusion in crystalline  $\alpha$ -Fe and Cu. Nachtrieb and Handler [1954] have proposed, that the mechanism of diffusion in solid metals occurs by movements within small regions of disorder, comprising of 12 to 14 atoms, in the crystal. This proposal has been later used by Seeger and Chik [1968], to define the diffusion mechanism in Si and Ge. The similarity of the diffusion parameters in metals and metallic glasses suggests similar diffusion mechanism in them.

Quantitative footing to the diffusion mechanism in metallic glasses has been given by Bokshiteyn et al. [1980] and recently by Frank et al. [1988]. In the following discussion we will consider the approach as mentioned by these authors. The diffusion in metallic glasses can be categorized as direct and indirect diffusion.

[a]Direct diffusion: In the direct mechanism, the atomic transport of the diffusing elements occurs by random walk without any cooperation of mobile 'defects', i.e., vacancies, which serves as diffusion vehicles. The diffusion can occur by random jumps of the diffusing elements in the interstitial positions, or by direct exchange of the diffusing atoms with the atoms of the host amorphous alloy. And the diffusivity is then expressed as:

$$D = D_0 \exp(-H_m/kT) \quad (5.6)$$

where

$$D_0 = \frac{1}{2} \eta_T \langle X_T^2 \rangle \nu_T \exp(S_m/k) \quad (5.7)$$

where  $H_m$  and  $S_m$  are the enthalpy and entropy of migration of the diffusing element,  $\eta_T$  is the number of possible paths for the jumps,  $\langle X_T^2 \rangle$  is the mean square of the jump distance and  $\nu$  is the jump attempt frequency.

[b]Indirect diffusion: In the indirect process the diffusion is aided by

mobile defects such as vacancies. If the concentration of these defects  $C_v$  are temperature independent the diffusivity is then given by:

$$D^v = D_0^v \exp(-H_m^v/kT) \quad (5.8)$$

$$\text{where} \quad D_0^v = \frac{1}{2} f_v \eta_v \langle X_v^2 \rangle \nu_v C_v \exp(S_m^v/k) \quad (5.9)$$

and  $H_m^v$  and  $S_m^v$  are the enthalpy and entropy of migration of the diffusing vehicles respectively.

The values of  $S_m$  and  $S_m^v$  can be estimated from the diffusion data, using Equations 5.6 to 5.9. Following values for the parameters [Frank et al. 1988] in Equations 5.7 and 5.9, have been used:  $\eta_T = \eta_v = 8$ ,  $\langle X_T^2 \rangle = \langle X_v^2 \rangle = 4 \exp(-20) \text{ m}^2$ ,  $\nu_T = \nu_v = 1 \exp(13) \text{ s}^{-1}$ ,  $f_v = 0.5$ , and  $C_v = 1 \exp(-2)$ . The absolute values for  $S_m$  have been calculated from the  $D_0$  values obtained for the various diffusion couples in the present study. For the diffusion of Ge, Au and Pd in Fe-B-Si alloys the absolute values of  $S_m$  lie in the range 20k to 30k (refer Table 5.20) while for Pd in the Fe-Ni-B-Mo alloy the value of  $S_m$  turns out to be 5.75k. The high absolute value of  $S_m$  is indicative of the fact that diffusion is occurring by a cooperative or collective motion via small displacements (4-6% of atomic distance) of individual atoms forming a group of 10-14 atoms [Seeger and Chik 1968, Bokshiteyn et al. 1980]. On the other hand, the low value of the entropy of motion is indicative of direct diffusion mechanism, which is assisted by local contraction of immobile spread-out quasi-vacancies, leading to the jumping of the diffusing atoms in to the so-produced vacant spaces. For the self-diffusion of Fe in amorphous Fe-B and Fe-B-Si alloys also, the direct mechanism involving cooperative motion of atoms has been suggested by Frank et al. [1988].

Based on the cooperative mechanism of atoms, Bokshiteyn et al. [1980] have presented a model for determining the relative value of the critical displacement ( $j_0/a$ ), resulting in diffusion transport in amorphous alloys, and the ratio of the mean vibration frequency in the ground and transient states ( $\frac{\nu}{\nu^*}$ ). They have shown that within the experimental margin of error,

TABLE 5.20

VALUES OF THE MIGRATION ENTROPIES OF DIFFUSING SPECIES and QUASI-VACANCIES, THE RELATIVE VALUE OF CRITICAL DISPLACEMENT, and THE MEAN VIBRATION FREQUENCY, IN THE METALLIC GLASSES STUDIED.

SYSTEM	$Q$ (eV)	$D_0$ ( $\text{m}^2/\text{s}$ )	$S_m$ $\frac{\text{m}}{\text{k}}$	$S_m^v$ $\frac{\text{m}}{\text{k}}$	$Q_0$ (eV)	$n = 4$		$n = 10$		$n = 14$	
						$j_0/a$	$\nu/\nu^*$	$j_0/a$	$\nu/\nu^*$	$j_0/a$	$\nu/\nu^*$
Au/Fe <sub>79</sub> B <sub>16</sub> Si <sub>5</sub>	0.70	$6.8 \times 10^{-16}$	-21.6	-16.3	2.71	0.0409	0.083	0.0259	0.605	0.0219	0.725
Au/Fe <sub>78</sub> B <sub>13</sub> Si <sub>9</sub>	0.77	$2.8 \times 10^{-15}$	-20.2	-14.9	2.71	0.0429	0.107	0.0271	0.641	0.0229	0.754
Ge/Fe <sub>79</sub> B <sub>16</sub> Si <sub>5</sub>	0.56	$9.1 \times 10^{-18}$	-25.9	-20.6	2.89	0.0355	0.069	0.0224	0.508	0.0189	0.647
Ge/Fe <sub>78</sub> B <sub>13</sub> Si <sub>9</sub>	0.62	$3.8 \times 10^{-17}$	-24.5	-19.2	2.89	0.0373	0.048	0.0236	0.538	0.0199	0.672
Pd/Fe <sub>79</sub> B <sub>16</sub> Si <sub>5</sub>	0.46	$8.4 \times 10^{-19}$	-28.3	-22.9	2.99	0.0316	0.024	0.0199	0.463	0.0169	0.608
Pd/Fe <sub>78</sub> B <sub>13</sub> Si <sub>9</sub>	0.31	$6.9 \times 10^{-20}$	-30.8	-25.5	2.99	0.0259	0.016	0.0164	0.422	0.0139	0.573
Pd/Fe <sub>40</sub> Ni <sub>38</sub> B <sub>18</sub> Mo <sub>4</sub>											
	1.57	$5.1 \times 10^{-9}$	-5.75	-0.45	2.99	0.0584	1.699	0.0369	1.168	0.0312	1.118

i) For the calculations of the entropies ( $S_m$  and  $S_m^v$ ), the values of various parameters used are given in the text and were taken from Frank et al. [1988].

ii) The  $Q$  and  $D_0$  values have been obtained for the temperature range 623-748 K.

iii) The value of  $Q_0$  (Sb) has been used instead of  $Q_0$  (Ge) and that of  $Q_0$  (Ag) instead of  $Q_0$  (Pd), since  $Q_0$  for Ge and Pd in  $\alpha$ -Fe are not available in literature. [CRC Handbook of Chemistry and Physics, 1979]

iv) lattice parameter for  $\alpha$ -Fe has been taken as  $a=2.866 \text{ \AA}$ . [CRC Handbook 1979]

v)  $\nu$  for all glasses has been taken as  $\nu_D = 7.70 \times 10^{12}$  of Fe<sub>79</sub>B<sub>11</sub>Si<sub>10</sub>. [Bokshteynet al. 1980]

$$D_0 = \frac{1}{6} \nu j_0^2 \left(\frac{\nu}{\nu^*}\right)^{3n-7} \quad (5.10)$$

$$Q = 38.5 Q_0 n (j_0/a)^2 \quad (5.11)$$

where  $Q$  and  $Q_0$  are the activation energies of the diffusing group of atoms of the amorphous alloy and the crystal respectively,  $j_0$  is the critical displacement,  $a$  is the lattice parameter of the crystal, and  $n$  is the number of atoms in the group. If  $Q$ ,  $Q_0$ ,  $D_0$  and  $a$  are known experimentally,  $(\frac{\nu}{\nu^*})$  and  $(j_0/a)$  can be calculated from Equations 5.10 and 5.11 respectively. *Bokshteyn et al.* [1980] have shown that these values are dependant on  $n$ . Similar results have been obtained by us too for  $n$  equal to 4, 10 and 14, as mentioned in Table 5.20. In these calculations,  $\nu$  was taken as equal to the Debye frequency  $\nu_D$  for  $\text{Fe}_{79}\text{B}_{11}\text{Si}_{10}$  [*Bokshteyn et al.* 1980], as  $\nu_D$  for the metallic glasses studied in the present thesis is not available in literature. The activation energies  $Q_0$  in crystals for the various diffusing elements were also not available in literature and hence taken for that of similar diffusing elements in crystalline  $\alpha$ -Fe [Askil 1979], viz., the value of  $Q_0$  for Sb in  $\alpha$ -Fe has been utilized in place of Ge, and for Pd the value of  $Q_0$  for Ag in  $\alpha$ -Fe has been used. The lattice parameter for  $\alpha$ -Fe has been taken as 2.866 Å [*Robie et al.* 1979]. As depicted in Table 5.20, the critical displacement for the Fe-B-Si alloys varies in value from approximately 2.6% to 4.3% of an atomic distance at  $n$  equal to 4; 1.6% to 2.7% at  $n$  equal to 10; and 1.4% to 2.3% at  $n$  equal to 14 (as against 16% for vacancy diffusion in crystals [*Flynn* 1968]). For a given  $n$ , the values of  $j_0/a$  depend on the activation energies only. Our estimates of the relative values of the critical jump distances are in good agreement with that obtained by *Bokshteyn et al.* [1980] for diffusion in Fe-B-Si and Pd-Cu-Si glasses and that obtained by *Sharma* [1986] for diffusion in Fe-B glasses. A general trend of increase in  $(\nu/\nu^*)$  with increase in  $n$  value is observed for the Fe-B-Si alloys whereas the reverse is observed for the Fe-Ni-B-Mo alloy. For the Fe-B-Si glasses, we consistently get  $(\nu/\nu^*)$  values less than 1, which would imply that

the transient state is "harder" than the ground state, as also observed by *Bokshteyn et al.* [1980], for the Fe-B-Si and Pd-Cu-Si amorphous alloys. For the Fe-Ni-B-Mo glass the value of  $(\nu/\nu^*)$  is greater than 1, implying a "softer" transient state, similar to that observed by *Sharma* [1986], for Fe-B glasses. However,  $(\nu/\nu^*)$  is dependant on  $D_0$  and hence is sensitive to errors in  $D_0$ .

In summary the diffusion measurements performed by us in the metallic glasses  $\text{Fe}_{79}\text{B}_{16}\text{Si}_5$  and  $\text{Fe}_{78}\text{B}_{13}\text{Si}_9$  indicate that the diffusion occurs via cooperative motion of a group of atoms. While for the  $\text{Fe}_{40}\text{Ni}_{38}\text{B}_{18}\text{Mo}_4$  glass, it occurs via spread-out vacancies. The present work clearly suggests that the  $D_0$  and  $Q$  values obtained by properly taking into account the relaxation effect should be used to identify the diffusion mechanism on the the basis of quantitative estimates for entropy of migration of the diffusing species, the vibration frequencies, and the mean critical displacements.

After the first measurement of diffusion in metallic glasses [*Gupta et al.* 1975], large number of studies have been carried out using variety of techniques. However in many of these measurements the variation in  $D$ -values as a function of annealing time was not considered and hence in many cases the reported  $D$ -values may not be truly representing the diffusion in the relaxed amorphous state. Apart from the present work, only *Horvath and coworkers* have done diffusion measurements in which the time dependence of diffusivity was studied to delineate the effect of relaxation. In fact in a recent review by *Mehrer and Dorner* [1989], the authors have stressed that the  $D_0$ -values and  $Q$ -values obtained without explicitly studying the effects of relaxation as a function of time are not physically meaningful for any quantitative estimates. For this reason we have not made comparison with all the data available in the literature, but limited the comparison to only those studies where relaxation effects were properly taken into account.



## CHAPTER 6

### CONCLUSIONS

In the present work we have studied the diffusion of various elements (Ge, Pd, Au, Ag) in amorphous metal-metalloid metallic glasses  $\text{Fe}_{79}\text{B}_{16}\text{Si}_5$ ,  $\text{Fe}_{78}\text{B}_{13}\text{Si}_9$  and  $\text{Fe}_{40}\text{Ni}_{38}\text{B}_{18}\text{Mo}_4$ .

*Transmission Mössbauer spectroscopy (TMS) and X-ray diffraction (XRD)* measurements were carried out on the Fe-B-Si metallic glasses. The samples were heat-treated at various temperatures from below to above glass transition temperature to identify the temperatures and annealing time-period which retains the amorphous structure of the metallic glasses.

The surface topography of the annealed films was examined after various annealing treatments using *Scanning electron microscopy (SEM)* to detect globule formation on the sample surface.

The diffusion studies were performed by annealing the diffusion couples at temperatures ranging from  $300^{\circ}\text{C}$  to  $475^{\circ}\text{C}$  for various time periods i.e., from 1 hr to 16 hr. The depth versus concentration profiles of the diffusing species in the metallic glass were obtained using *Rutherford backscattering spectrometry (RBS)*. The diffusion coefficients were obtained by comparing the experimentally observed depth profiles with those derived theoretically from the solution of the diffusion equation under appropriate boundary condition pertinent to the diffusion couple configuration.

The important conclusions of TMS and XRD studies are summarized below:

- (i) The glass transition temperature ( $T_g$ ) as reported in literature for  $\text{Fe}_{79}\text{B}_{16}\text{Si}_5$  is  $508^{\circ}\text{C}$  and for  $\text{Fe}_{78}\text{B}_{13}\text{Si}_9$  it is  $535^{\circ}\text{C}$ . As observed from X-ray

and Mössbauer studies these metallic glasses remains amorphous below  $450^{\circ}\text{C}$ . Further the TMS and XRD measurements definitely indicate precipitation of the crystalline phases in  $\text{Fe}_{79}\text{B}_{16}\text{Si}_5$  after heat-treatment for 4 hr at  $450^{\circ}\text{C}$ , while for  $\text{Fe}_{78}\text{B}_{13}\text{Si}_9$  the precipitation commences after heat-treatment for 1 hr at  $475^{\circ}\text{C}$ . These results indicate that the thermal stability increases as B is replaced by Si in the Fe-B-Si metallic glasses. The various phases precipitated above these temperatures and time period of annealing for the two metallic glasses are  $\text{t-Fe}_3\text{B}$ ,  $\text{t-Fe}_2\text{B}$ ,  $\alpha\text{-Fe}$  and  $\alpha\text{-(Fe-Si)}$ . However the amount of  $\text{Fe}_3\text{B}$  phase precipitated in  $\text{Fe}_{78}\text{B}_{13}\text{Si}_9$  was observed to be less than that in  $\text{Fe}_{79}\text{B}_{16}\text{Si}_5$ .

(ii) The X-ray diffraction studies of these metallic glasses after heat-treatment at  $600^{\circ}\text{C}$  for 2 hr and  $700^{\circ}\text{C}$  for 15 minutes, indicate that a complete conversion of  $\text{Fe}_3\text{B}$  to  $\text{Fe}_2\text{B}$  has not yet taken place at these temperatures, though these are much above the reported crystallization temperatures.

(iii) Metalloid dependence of the magnetic anisotropy (decrease in the angle  $(\theta)$  between the sample plane and the direction of magnetization with Si concentration) has been observed in the Fe-B-Si alloys. For the as-received sample of amorphous  $\text{Fe}_{79}\text{B}_{16}\text{Si}_5$  the value of  $\theta$  is  $90^{\circ}$ , whereas in the case of  $\text{Fe}_{78}\text{B}_{13}\text{Si}_9$  it is  $68^{\circ}$ . As the time-period of heat treatment, or the temperature is increased the magnetization direction rotates out of the plane for both the glasses. The results indicate that annealing does relieve internal stresses in the sample which are invariably present in the rapidly quenched alloys. Since the direction of magnetization is stress sensitive, this relief in the internal stress gets reflected in the directional change of the magnetization axis. The effects of annealing is usually interpreted in terms of a reduction of the number of vacancies and an increase in the topological order approaching a relaxed, ideal glass.

The conclusions inferred from the diffusion measurements, before and after relaxation of the metallic glasses (mentioned above) are summarized below

[a] before relaxation:

- (i) During the initial stages of relaxation (i.e., for annealing time-period  $\leq 1$  hr), the  $D$  vs  $1/T$  plots show zero activation energy similar to the one reported for radiation-enhanced type diffusion in crystalline solids. This similarity has been noticed and pointed out for the first time.
- (ii) All the three metallic glasses show a time-dependent diffusivity, which decrease continuously with annealing time-period to a plateau value. The diffusion studies of Ge in  $\text{Fe}_{79}\text{B}_{16}\text{Si}_5$  metallic glass indicate that the completion of the relaxation process is characterized by different  $\tau$  (duration of heat treatment) at various annealing temperatures  $T$ . Thus we observe in this case  $\tau = 1$  hr at  $T = 450^\circ\text{C}$ ,  $\tau = 2.5$  hr at  $400^\circ\text{C}$ ,  $\tau = 6$  hr at  $350^\circ\text{C}$ , and  $\tau = 10.5$  hr at  $300^\circ\text{C}$ .

[b] after relaxation:

- (i) The plot of  $D_p$  (plateau value of the diffusion coefficient) versus  $1/T$  shows Arrhenius behaviour for the diffusion of Pd and Ge in the Fe-B-Si metallic glasses and for Pd in the Fe-Ni-B-Mo metallic glass in the temperature range  $300^\circ\text{C}$ - $400^\circ\text{C}$ . On the other hand the diffusion of Au in the Fe-B-Si system shows Arrhenius behaviour only if the  $D(t)$  values obtained for lower annealing durations at higher temperatures and vice-versa are utilized. It is suspected that the kinetics of crystallization is affected by the presence of the diffusing species, which in turn, affects the diffusion process and hence the diffusion coefficient. However in this work a direct experimental evidence in support of such an effect could not be given.

The activation energies for diffusion of Pd, Ge and Au in  $\text{Fe}_{79}\text{B}_{16}\text{Si}_5$

are 0.46, 0.56, and 0.70 (eV) respectively; and the pre-exponential factors for the same are  $8.40 \times 10^{-19}$ ,  $9.10 \times 10^{-18}$ , and  $6.80 \times 10^{-16}$  ( $\text{m}^2/\text{s}$ ) respectively. The activation energies for diffusion of Pd, Ge and Au in  $\text{Fe}_{78}\text{B}_{13}\text{Si}_9$  are 0.31, 0.62, and 0.77 (eV) respectively; and the pre-exponential factors for the same are  $6.90 \times 10^{-20}$ ,  $3.80 \times 10^{-17}$ , and  $2.80 \times 10^{-15}$  ( $\text{m}^2/\text{s}$ ) respectively. The activation energy and the pre-exponential factor for diffusion of Pd in  $\text{Fe}_{40}\text{Ni}_{38}\text{B}_{18}\text{Mo}_4$  are 1.57 eV and  $5.10 \times 10^{-9}$   $\text{m}^2/\text{s}$  respectively.

- (ii) The D-values for the Fe-B-Si metallic glasses increases with the atomic radii (r) of the diffusing elements. This r versus D dependence is similar to the one observed for crystalline  $\alpha$ -Fe.
- (iii) Large absolute values of entropy of migration  $S_m$  ( $>20k$ ), are observed in the Fe-B-Si metallic glasses, which indicate that diffusion occurs in these alloys by a cooperative motion involving a group of atoms, which is a direct diffusion mechanism.
- (iv) For the metallic glass  $\text{Fe}_{40}\text{Ni}_{38}\text{B}_{18}\text{Mo}_4$ ,  $S_m$  is 5.7k, which indicates a direct diffusion mechanism involving quasi-vacancies.
- (v) A cooperative type of mechanism via small displacements (i.e., 4-6% of atomic distance) of individual atoms forming a group of 10-14 atoms, has also been inferred for the two Fe-B-Si metallic glasses, from the relative value of the critical jump distance ( $j_0/d$ ), resulting in diffusion transport, and the ratio of the mean vibration frequency in the ground and transient states ( $\nu/\nu^*$ ).
- (vi) In the diffusion measurements of amorphous alloys, it is essential to study the time-dependence of D, to delineate the effect of relaxation. The  $D_0$  and Q values obtained by properly taking into account the relaxation effect should be used to identify the diffusion mechanism on the basis of a theoretical formalism.

## REFERENCES

- Adda Y., Brebec G., Gupta R.P. and Limoge Y., in DIMETA 82 - Diffusion in Metals and Alloys, (eds.) K.F.J. Kedves and D.L. Beke, Diffusion and Defect Monograph Ser. 7, Trans Tech. Pub., 1983, 285.
- Ahmadzadeh M. and Cantor B., J. Non-Cryst. Solids 43 (1981) 189
- Anantharaman T.R. and Suryanarayan C., *Rapid Solidification Technology*, 1988.
- Anantharaman T.R., *Metallic Glasses: Production, Properties and Applications*, TransTech Pub., Switzerland, 1984.
- Askill J., *CRC Handbook of Chemistry and Physics*, 1979-80, p F-63.
- Ast D.G., and Krenitsky D.J., J. Mat. Sci. 14 (1979) 287.
- Baer D.R., Pederson L.R. and Thomas M.T., Mat. Sci. Eng. 48 (1981) 283.
- Bahgat A.A. and Shaisha E.E., J. Non-Cryst. Solids 56 (1983) 243.
- Bang J. and Lee R.Y., J. Non-Cryst. Solids 26 (1991) 4961.
- Barrue R., Bigot J., Faugieres J.C., Perron J.C., Railland J.F., Robert J. and Schwartz F., Phys. Scripta 37 (1988) 356.
- Battezzatti L., Antonione C. and Cossolo A., Z. Metallkd., 73 (1982) 185.
- Bauer-Grosse E., Le Caer G., and Fournes L., in *Book of Abstracts*, International conference on the applications of the Mössbauer effect, September 1985, p 1.13.
- Bennett C. H., J. Appl. Phys., 43 (1978) 2727.
- Bernal J.D., Nature 185 (1960) 68.
- Bernal J.D., Proc. Royal Soc. A 280 (1964) 299.
- Berry B.S., *Elastic and anelastic behaviour, Metallic Glasses*, American Society for Metals, Metals Park, OH, 1978, p 161.
- Berry B.S. and Pritchett W.C., Scripta Met. 15 (1981a) 637.
- Berry B.S. and Pritchett W.C., Phys. Rev. B 24 (1981b) 2299.
- Bevington P.R., *Data Reduction and Error Analysis for the Physical Sciences*, McGraw-Hill Book Co., New York.
- Bhanu Prasad B., Bhatnagar A.K. and Jagannathan R., J. Appl. Phys. 54 (1983) 2019.

Bhatnagar A.K. and Jagannathan R., *Metallic Glasses: Production, Properties and Applications*, (ed.) T.R. Anantharaman, TransTech Pub., Switzerland, (1985) p.1.

Bhatnagar A.K. and Ravi N., Phys.Rev. B 28 (1983) 359.

Bhatnagar A.K. and Ravi N., J. Non-Cryst. Solids, 56 (1983) 237.

Bhatnagar A.K., Ganesan D., Bhanu Prasad B., Parashar R.S. and Jagannathan R., *Rapidly Quenched Metals V*, (eds) S. Steeb and H. Warlimont, Elsevier Sci. Pub., B.V., (1985), p.295.

Birac C. and Lesuer D., Phys. Stat. Sol., A 36 (1976) 247.

Bohr N., Phil. Mag. 30 (1915) 581.

Bohac V., Luby S., Majkova F. and Vesely M., Defect and Diffusion Forum 66-69 (1989a) 561.

Bohac V., Majkova F., Luby S., Sandrik R. and Vesely M., Defect and Diffusion Forum 66-69 (1989b) 567.

Bohac V., Key. Eng. Mater. 40 (1990) 445.

Bokshtyn B.S., Klinger L.M., Razumovskiy I.M. and Uvarova Y.M., Phys. Met. Metall. 51 (1980) 93.

Bokstein B.S., Karpov I.V., Klinger L.M. and Nikolskij G.S., Defect and Diffusion Forum, 66-69 (1989) 545.

Bokstein B.S., et al. Phys. Met. Metall. 6 (1990) 159.

Borg R.J. and Dienes G.J., 'An Introduction to Solid state Diffusion', Acad. Press Inc. (London), 1988.

Bottiger J., Dyrbye K., Pampus K. and Torp B., Inter J. of Rapid Solidification, 2 (1986) 191.

Boudreax D.S. and Gregor J.M., J. Appl. Phys. 48 (1977a) 152.

Boudreax D.S. and Gregor J.M., J. Appl. Phys. 48 (1977b) 5057.

Braggs W.H. and Kleeman R., Phi. Mag. 10 (1905) 5318.

Brown D.K., Nowik I. and Paul D.I., Sol. State Comm., 24 (1977) 711.

Brüning R., Altouman Z. and Ström-Olsen J.O., J. Appl. Phys., (1978) 3633.

Caer G.Le and Dubois J.M., Phys. Stat. Sol., A 64 (1981) 275.

Cahn R.W., Evetts J.E., Patterson J., Somekh R.E. and Jackson C.K., J. Mat. Sci. 15 (1980) 702.

Cahn R.W., Pratten N.A., Scott M.G., Sinning H.R. and Leonardsson L., Mat. Res. Soc. Symp. Proc., 28 (1984) 241.

- Cantor B., *Amorphous Metals and Semiconductors*, (eds.) P. Hassen and R.I. Jaffee, Pergamon (1986) p.108.
- Cantor B., *Rapidly Quenched Metals IV*, (eds.) T. Masumoto and K. Suzuki, 1 (1982) p.595.
- Cantor B., *Rapidly Quenched Metals V*, (eds.) S. Steeb and H. Warlimont (1985) p.595.
- Cantor B. and Cahn R.W., *Amorphous Metallic Alloys*, (ed.) F.E. Luborsky, Butterworth & Co. Ltd., 1983, Ch.25.
- Cantor B. and Ramachandrarao P., *Rapidly Quenched Metals IV*, (eds.) T. Masumoto and K. Suzuki, 1 (1982) p.291.
- Chason E., Greer A.L., Kelton K.F., Pershan P.S., Sorenson L.B., Spaepen F. and Weiss A.H., Phys. Rev. B 32 (1985) 3399.
- Chaudhari P., J. Phys., C8 (1980) 267.
- Chen H.S. and Jackson K.A., *Metallic Glasses*, (eds.) J.J. Gilman and H.J. Leamy, American Society of Metals, Metals Park, Ohio, (1978), p.77.
- Chen H.S., Kimerling L.C., Poate J.M. and Brown W.L., Appl. Phys. Lett., 32 (1978) 461.
- Chen H.S., J. Non-Cryst. Solids, 46 (1981) 289.
- Chien C.L. and Hasegawa R., J.Phys C6 (1976) 759.
- Chien C.L. and Hasegawa R., *Amorphous Magnetism II*, (eds) R.A. Levy and R. Hasegawa, Plenum Press, (1977), p289.
- Chien C.L., Phys. Rev., B18 (1978) 1.
- Chien C.L. and Hasegawa R., Phys.Rev. B16 (1979) 3024.
- Chien C.L., Musser D., Gyorgy E.M., Sherwood R.C., Chen H.S., Luborsky F.E., and Walter J.L., Phys Rev B20 (1979) 283.
- Choo W.K. and Kaplow R., Metall. Trans. 8A (1977) 417.
- Chu W.K., Mayer J.W. and Nicolet M.A., *Backscattering Spectrometry*, Academic Press Inc. (London) Ltd. (1978).
- Cohen M.H. and Grest G.S., Phys. Rev. B20 (1979) 1077.
- Crank J., *The Mathematics of Diffusion*, Oxford Univ. Press (Clarendon), London, 1975.
- Cusido J.A., Isalgue A., and Tejada J., Phys. Status Solidi A87 (1985) 169.
- Darwin C.G., Phil. Mag. 28 (1914) 499.
- Davies H.A. and Lewis B.G., Scripta Met. 9 (1975) 1107.

- Davies H.A., *Phy. Chem. Glasses* 17 (1976) 159.
- Davies H.A., Aucote J. and Hull J.B., *Nature* 246 (1973) 13.
- Davies H.A. and Hull J.B., *J. Mat. Sci.* 11 (1976) 215.
- Davies H.A., *Amorphous metallic alloys*, (ed.) F.E. Luborsky, Butterworth & Co. (London) Ltd., 1983, Ch.2.
- Dearnaley G., *Radiation Effects*, 63 (1982) 25.
- Doi M., Itoh Y., Chang D.Y. and Imura T., *Phys. Stat. Solidi A* 83 (1984) 529.
- Donald I.W. and Davies H.A., *J. Non-Cryst. Solids*, 30 (1978) 77.
- Doolittle L.R., *Nucl. Instr. Meth.* B9 (1985) 334.
- Duwez P. and Lin S.C.H., *J. Appl. Phys.* 38 (1967) 4096.
- Duwez P. and Willens R., *Trans. Met. Soc. AIME*, 227 (1963) 362.
- Edelin G. and Tete C., *Scripta Met.* 15 (1981) 739.
- Egami T., *Mat. Res. Bull.* 13 (1978) 557.
- Egami T., *Proc. Internat. Workshop on Amorphous Metals and Semiconductors*, (eds.) P. Haasen and R.I. Jaffee, Pergamon, Oxford, 1986, p.222.
- Fick A., *Pogg. Ann.* 94 (1855) 59.
- Finney J.L., *Proc Royal Soc. A* 319 (1970) 679.
- Finney J.L., *Amorphous Metallic Alloys*, (ed.) F.E. Luborsky, (Butterworth & Co Ltd.) (1983), p.42.
- Finney J. L. and Wallace J., *J. Non-Cryst. Solids* 43 (1981) 165.
- Flynn C.P., *Phys. Rev.* 171 (1968) 682
- Frank W., Horvath J., and Kronmüller H., *Mat. Sci. Eng.* 97 (1988) 415.
- Gaskell P.H., *J. Non-Cryst. Solids* 32 (1979) 207.
- Gaskell P.H., *Glassy Metals II*, (1983), p.1.
- Geiger H. and Marsden E., *Phil. Mag.* 25 (1913) 606.
- Gerling R., Schimansky F. P. and Wagner R., *Rapidly Quenched Metals V*, (eds) S. Steeb & H. Warlimont, Elsevier Science Publishers (1985).
- Ghafari M., Gonser U., Wagner H.G. and Naka M., *Nucl. Instr. Methods* 199 (1982) 197.



- Glessen B.C., *Rapidly Quenched Metals IV*, (eds.) T. Masumoto, K. Suzuki, Japan Institute of Metals, Sendai (1982), p.213.
- Gonser U., Ghafari M., Ackermann M., Klein H.P., Baur J., and Wagner H.G., *Rapidly Quenched Metals IV*, (eds.) T.Masumoto, K.Suzuki, 1982, p.639.
- Goodfellow Metals and Materials Catalogue 1990/91, Goodfellow Metals Ltd., Cambridge, England.
- Gopinathan K.P. and Sunder C.S., *Metallic Glasses-Production, Properties and Applications*, (ed.) T.R. Anantharaman, TransTech. Pub., 1984, p.115.
- Greer A.L., Ann. Rev. Mat. Sc. 17 (1987) 219.
- Greer A.L., Lin C.J. and Spaepen F., *Rapidly Quenched Metals IV*, (eds.) T.Masumoto, K.Suzuki, 1982, p.567.
- Grant W.A., Ali A., Chadderton L.T., Grundy P.J. and Johnson E., Nature, 187 (1960) 63.
- Grest G.S. and Cohen M.H., Phys. Rev. B 21 (1980) 4113.
- Gupta D., Tu K.N. and Asai K.W., Phys. Rev. Lett. 35 (1975) 796.
- Gupta D., Tu K.N. and Asai K.W., Thin Film Solids 90 (1982)131.
- Hafner J. and Heine V., J. Phys. F 13 (1983) 2479.
- Hafner J., Pasturel A. and Hichter P., J. Phys. F 14 (1984) 1137.
- Hafner J., *Rapidly Quenched Metals V*, (eds.) S. Steeb and H Warlimont, Elsevier Science Publishers (1985), p.421.
- Hafner J., *Glassy Metals I*, (eds.) H. Beck and H.J. Güntherodt (Springer, Berlin) (1981), p.49.
- Haggstrom L., Granas L., Wappling R., and Devanarayanan, Phys. Scr. 7 (1973) 125.
- Hahn H., and Averback R.S., Phys. Rev. B, 37 (1988) 6533.
- Hahn H., Averback R.S. and Shyu H.M., J. less-common Metals, 140 (1988) 345.
- Heimendahl von L. and Hafner J., J. Phys. Rev. Lett. 42 (1979) 386.
- Hood G.M., J. Phys. F: Metal Phys. 8 (1978) 1677.
- Hood G.M., J. Nucl. Mater. 139 (1986) 179.
- Horvath J., Ott J., Pfahler K. and Ulfert W., Mat. Sci. Eng. 97 (1988) 409.
- Horvath J. and Mehrer H., Cryst. Latt. Def. and Amorph. Mat. 13 (1986) 1.
- Horvath J., Freitag K. and Mehrer H., Cryst. Latt. Def. and Amorph. Mat., 13 (1986) 15.

- Horvath J., Freitag K., and Mehrer H., in RQV (eds.) S. Steeb and H. Warlimont, North-Holland, 1985, 751
- Hoselitz A., Phys. Status Solidi A 53 (1979) K23.
- Hoshino K., Averbach R.S., Hahn H. and Rothman S.J., Defect and Diffusion Data, 59 (1988) 225.
- Hunger G., Fritsch H.U. and Bergmann H.W., Mat. Res. Soc. Symp. Proc. 28 (1984) 253.
- Ilonca G. and Florescu V., Mat. Sci. Eng. 99 (1988) 43.
- Inoue A., Chen H.S., Masumoto T. and Ajuria S.A., Sci. Rep. Res. Inst. Tohoku Univ., Ser.A, 32 (1985) 116.
- Johnson W.L., Atzmon M., van Rossum M., Dolgin B.P. and Yeh X.L, *Rapidly Quenched Metals V*, (eds.) S. Steeb and H. Warlimont, Elsevier Sci. Pub. BV, Amsterdam, 1985, p.1515.
- Jost W., *Diffusion in solids, liquids and gases*, Acad. Press Inc. New York, 1952.
- Kamal R., Bjarman S. and Wappling R., Phys. Scripta 23 (1981) 57.
- Kear B.H., Mayer J.W., Poate J.M. and Struti P.R., *Metallurgical Treatises*, (eds.) J.K.Tien and J.F.Elliott, American Institute of Mining, Metallurgical and Petroleum Engineers, Warrendale, PA., 1981, p.321.
- Kemeny T., Vincze I. and Fogarassy B., Phys. Rev. B 20 (1979) 476.
- Kijek M., D.Phil. Thesis, Sussex University (1984).
- Kimura M. and Yonezawa F., Springer Series in Solid State Science, 46 (1983) 80
- Kirchheim R., Sommer F. and Schluckebier G., Acta Metall. 30 (1982) 1059.
- Kirchheim R., and Huang X.Y., Phys. Stat. Sol. (b) 144 (1987) 253.
- Klein H.P., Ghafari M., Ackermann M., Gonser U., and Wagner H.G., Nucl. Instr. Methods 199 (1982) 159.
- Klement, W., Willens, R.H. and Duwez, P., Nature 187 (1960) 869.
- Komatsu T., Matusita K., and Yokota R., J. Non-Cryst. Solids 85 (1986a) 358
- Komatsu T., Sato S., and Matusita K., Acta Metall. 34 (1986) 1899.
- Köster U. and Herold U., *Glassy Metals I*, (eds.) H. Beck and H.J. Güntherodt, Springer, Berlin, 1981, p.225.
- Kubel Jr. E.J., Metal Progress 129 (1986) 61.
- Kulkarni V.N. and Singru R.M., Technical Report, I.I.T.Kanpur, TR/CNF/1987.

- Law V.J. and Bailey R.V., Chem. Eng. Sci. 18 (1963) 189.
- Lin S.T., Jang L.Y., and Chou L.S., Sol. State Comm. 38 (1981) 853.
- Lin C.J. and Spaepen F., Scripta Met. 17 (1983) 1259.
- Luborsky F.E., AIP Conf. Proc. 29 (1976) 209.
- Luborsky F.E. and Walter J.L., Mat. Sci. Eng. 35 (1978) 255.
- Luborsky F.E., Flanders P.J., Libermann H.H. and Walter J.L., IEEE Trans. Magn. MAG-15 (1979) 1961.
- Luborsky F.E., *Ferromagnetic Materials*, (ed.) Wolfarth P, North-Holland, Amsterdam (1979).
- Luborsky F.E. and Bacon F., *Rapidly Quenched Metals IV*, (eds.) T. Masumoto and K. Suzuki, Sendai, Japan, (1982), p.8561.
- Luborsky F.E., J. Appl. Phys, 54 (1983) 5732
- Luborsky F.E., *Amorphous Metallic Alloys*, Butterworths, London, 1983.
- Mallard W.C., Gardener A.B., Bess R.F., and Slifkin L.M., Phys. Rev. 129 (1963) 617.
- Manning J.R., *Diffusion Kinetics for atoms in Crystals*, Van Nostrand, Princeton, New Jersey, 1968.
- Marcus M. and Turnbull D., Mat. Sci. Eng. 23 (1976) 211.
- Margulies S. and Ehrman J.R., Nucl. Instr. and Methods 12 (1961) 131
- Marion J.B. and Young F.C., *Nuclear Reaction Analysis, Graphs and Tables*, Willey, New York (1968).
- Masumoto T., Kimura H., Inoue A. and Waseda Y., Mat. Sci. Eng., 23 (1976) 141.
- Mehl R.F., Trans AIME 122 (1936) 11.
- Mehrer H. and Dörner W., Defect and Diffusion Forum, 66-69 (1989) 189.
- Meng C. and Wang Y., J. Non-Cryst. Solids 81 (1986) 397.
- Misse U. and Methfessel S., *Rapidly Quenched Metals V*, (eds.) S. Steeb and H. Warlimont, Elsevier Sci.Pub., 1985.
- Mizgalski K.P., Inal O.T., Yost F.G. and Karnousky M.M., J. Mat. Sci. 16 (1981) 3357.
- Mössbauer R.L., Z. Physik 151 (1958) 124.
- Mrowec S.L., *Defect and Diffusion in Solids*, Elsevier Scientific Publishing Co. Amsterdam, Holland.

- Murch G.E. and Nowick A.S., *Diffusion in crystalline solids*, Acad. Press Inc., London, (1984).
- Nachtrieb N.H. and Handler G., *Acta Metall.*, 2 (1954) 797.
- Nagarajan T., Chidambaram Asari U., Srinivasan S., Sridharan V. and Narayanaswamy A., *Mat. Sci. Eng.*, 97 (1988) 355.
- Nagumo M. and Takahashi T., *Mat. Sci. Eng.* 23 (1976) 257.
- Narasimhan M., Allied Chemical Corp.: U.S. Patent No. 4142571 (March 6, 1979).
- Nowik I., Felner I., Wolfus Y. and Yeshurun Y., *J. Phys. F* 18 (1988) L181.
- Ok Hang Nam, Morrish A.H., *Phys. Rev. B* 22 (1980a) 3471.
- Ok Hang Nam, Morrish A.H., *Phys. Rev. B* 22 (1980b) 4215.
- Ok Hang Nam, Morrish A.H., *Phys. Rev. B* 23 (1981) 2257.
- Ok Hang Nam, Baek K.S., Kim C.S., *Phys. Rev. B* 24 (1981) 6600.
- Omari S., and Hashimoto Y., *Trans. J.I.M.* 18 (1977) 347.
- Oshima R. and Fujita F.E., *Jap. J. Appl. Phys.* 20 (1981) 1.
- Patterson J.P., and Jones D.R.H., *Acta Met.* 28 (1980) 675.
- Pfahler K., Horvath J., Frank W. and Mehrer H., *Rapidly Quenched Metals V*, (eds.) S. Steeb and H. Warlimont, Elsevier Sci. Publications (1985), p 755.
- Polk D.E., *Acta Metall.* 20 (1972) 585.
- Polk D.E. and Glessen B.C., *Metallic Glasses*, (eds.) J.J. Gilman, and H.J. Leamy, American Society of Metals, Metals Park, Ohio (1978), p.1.
- Pond Jr. R. and Maddin R., *Trans. Met. Soc. AIME* 245 (1969) 2475.
- Pond R.B., U.S. Patent No. 2976590 (March 28, 1961).
- Predecki P., Mullendore A.J., and Grant N.J., *Trans. Met. Soc. AIME* 233 (1965) 1581.
- Quivy A., Rzepski J., Chevalier J.P. and Yvonne C., *Rapidly Quenched Metals V*, (eds.) S. Steeb and H. Warlimont, Elsevier Sci. Pub. (1985), p.315.
- Ramanan V.R.V. and Fish G.E., *J. Appl. Phys.* 53 (1982) 2273.
- Ramchandrarao P., *Metallic Glasses: Production, Properties & Applications*, (ed.) T.R. Anantharaman, (1984), p.31.
- Ranganathan S. and Banerjee S., *Metallic Glasses: Production, Properties and Applications*, (ed.) T.R. Anantharaman, (1984) p.147.
- Reill W., Hoffman H. and Roll K., *J. Mat. Sci. Lett.* 4 (1985) 359.

- Robert-Austin W.C., Phil. Trans. Roy. Soc., London, A 187 (1896) 404.
- Robie R.A., Bethke P.M. and Beardsley K.M., *CRC Handbook of Chemistry and Physics*, 1979-80, p B-186.
- Rothman S.J., Nowick L.J. and Murch G.E., J. Phys. F 10 (1980) 383.
- Ruckman M.W., Levy R.A. and Kessler A., J. Non-Cryst. Sol. 40 (1980) 393.
- Rutherford E., Phil. Mag. 21 (1911) 669.
- Sadoc J.F., J. Non-Cryst. Sol. 44 (1981) 1.
- Sadoc J.F. and Wagner C.N.J., *Glassy Metals II*, (eds.) H.J. Güntherrodt and H. Beck (Springer, Berlin) (1983), p.51.
- Saegusa N. and Morrish A.H., Phys. Rev. B 26 (1982) 305.
- Sakamoto Y., Baba K., Kurahashki W., Takao T. and Takayama S., J. Non-Cryst. Sol. 61-62 (1984) 691.
- Sanchez F.M., Zhang Y.D., Budnick J.I. and Hasegawa R., J. Appl. Phys. 66 (1989) 1671.
- Schaafsma A.S. and Vander Woude F., *Amorphous Magnetism II*, (eds.) R.A. Levy and R. Hasegawa, Plenum Press, (1977), p.335.
- Schaafsma A.S., Ph.D. Thesis, Univ. of Groningen, 1981.
- Schuehnmacher J.J. and Guiraldeng P., Acta. Metall. 31 (1983) 2043.
- Schurer P.J. and Morrish A.H., J. Magn. Magn. Mat. 15-18 (1980) 577.
- Scott M.G., *Encyc. Mat. Sci. Engg.*, (ed.) M.B. Beyer, Pergamon Press, Oxford, 1986, p.2968.
- Scott M.G., *Amorphous Metallic Alloys*, (ed.) F.E. Luborsky, 1983, p.144.
- Seeger A. and Chik K.P., Phys. Stat. Sol., 29 (1968) 455.
- Seith W., *Diffusion in Metalen*, Springer, Berlin (1955).
- Sharma S.K. Ph.D. thesis, Aligarh University, (1986).
- Sharma S.K., Mukhopadhyay P., Kuldeep and Jain A.K., J. Non-Cryst. Sol. 94 (1987) 294.
- Sharma S.K., Banerjee S., Kuldeep and Jain A.K., Acta. Metall. 36 (1988a)
- Sharma S.K., Kuldeep and Jain A.K., Mat. Sci. Eng. 100 (1988b) 145.
- Sharma S.K., Banerjee S., Kuldeep and Jain A.K., Appl. Phys A45(1988c) 217.
- Sharma S.K., Banerjee S., Kuldeep and Jain A.K., J. Mater. Res. 4(1989)603.

- Sharma S.K., Kuldeep and Jain A.K., *Acta. Metall. Mater.* 38 (1990) 129.
- Sharma S.K., Kuldeep and Jain A.K., *Scr. Metall. Mater.* 25 (1991) 755.
- Sharon T.E. and Tsuei C.C., *Phys. Rev.* B5 (1972) 1047.
- Shenoy G.K. and Wagner F.E., *Mossbauer Isomer Shift*, North-Holland Pub. Co. Amsterdam, 1978.
- Singhal R. Ph.D. Thesis, IIT Kanpur, India, 1991.
- Singru R.M., Ramachandran T.R., in *Intl. Conf. on Progress in Metallurgical Research: Feb 11-15, 1985*, I.I.T., Kanpur, India.
- Sitek J. and Gabris F., *Nucl. Instr. Methods* 199 (1982) 187.
- Slifkin L., Lazarus D. and Tomizuka C.T., *J. Appl. Phys.* 23 (1952) 1032.
- Stelter E.C., Lazarus D., *Phys. Rev.* B36 (1987) 9545.
- Surinach S., Baro M.D. and Clavaguera N., *ibid* (1980) 323.
- Takacs L., Cadeville M.C. and Vincze I., *J. Phys. F* 5 (1975) 800.
- Takacs L., Hiltunen E.J. and Lehto J.A., *Rapidly Quenched Metals V*, (eds.) S. Steeb and H. Warlimont, *Els. Sci. Pub.* (1985).
- Takagi Y. and Kawamura K., *Trans. Japan Inst. Metals* 22 (1981) 677.
- Taniwaki M. and Maeda M., *Mat. Sci. Eng.* 99 (1988) 47.
- Taub A.I. and Spaepen F., *Acta. Metall.* 28 (1980) 1781.
- Taylor G.F., *Phys. Rev.* 23 (1924) 655.
- Thwaites D.I., *Rad. Res.* 95 (1983) 495.
- Tomizuka C.T., *Methods of Experimental Physics*, (eds.) K. Lark-Horovitz and Johnson, 6 (1959) 364.
- Tsao S.S., and Spaepen F., as quoted by Greer A.L., *J. Non-Cryst. Sol.* 61 (1984) 737.
- Tsuei C.C., Lilienthal H., *Phys Rev.* B13 (1976) 4899.
- Turnbull D. and Cohen M.H., *J. Chem. Phys.* 34 (1961) 120.
- Tyagi S., and Lord-Jr. A.E., *J Non-Cryst. Sol.* 30 (1979) 273.
- Ulfert W., *Diploma Thesis*, Stüttgart Universitat (1985).
- Valenta P., Maier K., Krönmüller H. and Freitag K., *Phys. Status Solidi B* 105 (1981a) 537.

- Valenta P., Maier K., Krönmüller H., and Freitag K., *Phys. Status Solidi B* 106 (1981b) 129.
- Van G.N., *Appl. Surf. Sci.* 26 (1986) 317.
- Volkert C.A. and Spaepen F., *Rapidly Quenched Metals VI*, (eds.) R.W. Cochrane and J.O. Ström-Olsen, *Mat. Sci. Eng.*, 97 (1988) 449.
- Wagner C.N.J., *Rapidly Quenched Metals V*, (eds.) S.Steeb and H. Warlimont, Elsevier Science Publishers (1985), 405.
- Walker L.R., Wertheim G.K., and Jaccarino V., *Phys. Rev. Lett.* 6 (1961) 98.
- Wehner C.K. and Anderson G.S., *Handbook of Thin Film Technology*, McGraw-Hill, New York, Ch.3., 1970.
- Wolny J., Zajac W. and Calka A., *Nucl. Instr. Meth.* 199 (1982) 179.
- Yamakawa K., Hohler B. and Kronmüller H., *Phys. Stat. Solidi, A* 111, (1989) 89.
- Yeh X.L., Samwer K. and Johnson W.L., *Appl. Phys. Lett.*, 42 (1983) 242.
- Yoon H.N., and Eisenberg A., *J Non-Cryst. Sol.* 29 (1978) 357.
- Zaluska A., Baran M. and Wronski Z., *Nucl. Instr. Methods*, 199 (1982) 187.
- Zaluska A. and Matyja H., *J. Mat. Sci.* 18 (1983) 2163.
- Zelinski P.G., Ostalek J., Kijek M. and Matyja H., *Rapidly Quenched Metals III*, vol I, (ed.) B. Cantor, The Metals Society, London (1978), p.337.
- Ziegler J.F., *Helium-Stopping powers and ranges in all elements* (Pergamon, New York, 1977)

# APPENDIX 1

## \*\*\* LINEAR REGRESSION ANALYSIS PROGRAM \*\*\*

\*\* PROGRAM TO CALCULATE THE ERRORS IN Q AND Do values \*\*  
 \*\* FROM THE ARRHENIUS PLOT, WITH/WITHOUT USING ERROR \*\*  
 \*\* IN THE D-VALUES \*\*

```

C          ** Define Parameters **
          DIMENSION WD(100),TEMPIN(100),DLn(100),TEMP(100),D(100)
          DIMENSION WEIGHT(100)
          CHARACTER*2 ANS
          CHARACTER*4 NAME
          CHARACTER*4 ELE
          CHARACTER*16 ALLOY
          DATA IY1,IY2/'Y','y'/
50         CONTINUE
C          ** Get the data file name and open input/output files **
          WRITE(*,2)
          FORMAT(1X,'GIVE FILE NAME, ELEMENT NAME, ALLOY NAME,',
1         'e.g., 79Pd Pd Fe79B16Si5')
          READ(*,3) NAME, ELE, ALLOY
          FORMAT(A4, A4, A16)
          OPEN(1,FILE='MG'//NAME//'.DAT')
          OPEN(2,FILE='MG'//NAME//'.Y.DAT')
          PRINT *, 'Give the number of data (x,y) points to read:'
          READ(*,*) N
          IF(N.EQ.0) GO TO 30
          WRITE(2,4) ELE, ALLOY
          FORMAT(//,5X,'DIFFUSION OF ',A4,' IN ',A16)
          WRITE(*,4) ELE, ALLOY
          WRITE(*,5)
          WRITE(2,5)
          FORMAT(4X,'-----')
          WRITE(*,6)
          WRITE(2,6)
          FORMAT(/,4X,'TEMP(K)',4X,'D(m.sq./s)',2X,'ERROR IN LnD',
1         ' values',/,27X,'(30% in D values)')
C          ** Read data from the input file and write in output file **
          DO 11 I = 1, N
          READ(1,7) TEMP(I), D(I), WEIGHT(I)
          FORMAT(F7.2, E15.4, F6.2)
          WRITE(2,8) TEMP(I), D(I), WEIGHT(I)
          WRITE(*,8) TEMP(I), D(I), WEIGHT(I)
          FORMAT(3X,F7.2, E15.4, 5X, F6.2)
C          ** Inverse the temperature (tempin) and take Ln of D (DLn) **
          TEMPIN(I) = 1/TEMP(I)
          DLn(I) = LOG(D(I))
          WD(I) = 1.
          IF (WEIGHT(I).NE.0) WD(I) = 1./(WEIGHT(I))**2
11         CONTINUE
  
```



```

C          ** OBTAIN WEIGHTED SUMS **
      SUM   = 0.0
      SUMX  = 0.0
      SUMY  = 0.0
      SUMX2 = 0.0
      SUMXY = 0.0
      DO 14 I = 1,N
      SUM = SUM + WD(I)
      SUMX = SUMX + TEMPIN(I)*WD(I)
      SUMY = SUMY + DLn(I)*WD(I)
      SUMX2 = SUMX2 + TEMPIN(I)*TEMPIN(I)*WD(I)
      SUMXY = SUMXY + TEMPIN(I)*DLn(I)*WD(I)
14  CONTINUE
      DIN = SUMX2*SUM - SUMX*SUMX
      ADIN = 1./DIN
C          ** Obtain Q/k (Qk) and Q and Ln Do (DoLn) and Do (D0) **
      Qk = (SUM*SUMXY - SUMX*SUMY)*ADIN
      DoLn = (SUMX2*SUMY - SUMX*SUMXY)*ADIN
      Q = -(Qk*0.8614)*1.0E-04
      D0 = EXP(DoLn)
C          ** Calculate errors in Q/k (errqk) and Ln Do (erdoLn) **
      ERRQk = SQRT(SUM*ADIN)
      ERDoLn = SQRT(SUMX2*ADIN)
C          ** Obtain the unweighted sums and the best fit chi-square value ( $\chi$ ) **
      CHI = 0.
      S1 = 0.
      S2 = 0.
      CHI2 = 0.
      DO 16 I=1, N
      S1 = S1 + (TEMPIN(I))**2
      S2 = S2 + TEMPIN(I)
      ANUM = Qk*TEMPIN(I) + DoLn - DLn(I)
      CHI = CHI + ANUM*ANUM*WD(I)
      CHI2 = CHI2 + ANUM*ANUM
16  CONTINUE
      SY = CHI2/(N-2)
      CHI = CHI/N
      WRITE(2,17) CHI
      WRITE(*,17) CHI
17  FORMAT(/,5X,'CHISQUARE FOR FIT = ',F7.5,/)
C          ** Obtain errors in Q using (eq1) and without using weightage in D (eq2) **
      DEL = N*S1 - S2*S2
      EA = SQRT(N*SY/DEL)
      EB = SQRT(SY*S1/DEL)
      EQ1 = (ERRQk*0.8614)*1.0E-04
      EQ2 = (EA*0.8614)*1.0E-04
C          **Calculate upper and lower limits of Ln Do value for both cases**
      B1 = DoLn + ERDoLn
      B2 = DoLn - ERDoLn
      B3 = DoLn + EB
      B4 = DoLn - EB
C          ** Calculate upper and lower limits of Do value for both cases**
      B1L = EXP(B1)
      B2L = EXP(B2)
      B3L = EXP(B3)
      B4L = EXP(B4)

```

```

DOU = B1L - D0
DOL = D0 - B2L
DOUU = B3L - D0
DOLL = D0 - B4L
C      ** Start writing results in output file **
      WRITE(*,18)
      WRITE(2,18)
18     FORMAT(1X,'RESULTS CONSIDERING WEIGHTAGE IN D-values!')
      WRITE(*,19) Q, EQ1
      WRITE(2,19) Q, EQ1
19     FORMAT(1X,'Q =',F5.2,'+/-',F4.2,' eV')
      WRITE(*,20) D0, DOU, DOL
      WRITE(2,20) D0, DOU, DOL
20     FORMAT(1X,'Do =',E9.2,' (+)',E9.2,' and (-)',E9.2,
1       ' (m.sq./s)')
      WRITE(*,21)
      WRITE(2,21)
21     FORMAT(/,1X,'RESULTS WITHOUT CONSIDERING WEIGHTAGE ',
1       'IN D-values!')
      WRITE(*,22) Q, EQ2
      WRITE(2,22) Q, EQ2
22     FORMAT(1X,'Q =',F5.2,'+/-',F4.2,' eV')
      WRITE(*,23) D0, DOUU, DOLL
      WRITE(2,23) D0, DOUU, DOLL
23     FORMAT(1X,'Do =',E9.2,' (+)',E9.2,' and (-)',E9.2,
1       ' (m.sq./s)')
C ** Calculate D-values at upper and lower limit of given temperature values. **
      D1 = D0*EXP(-Q*TEMPIN(1)/0.8614E-04)
      DN = D0*EXP(-Q*TEMPIN(N)/0.8614E-04)
      WRITE(*,24) TEMP(1), D1
      WRITE(2,24) TEMP(1), D1
24     FORMAT(/,1X,'D (AT', F5.0,'K) = ', E9.3,' m.sq./s')
      WRITE(*,25) TEMP(N), DN
      WRITE(2,25) TEMP(N), DN
25     FORMAT(1X,'D (AT', F5.0,'K) = ', E9.3,' m.sq./s',/)
C      ** restart the program for another set of data. **
      PRINT *, 'WANT TO ANALYSE ANOTHER DATA FILE ? GIVE Y or N'
      READ(*,32)IE
32     FORMAT(A1)
      IF(IE.EQ.IY1) GO TO 50
      CLOSE(1)
      CLOSE(2)
30     STOP
      END

```

**\*\* EXAMPLE OF INPUT FILE FOR LINEAR REGRESSION PROGRAM \*\***

723.00	3.000E-21	0.26
673.00	1.300E-21	0.26
623.00	0.400E-21	0.26
573.00	0.200E-21	0.26

**\*\* EXAMPLE OF OUTPUT FILE FOR LINEAR REGRESSION PROGRAM \*\***

DIFFUSION OF Pd IN Fe79B16Si5

TEMP(K)	D(m.sq./s)	ERROR IN LnD values (30% in D values)
723.00	0.3000E-20	0.26
673.00	0.1300E-20	0.26
623.00	0.4000E-21	0.26
573.00	0.2000E-21	0.26

CHISQUARE FOR FIT = 0.30800

RESULTS CONSIDERING WEIGHTAGE IN D-values!

Q = 0.66+/-0.08 eV  
 Do = 0.11E-15 (+) 0.39E-15 and (-) 0.86E-16 (m.sq./s)

RESULTS WITHOUT CONSIDERING WEIGHTAGE IN D-values!

Q = 0.66+/-0.07 eV  
 Do = 0.11E-15 (+) 0.25E-15 and (-) 0.77E-16 (m.sq./s)

D (AT 723.K) = 0.278E-20 m.sq./s  
 D (AT 573.K) = 0.174E-21 m.sq./s

TH  
539.7212

B223a

Date Slip

This book

date

PHY- 1992 - D - BAN A10